

Université du Québec
Institute National de la Recherche Scientifique
Centre Énergie, Matériaux et Télécommunications

In situ observation of laser induced crystallisation
in group IV semiconductors

Par
Liliya Nikolova

Thèse présentée pour l'obtention du grade de
Philosophiae doctor (Ph.D.)
en sciences de l'énergie et des matériaux

Jury d'évaluation

Président du jury et examineur interne	François Vidal Professeur, INRS Centre EMT
Examineur externe	Mohamed Siaj Professeur, Université du Québec à Montréal
Examineur externe	Nadi Braidy Professeur adjoint, Université de Sherbrook
Directeur de recherché	Federico Rosei Professeur et directeur, INRS Centre EMT

To my daughter
Never stop dreaming
Never stop moving

Abstract

The main objectives of this thesis were to study *in situ* the structure formation during laser induced crystallisation in group IV semiconductors. We were interested to reveal the sequence of change in the morphology during the growth of the different microstructures, to unveil the shape of the growth front during its propagation, to estimate the velocities of crystallisation and to shed light on the possible mechanisms of growth through estimation of the temperature within the films. For that, we used Dynamic Transmission Electron Microscopy (DTEM) because the technique offers the required combination of spatial and temporal resolutions for *in situ* visualisation of the phase transformation. We used free-standing and membrane-supported films with the goal of elucidating the influence of the supporting layer on the kinetics and thermodynamics of the phase transformation.

In the first part of this work, we studied the crystallisation dynamics in membrane-supported and self-sustained a-Ge films. We acquired time resolved images of the formation of the central nanocrystalline structure, the evolution of the size and the roughness of the crystallisation front during the two other structures growth i.e. dendritic and layered structure. This study allowed us to estimate the velocities of crystallisation and the evolution of the temperature within the film. We found that in the central region, nucleation from the bulk occurs at temperatures below the melting temperature of the crystalline material. We showed that the dendritic growth occurs by propagation of thin metastable liquid layer in front of the growing crystalline phase and is a result of high thermal instabilities at the growth front. We demonstrated that the growth of the layered structure takes place at temperature below the melting temperature of the crystalline material and proceeds in azimuthal direction, i.e. orthogonal to the direction of the net heat flow. However, the growth mechanisms remains similar to the dendritic growth because the heat diffusion can allow formation of very thin pocket-like layer to be formed and

propagate in the azimuthal direction. These findings allowed us to overturn earlier hypothesis based solely on the post-mortem equilibrium investigation of the structure.

In the second part of the thesis we studied the crystallisation dynamics in amorphous silicon. We showed that the formed structure is dependent on the fluence of the pump-laser. We demonstrated that at the fluences used in this study the process is melt-mediated favoring super-lateral growth. Nanocrystallization occurs at the periphery of the melted zone but with very limited extent. The crystallisation proceeds inward i.e. toward the center of the heated region resulting in the observed long-grained microstructure. Our observations are consistent with the earlier developed theory on super-lateral growth where the nucleation and nanocrystallisation occurs at the periphery of the heated region and the elongated grains are growing along the heat gradient i.e. toward the central part of the heated region. Our study contributed for better understanding of growth of these structures and permitted estimation of the evolution of the temperature within the film.



Liliya Nikolova
PhD student

Prof. Federico Rosei
Research supervisor

Acknowledgments

I would like to thank you to my supervisor professor Federico Rosei for his invitation to join the NanoFemtoLab group and giving me the opportunity to work on a multi-disciplinary collaborative project involving three major research institutions INRS and McGill University from Canada and Lawrence Livermore National Laboratory from USA. I am grateful for the financial support that he insured for all the trips to LLNL to perform the DTEM experiments and encouragement to present my results at national and international conferences.

Equally I would like to acknowledge the financial support and award that I received from the two major funding agencies in the country Natural Science and Engineering Research Council and Fonds de Recherche du Québec sur la Nature et les Technologies: the Alexander Graham Bell Canada Graduate Scholarship and Michael Smith Foreign Study Supplement Award from NSERC and the Doctoral Research Scholarship from FRQNT.

I want to express my gratitude to the DTEM group at LLNL namely to Dr. Thomas LaGrange for his time with me on the DTEM to run the experiments and his support for my visit during the summer of 2011 when I was able to operate the microscope by myself and to acquire more knowledge and experience on the OIM. Also, I highly appreciate all the enriching conversations that I had with him and Dr. Bryan Reed during the past years.

Also, I am grateful for the temperature modelling made at Dr. Bradley Siwick group at McGill University. A big thank to Mark Stern for his work.

I am grateful for the support that I received from Jean-Philippe Masse who is the TEM technician at École Polytechnique de Montréal and always was able to find time for my booking on the microscope and for lending me a hand with the alignments of the

instrument. I would like also to acknowledge the help for the e-beam equipment that I received from Dr. Richard Vernhes at the microfabrication facility at the same university.

I am thankful to Professor Guy Ross for all the scientific and not so scientific conversations that we had during the past years.

I would like also to acknowledge the help that I received from the administration at INRS namely Ms. Louise Hudon and Ms. Helene Sabourin.

It will be faire also to say thank you to my colleagues Thérèse Dembele and Afshin Dadvan for making me laugh even at rainy days.

At the end, I want simply to say to my family:

Thank you, for the understanding and being there for me!

Table of contents

Dedication	iii
Abstract	v
Acknowledgments	vii
Table of contents	ix
List of figures and tables	xiii
Chapter I – Introduction	1
1.1. Technological interest in germanium.....	1
1.2. Amorphous to crystalline transition in germanium.....	2
1.2.1. General background on a-Ge structure.....	2
1.2.2. Microstructures formed as a result of rapid crystallization.....	4
1.2.3. Theoretical descriptions of the amorphous to crystalline transition.....	6
1.3. Motivation and structure of the thesis.....	7
1.4. Bibliography.....	9
Chapter II – Experimental methods	15
2.1. Conventional TEM.....	15
2.1.1. Electron beam – sample interactions.....	16
2.1.2. Recent advances in conventional TEM.....	18
2.2. <i>In situ</i> TEM.....	18
2.2.1. Time resolved <i>in situ</i> TEM.....	19
2.2.2. Limitations related to the DTEM.....	21
2.3. Sample preparation.....	24
2.4. Bibliography.....	26

Chapter III – Crystallization in amorphous germanium films supported by silicon monoxide membrane.....	31
3.1. Microstructures formed.....	32
3.2. Investigation of the nucleation and nanocrystallization processes in a-Ge/SiO....	34
3.2.1. Evolution of the sizes of the nanocrystals with time and error analysis.....	34
3.2.2. Estimation of the nucleation rate.....	38
3.3. Investigation of the explosive crystallization in a-Ge/SiO in Zone II and III.....	40
3.3.1. Zone II.....	40
3.3.1.1. Evolution of the shape of the crystallization front with time and its roughness	42
3.3.2. Zone III.....	42
3.4. Discussion.....	47
3.4.1. Zone I.....	48
3.4.2. Zones II and III.....	51
3.5. Conclusion.....	61
3.6. Bibliography.....	63
Chapter IV- Crystallization in self-sustained amorphous germanium films.....	69
4.1. Microstructures formed.....	70
4.2. Formation times of the microstructures, shape of the growth front during propagation and respective velocities of crystallization.....	71
4.2.1. Zone I.....	71
4.2.2. Zone II.....	73
4.2.2.1. Shape of the crystallization front during its propagation and analysis of its roughness.....	73
4.2.2.2. Evolution of the mean length of Zone II in radial direction.....	76
4.2.2.3. Velocities of crystallization and error analysis.....	76
4.2.3. Zone III.....	78
4.2.3.1. Velocities of crystallization and error analysis.....	83
4.3. Discussion.....	84
4.3.1. Zone I.....	84
4.3.2. Zone II.....	85

4.3.2.a. Dendritic growth model (DG).....	89
4.3.2.b. Model of heat diffusion and generation in thin films (HD>F).....	90
4.3.3. Zone III.....	93
4.4. Conclusion.....	95
4.5. Concluding remarks on crystallization process observed in germanium.....	95
4.6. Bibliography.....	98
Chapter V – Crystallization in amorphous silicon films deposited onto silicon dioxide	
windows.....	101
5.1. Microstructures formed.....	102
5.2. Effect of the pump laser fluence on the post mortem structure.....	103
5.3. Time resolved study of the amorphous to crystalline phase transition in a-Si/SiO ₂	106
5.3.1. Fluence 130 mJ/cm ² ± 5%.....	107
5.3.2. Fluence 140 mJ/cm ² ± 5%.....	108
5.3.3. Fluence 155 mJ/cm ² ± 5%.....	109
5.3.4. Fluence 180 mJ/cm ² ± 5%.....	110
5.4. Discussion.....	112
5.5. Conclusion.....	118
5.6. Concluding remarks on the crystallization processes observed in germanium and silicon.....	119
5.7. Bibliography.....	122
General conclusion and outline.....	125
6.1. Objectives.....	126
6.2. Main results.....	128
6.3. Original contributions of the thesis.....	129
6.4. Perspectives.....	132
6.5. Bibliography.....	132
List of publications.....	135
Statement of Originality.....	137
Résumé en français.....	141

Annex A – Thermal modeling developed by M. Stern at McGill University under the supervision of prof. B. Siwick based on the DTEM images acquired by the author of the present work..... 159

Annex B – Thermal modeling developed by S. McGowan at McGill University under the supervision of prof. B. Siwick based on the DTEM images acquired by the author of the present work..... 167

List of figures and tables

List of figures

- Figure 1. Schematic representation of the free energy in the amorphous solid (blue curve) and the crystalline solid allowing crystallization to occur below the temperature for melt of the crystalline material (c-Ge and l-Ge are used to denote crystalline and liquid germanium respectively). Supercooled liquid may exist at temperature between the melting temperature of the amorphous material (T_{ma}) and the melting temperature of the crystalline material (T_{mc}). Figure adapted from [30]..... 3
- Figure 2. Conventional transmission electron microscopy (TEM) bright field (BF) image showing the three qualitatively distinct morphological regions produced after single-shot nanosecond laser induced crystallization in a-Ge. Radial symmetry is observed due to the circular laser spot used to initiate the crystallization. The observed three morphologies are denoted on the figure as follows: central coarse nanocrystalline structure (Zone I), large radially elongated crystals (Zone II) and the layered structure (Zone III). False coloring is used to accentuate the different morphologies. Figure reprinted with permission from [42]..... 5
- Figure 3. Schematic representation of the co-propagation of the two interfaces i.e. amorphous-liquid and crystal-liquid with a possible profile of the temperature. Figure adapted from [38] and [40]..... 6
- Figure 4. Possible interactions of the incident electron beam with the sample. The indicated direction for each signal shows where the signal is the strongest or where it is detected. Figure adapted from [1]..... 17

- Figure 5. Schematic representation of the DTEM developed at LLNL. The position of the molybdenum mirror is given on right instead in the electron beam path for more clarity of the pathways of the laser and electron beams. The inset gives a realistic representation of the cathode-drive laser beam and the mirror spatial positions. Figure adapted from [24]..... 20
- Figure 6. Conventional W-filament (left) and Ta-disc (right) used as effective photoemission electron source as offered by Kimball Physics Inc. [37] 23
- Figure 7. Configuration of the samples from left to right: self-sustained 110 nm a-Ge / 150-mesh Cu grid; 110 nm a-Ge / 40 nm SiO / 300-mesh Cu grid; 130 nm a-Si / 50 nm SiO₂ / Si substrate..... 25
- Figure 8. Partial view of the full microstructure formed after single-shot laser-induced crystallization in a-Ge/SiO. The central coarse nanocrystalline region (*Zone I*), LREC (*Zone II*), layered structure (*Zone III*) and the remaining amorphous material are annotated on the micrograph. The block images on right give magnified views of the morphologies observed for the respective zones..... 33
- Figure 9. Typical selective area diffraction pattern (post mortem) from Zone I showing random orientation of the crystals. Only the most intense diffraction rings are indexed on the micrograph..... 34
- Figure 10. Time-resolved images of the crystallization process in a-Ge/SiO in the central part of Zone I. The time delays are denoted at the upper right corner of each block image. The images denoted with “0 ns” and “∞ ns” show the structure of the film prior the crystallization and at the end of the process respectively. The scale bar is the same for all images and is given in the first block image (up-left). Figure reprinted with permission from [17] 35

Figure 11. Effect of the spatial superposition of particles in a TEM image and automatic size measurement and count of the particles. In the cross sectional view two particles are present but in the top view (which is the view in the images of this study) they might appear as one particle. Conventional bright field TEM (BFTEM) image would reveal that these are two particles. However, a DTEM image most likely would show them as one due to its lower spatial resolution arising from the lower number of electrons to form an image which, also results in lower contrast of the images and the dynamic operation of the instrument..... 37

Figure 12. Mean size of the nanocrystals in Zone I at different time delays for a-Ge/SiO. The long error bars (in grey color) represent the standard deviation of the data. The short error bars (in black) represent the standard error for the calculated mean size of the grains. The intersection of the linear fit (red line) and the polynomial fit (blue curve) allows estimation for the time for complete crystallization in this region. Figure adapted from [17] 38

Figure 13. Evolution with time of the number of nanocrystals per $1 \mu\text{m}^2$ in Zone I at different time delays for a-Ge/SiO at 128 mJ/cm^2 . The red curve shows the trend in the evolution. The error bars give the fluctuation of the number of nanocrystals for the same delay but at different regions on the sample. Figure adapted from [17]..... 39

Figure 14. About four LRECs growing from one nucleation center. The visible boundaries of the LREC coming from the nucleation center are pointed with magenta arrows..... 41

Figure 15. Time-resolved images of the LREC growth showing the shape of the crystallisation front during its propagation for a-Ge/SiO. The time delays are denoted in the upper right corner of each block image. The scale bar is the same and is given in the first block image (left)..... 41

Figure 16. Procedure applied for extraction of the RMS of the roughness of the growth front during its propagation (400 ns delay image was used in this figure). A) Outline of the growth front directly on the image (accentuated in yellow). B) Plot of the growth front (black curve) with parabolic fit (red curve)..... 42

Figure 17. Evolution of the RMS of the roughness of the growth front in Zone II for a-Ge/SiO and hypothetical tendency of the evolution (red curve)... 43

Figure 18. A) Bright field image of the end of the dendritic region (Zone II) and the beginning of the layered structure (Zone III). Scale bar: 500 nm. B) SAED pattern from the area surrounded by the white circle in A)..... 44

Figure 19. Post mortem images of two experiments presenting the width of Zone III for a-Ge/SiO to be variable (image A and B) as well as different width of the zone within the same experiment (image B shows about eight layers on the left side of the image and only four on the right side). The scale bar is the same for the two micrographs and is 5 μm 44

Figure 20. A) & C) Time-resolved images of the layered structure for a-Ge/SiO taken at 8500 ns and 7500 ns delays showing the azimuthal direction of growth in this structure (indicated by the arrows in all the images). B) & D) False color images showing overlay of the time-resolved and the corresponding post mortem image. The time-resolved image appears in magenda while the post mortem image in grey. The scale bar is the same for all the images and is 5 μm (given in block image B)..... 46

Figure 21. A) Time-resolved images of the layered structure for a-Ge/SiO taken at a 5500 ns delay showing the simultaneous growth of at least five layers. The dashed red arrows indicate the direction of the growth of the layers (the arrows are placed slightly above the layers for better clarity of the

figure). B) False color image showing an overlay of the time-resolved image with the corresponding post mortem image. The time-resolved image appears in magenta while the post mortem image in grey. The arrows are used as guide for the eye for the direction of the growth of the layers. The scale bar is the same for the two images and is 5 μm (given in block image A)..... 47

Figure 22. Schematic representation of the Gaussian distribution of the energy in the laser beam within the spot (black curve) and hypothetical responsive distribution of the total absorbed energy in the film over the laser spot (red curve) in normal direction to the sample's plane which will lead to more uniform absorption of the laser beam from the sample..... 50

Figure 23. Representation of Mullins-Sekerka thermal instability. A) Direction of the solidification front advancement in the supercooled liquid. B) Direction of the heat flow from the solid phase toward the supercooled liquid. C) Creation of a protrusion due to a nucleation center. D) Schematic representation of the heat flow direction at the dendrite's tip and the temperature difference where v is the velocity of growth, T_i is the temperature at the interface, T_{mc} is the temperature for melt of the crystalline material, T_∞ is the temperature far from the dendrite's tip and r is the radius of the tip. Figure adapted from [54] (A-C) and [51] (D)..... 55

Figure 24. Post mortem image of Zone II. Red circles outline some of the dendrites with tips with radii from left to right $\sim 1.8 \mu\text{m}$, $\sim 1.3 \mu\text{m}$, and $\sim 1.6 \mu\text{m}$. The scale bar is 2 μm 57

Figure 25. Evolution of the circularly symmetric radial temperature distribution in the film, $T(r)$ in Zones II and III in the vicinity of the crystallization front for 150 ns time-steps through Zone II and 1.8 μs time-steps through Zone III. The radial position of the crystallization front at each

time is indicated with a grey circle. The temperature decrease through Zone II approximately follows the decrease in $T(r)$ due to the Gaussian distribution of laser deposited energy (dotted baseline). The slower net radial crystallization through Zone III provides a better match with thermal diffusion and results in an approximately constant front temperature. The abrupt transition in crystallization dynamics occurs once $T(r)$ drops below a threshold for the radial ELPC process to occur.

Figure reprinted with permission from [57]..... 59

Figure 26. Partial view of all the microstructures formed after single shot laser induced crystallisation in 110 nm self-sustained a-Ge film. The white arcs give the approximated boundaries of the different morphologies i.e. the regions of the coarse nanocrystals (*Zone I*), large radially elongated crystals (LREC) (*Zone II*), layered structure (*Zone III*) and the remaining amorphous material (*A*). The regions are annotated in the upper part of the micrograph..... 70

Figure 27. Time resolved images of the crystallization process in self-supported a-Ge films in Zone I where the laser beam has deposited its energy. Nanocrystals are considered to be the dark features seen in the images. The large light color features mostly appearing as part of a ring next to the dark features (pointed with red arrows) are pores forming due to densification of the amorphous material upon its crystallization. The time delay is denoted in the upper right corner of each block image. The first image denoted with “0 ns” shows the film prior the crystallization, while the post mortem image i.e. at the end of the crystallization is denoted with “∞ ns”. The scale bar is the same for all images and is given in the first block image (up-left)..... 72

Figure 28. Time resolved images of the growth in Zone II showing the shape of the crystallisation front during its propagation. The time delays are

	denoted in the upper right corner of each block image. The annotation “∞ ns” indicates the post mortem image i.e. at the end of the crystallisation. The scale bar is given in each block image.....	74
Figure 29.	Evolution of the RMS of the roughness of the growth front in Zone II with time. The red curve shows the trend in the evolution.....	75
Figure 30.	Example for determination of the mean length of LREC in the time-resolved images. The green curve represents the beginning of the growth while the red curve gives the position of the growth front. This figure shows an image taken at 150 ns delay.....	77
Figure 31.	Evolution of the mean length of Zone II in radial direction. The error bars are coming from the uncertainty related to the measurement and the calculation of the mean length of Zone II in radial direction. The red curve represents the tendency seen in the increase of the mean length. The confidence band at 95 % is delimited by the green curves....	77
Figure 32.	Evolution of the average velocity of the growth in Zone II with time. The red curve shows the derivative of the trend curve used for fitting of the data of the position of the growth front with time in radial direction (see Figure 31). The green curves represent the upper and lower confidence bands of the trend curve at 95 %.....	78
Figure 33.	Conventional TEM high magnification image of the layered structure showing the textured nanocrystalline bands (pointed with white arrows) and the large tangentially oriented crystals bands (pointed with red arrows). Defects present in the film prior the laser heating are also visible (pointed with black arrows).....	80
Figure 34.	A) High magnification bright field image of the nanocrystalline band.	

B) Corresponding dark field image near the same location of the sample shown in A with slight shift to show the nanocrystalline band and the remaining amorphous material (the same magnification was kept as for image A) 80

Figure 35. Post mortem images of the layered structure in Zone III. A) & B) show visibly “thin”/“thick” LTOC bands to be formed at various positions in the layered structure. Some of the “thin” LTOC bands are highlighted directly on the image with solid red lines, while some of the “thick” layers are highlighted with dashed red lines. Images A) & B) show variable width of Zone III for different experiments as well as within the same experiment (A). See text for more details. Images A) & C) were obtained post-mortem by DTEM while image B) was obtained post-mortem by conventional TEM. All the scale bars are 5 μm 81

Figure 36. A) & C) Time-resolved images of the layered structure with the corresponding post mortem ones. The arrows indicate the direction of growth of the LTOC. B) & D) False color images showing an overlay of the time-resolved image appearing in red and the corresponding post mortem image appearing in yellow. The scale bar is of 2 μm in all the images... 82

Figure 37. A) TR image at 4500 ns (left) showing the simultaneous growth of multiple layers. The dashed red arrows indicate the direction of the growth of the layers (the arrows are placed slightly above the layers for more clarity). B) An overlay of the TR image and the corresponding post mortem image. The time-resolved image appears in magenta while the post mortem image in grey. The arrows are used as guide for the eye for the direction of the growth of the layers. The scale bar is the same for the two images and is 5 μm (given in block image A)..... 83

Figure 38. Evolution of the average radial velocity of growth in Zone III obtained from the discrete derivative of the growth front position. The red curve

shows the derivative of the trend curve of the growth front position..... 85

Figure 39. Dependence of the crystal growth rate and the rate of nucleation with the temperature for glasses where $T_M = T_l$ is the melting temperature of the crystalline material, T_2 is the glass transition temperature and T_3 is the temperature at which the nucleation rate is above zero. According to the definition a metastable liquid layer may exist in the interval $T_2 < T < T_l$ (the temperature interval is delimited on the figure with dashed lines). Figure taken from [16]..... 87

Figure 40. Compiling plot of the estimated heat diffusion lengths (filled black circles with black curve showing the trend) along with the Zone II mean length in radial direction (unfilled black triangles with black curve showing the trend) and the velocity of crystallisation (filled blue square) obtained from the discrete derivative of the position of the growth front in time with blue curve showing the derivative of the trend curve of the position of the growth front in time. The transition and explosive growth regimes are denoted on the figure..... 88

Figure 41. Evolution of the temperature in Zone II at the vicinity of the growth front according to the solution of the heat diffusion and generation equation in two dimensions (HD>F). The red curve represents the tendency in the evolution. The error bars are coming from the uncertainty related to the estimation of the position of the growth front and the calculation of the heat diffusion lengths..... 91

Figure 42. Evolution of the mean velocity of propagation of the growth front in radial direction in Zone II with increase of the temperature of the film at the vicinity of the growth front. The black filled squares represent the velocity obtained from the discrete derivative while the black curve is the velocity obtained by the differentiation of the trend curve in the

evolution of the growth front in radial direction.....	92
Figure 43. Post mortem image of the end of Zone III (image on left). Three layers are visible in the image. The orientation of the texture of the nanocrystalline bands suggests that their formation probably occurs due to explosive crystallisation similar to that seen in Zone II. The wide white stripe seen in the image is a crack in the film.....	94
Figure 44. Comparison between the position of the growth front of Zone III in radial direction and the heat diffusion lengths for the time delays of formation of Zone III.....	94
Figure 45. Typical morphology formed in single shot laser induced crystallisation in 130 nm a-Si on 50 nm SiO ₂ . The regions of the micro- and nanocrystalline structures are indicated on the micrograph.....	102
Figure 46. Post mortem high magnification images of a-Si/SiO ₂ of the microcrystalline (A) and the nanocrystalline regions (C) with the respective diffraction patterns (B & D) (only the first three diffractions are annotated on the figure)	103
Figure 47. Full view of the microstructures formed for different fluences after single shot laser induced crystallisation in a-Si/SiO ₂ . For fluences of 165 mJ/cm ² and higher, the central region of with lighter contrast is formed probably due to melting of the a-Si film. The large dark features seen in these micrographs are silicon droplets that crystallised upon cooling of the specimen. The scale bar is the same for all the images and it is given in the first block image. The fluences are indicated in each block image in the right upper corner.....	104
Figure 48. Mean length of the large crystals seen in the post mortem images of a-Si/SiO ₂ crystallised at different fluences. The red curve shows the	

tendency in the evolution of the mean length of the crystals with increase of the incident fluence..... 105

Figure 49. Time resolved images of the crystallisation in a-Si/SiO₂ at fluence of 130 mJ/cm². The time delays are shown in the upper right corner of each image. The ‘pm’ abbreviation stands for post mortem..... 107

Figure 50. Time resolved images of the crystallisation in a-Si/SiO₂ at fluence of 140 mJ/cm². The time delays are shown in the up-right corner of each image. The ‘pm’ abbreviation stands for post mortem..... 109

Figure 51. Time-resolved images of the crystallisation in a-Si/SiO₂ produced by a laser fluence of 155 mJ/cm². The time delays are shown in the upper right corner of each image. The ‘pm’ abbreviation stands for post mortem. The white arrows in the 200 ns time resolved image point the boundary from where the microcrystalline structure will grow. A similar boundary is clearly visible in the 300 ns delay image..... 110

Figure 52. Time-resolved images of the crystallisation in a-Si/SiO₂ at fluence of 180 mJ/cm². The time delays are shown in the upper right corner of each image. The ‘pm’ abbreviation stands for post mortem. The interface a-Si – partially melted Si is pointed with the white arrow on the two time resolved images..... 111

Figure 53. Analytical estimation of the evolution of the temperature in the depth of a-Si film at fluence 180 mJ/cm² assuming that the properties of the film do not change with time and with increase of the depth of the film. $t = 0$ corresponds to the temperature distribution immediately after the arrival of the laser pulse. Figure taken from [18]..... 113

Figure 54. Partial view image of the sample after irradiation with fluence of 180

mJ/cm². The red ellipse delimits the outer boundary of the region of complete melting of the film where the temperature was above the temperature for melt of silicon. The yellow ellipse delimits the outer boundary of the region of partial melting of the film. Beyond this limit, no melting of the material occurred..... 113

Figure 55. Temperature distribution within the 130 nm a-Si film in depth at different time delays where change in the optical and thermodynamic parameters of silicon with phase changes is assumed. Time zero is the beginning of the pump pulse, which has a duration of 15 ns at FWHM. Figure taken from [18]..... 114

Figure 56. Evolution of the temperature with the time in a-Si irradiated for different depths of the film at the melt boundary (A) and at the partially melted boundary (B). The equivalent pump laser intensity is also given in the graphs. Figure taken from [18]..... 116

Figure 57. Delamination of the a-Si film at fluence 135 mJ/cm². The images are denoted as follows: a) the sample prior the crystallisation, b) time resolved image at 100 ns delay showing the delamination of the a-Si film from the SiO₂ window, and c) the post mortem image where only small crystalline part of the film remained on the supporting window... 117

Figure 58. Dendritic growth in 110 nm a-Si film deposited onto 40 nm SiO at fluence of 150 mJ/cm² showing very large oscillations of the growth front. The delay is given in the left-upper corner of each micrograph..... 130

Figure 59. Formation of the layered structure in 110 nm a-Si film deposited onto 40 nm SiO at fluence 150 mJ/cm². The time delays are shown on left side images. The right side micrographs are the corresponding post-mortem images. The scale bar is 5 μm..... 131

List of tables

Table I. Comparative table on the crystallization behaviour for extracted and calculated data in free standing 110 nm a-Ge films and membrane supported 110 nm a-Ge / 40 nm SiO for the respective pump laser fluences.....	96
---	----

Chapter I

Introduction

1.1 Technological interest in germanium

Fifty years ago Gordon Moore defined the trend for the development of semiconductor devices [1]. Since then, a constant effort has been maintained to produce more compact, energy efficient and faster components mostly driven by economic considerations. For the past decades, silicon has been the main material incorporated in the design of electronic devices due to its ease of processing, good semiconducting properties and the good properties of its native oxide. However, recent prediction for attainment of maximal performance in silicon-based structures has prompted research into alternative materials compatible with the existing technology that could meet the requirements for faster devices with low cost of production [2]. Germanium, which is in the same group as silicon, is one of the targeted elements due to its lower bandgap and significantly higher carrier mobility than silicon¹ [3]. Historically, germanium was used as the active element in the fabrication of the very first diode and transistor [5] but the industry ultimately moved toward silicon due to the larger abundance of the element in nature and the stability of its oxide². The growing demand of today's market, however, has prompted renewed research on germanium. At present, this element finds applications in the fabrication of solar cells [6], infrared detectors [8] and high efficiency transistors [10] with ongoing fundamental research into topics such as laser processing of amorphous germanium (a-Ge) thin films for structural control [13], epitaxial growth on silicon substrates for decrease of the buffer layer thickness [11], [16], which typically is several microns and occurs as a result of the 4% lattice mismatch between Ge and Si leading to a very high density of defects in only a few monolayers [18], and investigation of the light emitting properties of germanium under strain [19] or germanium nanocrystals embedded in an insulating matrix [21].

¹ Germanium possess the highest hole mobility for all known semiconducting materials [3]

² Germanium oxides have been shown to be highly unstable [4]

1.2 Amorphous to crystalline transition in germanium

1.2.1 General background on a-Ge structure

One of the fundamental questions relating to a-Ge is that of its structure, and the prerequisites for a transition to the crystalline state of the material. It is well known that amorphous materials are in a metastable state. In contrast to crystalline solids, amorphous ones possess only short range order in their structure i.e. the nearest neighbours maintain on average a homogeneous interatomic distance but the periodicity in their arrangement rapidly disappears with increase of the number of atoms. Such a structure is similar to the structure of glasses, which are described as a ‘frozen’ liquid obtained by the rapid quenching of the liquefied material. A particular feature of glassy materials is their ability to undergo a phase transition to the crystalline state at temperatures above a critical temperature called temperature of the glass transition (T_g) but below the temperature for melting of the crystalline material (T_{mc}) ($T_g < T_{mc}$). Typically the glass transition temperature is in the range $1/3 T_{mc}$ to $2/3 T_{mc}$ depending on the cooling rate used for fabrication of the glass [23]. In the case of a-Ge, however, the temperature at which the amorphous to crystalline transition occurs is $T \approx 0.8 T_{mc}$ [24] which is slightly above the maximum of the typically seen range. This discrepancy could stem from the difference in the cooling rates used for fabrication of widely used glassy materials and the one used to obtain a-Ge. For instance, $10^6 - 10^8$ K/s cooling rates are used for the vitrification of most glass forming materials [25]. However, in the case of amorphous semiconductors like germanium, quenching of the liquid does not result in amorphous but in polycrystalline material. D. Adler suggests that this is a result from the nature of the germanium and silicon melt where “the short-range of liquid Ge and Si is metallic in nature” and, thus, preventing production of a-Ge by rapid quenching [27]³. Therefore, amorphous semiconductors are obtained by techniques such as e-beam evaporation or sputtering where the cooling rate is considered to be of the order of 10^{10} - 10^{12} K/s. Such high cooling rates used in the fabrication of these materials lead to a structure that allows the existence of the amorphous solid but a phase transition to the lower free-energy crystalline state can be induced at temperatures $T < T_{mc}$. It is also suggested that the methods to obtain the amorphous material can affect its properties [23], [26], [29].

³ It is known liquid germanium is metallic with approximately eight nearest neighbors [28], while crystalline and a-Ge four-coordinated covalent semiconductor.

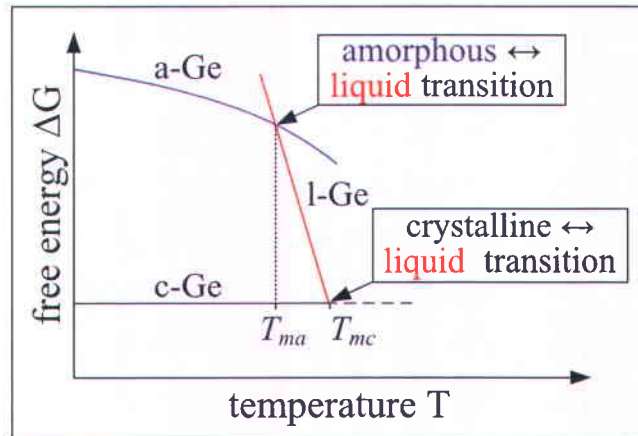


Figure 1. Schematic representation of the free energy in the amorphous solid (blue curve) and the crystalline solid allowing crystallization to occur below the temperature for melt of the crystalline material (c-Ge and l-Ge are used to denote crystalline and liquid germanium respectively). Supercooled liquid may exist at temperature between the melting temperature of the amorphous material (T_{ma}) and the melting temperature of the crystalline material (T_{mc}). Figure adapted from [30].

Crystallization in thin a-Ge films may be initiated at room temperature by heating or localised application of force with small, hard and sharp object on the surface of the material. The process is accompanied by the release of heat, sound and light and is referred as ‘explosive’ or avalanche crystallization [31]. Such behaviour is not limited to amorphous semiconductors. The phenomenon was observed for first time in antimony [31] but it is also common in metals [32] and insulators [35]. Figure 1 shows a qualitative representation of the free energy in the amorphous and the crystalline solid with the respective points of liquefaction. As the diagram shows, the amorphous phase is metastable at all temperatures with respect to the crystal since its free energy is always higher than c-Ge and there exists a pathway for amorphous to crystalline phase transition to occur below the melting temperature for the crystalline solid (T_{mc}). A prerequisite for such a transition is the significantly lower temperature for melting of the amorphous material (T_{ma}) in comparison with the temperature of liquefaction of the crystalline material T_{mc} . To describe the state of the material when heated at temperatures above the melting point of the amorphous solid but below the melting temperature for the crystalline one, i.e. $T_{ma} < T < T_{mc}$, the notion of ‘supercooled liquid’ is used. In this temperature range the material shows liquid-like

properties despite being at a temperature below the temperature of the liquid at thermodynamic equilibrium. Therefore, the liquid at a temperature situated in the range $T_{ma} < T < T_{mc}$ is supercooled in relation to the liquid defined for temperatures at or above T_{mc} . The state of the supercooled liquid is not well understood or described due to its short time of existence (estimated to be in the range of couple nanoseconds to couple hundreds picoseconds) and elevated temperatures, but it allows for the explanation of the observed velocities of crystallization. In fact, once the amorphous material is liquefied, the transition proceeds very rapidly. In the case of germanium such a liquid is estimated to exist for intervals as short as 10 ns from the observed high velocities of crystallization [37].

1.2.2 Microstructures formed as a result of rapid crystallization

Rapid high energy beam processing in silicon and germanium is widely used in modern semiconductor technology because of its low cost and additional control in the manufacturing sequences such as localised heating for diffusion of dopants or crystallization. The process has been exploited for the fabrication of solar cells, flat panel displays and infrared detectors, where crystallization in thin amorphous films is triggered by irradiation with a laser or electron beam. The resulting crystalline microstructure can be extremely complex with feature sizes ranging between ~ 10 nm and ~ 10 μ m growing from a few nanoseconds to a few tenths of microseconds after the arrival of the incident beam. The formation of these structures has been shown to be directly related to the details of the crystallization process, the heating geometry and a variety of possible instabilities through a subtle interplay of kinetics and thermodynamics [38].

Various investigations of this phenomenon have employed a number of geometries, including continuous wave laser beam scanning [44] and pulsed laser beam irradiation with either slit-shaped [38] or circular [40], [45] beam spot to elucidate the conditions for formation of the microstructures. Regardless of the heating pulse geometry, three distinct microstructures may grow separately or in a continuous fashion (Figure 2): (i) a coarse nano-crystalline structure, (ii) large elongated crystals referred to as a dendritic or columnar structure, and (iii) a layered, or ‘scalped’ structure, composed of alternating bands of fine nanocrystals and long microcrystalline grains oriented perpendicular to the direction of the crystallization front. Previous studies have shown that the coarse nanocrystalline structure

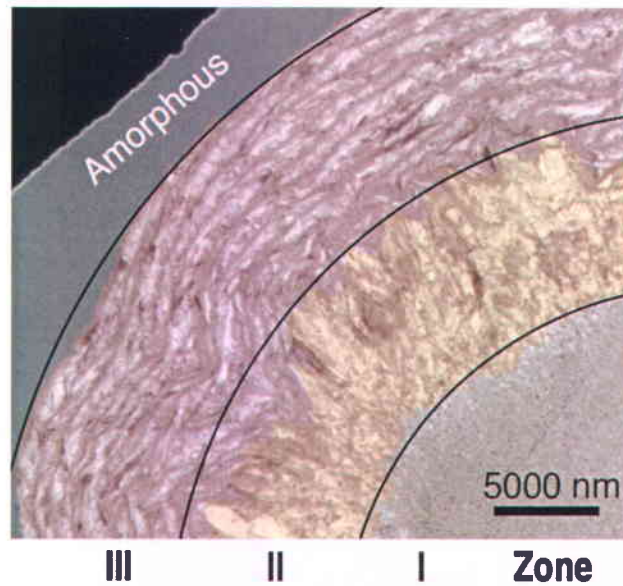


Figure 2. Conventional transmission electron microscopy (TEM) bright field (BF) image showing the three qualitatively distinct morphological regions produced after single-shot nanosecond laser induced crystallization in a-Ge. Radial symmetry is observed due to the circular laser spot used to initiate the crystallization. The observed three morphologies are denoted on the figure as follows: central coarse nanocrystalline structure (Zone I), large radially elongated crystals (Zone II) and the layered structure (Zone III). False coloring is used to accentuate the different morphologies. Figure reprinted with permission from [42].

forms within the bounds of the initial heating pulse [46] with growth speed of the nanocrystals ~ 4 m/s [47], while the large elongated crystals and the layered structure grow outside of the point of initiation with velocities of $8 - 15$ m/s and < 7 m/s, respectively [38], [39]. In all geometries, formation of the microstructures has been clearly shown to be dependent on the thermal balance with a key role played by the latent heat released at the crystallization front. In germanium, the equivalent local temperature rise⁴ is estimated to reach ~ 450 K [40], [48]. Therefore, over certain substrate temperature ranges this release of energy can be sufficient to sustain the propagation of the crystallization front for distances as long as several centimetres [38] until the heat loss in the substrate becomes predominant and the crystallization is arrested.

⁴ Obtained from the ratio of the released latent heat for the amorphous to crystalline transformation and the specific heat capacity of a-Ge

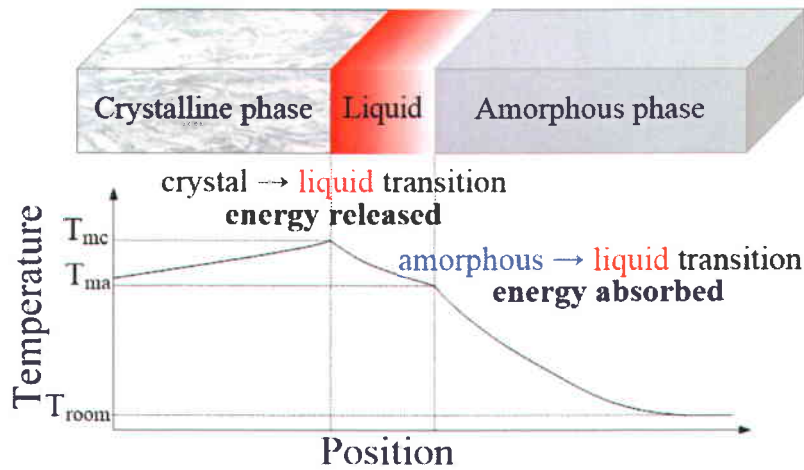


Figure 3. Schematic representation of the co-propagation of the two interfaces i.e. amorphous-liquid and crystal-liquid with a possible profile of the temperature. Figure adapted from [38] and [40].

1.2.3 Theoretical descriptions of the amorphous to crystalline transition

To describe these structures, two models were developed in the 1980s. One of the models suggests that different types of growth occur via solid state phase transition at particular thermal activation energies or large temperature instabilities at the growth front lead to the formation of different microstructures [48]. The other theory describes the process through existence of a metastable liquid layer propagating in front of the growing crystalline phase and involving the simultaneous propagation of two interfaces, a crystal-liquid interface at which crystallization occurs and heat is released and a liquid-amorphous interface some distance ahead from the other at which energy is absorbed (Figure 3). The existence of such a layer is possible due to the high difference in the melting temperatures (and enthalpies) between the amorphous and crystalline phases [30]. Different experimental and theoretical studies were conducted with the aim of estimating the dimensions [37], [40], [53], time of existence [40], [53], temperature [30], [39], [48], and the atomic coordination number [57] of the liquid layer. The melt-mediated model is primarily suggested as the growth mode of the large elongated crystals (Figure 2), thus describing the observed high velocities of crystallization. However, there is no consensus on the layered structure growth mechanism. Much remains to be understood about the formation of these structures, as evidenced by the ongoing debate surrounding matters as fundamental as shape of the

growth front during the growth of the large elongated crystals [45], [41] and the direction of growth in the layered structure region [38], [40].

1.3 Motivation and structure of the thesis

Laser annealing is commonly used in industry for the crystallization of thin amorphous films [58]. Despite its wide application, the process is not well understood leaving open questions on the thermodynamic pathways leading to the observed crystalline microstructures. With the renewed interest in laser induced crystallization in group IV semiconductors, the question of the mechanisms driving the phase transitions becomes of critical importance. As shown in the previous section, the process evolves in the range of a few nanoseconds to a few microseconds with growth of spatial features from nanocrystalline to microcrystalline range. Earlier studies by optical microscopy, time resolved optical transmissivity and reflectivity could not provide a complete picture of the growth mechanisms due to lack of spatial resolution [60]. Therefore, for in situ observation of the process a technique offering high spatial combined with high temporal resolution is required.

The present work describes an investigation of the evolution of the process in situ by dynamic transmission electron microscopy (DTEM). The technique provides resolution down to 10 nm (spatial) and 15 ns (temporal). The thesis will focus on laser induced crystallization in a-Ge with short comparative section describing laser induced crystallization in a-Si, similar to the industrially used process. This work aims to reveal the sequence in the growth of the different morphologies and to capture the shape of the crystallization front during its propagation for the different microstructures. In Chapter III a closer look will be taken at the crystallization behaviour in a-Ge films supported by SiO since the configuration mimics the approach currently used in industry. Calculation of the growth velocities and estimation of the temperature evolution according existing models and the observed microstructure will be given. The possible pathways for the phase transition will be discussed. In Chapter IV time-resolved investigation of the crystallization in self-supported layers of a-Ge will be presented. A comparison of the growth in the supported and self-sustained films will be given. This chapter will be followed by the

investigation of the crystallization in a-Si described in Chapter V. The mechanisms for this phase transition will be addressed. A comparison in the growth mechanisms observed in a-Ge and a-Si crystallization will be given. In the conclusion and summary of thesis, the original contributions of this work will be highlighted.

1.4 Bibliography

- [1] G. E. Moore, "Cramming more components onto integrated circuits," *Electronics*, vol. **38**, p. 1–4 (1965).
- [2] R. F. Service, "Is Silicon's Reign Nearing Its End?" *Science*, vol. **323**, p. 1000–1002 (2009).
- [3] R. Pillarisetty, "Academic and industry research progress in germanium nanodevices," *Nature*, vol. **479**, p. 324–328 (2011).
- [4] V. Craciun, I. N. Mihailescu, A. Luches, S. G. Kiyak, and G. N. Mikhailova, "Laser processing of germanium," *Advanced Techniques for Integrated Circuit Processing – Proceedings of the International Society for Optical Engineering* (editors: J. Bondur and T. Turner), vol. **1392**, p. 629–634 (1991).
- [5] APS News – This month in Physics History, November 17-December 23, 1947: Invention of the First Transistor
<http://www.aps.org/publications/apsnews/200011/history.cfm>
- [6] D. Crisp, A. Pathare, and R. C. Ewell, "The performance of gallium arsenide/germanium solar cells at the Martian surface," *Acta Astronautica*, vol. **54**, 83–101 (2003).
- [7] W. Guter, J. Schöne, S. P. Philipps, M. Steiner, G. Siefer, A. Wekkeli, E. Welsler, E. Oliva, A. W. Bett, and F. Dimroth, "Current-matched triple-junction solar cell reaching 41.1% conversion efficiency under concentrated sunlight," *Appl. Phys. Lett.*, vol. **94**, p. 223504-1–3 (2009).
- [8] R. Kaufmann, G. Isella, A. Sanchez-Amores, S. Neukom, A. Neels, L. Neumann, A. Brenzikofer, A. Dommann, C. Urban, and H. von Känel, "Near infrared image sensor with integrated germanium photodiodes," *J. Appl. Phys.*, vol. **110**, p. 023107-1–6 (2011).
- [9] L. Tang, S. E. Kocabas, S. Latif, A. K. Okyay, D.-S. Ly-Gagnon, K. C. Saraswat, and D. A. B. Miller, "Nanometre-scale germanium photodetector enhanced by a near-infrared dipole antenna," *Nature Photonics*, vol. **2**, p. 226–229 (2008).
- [10] S. C. Martin, L. M. Hitt, and J. J. Rosenberg. "p-Channel germanium MOSFET's with high channel mobility," *IEEE Electron Device Lett.*, vol. **10**, p. 325–326 (1989).
- [11] J. Mitard, B. De Jaeger, F. E. Leys, G. Hellings, K. Martens, G. Eneman, D. P. Brunco, R. Loo, J. C. Lin, D. Shamiryan, T. Vandeweyer, G. Winderickx, E.

- Vrancken, C. H. Yu, K. De Meyer, M. Caymax, L. Pantisano, M. Meuris, M. M. Heyns, "Record I_{ON}/I_{OFF} performance for 65 nm Ge pMOSFET and novel Si passivation scheme for improved EOT scalability," Tech. Digest IEEE Electron Devices Meeting, 2008. IEDM 2008. IEEE International, p. 873–876 (2008).
- [12] L. Gomez, C. Ni Chléirigh, P. Hashemi, J. L. Hoyt, "Enhanced hole mobility in high Ge content asymmetrically strained-SiGe p-MOSFETs," IEEE Electron Device Lett., vol. **31**, p. 782–784 (2010).
- [13] N. Misra, L. Xu, M. S. Rogers, S. H. Ko and C. P. Grigoropoulos, "Pulsed laser annealing of semiconductor structures for functional devices," Phys. Stat. Sol. (C), vol. **5**, p. 3264–3270 (2008).
- [14] W. Yeh, H. Chen, H. Huang, C. Hsiao, and J. Jeng, "Superlateral growth of a-Ge film by excimer laser annealing," Appl. Phys. Lett., vol. **93**, p. 094103-1–3 (2008).
- [15] O. Salihoglu, U. Kürüm, H. G. Yaglioglu, A. Elmali, and A. Aydinli, "Femtosecond laser crystallization of amorphous Ge," J. Appl. Phys., vol. **109**, p. 123108-1–6 (2011).
- [16] T. Irisawa, H. Miura, T. Ueno and Y. Shiraki, "Channel width dependence of mobility in Ge channel modulation doped structures." Jpn. J. Appl. Phys., vol. **40**, p. 2694–2696 (2001).
- [17] S. J. Koester, R. Hammond and J. O. Chu, "Extremely high transconductance Ge/Si_{0.4}Ge_{0.6} p-MODFET's grown by UHV-CVD," IEEE Electron Device Lett., vol. **21**, p. 110–112 (2000).
- [18] B. Streetman and S. Banerjee, Solid State Electronic Devices (6th edition), Pearson Prentice Hall, Upper Saddle River, N.J., USA (2006).
- [19] Nano Focus: Germanium lasers may close Moore's Gap. MRS Bulletin, vol. **37**, p. 988–988, doi:10.1557/mrs.2012.283 (2012)
- [20] L. Carroll, P. Friedli, S. Neuenschwander, H. Sigg, S. Cecchi, F. Isa, D. Chrastina, G. Isella, Y. Fedoryshyn, and J. Faist, "Direct-Gap Gain and Optical Absorption in Germanium Correlated to the Density of Photoexcited Carriers, Doping, and Strain," Phys. Rev. Lett., vol. **109**, p. 057402–1-3 (2012).
- [21] D. Riabinina, C. Durand, M. Chaker, N. Rowell and F. Rosei, "A novel approach to the synthesis of photoluminescent germanium nanoparticles by reactive laser ablation," Nanotechnology, vol. **17**, p. 2152–2155 (2006).

- [22] H.-C. Weissker, N. Ning, F. Bechstedt, and H. Vach, “Luminescence and absorption in germanium and silicon nanocrystals: The influence of compression, surface reconstruction, optical excitation, and spin-orbit splitting,” *Phys. Rev. B*, vol. **83**, 125413-1–6 (2011).
- [23] P. M. Ossi, Disordered Materials: An Introduction, 2nd ed., Springer-Verlag Berlin Heidelberg, (2006).
- [24] H. S. Chen and D. Turnbull, “Specific heat and heat of crystallization of amorphous germanium,” *J. Appl. Phys.*, vol. **40**, p. 4214–4215 (1969).
- [25] R. Zallen, The physics of amorphous solids, John Wiley & Sons, Inc., USA (1983).
- [26] N. E. Cusack, The physics of structurally disordered matter: An introduction, Adam Hilger – IOP Publishing, Philadelphia, PA, USA (1987).
- [27] D. Adler, Amorphous semiconductors, CRC Press, The Chemical rubber Co. Cleveland, OH, USA (1971).
- [28] V. M. Glazov, S. N. Chizhevskaya, and N. N. Glagoleva, “Physicochemical properties of molten elemental semiconductors: Silicon and germanium,” in A. Tybulewicz, ed., *Liquid Semiconductors* (Plenum Press), vol. **2** of *Monographs in Semiconductor Physics*, p. 55–83, (1969)
- [29] P. Nath and K. L. Chopra, “Thermal conductivity of amorphous and crystalline Ge and GeTe films,” *Phys. Rev. B*, vol. **10**, p. 3412–3418 (1974).
- [30] E. P. Donovan, F. Spaepen, D. Turnbull, J. M. Poate, and D. C. Jacobson, “Calorimetric studies of crystallization and relaxation of amorphous Si and Ge prepared by ion implantation,” *J. Appl. Phys.*, vol. **57**, p. 1795–1804 (1985).
- [31] G. Gore, “On a peculiar phenomenon in the electro-deposition of antimony,” *Philos. Mag.*, vol. **9**, p. 73–74 (1855).
- [32] V. M. Kuz'menko and V. I. Mel'nikov, “Avalanche crystallization of amorphous metals,” *Sov. Phys. JETP*, vol. **55**, p. 474–477 (1982)
- [33] V. M. Kuz'menko, V. I. Mel'nikov, and V. A. Rakhubovskii, “Mechanisms of spontaneous crystallization of amorphous metallic films,” *Sov. Phys. JETP*, vol. **59**, p. 612–617 (1984).
- [34] S. M. Zharkov and L. I. Kveglis, “Explosive crystallization initiated in nanocrystalline Iron-Carbon films by an electron beam,” *Doklady Physics*, vol. **47**, p. 281–285 (2002).

- [35] L. N. Aleksandrov and F. L. Edelman, "Shock crystallization in amorphous films of dielectrics," *Surf. Sci.*, vol. **86**, p.222–229, 1979.
- [36] G. J. Willems, D. J. Wouters, and H. E. Maes, "Explosive crystallization of amorphous Si₃N₄ films on silicon during silicon laser annealing," *J. Appl. Phys.* vol. **74**, p. 5196–5202 (1993).
- [37] G. H. Gilmer and H. J. Leamy, "An analysis of the explosive crystallization of amorphous layers," *MRS Symp. Proc.: Laser and Electron Beam Processing of Materials*, Cambridge, Massachusetts, USA, Academic Press, vol. **1**, p. 227–233 (1979).
- [38] A. Chojnacka and M. O. Thompson, "Morphological Instabilities during Explosive Crystallization of Germanium Films," *MRS Symp. Proc.*, vol. **648**, p. P11.12.1-1–8 (2001).
- [39] C. Grigoropoulos, M. Rogers, S. H. Ko, A. A. Golovin, and B. J. Matkowsky, "Explosive crystallization in the presence of melting," *Phys. Rev. B*, vol. **73**, p. 184125-1–15 (2006).
- [40] R. K. Sharma, S. K. Bansal, R. Nath, R. M. Mehra, K. Bahadur, R. P. Mall, K. L. Chaudhary, and C. L. Garg, "Electron beam induced explosive crystallization of unsupported amorphous germanium thin films," *J. Appl. Phys.*, vol. **55**, p. 387–394 (1984).
- [41] O. Bostanjoglo, R. P. Tornow, W. Tornow, "Nanosecond-exposure electron microscopy of laser-induced phase transformations," *Ultramicroscopy*, vol. **21**, p. 367–372 (1987).
- [42] L. Nikolova, T. LaGrange, M. J. Stern, J. M. MacLeod, B. W. Reed, H. Ibrahim, G. H. Campbell, F. Rosei, and B. J. Siwick, "Complex crystallization dynamics in amorphous germanium observed with dynamic transmission electron microscopy," *Phys. Rev. B*, vol. **87**, 064105–1-6 (2013).
- [43] T. LaGrange, B. W. Reed, M. K. Santala, J. T. McKeown, A. Kulovits, J. M. K. Wiezorek, L. Nikolova, F. Rosei, B. J. Siwick, G. H. Campbell, "Approaches for ultrafast imaging of transient materials processes in the transmission electron microscope," *Micron*, vol. **43**, p. 1108–1120 (2012).
- [44] R. L. Chapman, J. C. C. Fan, H. J. Zeiger, R. P. Gale, "Measurement of phase boundary dynamics during scanned laser crystallization of amorphous Ge films,"

- MRS Symp. Proc.: Laser and Electron Beam Solid Interactions and Materials Processing, Boston, Massachusetts, USA, Elsevier, vol. 1, p. 81–88 (1981).
- [45] O. Bostanjoglo, “Time-resolved TEM of pulsed crystallization of amorphous Si and Ge films,” *Phys. Stat. Sol. (A) Appl. Res.*, vol. 70, p. 473–481 (1982).
- [46] O. Bostanjoglo, F. E. Endruschat, W. Tornow, “Time resolved TEM of laser-induced phase transitions in a-Ge and a-Si/Al-films,” *MRS Symp. Proc.*, vol. 71, p. 345–350 (1986).
- [47] L. Nikolova, T. LaGrange, B. W. Reed, M. J. Stern, N. D. Browning, G. H. Campbell, J.-C. Kieffer, B. J. Siwick, and F. Rosei, “Nanocrystallization of amorphous germanium films observed with nanosecond temporal resolution,” *Appl. Phys. Lett.*, vol. 97, p. 203102-1–3 (2010).
- [48] D. A. Kurtze, W. Van Saarloos, J. D. Weeks, “Front propagation in self-sustained and laser-driven explosive crystal growth: Stability analysis and morphological aspects,” *Phys. Rev. B*, vol. 30, p. 1398–1415 (1984).
- [49] T. Takamori, R. Messier & R. Roy, “Phenomenology of the "explosive" crystallization of sputtered non-crystalline germanium films,” *J. of Mater. Sci.*, vol. 8, p. 1809–1816 (1973).
- [50] H. J. Zieger, J. C. C. Fan, B. J. Palm, R. P. Gale, R. L. Chapman, “Solid-phase crystallization produced by laser scanning of amorphous Ge films: the role of the latent heat in crystallization front dynamics,” *MRS Symp. Proc.: Laser and Electron Beam Processing of Materials*, Cambridge, Massachusetts, USA, Academic Press., vol. 1, p. 234–240 (1980).
- [51] T. Takamori, R. Messier & R. Roy, “New noncrystalline germanium which crystallizes “explosively” at room temperature,” *Appl. Phys. Lett.*, vol. 20, p. 201–203 (1972).
- [52] R. Messier, T. Takamori & R. Roy, “Observations on the "explosive" crystallization of non-crystalline Ge,” *Sol. Stat. Comm.*, vol. 16, p. 311–314 (1975).
- [53] R. B. Gold, J. F. Gobbons, T. J. Magee, J. Peng, R. Ormond, V. R. Deline, C. A. Evans, “Laser induced explosive radial crystallization of deposited Ge and Si thin films,” *MRS Symp. Proc.: Laser and Electron Beam Solid Interactions and Materials Processing*, Cambridge, Massachusetts, USA, Academic Press, vol. 1, p. 221–226 (1980).

- [54] H. J. Leamy, L. W. Brown, G. K. Celler, G. Foti, G. H. Gilmer, J. C. C. Fan, "Explosive crystallization of amorphous germanium films," MRS Symp. Proc.: Laser and Electron Beam Solid Interactions and Materials Processing, Boston, Massachusetts, USA, Elsevier, vol. **1**, p. 89–96 (1981).
- [55] H.-D. Geiler, E. Glaser, E. G. Gotz, G. M. Wagner, "Explosive crystallization in silicon," J. Appl. Phys., vol. **59**, p. 3091–3099 (1986).
- [56] E. J. Albenze, M. O. Thompson, P. Clancy, "Atomistic computer simulation of explosive crystallization in pure silicon and germanium," Phys. Rev. B, vol. **70**, p. 094110-1–10 (2004).
- [57] J. Koga, T. Yamaguchi, "Structural transitions in disordered phases of germanium under rapid quenching and pressuring," Phys. Chem. Glasses., vol. **46**, p. 425–432 (2004).
- [58] S. Uchikoga and N. Ibaraki, "Low temperature poly-Si TFT-LCD by excimer laser anneal" Thin Solid Films, vol. **383**, p. 19–24 (2001).
- [59] J. B. Boyce, P. Mei, R. T. Fulks, J. Ho, "Laser Processing of Polysilicon Thin-Film Transistors: Grain Growth and Device Fabrication," Phys. Stat. Sol. A, vol. **166**, p. 729–741, (1998).
- [60] C.-C. Kuo, W.-C. Yeh, J.-B. Chen, J.-Y. Jeng, "Monitoring explosive crystallization phenomenon of amorphous silicon thin films during short pulse duration XeF excimer laser annealing using real-time optical diagnostic measurements," Thin Solid Films, vol. **515**, p. 1651–1657 (2006).
- [61] G. Badertscher, R. P. Salathé and H. P. Weber, "Dynamics of laser crystallization in amorphous Ge films," Appl. Phys., vol. **25**, p. 91–93 (1981).
- [62] M. Mulato, D. Toet, G. Aichmayr, P. V. Santos, and I. Chambouleyron, "Laser crystallization and structuring of amorphous germanium," Appl. Phys. Lett., vol. **70**, p. 3570–3572 (1997).
- [63] M. Lee, S. Moon, C. P Grigoropoulos, "In situ visualization of interface dynamics during the double laser recrystallization of amorphous silicon thin films," J. Cryst. Growth, vol. **226**, p. 8–12 (2001).

Chapter II

Experimental methods

2.1 Conventional TEM

Transmission electron microscopy (TEM) is a powerful technique for the investigation of structure and chemical composition in materials and devices due to its exceptional spatial resolution [1]. The technique is based on the interaction of highly energetic electrons with a thin sample, taking advantage of the dual nature of the electron as a particle and as a wave. Thus, allowing image contrast to be formed due to diffraction to distinguish between crystalline and amorphous phase [2], to determine the crystalline structure [3] or to extract information on the chemical composition of the sample by quantification of the energy lost from the electrons during their pass through the sample [1].

The main drawback of TEM is the restriction on the samples that can be used with the instrument and the methods used for their preparation. The first condition for a sample to be appropriate for TEM observation is to be sufficiently thin so as to be transparent to electrons. In addition, depending on the analysis to be performed, the thickness has to be chosen so as to avoid multiple scattering of the incident beam within the sample. Obviously, any sample to be observed in the TEM has to be robust enough to endure electron beam heating i.e. to not exhibit a significant change in chemical composition or structure during or after TEM observation when successive observations are required. Although new methods have been developed for low-dose observations [4], not all materials may be used for TEM observation such as some polymers or living organisms. It is also worth noting that the sample must be no larger than a disc with diameter of 3 mm due to the design of the standard sample holders. The choice of method for preparation of the samples is also critical since uniform thickness and artifact-free samples are needed. Uniformity of the thickness in the area of observation is required to avoid mass-thickness effects leading to misinterpretation of the contrast in the micrograph. Also, artifacts such as implantation of Ga⁺ ions (if used for polishing of the sample) have to be taken into consideration upon analysis of the images or the chemical composition of the sample. Despite these limitations,

TEM is widely used in physics, chemistry, biology and materials science for its ability to deliver information on the chemistry and structure of the matter.

Hereafter, a short overview of the analysis that can be made in a TEM will be given with the objective of describing out the TEM-based techniques used in this work. An excellent reference on most of the types of imaging and spectroscopy that can be performed with a TEM instrument can be found in William and Carter [1]. The section to follow will present some of the recent advances in conventional TEM.

2.1.1. Electron beam – sample interactions

With the passage of a highly energetic electron from the incident beam through the sample, three types of interactions may occur: elastic scattering from the atoms of the sample (obeying Bragg's law), inelastic scattering and absorption of the electron. It is also possible for no interaction to occur. Figure 4 gives a schematic view of the highest probability direction for each of the signals or where they are detected. Since the primary detectors in the TEM are situated below the sample, a closer look will be taken at the possible information that can be extracted starting from the signals acquired below the sample.

The elastically scattered electrons participate in the formation of the dark field (DF) images. On other hand, if electrons from the directly transmitted beam are used to form an image, then bright field (BF) imaging is obtained (Figure 4 'direct beam'»). The direct beam accounts for most of the electrons below the sample; therefore, it is the strongest generated signal. Some researchers call "plane view" images the micrographs obtained with this beam. Elastically scattered electrons and the direct beam form the conventional high-resolution TEM (HRTEM) images. Rutherford scattering of the electrons is used in so-called Z-contrast imaging, taking advantage of the high angle of deviation of the incident electrons from the nuclei of the atoms in the sample, thus furnishing qualitative information on the chemical composition. Inelastically scattered electrons give information on the chemical composition of the sample by the quantity of energy they have lost during the passage through the sample; therefore, they are used in electron energy loss spectroscopy (EELS). Since heat is dissipated in all directions, it is detected both below and above the sample.

Above the sample, signals similar to those in scanning electron microscopy (SEM)

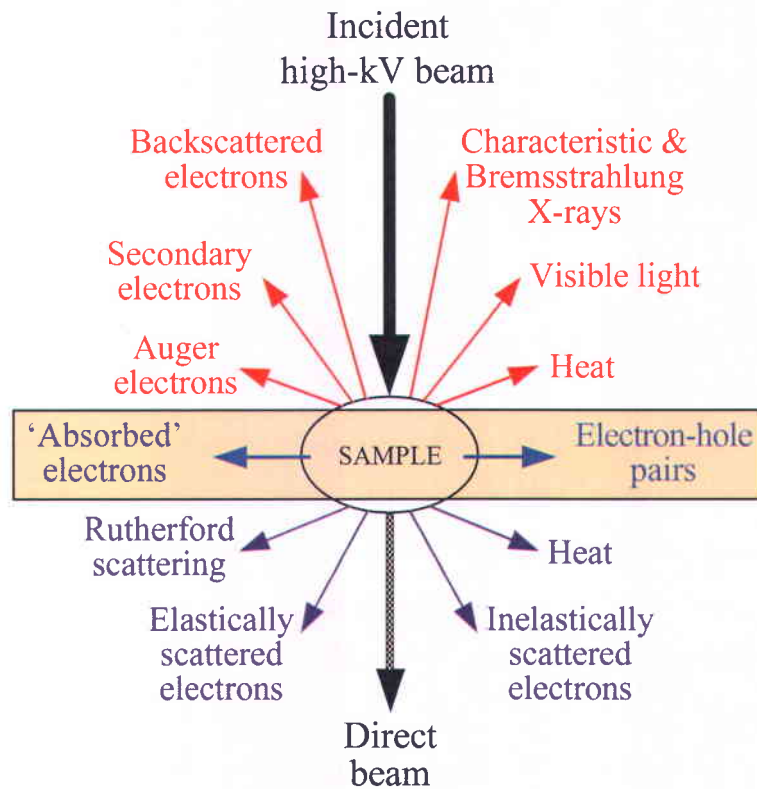


Figure 4. Possible interactions of the incident electron beam with the sample. The indicated direction for each signal shows where the signal is the strongest or where it is detected. Figure adapted from [1].

are generated: backscattered and Auger electrons along with the generated characteristic X-rays give information on the chemical composition of the sample, secondary electrons on the surface roughness of the sample, and visible light emission is used in investigation of the cathodoluminescence of the material. In contrast to SEM, in TEM the volume of interaction is very small, thus, the generated signals of backscattered, secondary and Auger electrons are much weaker. Therefore, their detection is more challenging in comparison with SEM. For modern TEM instruments advanced detection of the signals above the sample has been developed for the characteristic X-rays.

Finally, an electrical current can be detected at the plane of the sample due to the absorption of electrons from the incident electron beam or generation of electron-hole pairs in the material.

2.1.2. Recent advances in conventional TEM

In the conventional TEM imaging, aberration correction represents a major recent advance [5]. It is well known from light microscopy that the resolution limits depend on the light's wavelength [1], which stems from the Rayleigh diffraction criterion. Despite new approaches for improving the resolution in optical microscopy through near-field focusing and magnification by self-assembled nanoscale spherical lenses, the resolution cannot go down to angstrom level [7]. In the case of electron microscopy, because of the very small wavelength, the resolution is potentially very high. For comparison the wavelengths typically used in optical microscopy are in the range 200 nm to 800 nm, while a TEM operating at 200 kV offers 2.51 pm which is almost five orders shorter wavelength than one can obtain with an optical microscope [1]. However, due to imperfections in the electromagnetic lenses used in the TEM, aberrations limit the resolution to $\sim 1 \text{ \AA}$ [8]. Recent advances in correcting aberrations have permitted resolutions of 0.5 \AA [9], which help to detect single atoms (including hydrogen [10]), reveal buried defects and chemical variations in the sample [11] as well as three dimensional reconstruction of buried nanostructures through TEM imaging [14].

2.2 *In situ* TEM

Development of *in situ* TEM-based techniques attracts a lot of interest because TEM could bring crucial new insights on the structure of a material during a transformation, reaction to different environmental conditions or in response to an external field with extremely high spatial resolution. However, realisation of such experiments is not a trivial task because, in effect, the configuration has to be that of a 'small laboratory' inside the sample holder since the space between the two pole-pieces (where the sample is located) is very constricted [1], [16]. Therefore, a constant effort is maintained for development of new approaches for *in situ* studies. At present, *in situ* TEM developed from simple heating and cooling experiments to nanoindentation [17], environmental cells [18], high pressure simulation [19] and time resolved studies of nanosecond fast transformations in the materials by Dynamic TEM (DTEM) [20] or four dimensional ultrafast electron microscopy (4D-UEM) [22].

2.2.1. Time resolved *in situ* TEM

The instrument used for time-resolved *in situ* TEM investigations is a conventional transmission electron microscope which is modified to allow the visualisation of structural changes during transformation at the appropriate time and length scale. It is also known as pulsed photoelectron microscope. A schematic representation of such an instrument is given in Figure 5.

The concept of time-resolved TEM is to employ a packet of electrons with short duration as an imaging probe, so as to acquire a snapshot of the sample during its phase transition or reaction to an external field, i.e. the pump-probe approach is exploited. In conventional TEMs either thermionic or field emission electron guns are used. One way to obtain the short pulses needed for dynamic imaging is to use a different type of emission mechanism at the source of electrons. The electron pulses are generated via photoemission by irradiation of a photocathode with nanosecond or shorter UV laser pulses (called cathode-drive laser Figure 5). The laser beam is introduced into the column from outside and directed to the photocathode by a mirror (Figure 5 inset). Sample transformations are induced in the sample by a second laser (called sample-drive laser Figure 5) with wavelength and pulse duration depending on the process to be studied. Images of the structure are taken at different time delays after beginning of the transformation. Therefore, it is not mandatory to use an ultrafast electron detector system. With this type of modification to the microscope, it is possible to construct a movie which records the nanoscale motions as the process takes place.

There are two types of electron pulse generation proposed: either coherent electron packets containing less than 100 electrons per pulse, used in 4D-UEM [25] or a pulse with very high density of the charges, used in DTEM [21], [27]. Each method has advantages and drawbacks. In the first case the electron packets are liberated from the photocathode with femtosecond laser pulses, creating a train of electrons separated in time. The approach is *stroboscopic* since an image of a transient state is taken under multishot regime until the accumulation of a sufficient quantity of electrons is reached in the camera. That requires acquisition of a few million images in the camera i.e. a few million repetitions of the experiment. Therefore, the method is only applicable to studies of *reversible* processes (such as the dynamics of the reversible structural transition in VO₂ at 68 °C from

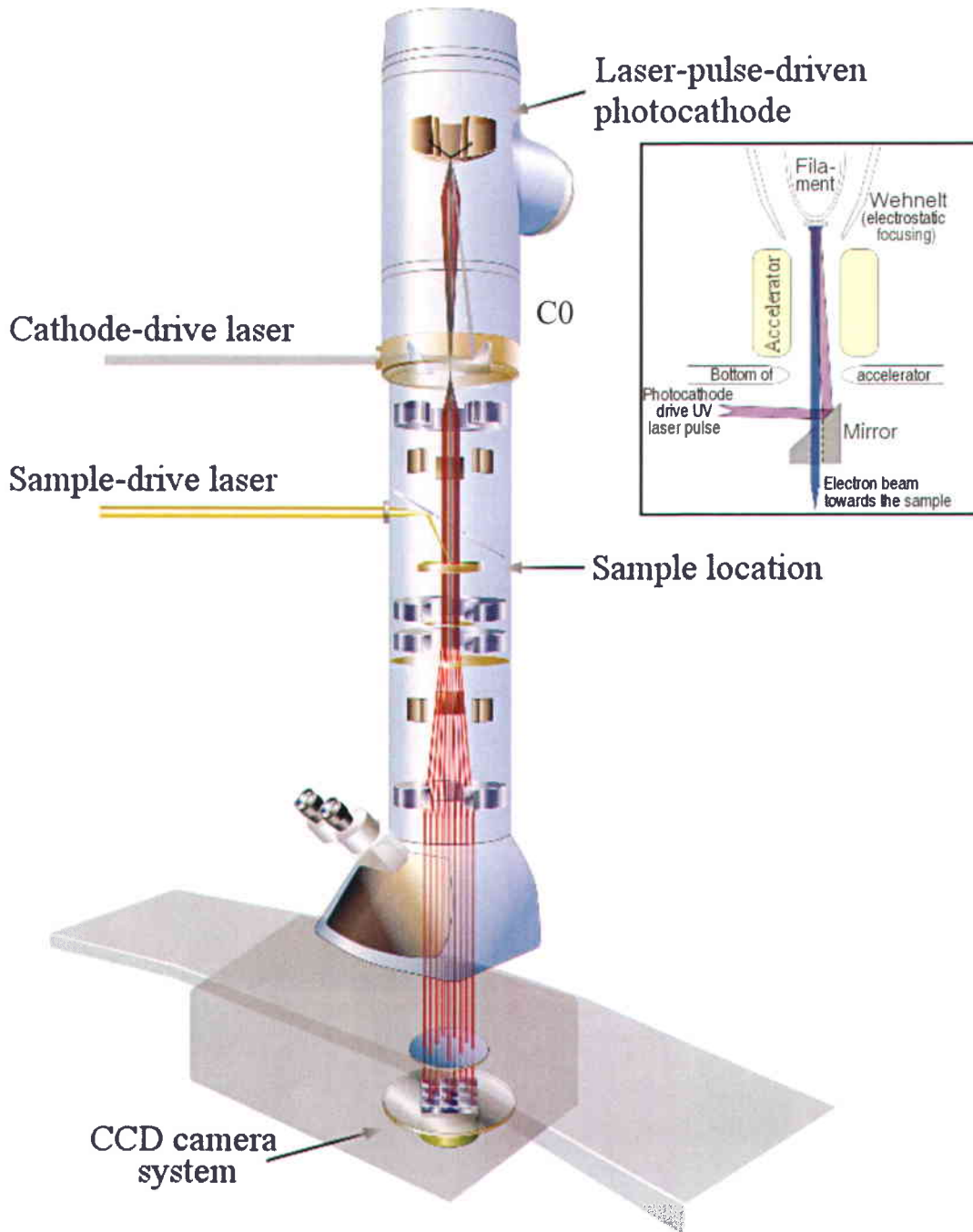


Figure 5. Schematic representation of the DTEM developed at LLNL. The position of the molybdenum mirror is given on right instead in the electron beam path for more clarity of the pathways of the laser and electron beams. The inset gives a realistic representation of the cathode-drive laser beam and the mirror spatial positions. Figure adapted from [24].

the low-temperature insulating or semiconducting monoclinic phase to the high-temperature metallic rutile tetragonal structure [28] or the dynamics of chemical bonding in materials [29]). For other cases, such as nucleation or crystallization of amorphous materials [30], phase transitions [31] or solid-state reactions [32], the 4D-UEM could not be used because the image cannot be accumulated on the same location on the sample. Hence, for studies of *irreversible* processes the second type of pulse generation is used i.e. the DTEM operating in a single shot mode with high density of charges. Since the image is formed with only one electron pulse, there is a limit on the minimum number of electrons per pulse to form the image; the value reported in the literature is 10^7 electrons per pulse [24]. At present, 10^9 electrons per pulse are generated in the DTEM at Lawrence Livermore National Laboratory (LLNL) [34] which was used for the work presented in this thesis.

Hereafter, a closer look will be taken on the limitations of the DTEM design and operation since this is the principal technique used in this work.

2.2.2. Limitations related to the DTEM

Since the DTEM operates in single-shot mode, there are some major limitations in the instrument function and a trade-off between the spatial and the temporal resolutions. In particular, the spatial resolution is degraded compared to that of a regular TEM. At first, the general limitations will be outlined and later more details will be given on the generation and collection of the photoelectrons, their trajectory through the column before the sample and detection of the electron beam after its interaction with the sample.

General limitations:

As already pointed out, for good image quality a density of at least 10^7 electrons per pulse is needed. Therefore, a high brightness electron source is required. In general, the collection efficiency for the emitted electrons is poor in the microscope. For conventional TEMs only 10% of the emitted electrons pass through the column [35]. This is not problematic for conventional TEM, since the images are acquired over a few seconds depending on the sample characteristics. Moreover, for very high beam quality most of the electrons that could cause aberrations are blocked with fixed apertures, over which the user has no control. Therefore, for conventional imaging, the electrons are relatively easily

guided through the lenses. In the case of the DTEM, the situation is completely different. The cathode-drive laser pulse generates a photoelectron current with spatial and temporal properties analogous to those of the incident laser pulse. Therefore, the electron beam (the packet of electrons) will have the same initial time duration of the pulse as the cathode-drive laser beam with energy distribution of the photoelectrons depending on the properties of the photocathode material and on the laser pulse. However, the generation of high brightness electron pulses is limited due to saturation of the current at the cathode, known as the Child–Langmuir effect [36]. After, due to the high charge density in the pulse, the electrons spread both in the longitudinal and the lateral direction of the electron beam axis, both homogeneously and inhomogeneously at various points in the electron-optical column. As a consequence, the number of electrons collected by the condenser system will be limited, particularly for the lateral outlying electrons, and the pulse is lengthened relative to its initial duration, causing degradation of the temporal resolution. Next, the TEM instrument is designed to filter a certain fraction of the electron beam by using a series of apertures, thus yielding a high quality beam at the sample (where far-from-paraxial electrons which generally give rise to additional aberrations have been removed). In the end, the influence of aberrations and accumulation of all these limitations will cause spatial degradation of the image quality. Since the image quality is directly related to the number of electrons acquired in the detector, high efficiency collection of electrons is needed.

Since electron microscopes are designed to focus and guide a very few electrons at a time through the column, the problem of how to handle a burst of 10^9 electrons per pulse is quite fundamental. One of the ideas applied on the DTEM instrument at LLNL is to install an additional lens immediately under the wehnelt, which increases the electron collection efficiency¹.

Choice of material for photoemitter:

The material of the photoemitter must have a high quantum efficiency assuring as many emitted electrons as possible with only one excitation pulse. Different materials have been used for this purpose. Bostanjoglo's research group at Optisches Institut der Technischen

¹ The lens below the wehnelt is placed in a collar extending the TEM column, which also allows more space to place the mirror that deflects the cathode-drive laser beam towards the electron source. The position of this lens is denoted with C0 on Figure 5 [35].

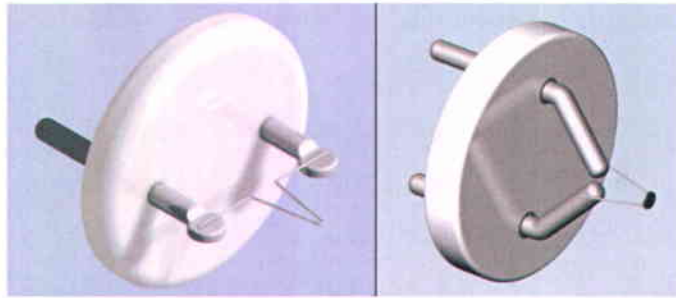


Figure 6. Conventional W-filament (left) and Ta-disc (right) used as effective photoemission electron source as offered by Kimball Physics Inc. [37].

Universitat Berlin (now retired) experimented with some variations based on a standard tungsten hairpin covered with photoelectron emitter material. They found that the best results were obtained from Zr/Ta, ZrC/Re and Zr/ZrC/Re sintered powders [20]. The DTEM group at LLNL uses a commercially available TEM-compatible tantalum disc (Ta-disc) cathode (Figure 6) [27]. In both cases the photocathode can be used in thermionic mode for the initial alignment of the microscope and pulsed mode for time resolved imaging. In the case of the Ta-disc, thermionic emission is achieved by welding the disk to the wolfram hairpin at a single point, which results in a unipotential and planar emission surface [37].

Steering the electron beam through the column

Another major problem for the DTEM is caused by aberrations in the column. The influence of lens aberrations is more significant for the single shot mode (rather than in standard image mode) due to the extremely high density of the charges in the pulse which are spread both in the longitudinal and the lateral direction of the electron beam axis homogeneously and inhomogeneously at various points in the electron-optical column [21]. The three main types of aberrations are astigmatism, spherical and chromatic. Astigmatism occurs when the electrons experience a nonuniform magnetic field as they spiral around the optical axis. It is usually due to imperfect machining, microstructural inhomogeneties of the magnetic lenses, imprecise centering on the axis or contaminated apertures, which can charge up and deflect the beam. Spherical aberration is caused by the lens field acting inhomogeneously on the off-axis rays. As a result, a point object is imaged as a disc of

finite size, which limits the ability to magnify detail. Therefore, the detail itself is lost due to the imaging process. Chromatic aberration is related to the colour, i.e. the energy, of the electrons. The objective lens focuses electrons of different energies at different focal points and thus a point in the object once again forms a disc image. Because of the pulse broadening present in the DTEM [35], which is insignificant in the conventional TEM [1], the chromatic aberration will be more important in dynamic imaging (in comparison with conventional TEM) and its effect adds to the final degradation of the spatial resolution.

Detection of the beam after the specimen

Finally, a highly-sensitive charged-coupled device (CCD) camera is used to collect as many photons generated by the electrons on a phosphorus screen as possible for formation of a high-quality image. This means that the signal read-out noise has to be as low as possible. For this single-electron detection CCD cameras are required. Since each pixel in an electron image requires a minimum electron dose to be registered in a single exposure, the spatial and temporal resolutions are not independent because higher quantity of electrons may give better spatial resolution but will degrade the temporal resolution due to the repulsion of the charges in the electron beam [24], [34].

2.3 Sample preparation

Three types of samples were used in this work with the following configurations (Figure 7):

- ⇒ **a-Ge** film with thickness of 110 nm deposited **on** 40 nm silicon monoxide (**SiO**) **layer** held on a standard 300-mesh Cu-grid
- ⇒ **self-sustained a-Ge** film with thickness of 110 nm held on standard 150-mesh copper grid (Cu-grid), and
- ⇒ **a-Si** film with thickness of 130 nm deposited **on** 50 nm silicon dioxide (**SiO₂**) **windows** formed on Si substrate.

The Cu-grids and the SiO layer on the Cu-grid were purchased from TedPella Inc., Redding, CA. The SiO₂ windows were fabricated by conventional photolithography and etching by our collaborators at McGill University. The configuration was of 9 windows with

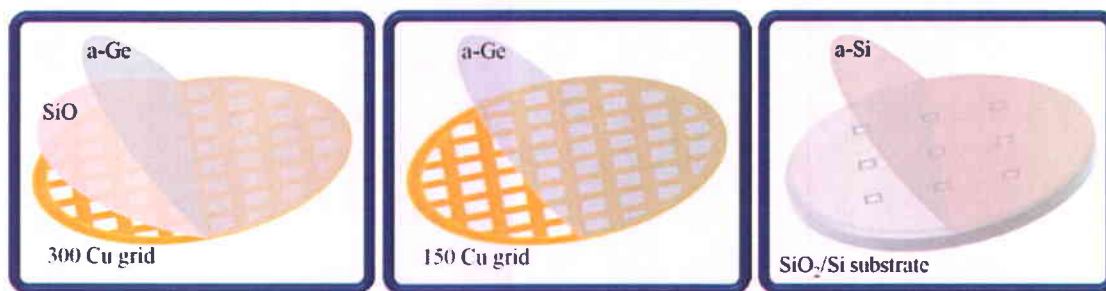


Figure 7. Configuration of the samples from left to right: 110 nm a-Ge / 40 nm SiO / 300-mesh Cu grid; self-sustained 110 nm a-Ge / 150-mesh Cu grid; 130 nm a-Si / 50 nm SiO₂ / Si substrate.

a size of $100\ \mu\text{m} \times 100\ \mu\text{m}$ in an array of 3×3 with separation of $400\ \mu\text{m}$ between the windows [38].

All amorphous semiconductor films were deposited at room temperature by e-beam evaporation onto grids with pre-existing SiO support layers or SiO₂ windows. For the preparation of the self-sustained a-Ge samples, the films were deposited on optically polished rock salt purchased from Alfa Aesar, Ward Hill, MA. Vacuum of 10^{-7} torr was achieved prior to deposition. The deposition rate for germanium was kept at $1.4\ \text{\AA}/\text{min}$, while for silicon it was held at $1.8\ \text{\AA}/\text{min}$. The thickness of the films was verified by profilometer for germanium² and by ellipsometry for silicon.

Self-sustained a-Ge films were prepared by dissolving of the rock-salt in deionised water and deposition of the floating film onto the Cu-grid.

² Ellipsometry was not used for measurement of the thickness of the a-Ge film because the layers were not transparent.

2.4 Bibliography

- [1] D. B. Williams and C. B. Carter, Transmission Electron Microscopy – A Textbook for Materials Science (2nd edition), Springer, New York, NY, USA (2009).
- [2] L. Nikolova, R. G. Saint-Jacques, G. G. Ross, “Characterization of Si nanocrystals by different TEM-based techniques,” *Ultramicroscopy*, vol. **110**, p. 144–150 (2010).
- [3] C. Yan, L. Nikolova, A. Dadvand, C. Harnagea, A. Sarkissian, D. F. Perepichka, D. Xue and F. Rosei, “Multiple NaNbO₃/Nb₂O₅ Heterostructure Nanotubes: A New Class of Ferroelectric/Semiconductor Nanomaterials,” *Adv. Mater.*, vol. **22**, p. 1741–1745 (2010).
- [4] J. P. Buban, Q. Ramasse, B. Gipson, N. D. Browning, and H. Stahlberg, “High-resolution low-dose scanning transmission electron microscopy,” *J. El. Microsc.*, vol. **59**, p. 103–112 (2010).
- [5] D. J. Smith, “Development of Aberration-Corrected Electron Microscopy,” *Microsc. and Microan.*, vol. **14**, p. 2–15 (2008).
- [6] H. Rose, “Correction of aberrations, a promising means for improving the spatial and energy resolution of energy-filtering electron microscopes,” *Ultramicroscopy*, vol. **56**, p.11–25 (1994).
- [7] J. Y. Lee, B. H. Hong, W. Y. Kim, S. K. Min, Y. Kim, M. V. Jouravlev, R. Bose, K. S. Kim, I.-C. Hwang, L. J. Kaufman, C. W. Wong, P. Kim & K. S. Kim, “Near-field focusing and magnification through self-assembled nanoscale spherical lenses” *Nature*, vol. **460**, p. 498–501 (2009).
- [8] D. J. Smith, “Ultimate resolution in the electron microscope?” *Mater. Today. Microscopy Special Issue*, p. 30–38 (2008).
- [9] C. Kisielowski, R. Erni, and B. Freitag, “Object-defined Resolution Below 0.5Å in Transmission Electron Microscopy – Recent Advances on the TEAM 0.5 Instrument,” *Microsc. and Microan.*, vol. **14**, p. 78–79 (2008).
- [10] R. Ishikawa, E. Okunishi, H. Sawada, Y. Kondo, F. Hosokawa & E. Abe, “Direct imaging of hydrogen-atom columns in a crystal by annular bright-field electron microscopy,” *Nature Mat.*, vol. **10**, p. 278–281 (2011).
- [11] C. Kisielowski, B. Freitag, M. Bischoff, H. van Lin, S. Lazar, G. Knippels, P. Tiemeijer, M. van der Stam, S. von Harrach, M. Stekelenburg, M. Haider, S.

- Uhlemann, H. Müller, P. Hartel, B. Kabius, D. Miller, I. Petrov, E.A. Olson, T. Donchev, E.A. Kenik, A.R. Lupini, J. Bentley, S.J. Pennycook, I.M. Anderson, A.M. Minor, A.K. Schmid, T. Duden, V. Radmilovic, Q.M. Ramasse, M. Watanabe, R. Erni, E.A. Stach, P. Denes and U. Dahmen, “Detection of Single Atoms and Buried Defects in Three Dimensions by Aberration-Corrected Electron Microscope with 0.5-Å Information Limit,” *Microsc. and Microan.*, vol. **14**, p. 469–477 (2008).
- [12] W. D. Pyrz, D. A. Blom, V. V. Gulians, T. Vogt and D. J. Buttrey, “Using Aberration-corrected STEM Imaging to Explore Chemical and Structural Variations in the M1 Phase of the MoVNbTeO Oxidation Catalyst,” *Microsc. and Microan.*, vol. **14**, p. 2–3 (2008).
- [13] D. A. Muller, L. Fitting Kourkoutis, M. Murfitt, J. H. Song, H. Y. Hwang, J. Silcox, N. Dellby, and O. L. Krivanek, “Atomic-Scale Chemical Imaging of Composition and Bonding by Aberration-Corrected Microscopy,” *Science*, vol. **319**, p. 1073–1076 (2008).
- [14] I. Arslan, T. J. V. Yates, N. D. Browning, and P. A. Midgley, “Embedded Nanostructures Revealed in Three Dimensions,” *Science*, vol. **309**, p. 2195–2198 (2005).
- [15] P. A. Midgley and M. Weyland, “3D electron microscopy in the physical sciences: the development of Z-contrast and EFTEM tomography,” *Ultramicroscopy*, vol. **96**, p. 413–431 (2003).
- [16] E. Stach, “Realtime observations with electron microscopy,” *Mater. Today Microscopy Special Issue*, p. 50–58 (2008).
- [17] A. M. Minor, E. T. Lilleodden, E. A. Stach and J. W. Morris, “In-situ transmission electron microscopy study of the nanoindentation behavior of Al,” *J. Electron. Mater.*, vol. **31**, p. 958–964 (2002).
- [18] P. A. Crozier, R. Wang and R. Sharma, “In situ environmental TEM studies of dynamic changes in cerium-based oxides nanoparticles during redox processes,” *Ultramicroscopy*, vol. **108**, p. 1432–1440 (2008).
- [19] Z. Wang, and Y. Zhao, “High-Pressure Microscopy,” *Science*, vol. **312**, p. 1150–1151 (2006).

- [20] O. Bonstanjoglo, R. Elschner, Z. Mao, T. Nink, M. Weingärtner, “Nanosecond electron microscope,” *Ultramicroscopy*, vol. **81**, p. 141–147 (2000).
- [21] W. E. King, G. H. Campbell, A. Frank, B. W. Reed, J. F. Schmerge, B. J. Siwick, B. C. Stuart, and P. M. Weber, “Ultrafast electron microscopy in materials science, biology, and chemistry,” *J. Appl. Phys.*, vol. **97**, p. 111101-1–27 (2005).
- [22] A. Zewail, “4D Ultrafast Electron Diffraction, Crystallography, and Microscopy,” *Annual Rev. Phys. Chem.*, vol. **57**, p. 65–103 (2006).
- [23] J. M. Thomas, “A Revolution in Electron Microscopy,” *Angew. Chem. Int. Ed.* vol. **44**, p. 5563–5566 (2005).
- [24] M. R. Armstrong, K. Boyden, N. D. Browning, G. H. Campbell, J. D. Colvin, W. J. DeHope, A. M. Frank, D. J. Gibson, F. Hartemann, J. S. Kim, W. E. King, T. B. LaGrange, B. J. Pyke, B. W. Reed, R. M. Shuttlesworth, B. C. Stuart, B. R. Torralva, “Practical considerations for high spatial and temporal resolution dynamic transmission electron microscopy,” *Ultramicroscopy*, vol. **107**, p. 356–367 (2007).
- [25] A. H. Zewail, “Four-Dimensional Electron Microscopy,” *Science*, vol. **328**, p. 187–193 (2010).
- [26] P. Baum and A. H. Zewail, “Breaking resolution limits in ultrafast electron diffraction and microscopy,” *Proc. Nat. Acad. Sci.*, vol. **103**, p. 16105–16110 (2006).
- [27] T. LaGrange, M. R. Armstrong, K. Boyden, C. G. Brown, G. H. Campbell, J. D. Colvin, W. J. DeHope, A. M. Frank, D. J. Gibson, F. V. Hartemann, J. S. Kim, W. E. King, B. J. Pyke, B. W. Reed, M. D. Shirk, R. M. Shuttlesworth, B. C. Stuart, B. R. Torralva, and N. D. Browning, “Single-shot dynamic transmission electron microscopy,” *Appl. Phys. Lett.*, vol. **89**, p. 044105–044107 (2006).
- [28] V. A. Lobastov, J. Weissenrieder, J. Tang, and A. H. Zewail, “Ultrafast Electron Microscopy (UEM): Four-Dimensional Imaging and Diffraction of Nanostructures during Phase Transitions,” *Nanoletters*, vol. **7**, p. 2552–2558 (2007).
- [29] F. Carbone, O.-H. Kwon, A. H. Zewail, “Dynamics of Chemical Bonding Mapped by Energy-Resolved 4D Electron Microscopy,” *Science*, vol. **325**, p. 181–184 (2009).
- [30] L. Nikolova, T. LaGrange, B. W. Reed, M. J. Stern, N. D. Browning, G. H. Campbell, J.-C. Kieffer, B. J. Siwick, and F. Rosei, “Nanocrystallization of amorphous

- germanium films observed with nanosecond temporal resolution,” *Appl. Phys. Lett.*, vol. **97**, p. 203102-1–3 (2010).
- [31] T. LaGrange, G. H. Campbell, P. E. A. Turchi, W. E. King. “Rapid phase transformation kinetics on a nanoscale: Studies of the a-b transformation in pure, nanocrystalline Ti using the nanosecond dynamic transmission electron microscope,” *Act. Mat.*, vol. **55**, p. 5211–5224 (2007).
- [32] J. S. Kim, Thomas LaGrange, B. W. Reed, M. L. Taheri, M. R. Armstrong, W. E. King, N. D. Browning, and G. H. Campbell, “Imaging of Transient Structures Using Nanosecond in Situ TEM,” *Science*, vol. **321**, p. 1472–1475 (2008).
- [33] J. S. Kim, B. W. Reed, N. D. Browning and G. H. Campbell, “Observation of Transient Phase Formation in Reactive Multilayer Foils using Conventional and Dynamic Transmission Electron Microscopy (DTEM),” *Microsc. and Microan.*, vol. **12**, p. 148–149 (2006).
- [34] B. W. Reed, M. R. Armstrong, N. D. Browning, G. H. Campbell, J. E. Evans, T. LaGrange and D. J. Masiel, “The Evolution of Ultrafast Electron Microscope Instrumentation,” *Microsc. Microanal.*, vol. **15**, p. 272–281 (2009).
- [35] T. LaGrange, G. H. Campbell, B.W. Reed, M. Taheri, J. B. Pesavento, J. S. Kim, N. D. Browning, “Nanosecond time-resolved investigations using the in situ of dynamic transmission electron microscope (DTEM)”, *Ultramicroscopy*, vol. **108**, p. 1441–1449 (2008).
- [36] I. Langmuir and K. T. Compton, “Electrical Discharges in Gases Part II. Fundamental Phenomena in Electrical Discharges,” *Rev. Mod. Phys.*, vol. **3**, p.191–257 (1931).
- [37] Kimball Physics website: www.kimballphysics.com/
- [38] S. McGowan, MSc Thesis: “In situ study of amorphous semiconductor crystallization by Dynamic Transmission Electron Microscopy,” McGill University, Montréal, Québec, Canada (2009).

Chapter III

Crystallization in amorphous germanium films supported by silicon monoxide membrane

In this chapter we describe laser induced crystallization processes in membrane-supported amorphous germanium (a-Ge) films observed *in situ* by DTEM. The sample geometry was chosen because it mimics the one used in industry for the fabrication of solar cells, thin film transistors and flat panel displays where amorphous semiconductor films (silicon or germanium) are deposited on quartz or glass and crystallised via laser heating [1]. As presented in the previous chapter the DTEM developed at LLNL, at the time of the experiments presented in this study, was the only instrument in the world offering the appropriate combination of high spatial and high temporal resolutions for *in situ* investigation of fast-evolving irreversible laser-induced processes. For imaging we used bright field imaging mode. Although dark field imaging in general provides higher contrast and, thus, better ease in interpretation of the contrast in the micrographs [7], that mode of operation was not chosen due to the significantly lower signal obtained in the camera of the microscope. The brightness and the contrast of the images in single shot operation of the DTEM is limited by the quantity of electrons in the single pulse [8], so the user does not have access to the usual means for improving the signal to noise ratio of the micrograph by longer exposure time, as is usually done in conventional TEM.

The objectives of this study were to reveal the sequence in change of the morphology of the film in time, the shape of the crystallization front during its propagation along with quantification of its roughness, to determine the velocities of crystallization and to estimate the temperature of the film during the growth of the different microstructures. To that end, we measured the sizes of the crystals and the times for formation of the different microstructures were given, and used them to estimate the respective growth velocities. The uncertainties related to the calculations will be discussed in each section. In the discussion section at the end of this chapter, we will address the possible growth modes

along with an estimate of the temperature evolution with time and in the radial direction.

In this study, we used 110 nm thick a-Ge films deposited onto 40 nm silicon monoxide (SiO) membranes¹ held on 300-mesh Cu grids. The procedure for fabrication of the films was described in Chapter II. For shortness and clarity of the text, the abbreviation “a-Ge/SiO” will be used for this sample configuration. The pump laser wavelength was 532 nm, selected to optimize the absorption of light since the absorption depth in a-Ge is 50 nm [9], with pulse duration of 15 ns and fluences of $\sim 110 \text{ mJ/cm}^2 \pm 5\%$ and $128 \text{ mJ/cm}^2 \pm 5\%$ with fluctuation of the fluence coming from the pump laser itself. The fluence was calculated from the energy deposited by the laser beam pulse divided by the area of the laser beam spot on the sample where a radius of $1/e^2$ was taken to estimate the area ($45 \mu\text{m}$ in this study). We acquired time-resolved images with delays ranging between 20 ns and 50 μs . The time range was chosen according to earlier studies on laser-induced crystallization in germanium by time-resolved optical reflectivity and transmissivity [10] and the initial *in situ* observations of the process with the first generation DTEM instrument made by O. Bostanjoglo (now retired) at the Optisches Institut der Technischen Universitat Berlin [12]². Since the process is irreversible, for each new experiment (i.e. time delay) a fresh window on the sample was used. When there were no more available windows, the sample was replaced with a new one obtained in the same fabrication batch. Time zero, i.e. $t = 0$ ns, for the probe pulse was defined as the moment at which the pump laser pulse initiating the crystallisation was released.

3.1. Microstructures formed

Single-shot laser heating provokes crystallization in a-Ge/SiO with formation of three distinct microstructures (Figure 8): Zone I – coarse nanocrystalline region within the bounds

¹ We used silicon monoxide membrane instead of silicon dioxide (SiO₂) windows as supporting layer for the a-Ge films in these investigations because SiO₂ showed to be very fragile and difficult to obtain with uniform thickness over large area which is required for samples used in the DTEM experiments. In addition, more than 50% of the membranes obtained by our collaborator at McGill could not support the e-beam deposition process. As a consequence, it was extremely difficult to do the required alignments of the laser and electron beams on the sample and to perform experimental work simply due to lack of available space on the sample for these procedures.

² The spatial resolution of the first generation DTEM was of ~ 200 nm [13] and, thus, not sufficient for observation of the process and extraction of the information presented in this work.

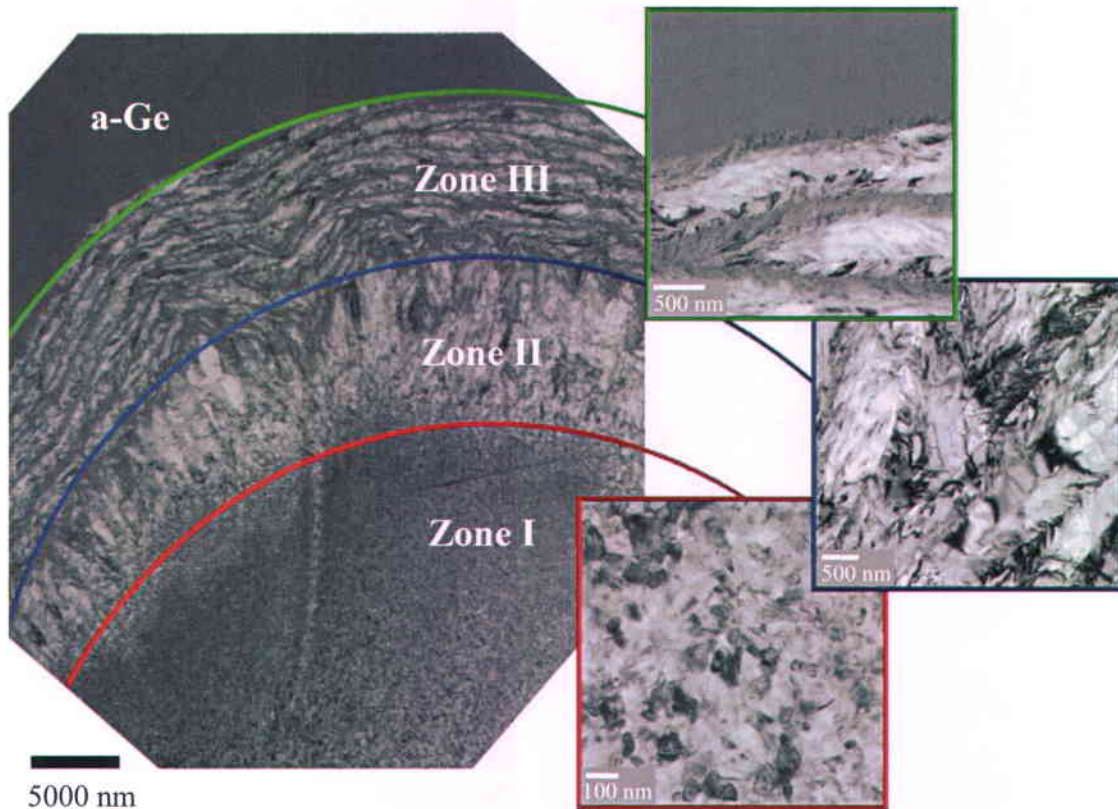


Figure 8. Partial view of the full microstructure formed after single-shot laser-induced crystallization in a-Ge/SiO. The central coarse nanocrystalline region (**Zone I**), LREC (**Zone II**), layered structure (**Zone III**) and the remaining amorphous material are annotated on the micrograph. The block images on right give magnified views of the morphologies observed for the respective zones.

of the pump laser beam ($r_{beam} = 45 \mu\text{m}$); Zone II – consists of large radially elongated crystals (LREC) situated outside of the laser beam spot with the inner radius of the zone at $\sim 45 \mu\text{m}$ and outer radius $\sim 53 \mu\text{m}$; and Zone III – layered structure composed of nanocrystalline bands exhibiting some texture and large tangentially oriented crystals (LTOC) giving an inner radius of $\sim 53 \mu\text{m}$ and variable outer radius from $\sim 58 \mu\text{m}$ to $\sim 70 \mu\text{m}$. Each microstructure and the information obtained for the crystallization in the respective region will be presented separately in the following subsections of this chapter.

Hereafter, we show first the investigation of the nucleation and nanocrystallization processes in the central part of the crystallised film with the corresponding analysis. After that, we will present the investigation of the explosive crystallization in Zones II and III. Earlier

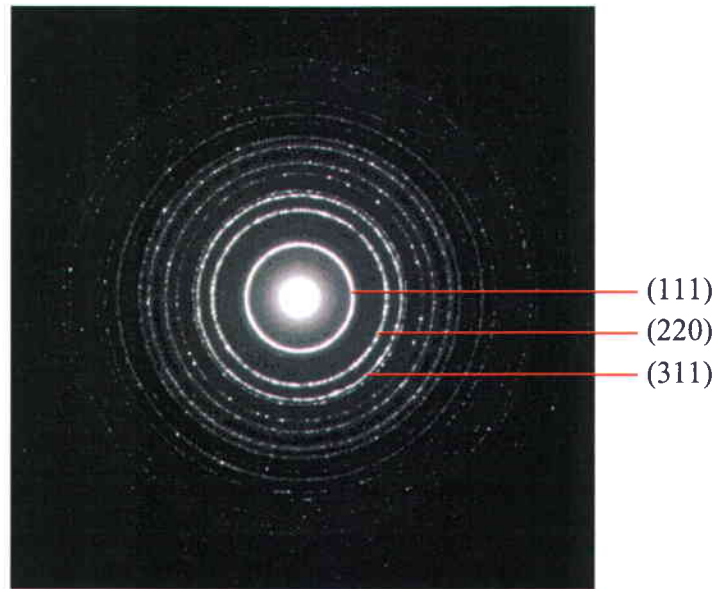


Figure 9. Typical selective area diffraction pattern (post mortem) from Zone I showing random orientation of the crystals. Only the most intense diffraction rings are indexed on the micrograph.

studies showed that the deposited energy from the laser beam pulse has little direct influence on the large radially elongated crystals and the layered structure growth [14].

3.2. Investigation of the nucleation and nanocrystallization processes in a-Ge/SiO

Following laser irradiation, the structure of the germanium film within the bounds of the laser beam is nanocrystalline. The grains were shown to exhibit random orientation using selective area electron diffraction (SAED), as presented in Figure 9. The sizes of the crystals are ranging between ~ 10 nm and ~ 300 nm [16]. We acquired time-resolved images at the central part of Zone I with the objective to extract the evolution of the sizes of the nanocrystals with time (Figure 10). We used a fluence of $128 \text{ mJ/cm}^2 \pm 5\%$ for these experiments.

3.2.1. Evolution of the sizes of the nanocrystals with time and error analysis.

To extract the evolution of the sizes of the nanocrystals with time and estimate their number in the time-resolved images, the following image treatment procedure was applied

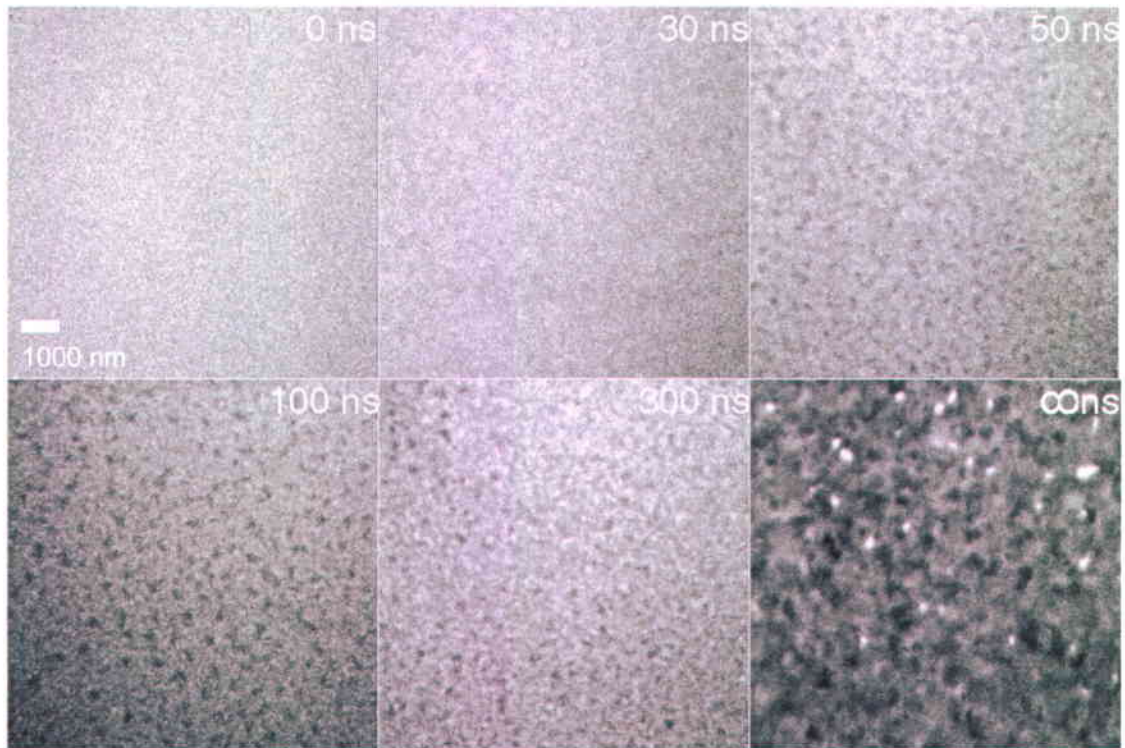


Figure 10. Time-resolved images of the crystallization process in a-Ge/SiO in the central part of Zone I. The time delays are denoted at the upper right corner of each block image. The images denoted with “0 ns” and “∞ ns” show the structure of the film prior the crystallization and at the end of the process respectively. The scale bar is the same for all images and is given in the first block image (up-left). Figure reprinted with permission from [17].

to the time-resolved images. Image J software³ [18] was used to smooth the images and to adjust the brightness and contrast of the micrographs.

Procedure for image treatment applied to all micrographs

From each time-resolved image we selected a $1 \times 1 \mu\text{m}^2$ region, near the center of the reacted area where the laser beam deposited its energy, to be used for image treatment and data analysis. A band pass filter was applied to the image to filter objects smaller than

³ The software is free for download (rsb.info.nih.gov/ij/) and is suitable for treatment of TEM images such as improvement of the brightness and the contrast, automatic measurement of the sizes of the particles present in the image and count of their number.

30 nm⁴ and leave the larger features unchanged. Next, a threshold on the level of grey present in the image was applied to features which were at least 20 % darker than the surrounding amorphous material to be identified by the software as particles. An automatic count of the number of particles identified through this treatment was made, along with a measurement of their size, and elliptical contours were fit to each particle. In the end, a manual verification of the particles was made to ensure that the automatic fitting identified the particles correctly by comparison of the automatically generated outlines of the particles with the particles seen in the image.

This procedure has the advantage of permitting automatic determination of the number and sizes of the particles, but unavoidably leads to uncertainty in the determined values due to the possible spatial superposition of adjacent crystals. This is an inevitable side effect of the bright field imaging mode. In this mode, a stronger signal is obtained resulting in brighter images, but with lower contrast compared to images obtained in dark field mode. This is because, in bright field mode, crystals diffracting at different angles give only different level of gray in the final image, making it difficult to determine where a crystal ends and another nearby crystal begins. The consequence is an overestimation of the mean size and underestimation of the total number of crystals. This effect is schematically represented in Figure 11. Let us assume that two particles are growing close to each other within the thickness of the film (Figure 11 – cross sectional view). Then, in top view, which is the direction of observation, they would appear as one particle (Figure 11 – top view). Conventional bright field TEM image will reveal the presence of two particles due to change in the contrast in the region of their spatial superposition (Figure 11 – BFTEM image). However, in a DTEM bright field micrograph the change of contrast is most likely to be lost due to the significantly lower resolution achieved and the limitation on the electron beam focusing which are results of the space-charge effects⁵ (Figure 11 – DTEM image). As a consequence, the measurement of the particles in the DTEM image will reveal a single particle with a size that is some fraction

⁴ We found that the largest feature seen in the film prior the crystallization is with size of 40 nm. For this reason a slightly lower limit was set for the band pass filter to insure that features of 40 nm and above are not destroyed due to the image treatment.

⁵ At present, 1 Å spatial resolution is easily achievable with modern TEM instruments [1], while the DTEM can offer only ~10 nm spatial resolution due to the significantly lower number of electrons used to form an image [8], [20].

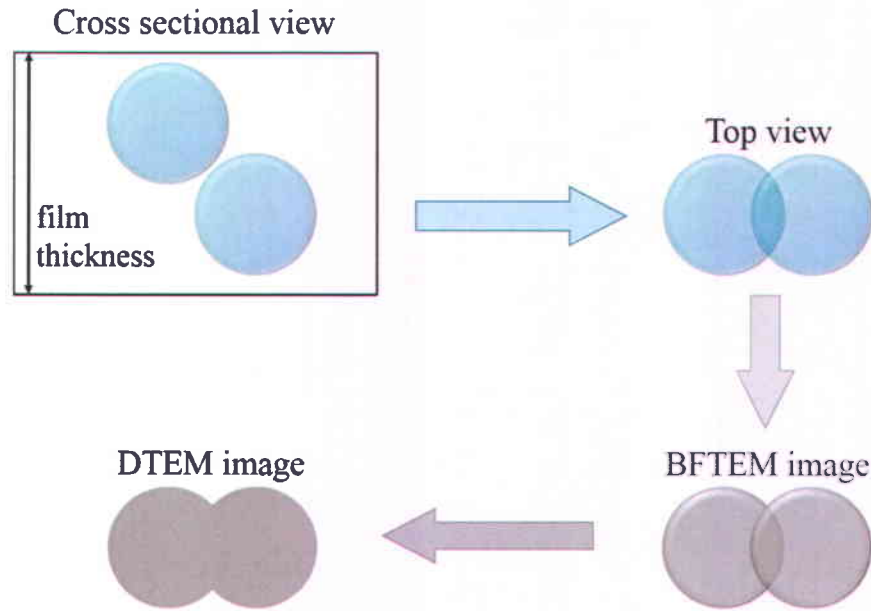


Figure 11. Effect of the spatial superposition of particles in a TEM image and automatic size measurement and count of the particles. In the cross sectional view two particles are present but in the top view (which is the view in the images of this study) they might appear as just one particle. Conventional bright field TEM (BFTEM) image would reveal that these are in fact two particles. However, a DTEM image most likely would show them as one due to its lower spatial resolution arising from the lower number of electrons to form an image which, also results in lower contrast of the images and the dynamic operation of the instrument.

of the sum of the sizes of the two particles. This will result in an overestimation of the size of the particles and underestimation of their number. For these reasons, where evident, adjacent crystals were separated after this procedure was applied to the time-resolved images i.e. crystals with shape appearing as ‘infinity’ or number eight signs were separated. In addition, for the automatic count of the particles and measurement of their sizes, the minimal size threshold was set at 40 nm. The latter value corresponds to the size of the largest feature seen in the DTEM image of the a-Ge film prior to crystallization.

Application of this procedure to the time-resolved images allowed us to reveal the time evolution of the mean size of the crystals. The results shown in Figure 12 indicate that the size of the nanocrystals increases linearly from ~75 nm to ~125 nm starting from 20 ns

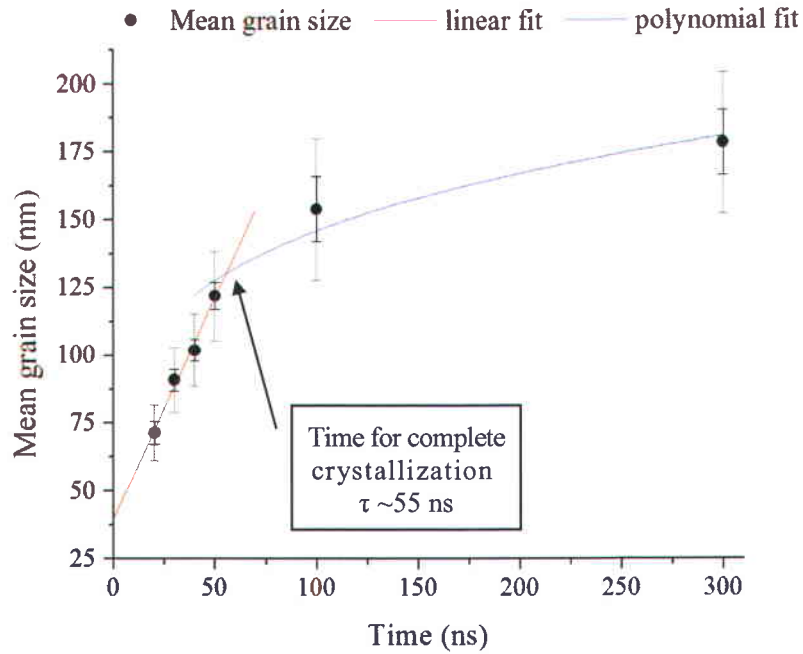


Figure 12. Mean size of the nanocrystals in Zone I at different time delays for a-Ge/SiO. The long error bars (in grey color) represent the standard deviation of the data. The short error bars (in black) represent the standard error for the calculated mean size of the grains. The intersection of the linear fit (red line) and the polynomial fit (blue curve) allows estimation for the time for complete crystallization in this region. Figure adapted from [17].

delay up to about 50 ns, suggesting a two dimensional growth of isolated crystals. For longer delays the mean size of the nanocrystals increases more slowly in parabolic fashion up to ~175 nm. This indicates diffusion-controlled ripening of the crystals and possible coalescence of adjacent crystals with low crystallographic misorientation. The intersection between the linear fit (i.e. the two dimensional growth) and the polynomial curve (i.e. the ripening and coalescence of adjacent crystals) gives an estimation for the time for complete crystallization of the film τ to be ~55 ns.

3.2.2. Estimation of the nucleation rate

By counting the number of nuclei in each time-resolved image, we were able to evaluate the nucleation rate *in situ*. The evolution of the number of nanocrystals with time is shown in Figure 13. The number of nanocrystals increases from 20 ns up to ~40 ns followed

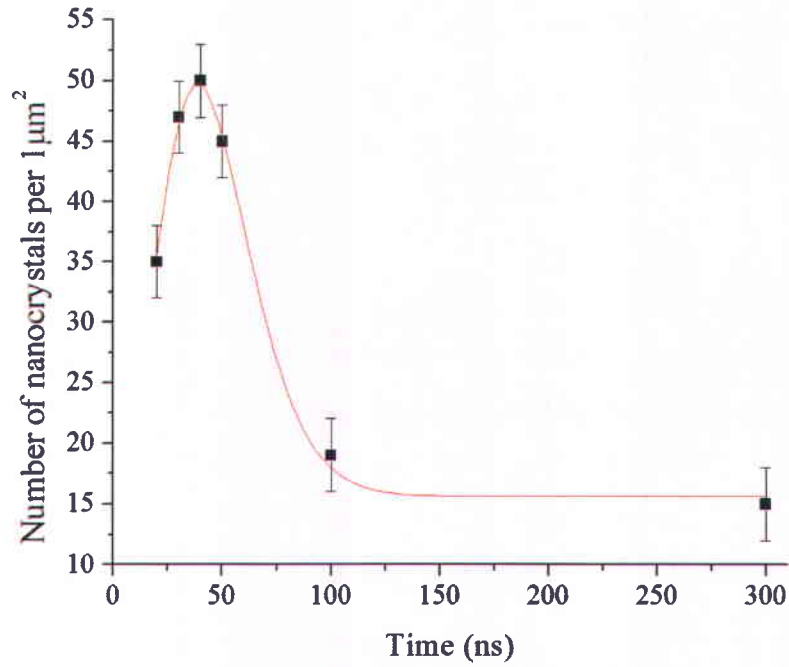


Figure 13. Evolution with time of the number of nanocrystals per 1 μm^2 in Zone I at different time delays for a-Ge/SiO at 128 mJ/cm^2 . The red curve shows the trend in the evolution. The error bars give the fluctuation of the number of nanocrystals for the same delay but at different regions on the sample. Figure adapted from [17].

by sharp decrease. Therefore, our estimate of the time needed for complete crystallization at ~ 55 ns is consistent with the results on the number of nuclei observed in the time-resolved images. The error bars in Figure 13 originate from considering the number of nanocrystals in different regions on the sample at the same time delay.

The nucleation rate per unit volume N can be calculated as follows:

$$N = \frac{N_{TR}}{V \cdot t} \quad (1)$$

where N_{TR} is the number of nuclei seen in the time-resolved image, V is the volume of the probed material and t is the time delay. For the maximal nucleation rate at 20 ns delay, we obtained $N = 1.6 \cdot 10^{22} \frac{\text{nuclei}}{\text{cm}^3 \cdot \text{s}}$. Based on the number of crystals seen in the post mortem images and supposing that the nuclei have spherical shape, W. Marine and J. Marfaing [21] estimated that the nucleation rate for nanosecond induced crystallization in a-Ge ranges

between 10^{23} and $10^{25} \frac{\text{nuclei}}{\text{cm}^3 \cdot \text{s}}$. Our value for the nucleation rate is slightly lower, probably due to the limited spatial resolution of the DTEM images where only crystals larger than 40 nm were counted, as described earlier.

3.3. Investigation of the explosive crystallization in a-Ge/SiO in Zone II and III

Hereafter, we focus on the explosive character of the crystallization process in a-Ge resulting in the formation of the dendritic and layered structures. The DTEM allows us to investigate in detail the formation of these structures with the best possible temporal and spatial resolutions. We used a fluence of $110 \text{ mJ/cm}^2 \pm 5\%$ due to the more stable operation of the instrument during the experimental session.

3.3.1. Zone II

The microstructure in this zone is characterised by the presence of large crystals oriented in the radial direction. Their length varies between $6 \mu\text{m}$ and $10 \mu\text{m}$. Their structure is highly faceted and they terminate in a wedge shape, forming a dendritic morphology. These crystals are often referred to as dendrites [12], [21]. Much remains to be understood on the mechanism of their formation since their final morphology does not indicate that their growth occurs via the twinning mechanism which is commonly seen in silicon crystallised at high cooling rates [16], [22], similar to the experimental conditions of this study. In addition, several dendrites form from one nucleation center. Figure 14 shows an example of this situation where about four dendrites grew from one nucleation center. Some authors refer to the structure in Zone II as a “columnar structure” due to the pattern that these crystals form upon laser-triggered crystallization in pre-heated a-Ge films [14]. In the text that follows we will refer to these crystals as large radially elongated crystals (LREC), which corresponds to their spatial orientation in the images, or dendrites. The growth in this zone is initiated at $\sim 275 \text{ ns}$ and completed at $\sim 1300 \text{ ns}$ giving an average velocity of growth of $\sim 8 \text{ m/s} \pm 2 \text{ m/s}$ (estimated from the post-mortem images)⁶.

⁶ Time-resolved estimation of the mean velocity is not justified due to the limited number of measurements, thus, the uncertainties associated with the calculations would be very large.

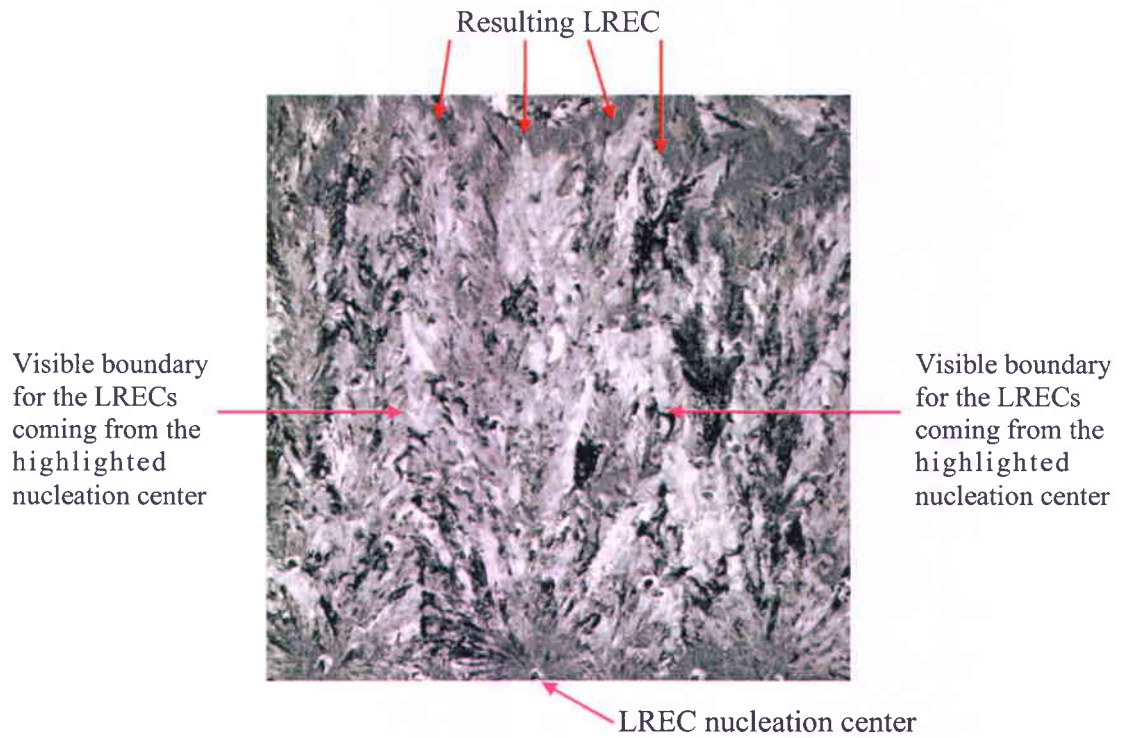


Figure 14. About four LRECs growing from one nucleation center. The visible boundaries of the LREC coming from the nucleation center are pointed with magenta arrows.

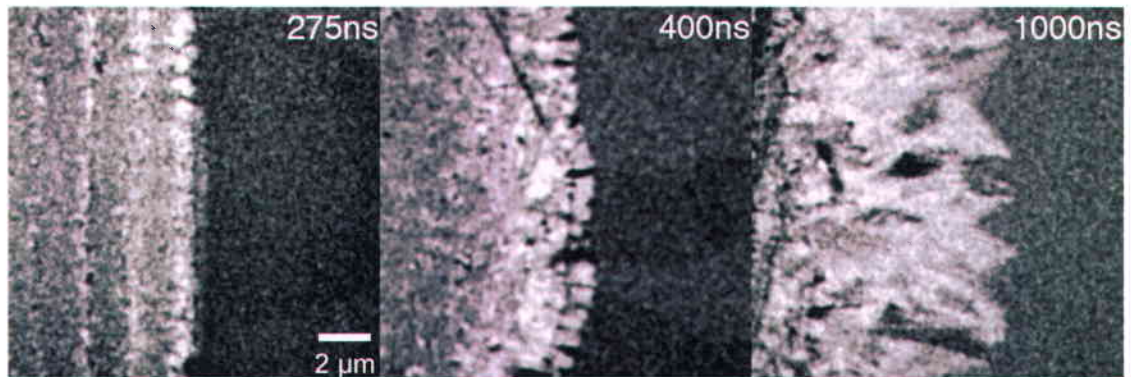


Figure 15. Time-resolved images of the LREC growth showing the shape of the crystallization front during its propagation for a-Ge/SiO. The time delays are denoted in the upper right corner of each block image. The scale bar is the same and is given in the first block image (left).

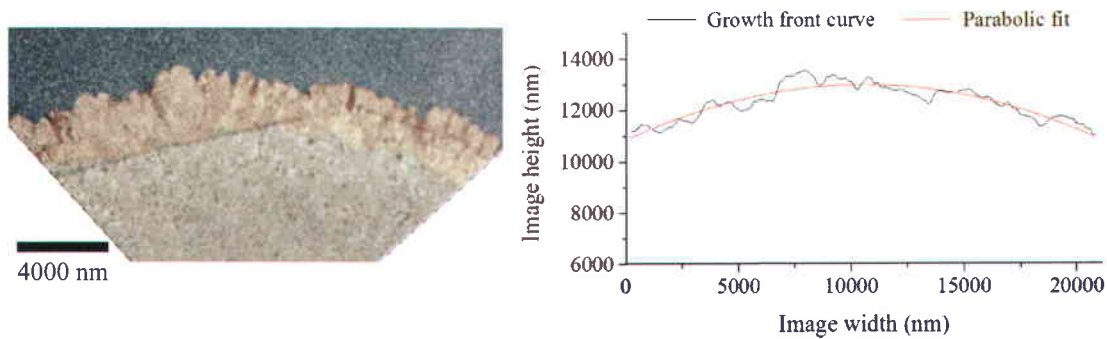


Figure 16. Procedure applied for extraction of the RMS of the roughness of the growth front during its propagation (400 ns delay image was used in this figure). A) Outline of the growth front directly on the image (accentuated in yellow). B) Plot of the growth front (black curve) with parabolic fit (red curve).

3.3.1.1. Evolution of the shape of the crystallization front with time and its roughness

Figure 15 shows time-resolved images of the crystallization process in Zone II. In the initial stages of growth the front is relatively flat with protrusions probably due to anisotropic growth since the LREC are seeded in the central coarse nanocrystalline Zone I where the crystals have random orientations (Figure 15 – 275 ns delay image). However, the roughness rapidly evolves (Figure 15 – 400 ns & 1000 ns delays images). To quantify the evolution of the roughness with time we extracted the root mean square (RMS) of the roughness of the growth front with the following procedure. At first, the growth front was outlined directly on the image (Figure 16 A). After that, the curve defining the growth front was converted into (x,y) coordinates and plotted in a graph (Figure 16 B). The next step was to apply an automatic parabolic fit. A parabolic fit was used because the crystallization front appeared as an arc due to the circular symmetry of the incident laser beam. Finally, the root mean square deviation of the actual growth front from the fit was calculated. The results of these calculations are plotted in Figure 17. The data suggest that the roughness is low in the initial stages of growth of the LREC (~ 250 nm at 275 ns delay) and reaches its maximum of ~ 800 nm at 1000 ns delay.

3.3.2. Zone III

The layered structure is the last to form upon laser heating of the a-Ge film and introduces an abrupt transition from the microstructure of Zone II (radially oriented dendrites).

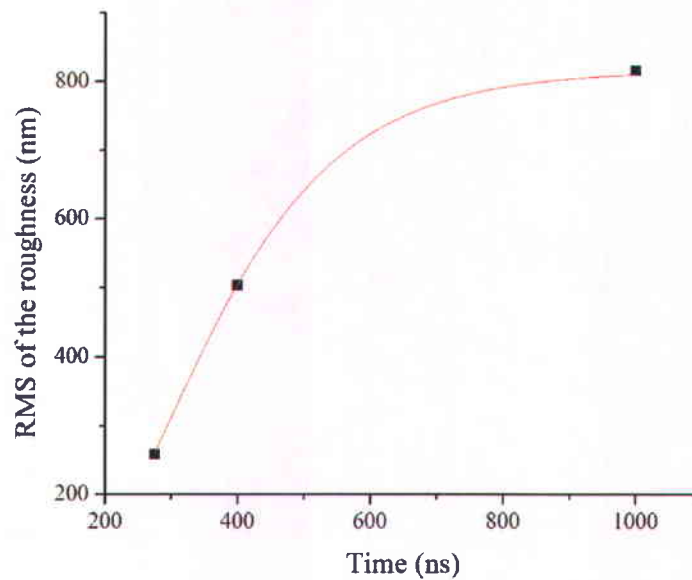


Figure 17. Evolution of the RMS of the roughness of the growth front in Zone II for a-Ge/SiO and hypothetical tendency of the evolution (red curve).

Some authors refer to this structure as scalloped [6], [14] due to the crystalline pattern produced with the geometry used in their experiments. In the text that follows we will refer to this structure as layered due to the spatial orientation of the grains.

High-magnification images show that the layered structure is composed of nanocrystalline bands with some texture and azimuthally tilted large crystals. Figure 18 shows a bright field image of part of the layered structure (image A) with SAED pattern of the nanocrystalline band (image B). The diffraction pattern suggests that the nanocrystalline band is composed of crystals with random orientation. The stronger spots seen in the diffraction pattern originate from the adjacent LREC and LTOC. The width of the nanocrystalline bands varies between ~ 150 nm and ~ 400 nm while the LTOC bands have widths ranging between ~ 250 nm and 1400 nm without any particular ordering of the widths of these bands in the radial direction. Our observation is not in agreement with earlier studies where it was suggested that the “wavelength” of the LTOC and the nanocrystalline bands decreases in the radial direction [23]. Formation of this structure appears to be very irregular since the width of the zone varies within the same experiment depending on the proximity to the TEM copper grid supporting the SiO membrane and the a-Ge film and from shot to shot. This



Figure 18. A) Bright field image of the end of the dendritic region (Zone II) and the beginning of the layered structure (Zone III). Scale bar: 500 nm. B) SAED pattern from the area surrounded by the white circle in A).

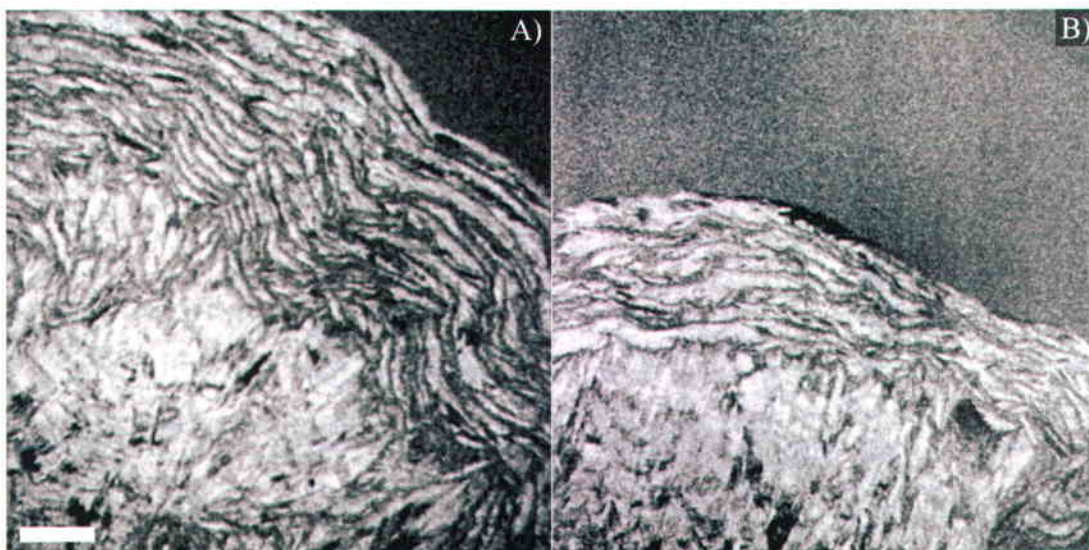


Figure 19. Post mortem images of two experiments presenting the width of Zone III for a-Ge/SiO to be variable (image A and B) as well as different width of the zone within the same experiment (image B shows about eight layers on the left side of the image and only four on the right side). The scale bar is the same for the two micrographs and is 5 μm .

is probably due to different heat losses which creates variability in the formation of this structure. Figure 19 presents two experiments where the width of the layered structure is about 17 μm (image A) and about 10 μm (image B), even when the same fluence was used for crystallization of the a-Ge film. In addition, the number of layers in the layered structure may vary within one experiment. Image B in Figure 19 shows such a variation from ~ 4 layers at the right side of the image to about 8 layers at the left side of the image. The structure starts growing at $\sim 1.3 \mu\text{s}$ and finishes at various times up to $\sim 10 \mu\text{s}$ resulting in an average velocity of $\sim 1 \text{ m/s}$ in radial direction. While the radial velocity of advancement of the growth front is accessible from our data, the orthogonal velocity i.e. parallel to the azimuthal direction of growth of the layered structure cannot be obtained with the current single shot operation mode of the DTEM because only a single image can be acquired for one excitation of the sample.

To investigate the crystallization process in this zone, we provoked crystallization using the same fluence as for Zone II, 110 mJ/cm^2 . Time-resolved images of the growth of this structure showed that the growth front is relatively smooth, without the large oscillations (magnitude of roughness) observed in Zone II (Figure 20 and Figure 21). The front advances through the growth of large crystals in the azimuthal direction. Figure 20 shows time-resolved images at 8500 ns and 7500 ns (images A) and C)). Comparison with the respective post mortem image gives an unambiguous indication of the azimuthal direction of the growth in this structure. The false-color images (Figure 21 B) and D)) present an overlay of the time-resolved image appearing in magenta and the post-mortem image appearing in grey which clearly show the growth direction of this structure. Simultaneous growth of multiple layers may also occur. Figure 20 shows the growth of about five layers simultaneously. Therefore, the growth in Zone III may not proceed layer by layer (i.e. after the growth of one layer is completed the next layer begins its growth) but large thermal instabilities at the growth front can allow the simultaneous formation of the multiple layers to take place. As Figure 21 shows, multiple layers are advancing (in clockwise and counter clockwise directions) but their respective growth fronts are spatially separated from each other from $\sim 2 \mu\text{m}$ to $\sim 10 \mu\text{m}$.

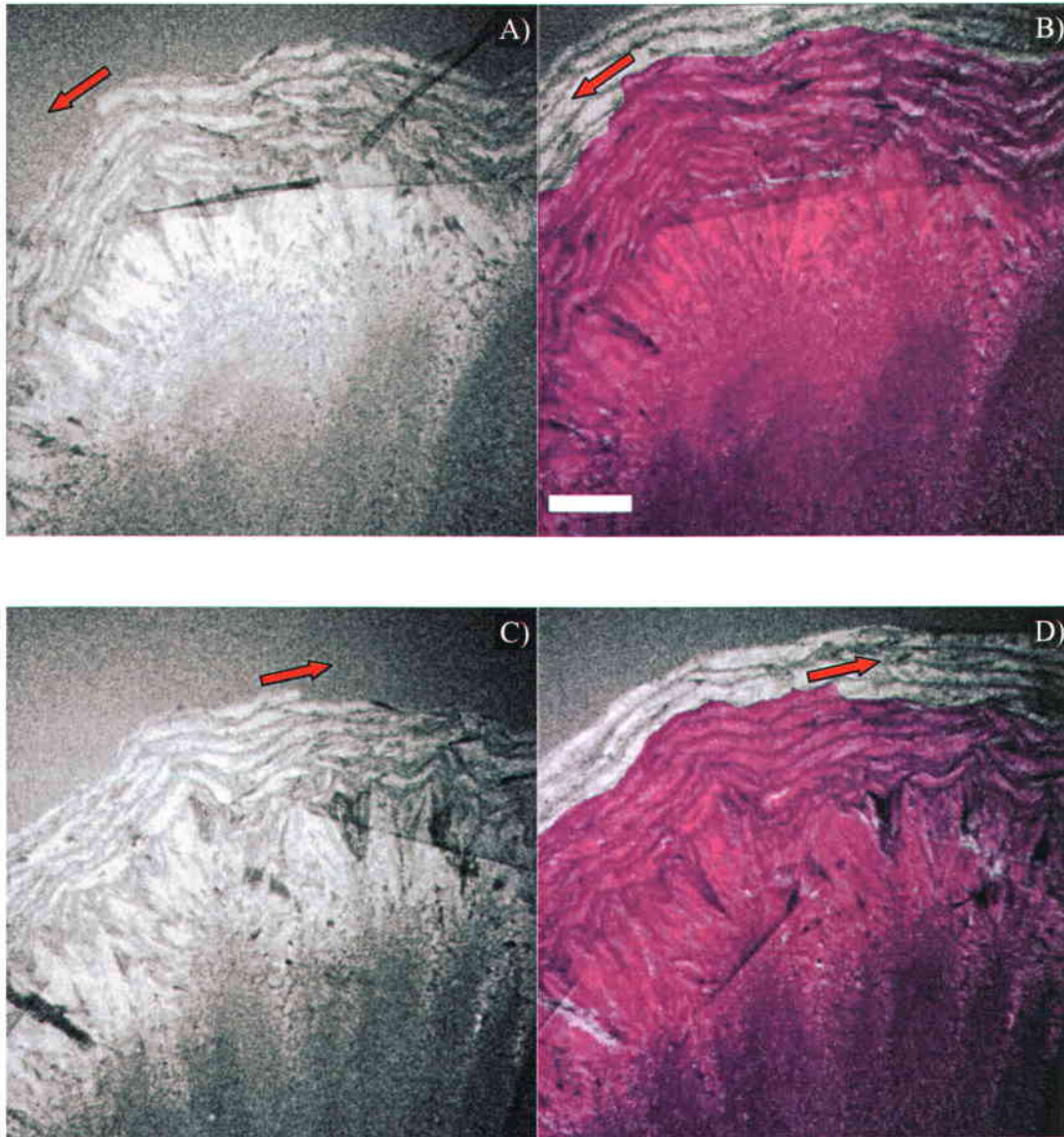


Figure 20. A) & C) Time-resolved images of the layered structure for a-Ge/SiO taken at 8500 ns and 7500 ns delays showing the azimuthal direction of growth in this structure (indicated by the arrows in all the images). B) & D) False color images showing overlay of the time-resolved and the corresponding post mortem image. The time-resolved image appears in magenta while the post mortem image in grey. The scale bar is the same for all the images and is 5 μm (given in block image B).

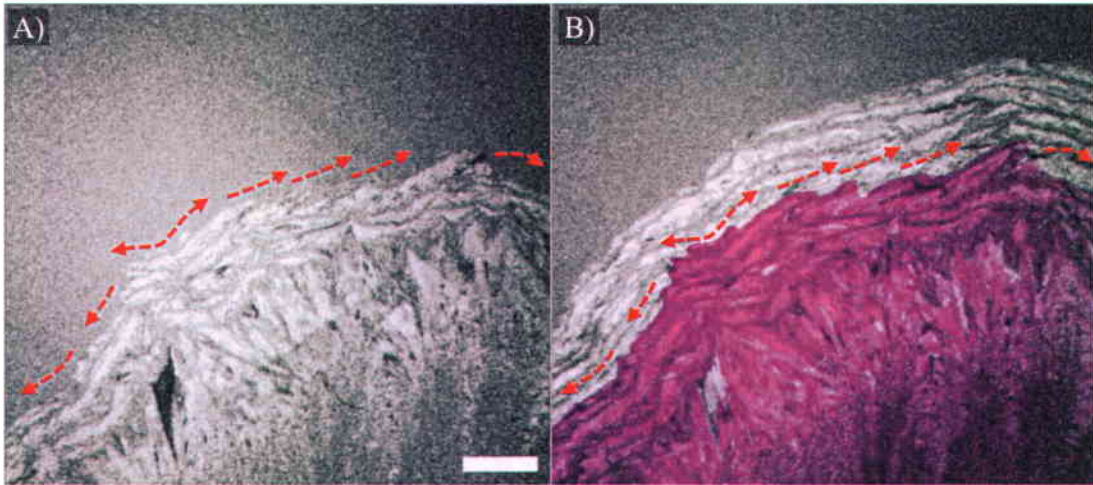


Figure 21. A) Time-resolved images of the layered structure for a-Ge/SiO taken at a 5500 ns delay showing the simultaneous growth of at least five layers. The dashed red arrows indicate the direction of the growth of the layers (the arrows are placed slightly above the layers for more clarity). B) False color image showing an overlay of the time-resolved image with the corresponding post mortem image. The time-resolved image appears in magenta while the post mortem image in grey. The arrows are used as guide for the eye for the direction of the growth of the layers. The scale bar is the same for the two images and is 5 μm (given in block image A).

3.4. Discussion

Crystallization in amorphous semiconductors can occur either in the solid state or as a melt-mediated process [6], [14], [24]. Crystallization in the solid state is defined to occur at temperature below the melting temperature of the amorphous material (T_{ma}), while the melt-mediated process takes place at temperature above T_{ma} but below the melting temperature of the crystalline material (T_{mc}). As a result, the two processes proceed at different velocities. The solid state crystallization takes place at velocities below 5 m/s, while the melt-mediated process occurs at higher velocities [27]. The following classification for the crystallization in group IV semiconductors is given in the literature [28], [26]: (i) explosive solid phase random crystallization (ESPRC) governed by bulk nucleation and growth in the solid state; (ii) explosive solid phase crystallization (ESPC) occurring through epitaxial growth in the solid state; (iii) explosive liquid phase random crystallization (ELPRC) governed by bulk nucleation and growth in a melt; and (iv) explosive liquid phase

crystallization (ELPC) taking place through epitaxial growth from a melt. Crystallization in a-Ge and a-Si is suggested to occur not in only one of these growth modes but through a combination of them [6]. To clarify which pathway the system follows during the phase transformation studied in this work, an estimate of the temperature evolution in time in the radial direction is needed. At present, there are no sufficiently small and fast detectors offering spatial resolution of a few micrometers for *in situ* measurement of the temperature in the film. Therefore, simulation of the heat generation and diffusion within the film is necessary. Hereafter, an estimate of the temperature in each zone will be provided in an attempt to reveal the relationship between the observed microstructure and the temperature within the film for a better understanding of the pathways for growth of these structures.

3.4.1. Zone I

The central coarse nanocrystalline zone (Zone I) forms within the bounds of the incident pump laser pulse. This is also observed as for pulsed-laser-induced crystallization as well as for electron-beam-induced crystallization [21], [29]. In particular, the important questions are: what is the temperature of the film after arrival of the laser pulse and why does the central region form within the bounds of the pump-laser spot? An estimate of the temperature within the film after the arrival of the laser pulse can be obtained by knowing the heat capacity of the film and assuming that the energy in the pulse is instantly and fully converted into heat ΔQ . Then the temperature increase ΔT will be:

$$\Delta T = \frac{\Delta Q}{C_p m}, \quad (2)$$

where C_p is the specific heat capacity of a-Ge and m is the mass of the material (in our case the mass of the film in the boundaries of the laser beam spot). The dependence of the specific heat capacity of a-Ge on temperature is usually expressed as the specific heat capacity for crystalline Ge with a correction for the amorphous phase. The specific heat capacity of crystalline germanium taken from the Smithells Metals Reference Book for the temperature interval 298 K – 1210 K [30] with the correction for a-Ge given in the work of Turnbull and co-workers [31] results in the following expression for the specific heat

capacity in a-Ge $C_p(T)$ (with units J/kg·K):

$$C_p(T) = C_{p \text{ crystalline Ge}}(T) + C_{p \text{ amorphous Ge}}(T) \quad (3)$$

$$C_p(T) = 0.577 \times (516 + 0.140 \times T) + 57.61 \times (-0.05 + 9.35 \times 10^{-4} \times T)$$

The energy of the laser pulse used in our experiments is $\sim 8 \mu\text{J}$ which is equivalent to fluence of 128 mJ/cm^2 because it is spread over area defined by the $1/e^2$ radius of the beam. As a consequence, the increase in temperature in our 110 nm thick a-Ge film would raise the temperature to above 2000 K within the limits of the laser beam spot with radius $r_{beam} = 45 \mu\text{m}$ taking into account that the reflectivity of solid a-Ge is $\sim 47\%$ at 532 nm [9]. This temperature increase would bring germanium to its thermodynamically stable liquid state. Supposing that such a liquid was present on the surface of the film (melting of the entire a-Ge film is not considered because if the film melted it would coalesce in droplets which would crystallise as very big particles on the SiO membrane as we observed previously [32]), then, the crystal's growth is expected to occur inwards i.e. toward the center of the laser beam spot following the temperature gradient as observed in the case of amorphous silicon melt-mediated crystallization [32].

A closer look at how the energy from the pulse is deposited in the material raises the question of why the central coarse nanocrystalline region forms within the bounds of the laser beam spot i.e. with radius $\sim 1/e^2$ of the diameter of the pump pulse. The laser beam used in our experiments has a circularly symmetric Gaussian distribution in the plane of the sample leading to an intensity which decays very rapidly from its maximum (at the center of the laser spot) to $\sim 10\%$ at its periphery. Figure 22 (black curve) shows the Gaussian distribution of the laser energy in the pulse deposited on the sample in the radial direction. Thus, the energy in the laser pulse will not be distributed equally over the area of the laser beam spot. For Gaussian distribution of the intensity, the energy received at the periphery of Zone I should be only 10 % of the energy received in the center of the same region and might not be sufficient to provoke crystallization. However, considering that the reflectivity of a-Ge at 532 nm is $\sim 47\%$ in the solid state [9] and $\sim 72\%$ in its thermodynamically stable liquid [35], we made the hypothesis that the amorphous to metastable liquid transition may occur before the full absorption of the laser pulse. As a result, the increased

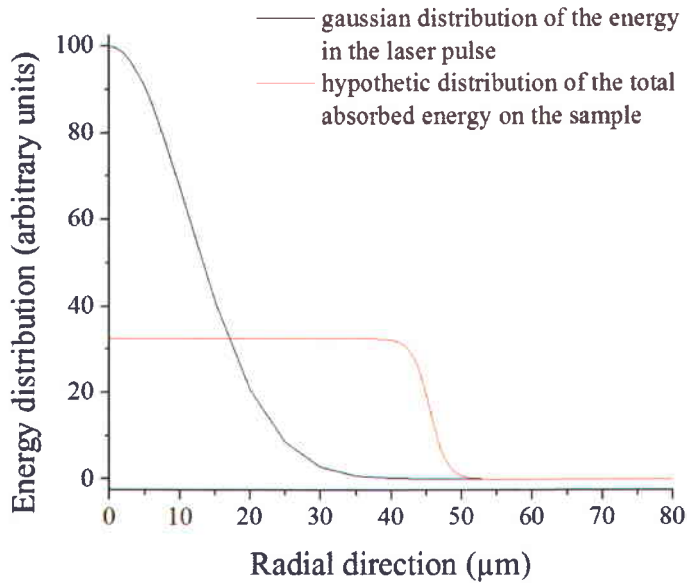


Figure 22. Schematic representation of the Gaussian distribution of the energy in the laser beam within the spot (black curve) and hypothetical responsive distribution of the total absorbed energy in the film over the laser spot (red curve) in normal direction to the sample's plane which will lead to more uniform absorption of the laser beam from the sample.

reflectivity of the metastable liquid impedes the full absorption of the energy in the laser pulse and its conversion into heat. Therefore, if the transition from solid a-Ge to its metastable liquid phase, characterised by much higher reflectivity, occurs rapidly following the arrival of the laser pulse in a cascade fashion i.e. from the center of the beam spot toward the periphery, then a more uniform thermal distribution will be achieved within the bounds of the laser spot. The red curve in Figure 22 shows such hypothetic distribution of the total absorbed energy on the sample. A more uniform thermal distribution of the heat within the bounds of the pump laser may also explain the absence of a thermodynamically stable liquid (we observed the same situation also in the case of laser induced crystallization in self-sustained a-Ge films which will be presented in detail in Chapter IV). Calculation of the temperature of the a-Ge film made by M. Stern [36] gave an estimate for the maximal temperature of the a-Ge film after arrival of the laser pulse to be ~ 1100 K. For these reasons the nucleation and nanocrystallization in a-Ge in Zone I is most likely to be described as random nucleation from the bulk at temperatures below the temperature for melt of

crystalline germanium but above the temperature for melt of the amorphous material.

Using this estimated temperature of the film, the activation energy E_C of the process could be evaluated. Since a-Ge is similar to a glass but obtained at higher cooling rate as described in Chapter II, an assumption could be made that the material will exhibit behaviour similar to a glass. Supposing that the time for full crystallization τ of the a-Ge film follows an Arrhenius type relationship applicable for glasses [37],

$$\tau = \tau_0 \exp\left(\frac{E_C}{k_B T}\right), \quad (4)$$

where τ_0 is a prefactor accounting for the characteristic time for microscopic interaction between neighboring atoms, k_B is Boltzmann's constant and T is the temperature of the film, then the activation energy of the process E_C can be estimated. Taking the value of the prefactor given by Blum and Feldman $\tau_0 = 4 \times 10^{-17}$ s [38], the Boltzmann's constant $k_B = 8.617 \times 10^{-5}$ eV·K⁻¹ along with our estimation of the temperature at ~55 ns to be between ~850 and ~1100 K [17], [36], we estimate the activation energy to be in the interval 1.4 eV to 1.9 eV. The reported values for E_C range between 1.4 eV [39] and 3.5 eV [38], [41]. The mean value for the activation energy that we obtain (~1.7 eV) is similar to that obtained by W. Marine and J. Marfaing of 1.8 ± 0.1 eV [42].

3.4.2. Zones II and III

Growth in Zones II and III is usually described as melt-mediated crystallization. As introduced in Chapter I, the existence of a liquid layer is possible due to the difference in the melting temperatures between the amorphous and the crystalline phases (~245 K [43]). An essential feature of the crystallization in these regions is the latent heat released at the crystallization front, which is significant; in Ge, the latent heat for the amorphous-crystalline transformation divided by the specific heat capacity is ~450 K [23]. As previously mentioned, over certain substrate temperature ranges this release of energy can be sufficient to fuel a self-sustained crystallization front that can propagate for distances as large as several centimeters. The presence of a metastable liquid layer has been observed by transient conductance [27] in heated a-Ge films, real-time reflectivity measurements [44] and deduced from redistribution of dopant impurities [45].

The melt-mediated mechanism of growth in Zone II is described to occur via a thin metastable liquid layer propagating in front of the growing large radially elongated crystals. Gilmer and Leamy [46] were among the first to suggest that such metastable layer exists. They were led to this hypothesis due to their observed high velocities of crystallization (for comparison solid state crystallization occurs at velocity of growth ranging between ~ 1 m/s and ~ 4 m/s [27]). In their work they estimated the width of the layer in direction parallel to the heat flow to range between 2% and 10% of the thickness of the a-Ge film. Later Gold and co-workers evaluated the time of existence of the liquid at each point during the propagation of the liquid front. They estimated that the supercooled liquid is present for ~ 6 ns [47] at each point of the crystallization front. Recent work on atomic simulations of the crystallization process in a-Ge made by Albenze and co-workers estimated the width of this layer to be of the order of ~ 150 angstroms with time of existence of ~ 200 picoseconds [48]. In addition, they showed that once the liquid layer has been created due to the laser heating, its existence is determined exclusively by the heat supplied from the exothermic reaction of the liquid to crystalline phase transition.

Growth in Zone III is also suggested to occur through a melt-mediated mechanism. However, there is no agreement on the exact pathway. Sharma and co-workers proposed a model which suggests that the growth in this zone proceeds at a higher temperature than the temperature in Zone II (even above T_{mc}), thus, creating large regions of molten material [23]. Then, the growth of the layers occurs inward in the radial direction. Sharma's hypothetical pathway of growth was based solely on the observed post-mortem spatial oscillation of the layered structure in the radial direction. On other the hand, Chojnacka (PhD thesis) proposed that the layered structure is formed due to propagation of the growth front in a zigzag fashion where pockets of melted material are formed at the growth front allowing its advancement in a direction orthogonal to the heat flow [6]. Due to lack of the required combination of spatial and temporal resolution for in situ visualisation of the process, neither of these hypotheses has been confirmed.

The major challenge in applying the theoretical predictions to our results is the spatial and temporal resolutions needed to confirm them. According to the studies mentioned above the width of the liquid layer in our 110 nm a-Ge film has to be between

~3 nm [46] and ~15 nm [48] which corresponds to 5 to 26 lattice parameters⁷ and time of existence between ~6 ns and ~200 ps [47]. This implies that, for propagation of the crystallization front in radial direction to occur, the width of the liquid layer has to be very small and the times for transition from amorphous phase to supercooled liquid and from supercooled liquid to crystalline phase are very short. Although we cannot evaluate the time of existence of the supercooled liquid or distinguish it in the time-resolved images from the crystalline or the amorphous material, we can estimate the temperature in the film according to the evolution of the microstructure that we observed. This information will allow further elucidation of the mechanisms of crystallization in a-Ge.

As shown in the experimental part of this chapter, DTEM images have revealed that these zones are formed following a rapid burst of nucleation-controlled crystallization that leaves the film fine grained and polycrystalline inside the $1/e^2$ diameter of the laser spot (within approximately 275 ns). To estimate the influence of the initial input of energy from the laser beam onto the spatial position of the LREC and the layered structure, the lateral heat diffusion length can be estimated as follows:

$$L_D = 2\sqrt{Dt}, \quad (5)$$

where D is the thermal diffusivity ($D = 0.1 \text{ cm}^2/\text{s}$ for a-Ge [23]) and t is the time. For this estimation the thermal diffusivity is considered to be independent on the temperature with objective to evaluate the order of the heat diffusion length. Over the brief time scale before the growth in Zones II and III, the lateral thermal diffusivity using eq. (5) is estimated to be ~3 μm at 275 ns. Since the laser beam diameter is very large (~90 μm) in comparison with the heat diffusion length, within the limits of the uncertainties related to the measurement of the size of the crystallised area in respect to the size of the laser spot on the sample, the redistribution of thermal energy from the central polycrystalline region to the surrounding region (i.e., the area that will become Zone II and Zone III) is limited before crystallization in Zone II begins.

The morphology and growth dynamics of the LREC formed within Zone II suggest a change in the crystallization mode from nucleation dominated to growth controlled. The

⁷ In this calculation, crystal lattice parameter for Ge of 564.613 pm was taken [49].

grains formed at the outer edge of Zone I act as the nuclei from which LREC grow. Once initiated, this growth mode is self-sustaining over a distance of $\sim 10 \mu\text{m}$ due to the exothermic character of the crystallization and the underlying Gaussian temperature profile created due to the laser excitation (see Figure 22).

A feature of the Zone II crystallization that has been revealed through the time-resolved images is the development of protrusions on the initially flat crystallization front (Figure 15 and Figure 17). Earlier work has suggested that the growth front of the LREC should remain smooth under the conditions of our experiment due to the Gibbs-Thomson effect where once a protrusion in the growth front is created it will not be stable and will disappear, resulting in smoothing of the crystallization front [50]. We find that this effect is insufficient to maintain a flat interface in Zone II. Instead, the increasing amplitude of these protrusions is indicative of a Mullins-Sekerka-type instability [51] influencing the roughness of the advancing interface and giving rise to the dendritic morphology in Zone II. For this type of instability to occur, the growing crystal has to be surrounded by supercooled liquid i.e. the material has to be at a temperature above the melting temperature of the amorphous material but below the melting temperature of the crystalline material. A schematic representation of the conditions for this type of instability to take place is shown in Figure 23. Consider a solid-liquid interface advancing in the direction of the (supercooled) liquid (Figure 23A). The heat generated from the liquid to crystalline phase transition will be transferred to the liquid since the solid is at higher temperature resulting in a negative temperature gradient with respect to the surrounding material. In the beginning of such growth, the isotherm will be planar (Figure 23 B). However, once a protrusion is created (Figure 23C), the initially negative temperature gradient becomes more negative permitting more efficient evacuation of the heat at the tip of the protrusion than from the surrounding regions (Figure 23D). As a consequence, the protrusion will grow preferentially. Therefore, a solid-liquid interface advancing in a supercooled liquid is inherently unstable. In the case of LREC growth, Mullins-Sekerka-type instability can be initiated as a result of growth anisotropies, which will perturb the local temperature profile (it is well known that different crystallographic planes grow at different velocities, introducing anisotropy at the growth front [53]). Once started, the instability grows due to the higher rate of heat dissipation at the tip of the protrusion roughening the planar crystallization front and producing the observed

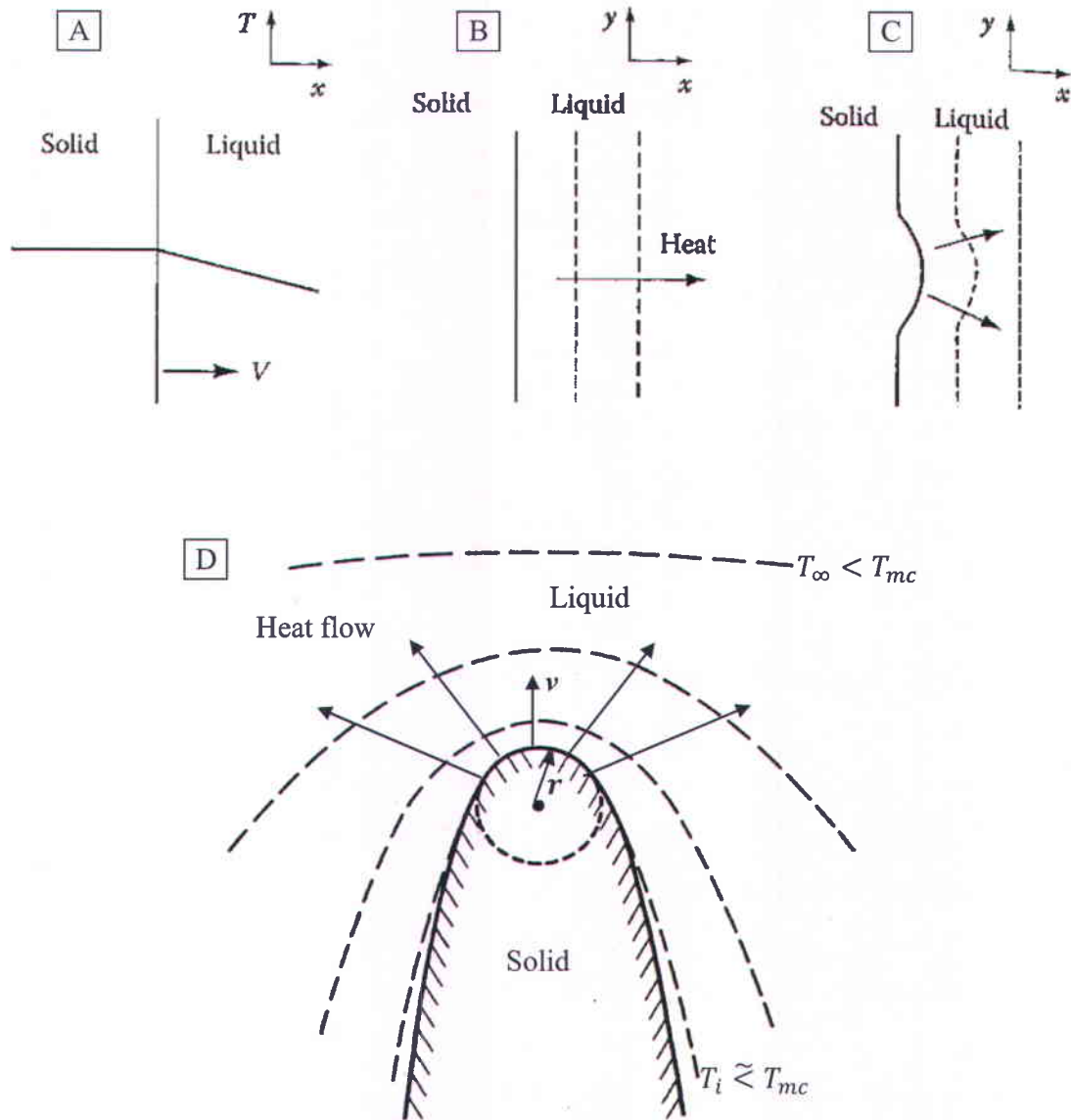


Figure 23. Representation of Mullins-Sekerka thermal instability. A) Direction of the solidification front advancement in the supercooled liquid. B) Direction of the heat flow from the solid phase toward the supercooled liquid. C) Creation of a protrusion due to a nucleation center. D) Schematic representation of the heat flow direction at the dendrite's tip and the temperature difference where v is the velocity of growth, T_i is the temperature at the interface, T_{mc} is the temperature for melt of the crystalline material, T_∞ is the temperature far from the dendrite's tip and r is the radius of the tip. Figure adapted from [54] (A-C) and [51] (D).

LREC. This kind of instability can explain the formation of the LREC and their final shape seen in the post mortem images.

For qualitative interpretation of the growth mechanism a simplified model that relates the growth rate of the dendrite (v) to its radius (r) (Figure 23D), thermal conductivity (κ), latent heat of crystallization (L_c), and temperature difference ($T_i - T_\infty$) between the interface (T_i) and surrounding material held at room temperature (T_∞) can be used as follows (detailed description of the model, which was originally developed for dendritic growth in metallic systems, is given in [54]):

$$v_{dendritic\ growth} = \frac{\kappa}{L_c r} (T_i - T_\infty). \quad (6)$$

For a molten layer to propagate in front of the growing dendrite at 8 m/s, a temperature between T_{ma} and T_{mc} is required [43], [55]. Therefore, the radii of the growing dendrites should range between $\sim 1.3 \mu\text{m}$ and $\sim 1.9 \mu\text{m}$. Comparison of these values with the post mortem images showed that some LRECs in Zone II possess radii in this range. Figure 24 shows crystals with radii of $\sim 1.8 \mu\text{m}$ to $1.3 \mu\text{m}$. The observed instability of the growth front and this qualitative description of the growth support the interpretation that the crystallization in Zone II proceeds via an ELPC mechanism with co-propagating crystal-liquid and liquid-amorphous interfaces. However, solving the reverse problem i.e. evaluation of the temperature at which the dendrites grew with this model showed to be challenging because the LREC tips exhibit mostly edge shape than semi-circular shape, thus, it is not straight forward to assign a radius of the dendrites' tips that will result in confident evaluation of the temperature. For these reasons and to further investigate this process, hereafter, a quantitative estimation of the temperature of the film in time will be presented.

Important questions to be addressed regarding the growth in this zone relate to the quantification of the temperature evolution of the film and the change in crystallization dynamics at the outer edge of Zone II, where an abrupt change in crystallization behavior is evident. To address these points, computations of the time-evolving average radial temperature profile [i.e., $T(r)$] in the film were made. In his MSc Thesis, M Stern proposed the following model to estimate the temperature of the film in the radial direction [36]. To calculate the time dependent two dimensional (2D) temperature profile of a thin film, the heat



Figure 24. Post mortem image of Zone II. Red circles outline some of the dendrites with tips with radii from left to right $\sim 1.8 \mu\text{m}$, $\sim 1.3 \mu\text{m}$, and $\sim 1.6 \mu\text{m}$. The scale bar is $2 \mu\text{m}$.

equation can be numerically solved using a finite element method. The model is two dimensional because the heat released from the liquid-to-crystal phase transition at one point serves to heat and crystallise larger area (and volume). Consider the 2D time dependent heat equation with a source term:

$$\frac{\partial u(x, y, t)}{\partial t} = D\Delta u(x, y, t) + f(x, y, t), \quad (7)$$

where $u(x, y, t)$ is the temperature of the film at position x, y and time t , $f(x, y, t)$ is the source term representing the rate at which thermal energy is added or subtracted to the system, and D is the thermal diffusivity of the material given by [56]:

$$D = \frac{k}{\rho C_p}, \quad (8)$$

where k is the thermal conductivity, ρ is the mass density and C_p is the specific heat at

constant pressure of the material. To calculate the time dependent temperature profile of the thin film, the heat equation can be numerically solved using a finite element method. The assumptions used in the calculations are that the edges of the film are fixed at room temperature and far from the laser spot and the rate of heat diffusion perpendicular to the film is instantaneous. At nanosecond timescales, the error coming from these assumptions will be negligible since the film thickness is small compared to the heat diffusion length. For the simulation, the source term, $f(x, y, t)$ was determined phenomenologically to account for the exothermic nature of the amorphous to crystalline phase transition. Using known values for the amorphous to crystalline heat of transformation, $k = 130 \text{ mW/cm}\cdot\text{K}$, $\rho = 5.0 \text{ g/cm}^3$ [23], [57] and the estimated positions of the growth front in Zone II and III from the DTEM images, the source term is constructed to simulate the heat released and absorbed near the crystalline growth front. The heat absorbed from the laser pulse is not included in the source term; it is instead used to calculate the initial temperature profile of the film. It is important to note that the heat of crystallization, not the initial pump energy, drives the two dimensional temperature dynamics in the plane of the sample. The initial heat absorbed from the excitation pulse brings the temperature high enough to crystallize the film within the bounds of the incident beam, but diffuses too slowly to cause dynamics at the time scales observed. Instead, the localized exothermic heat drives further crystallization outward in a self-sustaining manner. The algorithm was implemented in MATLAB by triangulating the domain into finite elements and using matrix methods to solve for the temperature, $u(x, y, t)$ (more details on the model are given in Annex A and the complete code can be found in ref.[36]).

The calculations showed that, in the geometry of our experiment, crystallization in Zone II is initiated on a temperature profile slightly perturbed from the initial, circularly symmetric Gaussian temperature field produced through the laser excitation of the a-Ge material (Figure 25). Also, the average temperature at the crystallization front drops through Zone II. The temperature approximately follows the decline of the underlying Gaussian temperature profile (coming from the laser beam) over the same distance (Figure 25 – dotted baseline). The decrease of the temperature favouring development of instabilities at the growth front can be in the origin of the increased faceting, i.e. the observation in the time-resolved images that initially rounded/smooth protrusions become increasingly faceted as

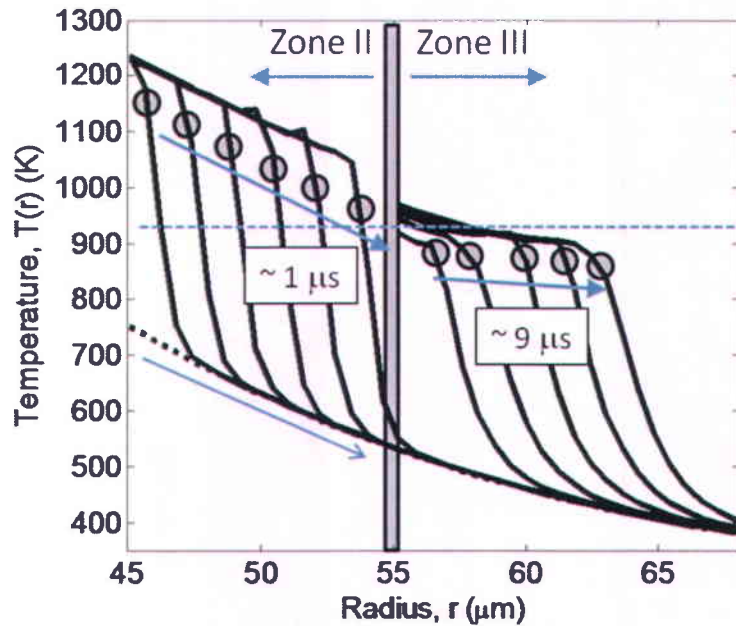


Figure 25. Evolution of the circularly symmetric radial temperature distribution in the film, $T(r)$ in Zones II and III in the vicinity of the crystallization front for 150 ns time-steps through Zone II and 1.8 μs time-steps through Zone III. The radial position of the crystallization front at each time is indicated with a grey circle. The temperature decrease through Zone II approximately follows the decrease in $T(r)$ due to the Gaussian distribution of laser deposited energy (dotted baseline). The slower net radial crystallization through Zone III provides a better match with thermal diffusion and results in an approximately constant front temperature. The abrupt transition in crystallization dynamics occurs once $T(r)$ drops below a threshold for the radial ELPC process to occur. Figure reprinted with permission from [58].

growth becomes more anisotropic through Zone II (see also Figure 15). In addition, these calculations suggest that the abrupt change in the crystallization dynamics occurs once the temperature at the rapidly advancing Zone II crystallization front drops below the lower threshold for the ELPC process. This transition occurs after approximately 10 μm of Zone II growth in the geometry of our experiment. Earlier work has proposed that once Zone II crystallization is complete there is a pause in the crystallization as the heat initially deposited by the pump pulse traverses the LREC region [50] and that Zone III crystallization is initiated by the resulting rise in temperature [23], [50]. Also, as mentioned in the beginning of this section, it was suggested that Zone III crystallization proceeds at higher temperatures

than Zone II due to this redistribution of thermal energy [23]. Such a view is inconsistent with the time-resolved measurements, since we do not observe such a delay in DTEM images of the time-evolving microstructure.

As shown in the previous section crystallization in Zone III begins after completion of the dendritic growth. An earlier model for Zone III crystallization suggested that the observed layering forms through inward (i.e., radial) crystallization of bands of molten material [23], however, our data does not support this model. The DTEM images clearly show that, outside the transition region, the local growth front velocity is azimuthally directed in Zone III. The dramatic change in crystallization behavior in Zone III produces patterns of crystallization orthogonal to the net radial heat flow and is accompanied by a reduction in the rate at which crystallization advances in the radial direction by almost an order of magnitude. Taken together with the thermal modeling results, the DTEM observations suggest another mechanism for Zone III crystallization and an explanation for the observed layered microstructure. Once $T(r)$ drops below T_{ma} the rapid (~ 8 m/s) radial advance of the Zone II dendrites by the ELPC mechanism can no longer be sustained; crystal growth in Zone II has outpaced the thermal diffusion due to the initiating laser and the crystallization front has penetrated into a region below the threshold temperature supporting this growth mode. Previous work has demonstrated the sensitive dependence of crystallization mode with substrate temperature in other geometries [6], [14]. A similar melt-mediated mechanism can be supported, however, along the narrow (~ 1 μm) bands in the orthogonal direction where the crystallization front follows an approximately isothermal curve at the appropriate temperature. An important feature of this new growth mode is that it better matches the radial advance of crystallization with thermal diffusion in the radial direction (i.e., thermal diffusion of both the newly evolved energy at the crystallization front and that flowing from the previously crystallized Zone II). At ELPC growth rates a typical 8- μm long single layer is formed in ~ 1 μs . The diffusion length over this period is ~ 6 μm , sufficient to prepare a narrow adjacent band of material to support growth of an additional layer. The good match between thermal diffusion and the radial advance of crystallization is evident in the temperature profiles shown in Figure 25, which show that this layered growth mode results in an almost constant temperature at the radius in which new layers are growing through Zone III. This growth mode is similar to the

zigzag growth described by Chojnacka proposed for the observed scalloped microstructure in explosively crystallized films in a different experimental geometry [6].

The crystallization process in this zone ceases when the temperature of the adjacent amorphous material drops below a critical level and can no longer support growth of a new layer through the mechanism described above.

3.5. Conclusion

We observed the crystallization process in a-Ge films supported on an insulating substrate *in situ* by DTEM. We were able to reveal the events of nucleation and nanocrystallization, to estimate the maximal nucleation rate in Zone I, to determine the velocities of crystallization and to give an estimate of the temperature of the film during the growth of the different microstructures. The study provided important insights into the crystallization dynamics and mechanisms involved in the formation of the three qualitatively distinct morphological zones evident in the final structure.

We found that the crystallization in Zone I develops via random nucleation from the bulk at temperature above the melting temperature of the amorphous material but below the melting temperature of the crystalline semiconductor. Based on the time-resolved images, we made estimations on the time for complete crystallization in this region and the nucleation rate to be ~ 55 ns and $\sim 1.6 \times 10^{22} \frac{\text{nuclei}}{\text{cm}^3 \cdot \text{s}}$ respectively [17]. However, these values need to be confirmed by theoretical modeling of the nucleation process to relate the findings obtained from the time-resolved image and the data from the post mortem images.

Through direct measurements of the crystallization front, we have shown that growth through Zone II is subject to a Mullins-Sekerka-like instability that results in dendritic morphology of the crystals with increased faceting towards the boundary of this zone [58]. We have also shown an abrupt transition in the nature of the crystal growth front in Zone III, where the growth of single-crystal regions is perpendicular to the macroscopic crystallization direction (or net heat flow), and that formation of the layered structure is consistent with a zigzag growth mode [6], [58]. The direct measurement of the time scales involved in the crystal growth and a comparison with thermal diffusion timescales show that crystallization in both Zones II and III is explosive in the sense that it is driven by latent

heat released at the crystallization interface and not thermal diffusion of laser-deposited energy. These time scales suggest an explosive liquid phase assisted transformation is the dominant mechanism in both Zone II and Zone III crystallization, despite the radial advance of crystallization preceding an order of magnitude more slowly in Zone III.

The use of dynamic transmission electron microscopy in the study of laser induced crystallization in a-Ge proved to be critically important due to the irreversible nature of the process which precludes the use of the related multi-shot time-resolved techniques.

3.6. Bibliography

- [1] M. Hatano, S. Moon, M. Lee, K. Suzuki, and C. P. Grigoropoulos, "Excimer laser-induced temperature field in melting and resolidification of Si thin films," *J. Appl. Phys.*, vol. **87**, p. 36–43 (2000).
- [2] G. Andrä, J. Bergmann, F. Falk, E. Ose and H. Stafast, "Laser induced crystallization of amorphous silicon films on glass for thin film solar cells," *Phys. Stat. Sol. A*, vol. **166**, p. 629–634 (1998).
- [3] F. Vega, R. Serna, C. N. Afonso, D. Bermejo, and G. Tejada, "Relaxation and crystallization kinetics of amorphous germanium films by nanosecond laser pulses," *J. Appl. Phys.*, vol. **75**, p. 7287–7291 (1994).
- [4] S. Uchikoga and N. Ibaraki, "Low temperature poly-Si TFT-LCD by excimer laser anneal," *Thin Solid Films*, vol. **383**, p. 19–24 (2001).
- [5] J. B. Boyce, P. Mei, R. T. Fulks and J. Ho, "Laser processing of polysilicon thin-film transistors: Grain growth and device fabrication," *Phys. Stat. Sol. A*, vol. **166**, p. 729–741 (1998).
- [6] A. P. Chojnacka, PhD Thesis: Explosive crystallization of germanium films: Kinetics and morphologies, Cornell University (2002).
- [7] D. B. Williams and C. B. Carter, Transmission Electron Microscopy – A Textbook for Materials Science (2nd edition), Springer, New York, NY, USA (2009).
- [8] B. W. Reed, M. R. Armstrong, N. D. Browning, G. H. Campbell, J. E. Evans, T. LaGrange, and D. J. Masiel, "The Evolution of Ultrafast Electron Microscope Instrumentation," *Microsc. Microanal.*, vol. **15**, p. 272–281 (2009).
- [9] M. Von Allmen, Laser-Beam Interactions with Materials. Physical Principles and applications, Springer-Verlag Berlin Heidelberg (Germany) (1987).
- [10] G. Badertscher, R. P. Salathé and H. P. Weber, "Dynamics of laser crystallization in amorphous Ge films," *Appl. Phys. A*, vol. **25**, p. 91–93 (1981).
- [11] M. Mulato, D. Toet, G. Aichmayr, P. V. Santos, and I. Chambouleyron, "Laser crystallization and structuring of amorphous germanium," *Appl. Phys. Lett.*, vol. **70**, p. 3570–3572 (1997).
- [12] O. Bostanjoglo and E. Endruschat, "Kinetics of laser-induced crystallization of amorphous germanium films," *Phys. Stat. Sol. (A)*, vol. **91**, p. 17–28 (1985).

- [13] T. LaGrange, B. W. Reed, M. K. Santala, J. T. McKeown, A. Kulovits, J. M. K. Wiezorek, L. Nikolova, F. Rosei, B. J. Siwick, G. H. Campbell, "Approaches for ultrafast imaging of transient materials processes in the transmission electron microscope," *Micron*, vol. **43**, p. 1108–1120 (2012).
- [14] C. Grigoropoulos, M. Rogers, S. H. Ko, A. A. Golovin, and B. J. Matkowsky, "Explosive crystallization in the presence of melting," *Phys. Rev. B*, vol. **73**, p. 184125-1–15 (2006).
- [15] A. Chojnacka and M. O. Thompson "Morphological instabilities during explosive crystallization of germanium films," *MRS Symposia Proc.*, vol. **648**, p. P11.12.1–8 (2001).
- [16] Initial results from orientation imaging microscopy (OIM) obtained at LLNL by T. LaGrange. The OIM is a TEM-based technique that allows for automatic acquisition of diffraction patterns and indexation of the crystallographic orientations of the crystals in a predefined region. The technique allows identification of the misorientation between the grains and the type of defects present within one grain. The crystallographic orientations could be seen along the three directions i.e. normal to the plane of the sample, parallel to the growth direction of the crystal and perpendicular to it. Also, OIM allows automatic determination of the sizes of the grains in polycrystalline samples. The advantage of this technique in comparison with conventional dark field imaging is the possibility to visualise all the crystals in the same time in the chosen region to obtain more reliable estimation of the mean size of the nanocrystals. The disadvantage is the difficulty in determination of the crystals' orientations for sizes below 100 nm due to overlapping of the grains. This leads to large uncertainties (on the order on the size of the crystals) on the determined size distribution and mean size of the grains. NanoMegas Com (offering OIM systems) website www.nanomegas.com.
- [17] L. Nikolova, T. LaGrange, B. W. Reed, M. J. Stern, N. D. Browning, G. H. Campbell, J.-C. Kieffer, B. J. Siwick, and F. Rosei, "Nanocrystallization of amorphous germanium films observed with nanosecond temporal resolution," *Appl. Phys. Lett.*, vol. **97**, p. 203102-1–3 (2010).

- [18] C. A. Schneider, W. S. Rasband, & K. W. Eliceiri, "NIH Image to ImageJ: 25 years of image analysis," *Nature Methods*, vol. **9**, p. 671–675 (2012).
- [19] Image J website: rsb.info.nih.gov/ij/
- [20] T. LaGrange, G. H. Campbell, B. W. Reed, M. Taheri, J. B. Pesavento, J. S. Kim, N. D. Browning, "Nanosecond time-resolved investigations using the in situ of dynamic transmission electron microscope (DTEM)," *Ultramicroscopy*, vol. **108**, p. 1441–1449 (2008).
- [21] W. Marine and J. Marfaing, "Laser Pulse Triggering of the Explosive Crystallization in Amorphous Si and Ge Thin Films," *MRS Symp. Proc.*, vol. **157**, p. 449–454 (1989).
- [22] K. Nagashio and K. Kuribayashi, "Growth mechanism of twin-related and twin-free facet Si dendrites." *Acta Mater.*, vol. **53**, p. 3021–3029 (2005).
- [23] R. K. Sharma, S. K. Bansal, R. Nath, R. M. Mehra, K. Bahadur, R. P. Mall, K. L. Chaudhary, and C. L. Garg, "Electron beam induced explosive crystallization of unsupported amorphous germanium thin films," *J. Appl. Phys.*, vol. **55**, p. 387–394 (1984).
- [24] T. Takamori, R. Messier & R. Roy, "Phenomenology of the "explosive" crystallization of sputtered non-crystalline germanium films," *J. of Mater. Sci.*, vol. **8**, p. 1809–1816 (1973).
- [25] H. J. Zieger, J. C. C. Fan, B. J. Palm, R. P. Gale, R. L. Chapman, "Solid-phase crystallization produced by laser scanning of amorphous Ge films: the role of the latent heat in crystallization front dynamics," *MRS Symp. Proc.: Laser and Electron Beam Processing of Materials*, Cambridge, Massachusetts, USA, Academic Pres., vol. **1**, p. 234–240 (1980).
- [26] W. C. Sinke, A. Polman, S. Roorda, P.A. Stolk, "Explosive crystallization of amorphous silicon: Triggering and propagation," *Appl. Surf. Sci.*, vol. **43**, p. 128–135 (1989).
- [27] M. O. Thompson and G. J. Galvin, "Time resolved measurements of interface dynamics during pulsed laser melting observed by transient conductance," *MRS Symp. Proc.*, Elsevier Science Publishing Co., Inc., vol. **13**, p. 57–67 (1983).

- [28] H. D. Geiler, E. Glaser, G. Götz, and M. Wagner, “Explosive crystallization in silicon,” *J. Appl. Phys.*, vol. **59**, p. 3091–3099 (1986).
- [29] O. Bostanjoglo, F. E. Endruschat, W. Tornow, “Time resolved TEM of laser-induced phase transitions in a-Ge and a-Si/Al-films,” *MRS Symp. Proc.*, vol. **71**, p. 345–350 (1986).
- [30] E. A. Brandes, ed., Smithells Metals Reference Book, 6th ed., Butterworths (1983).
- [31] H. S. Chen and D. Turnbull, “Specific heat and heat of crystallization of amorphous germanium,” *J. Appl. Phys.*, vol. **40**, p. 4214–4215 (1969).
- [32] S. McGowan, M.Sc. Thesis: In situ study of amorphous semiconductor crystallization by Dynamic Transmission Electron Microscopy, McGill University, Montréal, Québec, Canada (2009).
- [33] M. L. Taheri, S. McGowan, L. Nikolova, J. E. Evans, N. Teslich, J. P. Lu, T. LaGrange, F. Rosei, B. J. Siwick, and N. D. Browning, “In situ laser crystallization of amorphous silicon: Controlled nanosecond studies in the dynamic transmission electron microscope,” *Appl. Phys. Lett.*, vol. **97**, p. 032102-1–3 (2010).
- [34] M. Lee, S. Moon, C. P. Grigoropoulos, “In situ visualization of interface dynamics during the double laser recrystallization of amorphous silicon thin films,” *J. Cryst. Growth*, vol. **226**, p. 8–12 (2001).
- [35] G. E. Jellison, D. H. Lowndes, D. N. Mashburn, R. F. Wood, “Time-resolved reflectivity measurements on silicon and germanium using a pulsed excimer KrF laser heating beam,” *Phys. Rev. B*, vol. **34**, p. 2407–2415 (1986).
- [36] M. Stern, MSc Thesis: Time resolved transmission electron microscopy: the structural dynamics of explosive crystallization in amorphous germanium, McGill University, Montréal, Québec, Canada (2012).
- [37] N. E. Cusack, The physics of structurally disordered matter: An Introduction, Adam Hilger, IOP Publishing (1987).
- [38] N. A. Blum and C. Feldman, “The crystallization of amorphous germanium films,” *J. Non-Cryst. Solids* vol. **22**, p. 29–35 (1976).
- [39] P. Germain, S. Squelard, J. Bourgoïn, and A. Gheorghiu, “Crystallization kinetics of amorphous germanium,” *J. Appl. Phys.*, vol. **48**, p. 1909–1913 (1977).

- [40] R. F. Adamski, "Effect of Deposition Parameters on the Crystallinity of Evaporated Germanium Films," *J. Appl. Phys.*, vol. **40**, p. 4301-1-5 (1969).
- [41] K. P. Chik, P. K. Lim, "Annealing and crystallization of amorphous germanium thin films," *Thin Solid Films*, vol. **35**, p. 45-56 (1976).
- [42] W. Marine and J. Marfaing, "Solid state nucleation rate of Si and Ge near melting point," *Phase Trans.: A Multinational J.*, vol. **31**, p. 299-308 (1991).
- [43] E. P. Donovan, F. Spaepen, D. Turnbull, J. M. Poate, and D. C. Jacobson, "Calorimetric studies of crystallization and relaxation of amorphous Si and Ge prepared by ion implantation," *J. Appl. Phys.*, vol. **57**, p. 1795-1804 (1985).
- [44] F. Vega, N. Chaoui, J. Solis, J. Armengol, C. N. Afonso, "Optical evidence for a self-propagating molten buried layer in germanium films upon nanosecond laser irradiation," *J. Appl. Phys.*, vol. **97**, p. 103519-1-6. (2005).
- [45] H. J. Leamy, L. W. Brown, G. K. Celler, G. Foti, G. H. Gilmer, J. C. C. Fan, , "Explosive crystallization of amorphous germanium films," *MRS Symp. Proc.: Laser and electron-beam solid interactions and materials processing*, Boston, Massachusetts, USA, Elsevier, vol. **1**, p. 89-96 (1981).
- [46] G. H. Gilmer and H. J. Leamy, "An analysis of the explosive crystallization of amorphous layers," *MRS Symp. Proc.: Laser and Electron Beam Processing of Materials*, Cambridge, Massachusetts, USA, Academic Press, p. 227-233 (1979).
- [47] R. B. Gold, J. F. Gobbons, T. J. Magee, J. Peng, R. Ormond, V. R. Deline, C. A. Evans, , "Laser induced explosive radial crystallization of deposited Ge and Si thin films," *MRS Symp. Proc.: Laser and Electron-Beam Solid Interactions and Materials Processing*, Cambridge, Massachusetts, USA, Elsevier, vol. **1**, p. 221-226 (1980).
- [48] E. J. Albenze, M. O. Thompson and P. Clancy, "Atomistic computer simulation of explosive crystallization in pure silicon and germanium," *Phys. Rev. B*, vol. **70**, p. 094110-1-10 (2004).
- [49] H. Mehrer, *Diffusion in Solids – Fundamentals, Methods, Materials, Diffusion-Controlled Processes*, Springer-Verlag Berlin Heidelberg (2007).
- [50] O. Bostanjoglo, R. P. Tornow and W. Tornow, "Nanosecond-exposure electron microscopy of laser-induced phase transformations," *Ultramicroscopy*, vol. **21**, p. 367-372 (1987).

- [51] J. S. Langer, “Instabilities and pattern forestation in crystal growth,” *Rev. Mod. Phys.*, vol. **52**, p. 1–30 (1980).
- [52] W. W. Mullins, and B. F. Sekerka, “Morphological Stability of a Particle Growing by Diffusion or Heat Flow,” *J. Appl. Phys.*, vol. **34**, p. 323–329 (1963).
- [53] L. Csepregi, R. P. Kullen, J. W. Mayer, and T. W. Sigmon, “Regrowth kinetics of amorphous Ge layers created by ^{74}Ge and ^{28}Si implantation of Ge crystals,” *Solid State Commun.*, vol. **21**, p. 1019–21 (1977).
- [54] D. A. Porter, K. E. Easterling and M. Y. Sherif, Phase transformation in metal and alloys, 3rd ed., CRC Press – Taylor and Francis Group LLC (2009).
- [55] R. R. Hultgren, Selected values of the thermodynamic properties of the elements, American Society for Metals, Metals Park, Ohio (1973).
- [56] D. R. Lide, Handbook of Chemistry and Physics (90 ed.), Boca Raton, Florida: CRC Press (2009).
- [57] P. Nath and K. L. Chopra, “Thermal conductivity of amorphous and crystalline Ge and GeTe films,” *Phys. Rev. B*, vol. **10**, p. 3412–3418 (1974).
- [58] L. Nikolova, T. Lagrange, M. J. Stern, J. M. MacLeod, B. W. Reed, H. Ibrahim, G. H. Campbell, F. Rosei, B. J. Siwick, “Complex crystallization dynamics in amorphous germanium followed with dynamic transmission electron microscopy,” *Phys. Rev. B*, vol. **87**, p. 064105-1–6 (2013).

Chapter IV

Crystallization in self-sustained amorphous germanium films

In this chapter we describe the behaviour of amorphous germanium free standing films upon laser induced crystallization observed *in situ* by DTEM. As presented in the previous chapters the DTEM developed at LLNL is the only instrument in the world offering the appropriate combination of high spatial and high temporal resolutions for *in situ* investigation of fast-evolving laser-induced processes. We again used bright field imaging mode for acquisition of time-resolved images. The objectives of this study were to reveal the change of the morphology of the film in time, the shape of the crystallization front during its propagation along with quantification of its roughness, to determine the velocities of crystallization and to give an estimation of the temperature of the film during the growth of the different microstructures. We will focus on the investigation of the explosive character of the crystallization in a-Ge. For that, measurement of the sizes of the crystals was made and the times for formation of the different microstructures were given, and used to estimate the respective growth velocities. The uncertainties related to the calculations will be discussed in each section. In the discussion section at the end of this chapter, we will address the possible growth modes along with an estimate of the temperature evolution with the time and in radial direction. We will conclude the chapter with a short comparison of the crystallization behaviour observed in self-sustained a-Ge films and a-Ge supported by thin membrane. The comparison is justified since we made the experiments under similar conditions and will help clarify the influence of the supporting layer on the crystallization dynamics in a-Ge.

In this study, we used 110 nm thick a-Ge films supported on a 150-mesh Cu grid. The procedure for fabrication of the films was described in Chapter II. As in the case of a-Ge/SiO₂, we used pump laser wavelength at 532 nm with pulse duration of 15 ns and a constant fluence of $\sim 110 \text{ mJ/cm}^2 \pm 5\%$ with fluctuation of the fluence coming from the pump laser itself (note that the fluence was calculated in the same way as described in

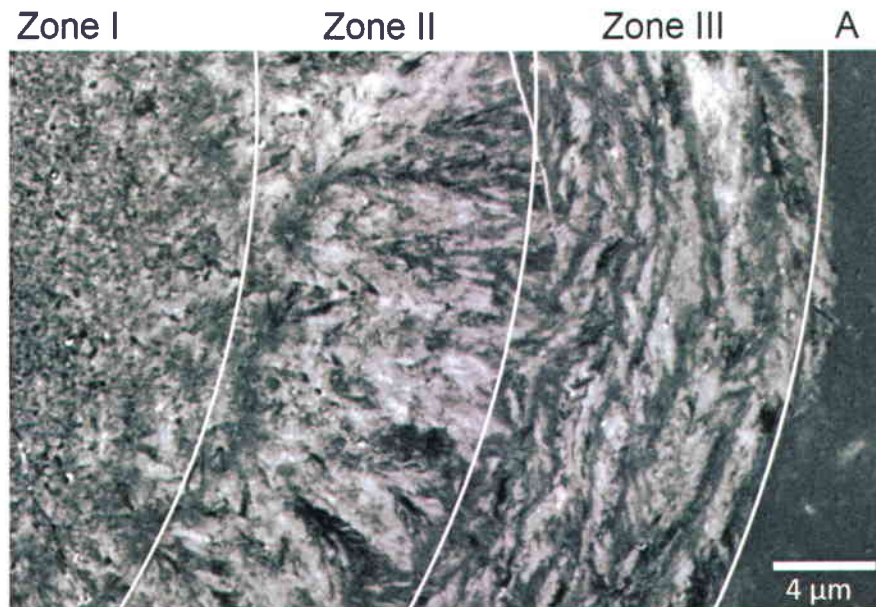


Figure 26. Partial view of all the microstructures formed after single shot laser induced crystallization in 110 nm self-sustained a-Ge film. The white arcs give the approximated boundaries of the different morphologies i.e. the regions of the coarse nanocrystals (*Zone I*), large radially elongated crystals (LREC) (*Zone II*), layered structure (*Zone III*) and the remaining amorphous material (*A*). The regions are annotated in the upper part of the micrograph.

Chapter III with radius of the laser beam spot of 45 μm). We took time resolved images with delays ranging between 20 ns and 10 μs . Since the process is irreversible, for each new experiment (i.e. time delay) a fresh window on the sample was used. When there were no more available windows, the sample was replaced with a new one obtained in the same fabrication lot.

4.1. Microstructures formed

Upon single shot laser heating germanium crystallises into the same three distinct morphologies as observed in the case of laser induced crystallization of a-Ge supported by insulating membrane (see Chapter III). We use the same labels as follows (Figure 26): Zone I – a coarse nanocrystalline region within the bounds of the incident laser beam i.e. with

radius r_{beam} approximately equal to the $1/e^2$ radius of the Gaussian laser beam spot that initiates the crystallization ($r_{beam} = 45 \mu\text{m}$ in this study); Zone II – consists of large radially elongated crystals (LREC) situated outside of the $1/e^2$ radius of the laser beam spot, extending from an inner radius of $\sim 45 \mu\text{m}$ to an outer radius of $\sim 52 \mu\text{m}$; and Zone III – layered structure composed of nanocrystalline bands exhibiting a feather-like morphology and large tangentially oriented crystals (LTOC) starting from an inner radius of $\sim 52 \mu\text{m}$ and with a variable outer radius from $\sim 57 \mu\text{m}$ to $\sim 59 \mu\text{m}$. A detailed description of each microstructure and the information obtained for the crystallization in the respective region will be presented separately in the following subsections of this chapter.

4.2. Formation times of the microstructures, shape of the growth front during propagation and respective velocities of crystallization

4.2.1. Zone I

Nanocrystallinity is the primary characteristic of Zone I. The constituent nanocrystals have sizes ranging from $\sim 5 \text{ nm}$ to $\sim 200 \text{ nm}$ with random orientation confirmed by SAED. With the objective of studying the nucleation and growth of these crystals, we acquired time-resolved images of the central part of the region where the laser beam deposited most of its energy. Figure 27 shows a series of time-resolved images taken at the center of Zone I, labelled with their respective time delays. The dark features seen in the images are considered to be nanocrystals since they lead to strong electron scattering expected to occur when a crystalline phase appears. The large bright features seen in the images (appearing mostly as part of a ring) are mostly pores forming due to the densification of the a-Ge upon crystallization, since a-Ge has a lower density than the crystalline material [1]. Comparison of the image acquired prior to crystallization (denoted with “0 ns” in the figure) with the first time resolved image, taken at 20 ns, suggests that the crystallization process has already started since change in the morphology was observed. This suggests that nucleation and growth in this zone initiates at time less than 20 ns after arrival of the pump pulse, in agreement with earlier studies of the process [2]. We did not attempt accurately to determine the time for initiation of the crystallization because with the single shot setup it is not possible to monitor in continuous fashion the process *in situ*.

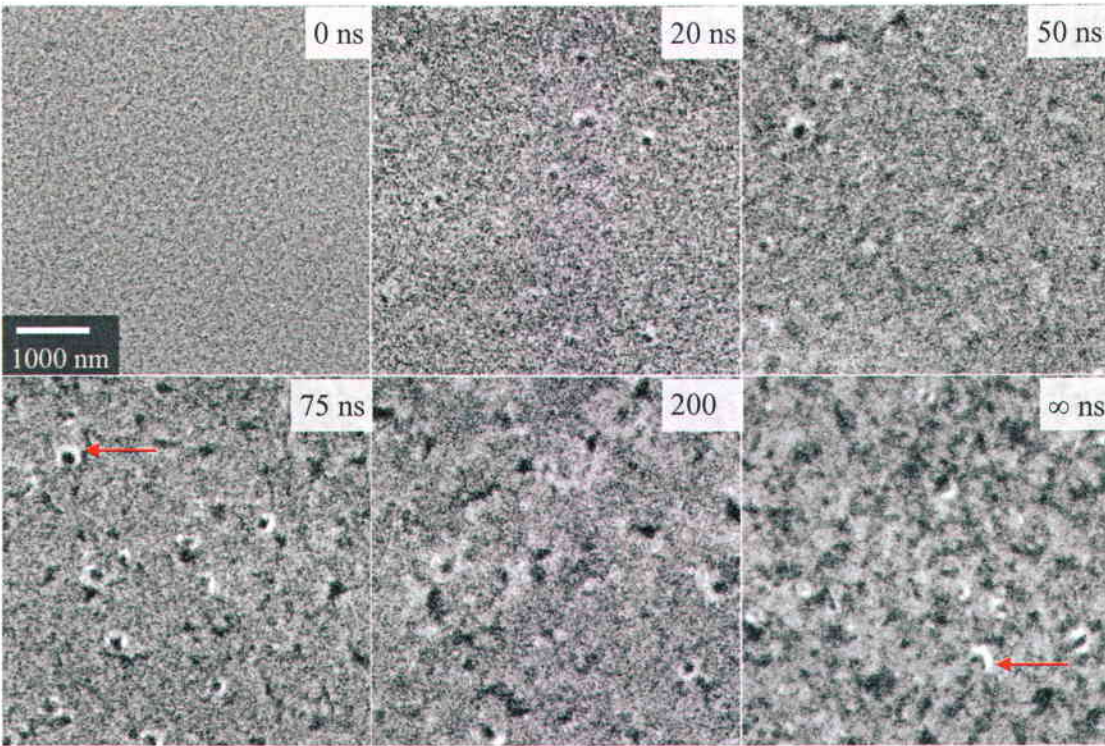


Figure 27. Time resolved images of the crystallization process in self-supported a-Ge films in Zone I where the laser beam has deposited its energy. Nanocrystals are considered to be the dark features seen in the images. The large light color features mostly appearing as part of a ring next to the dark features (pointed with red arrows) are pores forming due to densification of the amorphous material upon its crystallization. The time delay is denoted in the upper right corner of each block image. The first image denoted with “0 ns” shows the film prior the crystallization, while the post mortem image i.e. at the end of the crystallization is denoted with “∞ ns”. The scale bar is the same for all images and is given in the first block image (up-left).

We attempted to extract the evolution of the sizes of the nanocrystals with time and estimate their number from the time resolved micrographs through image treatment using Image J software [3] because the images showed development of spatially varying contrast which relates to evolution of the morphology. However, due to instability of the DTEM performance¹ and the limited experimental time on the instrument, we could not

¹ The cathode-drive laser used in the operation of the DTEM is a custom-made laser designed at LLNL. The fifth harmonic (211 nm) is used to excite the electron source. Therefore, the laser operation is highly sensitive

acquire reliable data for a consecutive analysis.

4.2.2. Zone II

The microstructure in this zone is characterised by the presence of large crystals oriented in the radial direction. Their length varies between 5 μm and 9 μm . As described previously, their structure is highly faceted, they terminate in a wedge shape forming a dendritic morphology and several dendrites form from one nucleation center (as seen in Figure 14 in Chapter III). The growth in this zone is initiated at ~ 100 ns and completed at ~ 1000 ns giving an average velocity of growth of $\sim 8 \text{ m/s} \pm 2 \text{ m/s}$.

4.2.2.1. Shape of the crystallization front during its propagation and analysis of its roughness

One of the important questions in understanding this crystallization process is: what is the shape and roughness of the growth front during the crystallization in Zone II? The answer to this question will give a qualitative indication of how the temperature of the film evolves during the growth of these crystals and when the instabilities at the growth front become predominant, resulting in the final wedge shape of these crystals. This information is important for a proper description of the behaviour of crystallization of a-Ge and will be addressed in the discussion section of this chapter. Figure 28 shows time-resolved images of the crystallization process in Zone II. In its initial stages, the growth front is relatively flat with small protrusions, similar to the case of a-Ge/SiO. These protrusions may be caused by anisotropic growth because different crystallographic planes can grow at different velocities along the direction of the thermal gradient [5]. Since the LREC are seeded in the central coarse nanocrystalline Zone I where the crystals have random orientations (Figure 28 – 100 ns to 150 ns delays images) such anisotropy may occur. For delays up to ~ 350 ns the roughness visibly decreases, while for longer delays, the roughness increases significantly (Figure 28 – 500 ns and 1000 ns delays and post mortem image denoted with “ ∞ ns”).

Since the spatial oscillations in the growth front are important, we took higher magnification images for better resolution and determined the root mean square (RMS) of

to temperature and humidity variation of the room where the DTEM is located. Instability of the operation of the DTEM was provoked due to temporal problems with control of the temperature in the room.

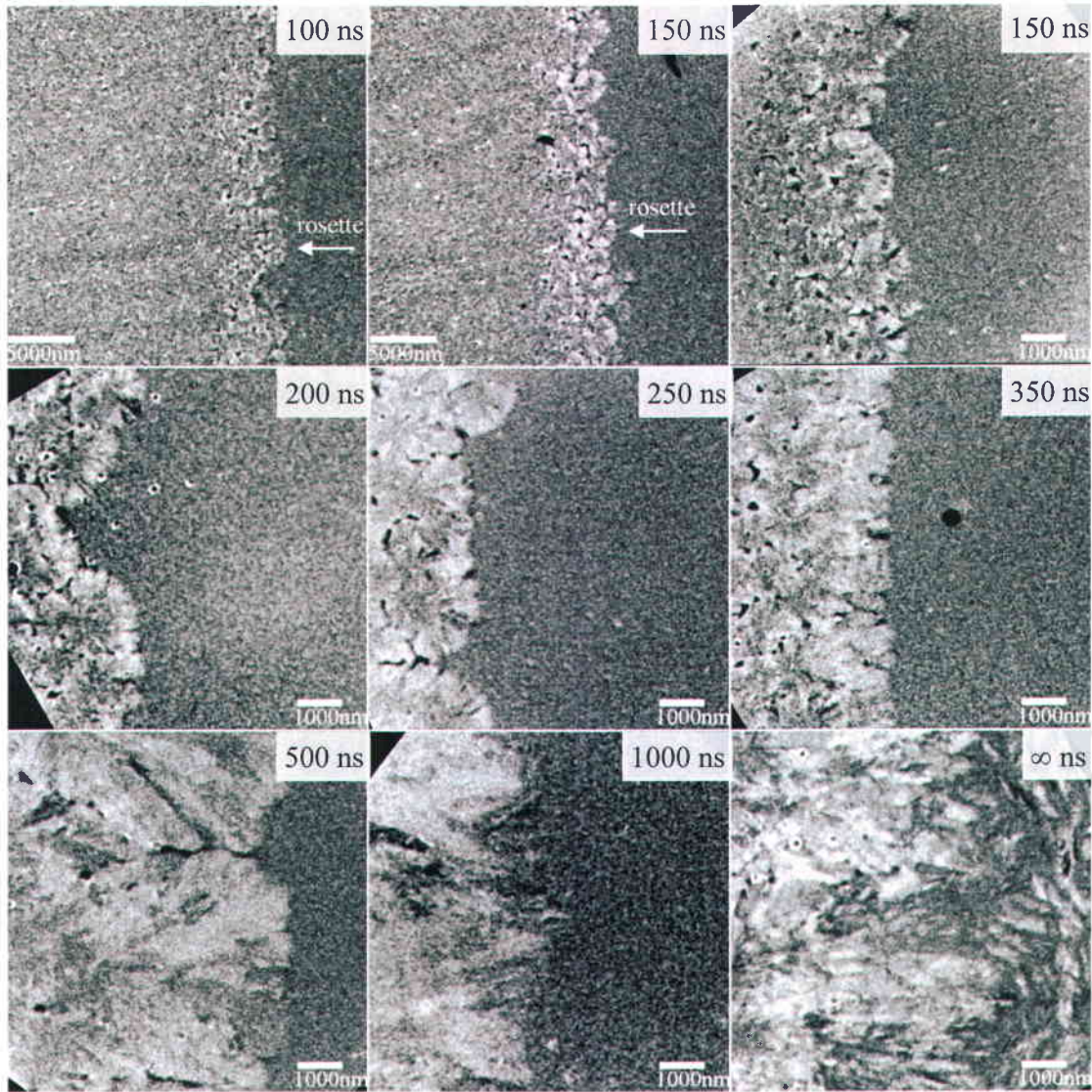


Figure 28. Time resolved images of the growth in Zone II showing the shape of the crystallization front during its propagation. The time delays are denoted in the upper right corner of each block image. The annotation “∞ ns” indicates the post mortem image i.e. at the end of the crystallization. The scale bar is given in each block image.

the roughness. For extraction of the RMS of the growth front, we used the same procedure as described in Chapter III section 3.3.1.1 (we applied an automatic linear fit to the growth front curve because, due to the high magnification of the images and the limited view of the growth front, the front appeared mostly linear. Parabolic fit was also tested and it gave

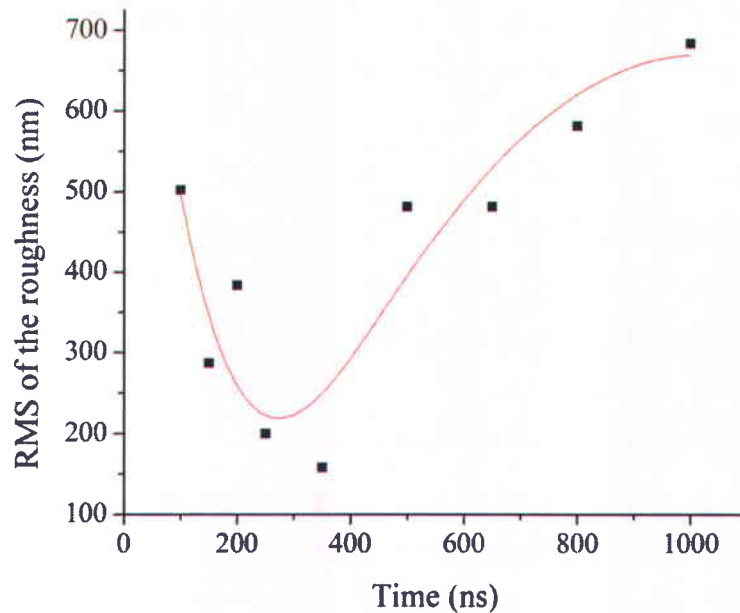


Figure 29. Evolution of the RMS of the roughness of the growth front in Zone II with time. The red curve is a guide to the eye and shows the trend in the evolution.

similar results). The results of these calculations are plotted in Figure 29. The data suggest that the roughness is moderate in the initial stages of growth of the LREC (~500 nm at 100 ns delay) probably due to the presence of nucleation centers where the crystallization explodes in all directions in a rosette shape (see Figure 28 – 100 ns & 150 ns delay images). For higher delays the RMS of the roughness decreases up to ~250 ns as indicated by the trend curve shown on the figure. This decrease may be provoked by capillary effects [6] having more influence on the interface roughness than the anisotropy in the growth due to different velocities of growth for different planes along the direction of the heat diffusion, or perhaps the shape of the LREC during growth is not independent of the formation temperature. Such decrease of the roughness could also be due to a transition region between the nanocrystalline structure in the central coarse nanocrystalline structure and the dendritic structure. For higher delays the front rapidly roughens reaching its maximum at the end of the growth process giving RMS of the roughness to be ~700 nm at 1000 ns and at the post-mortem images. Such increase of the roughness may be due to explosive regime of the crystallization. We will return to the hypotheses outlined here in the discussion section of this chapter.

4.2.2.2. Evolution of the mean length of Zone II in radial direction.

An estimation of the mean length of Zone II in radial direction is required for estimation of the mean velocity of propagation of the growth front which can give an indication of the temperature evolution in radial direction. For estimation of the mean length of Zone II we used the following procedure. We outlined two curves directly on the image (Figure 30): the first one delimited the beginning of the LREC (green curve) while the second one delimited the position of the growth front in the time resolved image (red curve). Next, we calculated the difference between the two curves for points which are parallel to the heat flow direction and that gave us the average length of these crystals. The results of these measurements are given in Figure 31 where the red curve represents the trend seen in the increase of the crystals' mean length with the confidence band at 95 % delimited by the green curves. The data suggest that the LREC's mean length increases slowly in the beginning of the growth up to ~250 ns followed by sharp increase of the lengths to up ~600 ns. At the end of the growth (above ~600 ns), the length of Zone II again shows low increase. The low growth up to ~250 ns could be due to formation of a transition region between the coarse nanocrystalline structure and the dendritic structure. The significant increase of the lengths for delays above ~250 ns could result from explosive crystallization. We will return to these hypotheses in the discussion part of this chapter.

4.2.2.3. Velocities of crystallization and error analysis

An estimation of the velocity of propagation of the growth front can give an indication of the temperature evolution in radial direction. To estimate the average velocity of propagation of the growth front we took the discrete derivative of the position of the growth front in time and the derivative of the trend curve of the evolution of Zone II mean length in radial direction (Figure 31). The results are plotted in Figure 32 where the black squares represent the discrete derivative of the position of the growth front, the red curve the derivative of the trend curve of the evolution of Zone II mean length in radial direction and the green curves are the derivatives of the lower and upper confidence bands at 95% of the trend curve. The graph indicates that the velocity of Zone II growth is not a constant but has a maximum. In the beginning of the growth in this zone, the velocity is low ~2 m/s and reaches a maximum at ~500 ns of ~16 m/s. For higher delays the mean velocity is decreasing

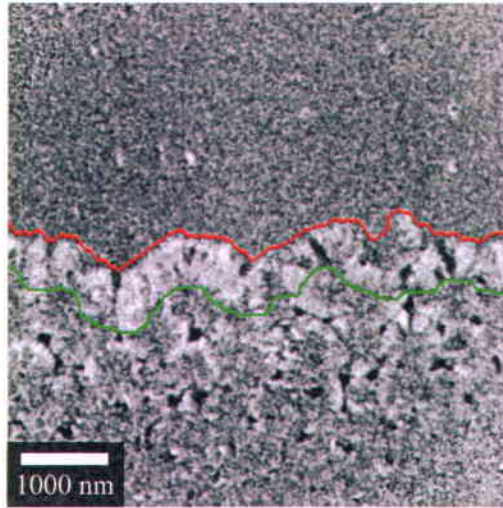


Figure 30. Example for determination of the mean length of LREC in the time-resolved images. The green curve represents the beginning of the growth while the red curve gives the position of the growth front. This figure shows an image taken at 150 ns delay.

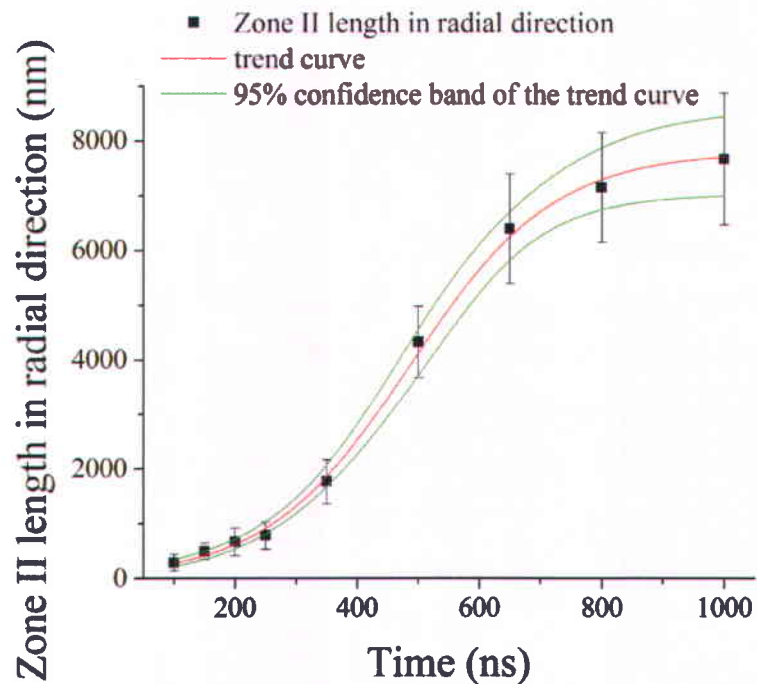


Figure 31. Evolution of the mean length of Zone II in radial direction. The error bars are coming from the uncertainty related to the measurement and the calculation of the mean length of Zone II in radial direction. The red curve represents the tendency seen in the increase of the mean length. The confidence band at 95 % is delimited by the green curves.

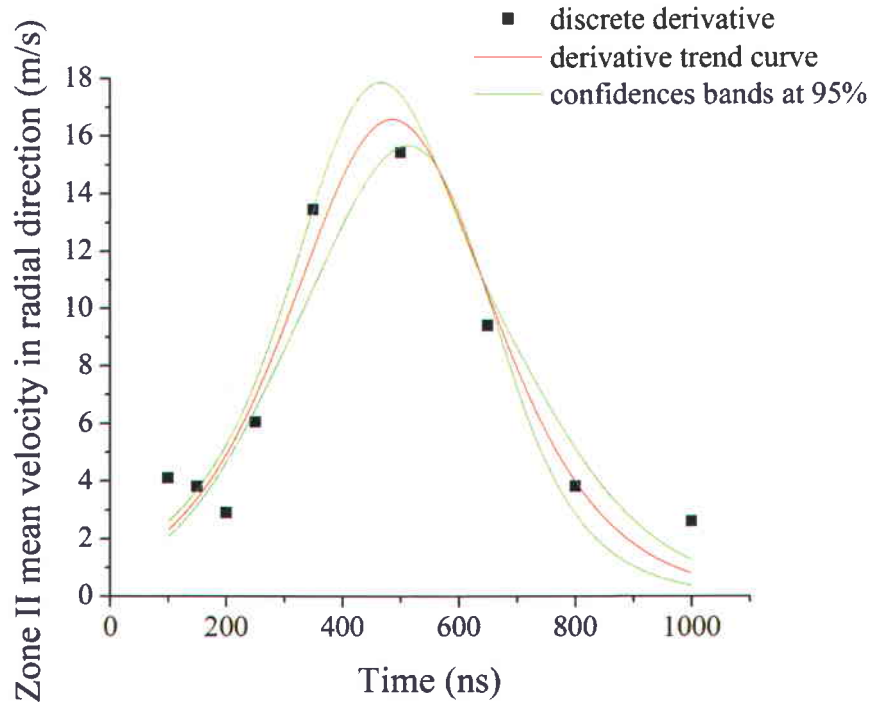


Figure 32. Evolution of the average velocity of the growth in Zone II with time. The red curve shows the derivative of the trend curve used for fitting of the data of the position of the growth front with time in radial direction (see Figure 31). The green curves represent the upper and lower confidence bands of the trend curve at 95 %.

and attains ~ 1 m/s at the end of the LRECs growth. It is notable that the velocity of crystallization obtained by the discrete derivative is decreasing up to ~ 200 ns which is not detected by the derivative of the trend curve; however, considering the dispersion of the data, this discrepancy could be stemming from the uncertainty related to the calculation of the discrete derivative or due to formation of transition region between the coarse nanocrystalline structure and the dendritic structure. We will return to these hypotheses later in the discussion section of this chapter.

4.2.3. Zone III

Once again, the layered structure is the last to form upon laser heating of the a-Ge film. High magnification images show that the layered structure is composed of alternating

bands of nanocrystalline material exhibiting some morphology, appearing in dark grey, and large tangentially oriented crystals (LTOC), appearing in light grey (Figure 33). Zone III always begins and completes with a nanocrystalline band (Figure 26 & Figure 33). As in the case of a-Ge/SiO, SAED patterns obtained on one of the nanocrystalline bands showed random orientation of the nanocrystals. A dark field image of the region shown in Figure 34A confirmed that the nanocrystalline bands possess some morphology (Figure 34B). The initial results of orientation imaging microscopy (OIM)² of the LTOC structure showed that these crystals possess a lot of twinning defects but more investigation is needed to clarify if they exhibit preferential orientation [7]. The width of the nanocrystalline bands varies between ~150 nm and ~400 nm while the LTOC bands have widths typically ranging between ~200 nm and ~1500 nm without any particular order of the widths of these bands in the radial direction. Figure 35A shows that visibly “thin”/“thick” LTOC bands may form at the beginning, the center and at the end of the layered structure. Also, “thinner” LTOC band may form between two “thicker” bands (Figure 35C). Once again, our observations are not in agreement with earlier studies where it was suggested that the “wavelength” of the large crystals and the nanocrystalline bands decreases in the radial direction [1]. The formation of this structure appears to be very irregular since the total width of the zone varies spatially within the same experiment according to the proximity to the TEM grid, and also from experiment to experiment. Figure 35 shows different widths of the layered structure for two experiments: in image A) the width of Zone III varies between ~4 μm and ~8 μm ; in image C) the width is almost uniform ~7 μm . In addition the number of layers in the layered structure may vary within one experiment: in Figure 35 A) the number of layers varies from four (on the right side of the image) to seven (on the left side of the image) while in image C) the number of layers is seven. The structure starts its growth at ~1 μs and finishes at various times up to ~10 μs . Comparison of the width of the layered structure in self-sustained a-Ge films and zone III in a-Ge/SiO shows that the layered structure may develop more in a-Ge deposited on a substrate (maximal width of Zone III in self-sustained a-Ge is ~7 μm compared to ~17 μm in a-Ge/SiO). This discrepancy may be stemming from the difference in the cooling efficiency or difference in the heat transport

² The OIM is a TEM-based technique that allows for automatic acquisition of diffraction patterns and indexing of the crystallographic orientations of the crystals in a predefined region. NanoMegas Com offers such systems (website www.nanomegas.com).

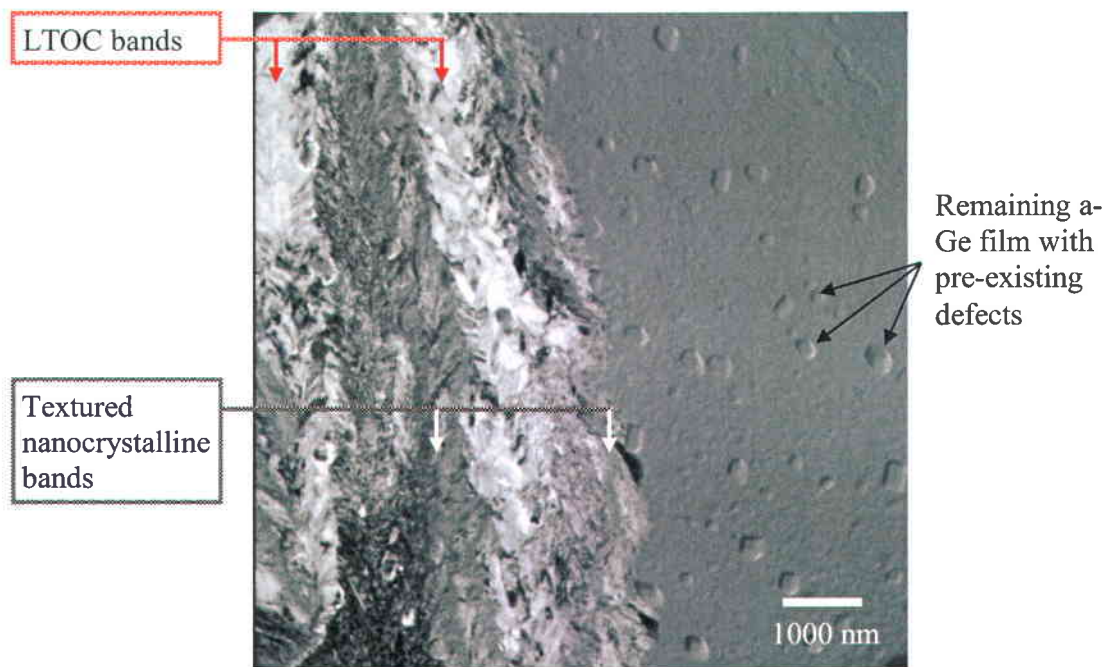


Figure 33. Conventional TEM high magnification image of the layered structure showing the textured nanocrystalline bands (pointed with white arrows) and the large tangentially oriented crystals bands (pointed with red arrows). Defects present in the film prior the laser heating are also visible (pointed with black arrows).

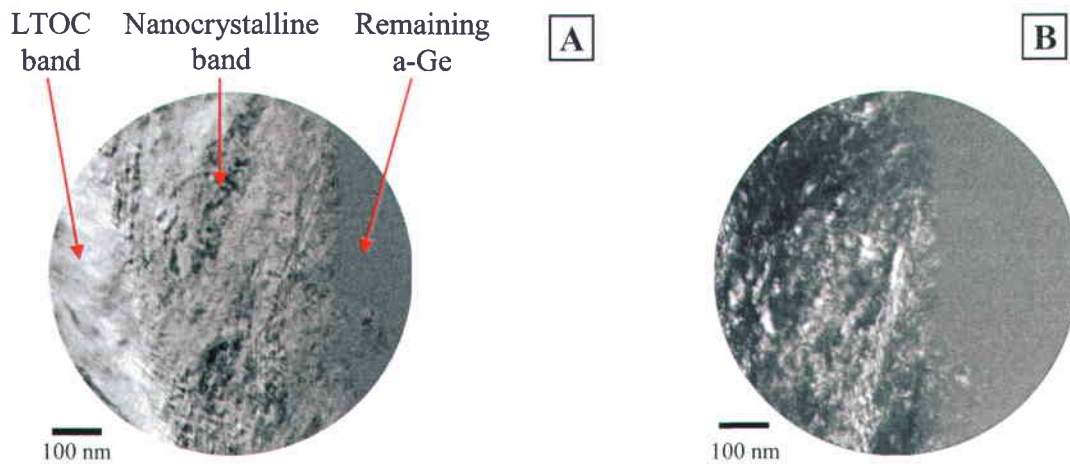


Figure 34. A) High magnification bright field image of the nanocrystalline band. B) Corresponding dark field image near the same location of the sample shown in A with slight shift to show the nanocrystalline band and the remaining amorphous material (the same magnification was kept as for image A).

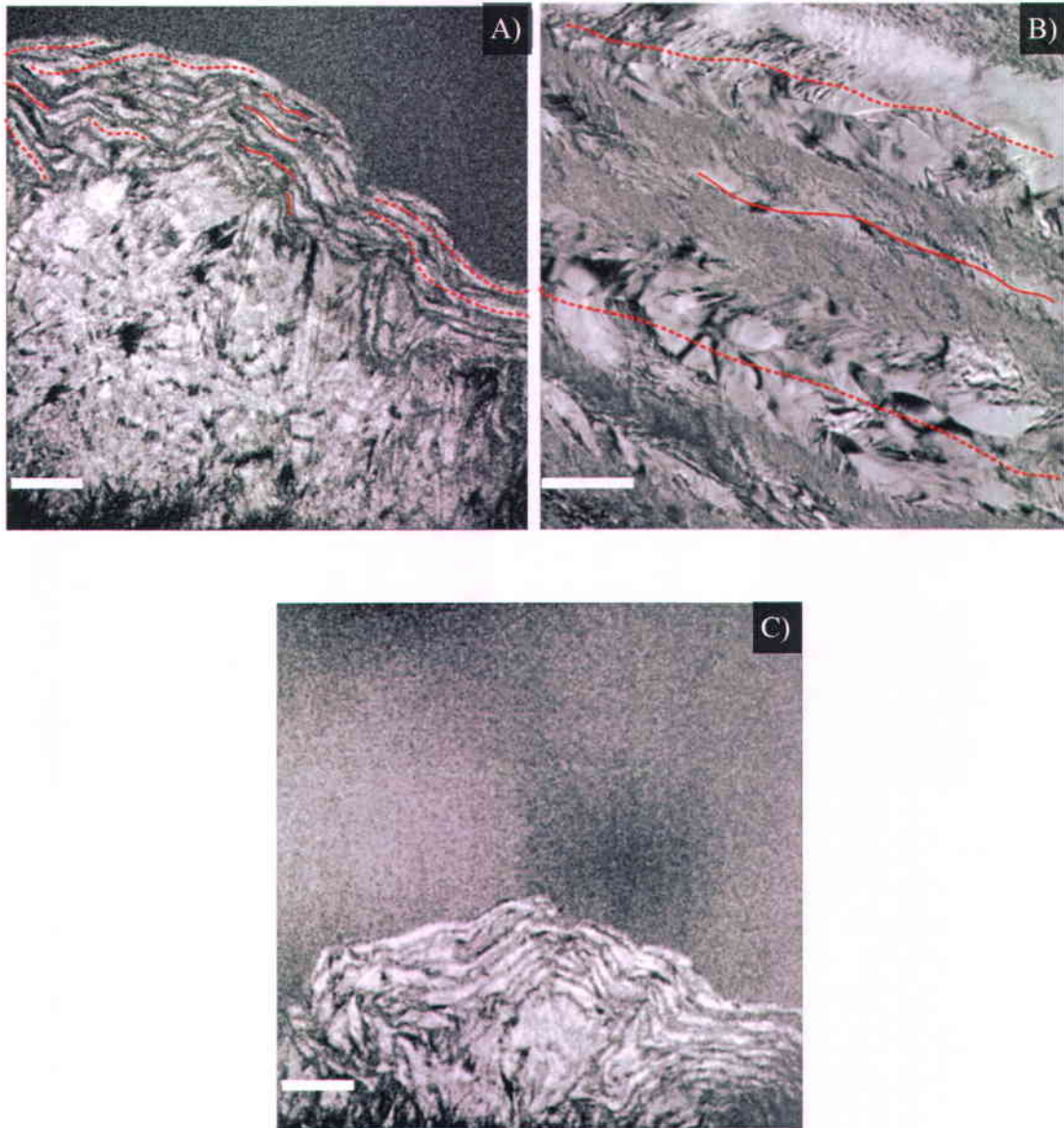


Figure 35. Post mortem images of the layered structure in Zone III. A) & B) show visibly “thin”/“thick” LTOC bands to be formed at various positions in the layered structure. Some of the “thin” LTOC bands are highlighted directly on the image with solid red lines, while some of the “thick” layers are highlighted with dashed red lines. Images A) & B) show variable width of Zone III for different experiments as well as within the same experiment (A). See text for more details. Images A) & C) were obtained post-mortem by DTEM while image B) was obtained post-mortem by conventional TEM. All the scale bars are 5 μm .

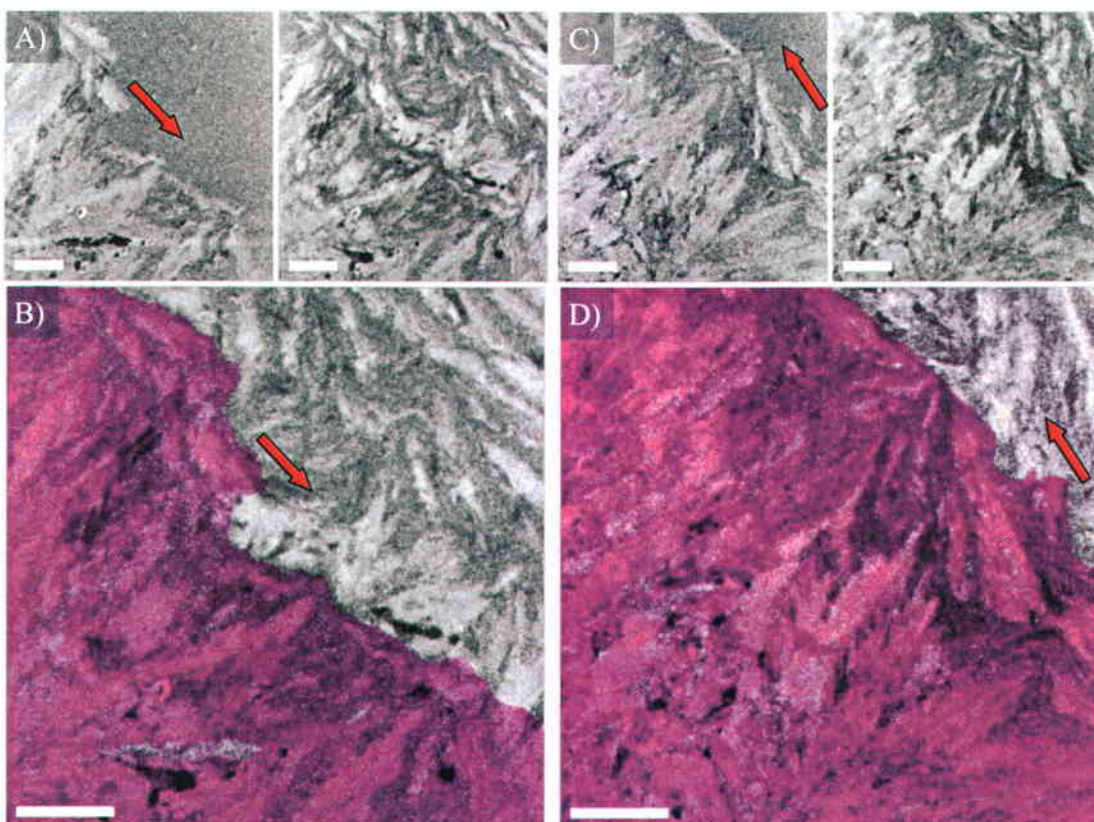


Figure 36. A) & C) Time-resolved images of the layered structure with the corresponding post mortem ones. The arrows indicate the direction of growth of the LTOC. B) & D) False color images showing an overlay of the time-resolved image appearing in magenta and the corresponding post mortem image appearing in grey. The scale bar is of 2 μm in all the images.

in the two configurations of the samples.

Time-resolved images of the growth of this structure showed that the growth front does not exhibit the large magnitude of the roughness as seen in Zone II (0 and Figure 37) and again the growth front in this zone advances mainly in the azimuthal direction with no preferential direction (i.e. clockwise or counter clockwise). 0 shows time-resolved images taken at 2000 ns and 3000 ns (images A) and C)). Comparison with the respective post mortem image (denoted with “ ∞ ns” on the figure) gives an unambiguous indication that the direction of growth in this structure is azimuthal. The false-color images (0 B) and D)) present an overlay of the time resolved image appearing in magenta on the

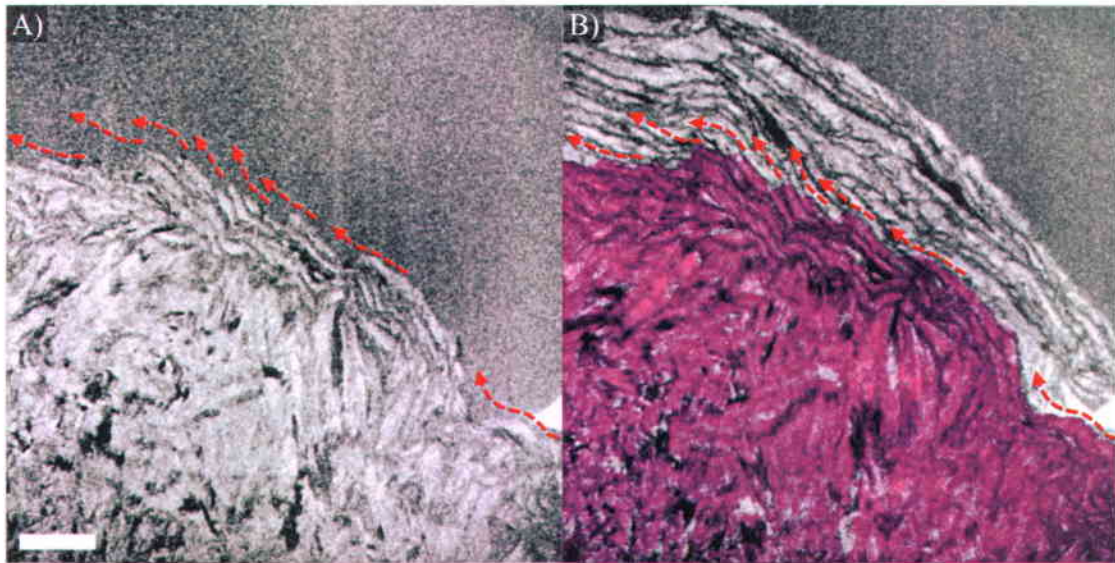


Figure 37. A) TR image at 4500 ns (left) showing the simultaneous growth of multiple layers. The dashed red arrows indicate the direction of the growth of the layers (the arrows are placed slightly above the layers for more clarity). B) An overlay of the TR image and the corresponding post mortem image. The time-resolved image appears in magenta while the post mortem image in grey. The arrows are used as guide for the eye for the direction of the growth of the layers. The scale bar is the same for the two images and is 5 μm (given in block image A).

post-mortem image appearing in grey which clearly shows the growth direction of this structure. It is also notable that simultaneous growth of multiple layers may occur. Figure 37 shows such a growth of about eight layers advancing in counter clockwise direction.

4.2.3.1. Velocities of crystallization and error analysis

The velocities of propagation of the growth front in the radial direction for this structure are accessible, whereas the growth velocity in the azimuthal direction could not be measured with the present set up of the DTEM because the instrument operates in single shot regime with the acquisition of only one image per one delay i.e. per one experiment of laser induced crystallisation. Therefore, we cannot measure the change in length of a single LTOC at different times after the initiation of its growth. A post-mortem estimation of the mean velocity of crystallization in the azimuthal direction cannot be done as was obtained for crystallization in Zone II because it is ambiguous where one tangentially oriented crystal

starts or finishes.

The velocities of crystallization in the radial direction were estimated by taking the discrete derivative of the position of the growth front in the radial direction and the trend curve in the same way as described for the growth in Zone II. The uncertainties ascribed to these calculations are very high due to the variation of the crystallization in this zone which occurs within the same experiment and between experiments (as shown in the beginning of section 4.2.3). Therefore, the velocities given here should be taken as indicative only as an order of magnitude and the range of values of the growth velocity for this structure.

The results of the calculations of the velocities in the radial direction are shown in Figure 38. They indicate that the velocity of the growth front in radial direction decreases from ~ 1.2 m/s to less than 1 m/s. These velocities are very low in comparison with the observed average velocity in Zone II (~ 8 m/s).

4.3. Discussion

Here, we will focus on the explosive crystallization in self-sustained a-Ge observed for Zones II and III. An estimate of the temperature will be provided in an attempt to reveal the relationship between the observed microstructure and the temperature within the film for a better understanding of the pathways for growth of these structures.

4.3.1. Zone I

As discussed in the previous chapter, a simple estimation of the temperature within the film after arrival of the pump laser pulse does not correspond to our observations. Therefore, again we will consider that the reflectivity of the a-Ge films changes more rapidly than the arrival of the laser pulse and the absorbed energy is lower than the energy contained in the pulse in the central part of the illumination. An estimation of the temperature in the central nanocrystalline region showed that the temperature will rise to ~ 1100 K due to the deposited energy from the laser beam [8].

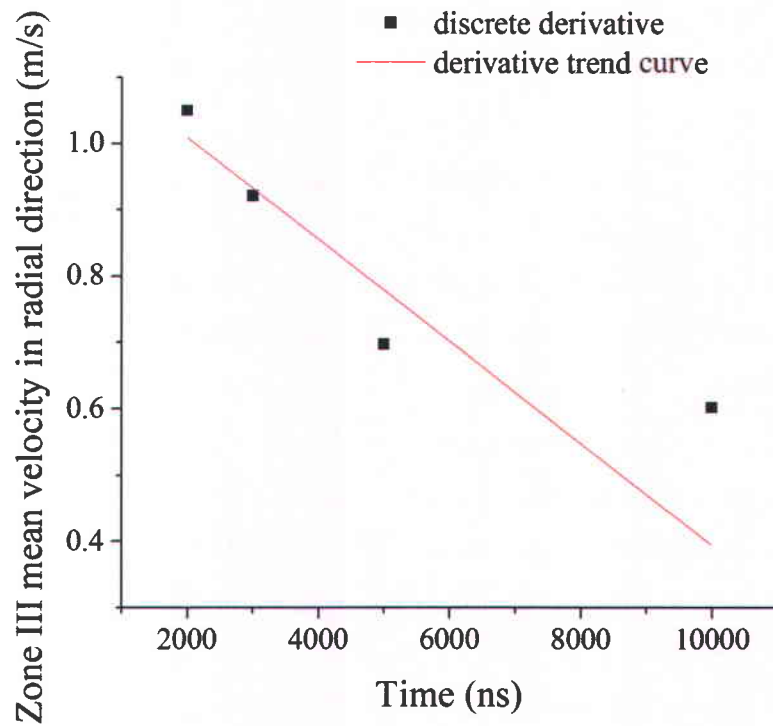


Figure 38. Evolution of the average radial velocity of growth in Zone III obtained from the discrete derivative of the growth front position. The red curve shows the derivative of the trend curve of the growth front position.

4.3.2. Zone II

As mentioned in the previous chapter, growth in this zone is described as melt-mediated crystallization where a thin metastable liquid layer is propagating in front of the growing large radially elongated crystals which is possible due to the difference in the melting temperatures between the amorphous and the crystalline phases which is ~ 245 K [9]. Therefore, two interfaces are present: crystal-liquid and amorphous-liquid some distance ahead.

A qualitative estimation of the temperature can be made by analysing the evolution of the roughness of the growth front. As described in section 4.2.2.1 the roughness of the crystallization front decreases from the beginning of the LREC growth until ~ 250 ns followed by an increase with the further advancement of the crystallization front (Figure 29). Such decrease of the roughness could be due to the formation of transition region between the coarse nanocrystalline structure in the central part of the film and the dendritic

structure. Formation of transition region has been previously observed during laser induced crystallization in heated a-Ge films [11]. The decrease of the roughness can be a consequence of the Gibbs-Thompson capillary effect where once a protrusion in the growth front is created it will not be stable and will disappear, resulting in smoothing of the crystallization front [6]. Another description of the process is given by Mullins and Sekerka, who suggested that a critical radius of the protrusion is required for its subsequent stable growth. As a result, protrusions with radii below the critical radius will disappear due to the surface tension of the metastable liquid which will keep the growth front smooth [10]. For delays above 250 ns, the roughness increases which is an indication for thermal instabilities at the growth front and the absence of planar isotherm. Such oscillations are expected for grain growth in supercooled liquid and may occur due to a Mullins-Sekerka type instability as described in Chapter III [10], [12]. This kind of instability can explain the formation of the LREC and their final shape seen in the post mortem images. The splitting of the dendrite's tip to form a few dendrites from one nucleation center (see Figure 14, Chapter III) could result from vanishing of the surface tension probably due to decrease of the width of the supercooled liquid [12] and allowing increase of the instabilities at the growth front. In this context the LREC can be described as "freely grown" dendrites, a term used by Langer for crystals growing in a supercooled liquid which results in dendritic morphology but do not necessary exhibit the same structure as dendrites grown at equilibrium conditions [12].

The degree of undercooling ($\Delta T = T_{melt\ crystalline\ material} - T_{tip\ of\ the\ growing\ crystal}$) of a supercooled liquid plays a critical role during the crystallization process [13]. Low undercooling (equivalent to high temperature at the interface of the growing crystals) results in low velocities of crystallization and high undercooling favours high growth velocities. However, the growth velocity increases with the increase of the undercooling up to a point where the undercooling becomes too high and the velocity of growth decreases again, thus, giving a Gaussian type of the dependence of the growth velocity on the temperature. A schematic representation of the dependence of the velocity of growth on temperature is given in Figure 39 where the dependence of the nucleation rate on temperature is also given. In these terms the velocity of crystallization is highly sensitive to the temperature at the interface (the tip of the dendrite) which will be influenced by the temperatures of the two heat baths between which the interface is located i.e. the temperature of the growing crystal

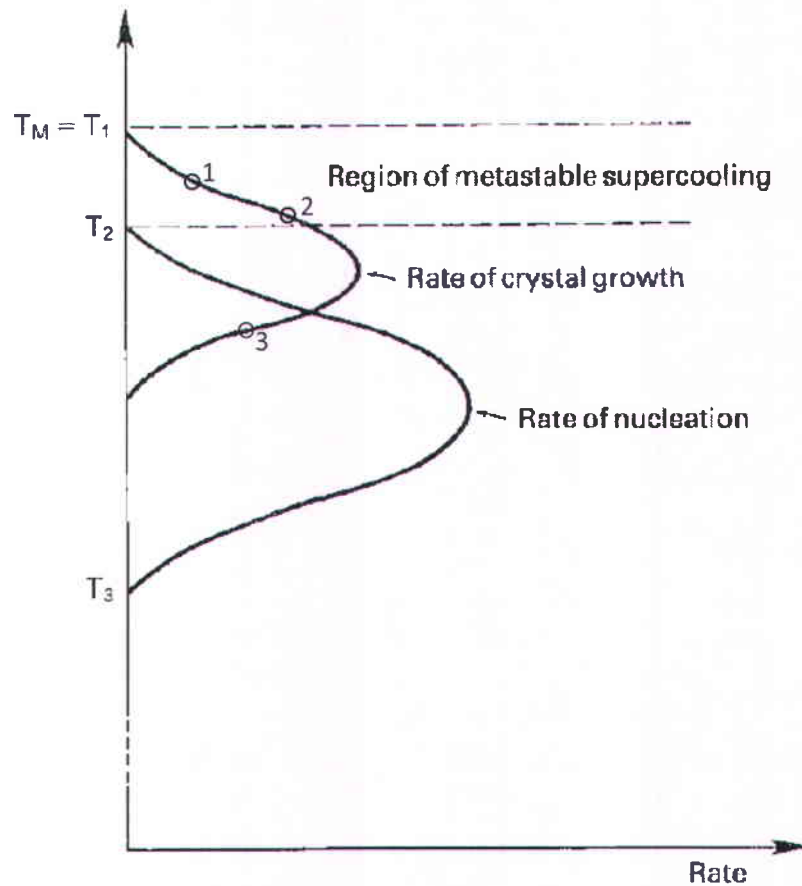


Figure 39. Dependence of the crystal growth rate and the rate of nucleation with the temperature for glasses where $T_M = T_1$ is the melting temperature of the crystalline material, T_2 is the glass transition temperature and T_3 is the temperature at which the nucleation rate is above zero. According to the definition a metastable liquid layer may exist in the interval $T_2 < T < T_1$ (the temperature interval is delimited on the figure with dashed lines). Figure taken from [16].

and the temperature of the surrounding material. Returning to the observed velocities of crystallization in Zone II (see Figure 32) one notes that in the beginning the velocity of propagation of the crystallization front is low (< 6 m/s up to ~ 250 ns). Such low velocities of crystallization could be result of the heat diffusion which does not allow high undercooling to occur and will reflect in low velocities. To evaluate the credibility of this hypothesis as first order approximation we can estimate the increase of the heat diffusion length L_D with time by using equation (5) which was introduced in Chapter III. In

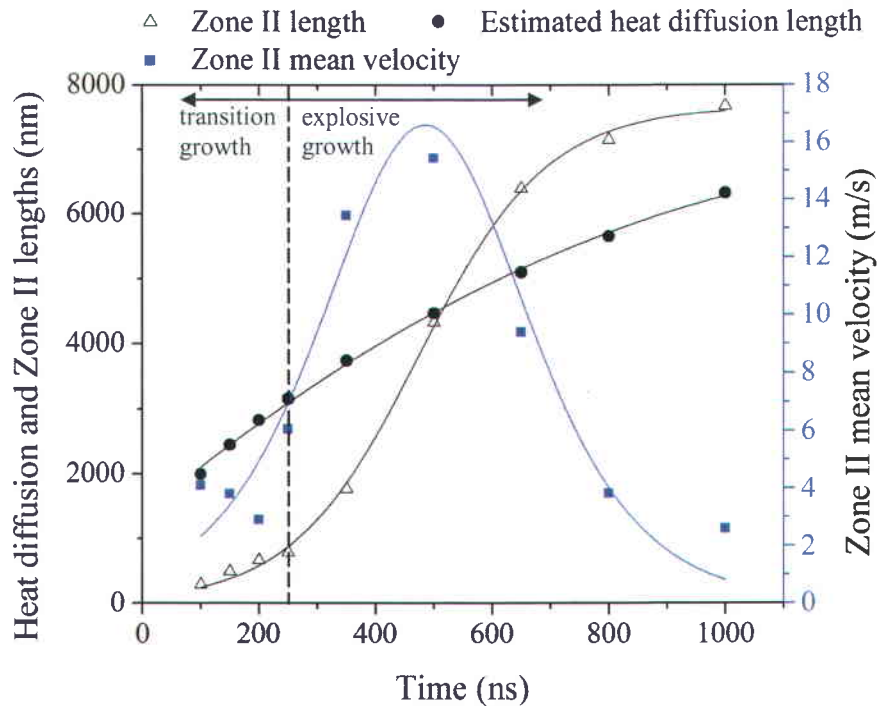


Figure 40. Compiling plot of the estimated heat diffusion lengths (filled black circles with black curve showing the trend) along with the Zone II mean length in radial direction (unfilled black triangles with black curve showing the trend) and the velocity of crystallization (filled blue square) obtained from the discrete derivative of the position of the growth front in time with blue curve showing the derivative of the trend curve of the position of the growth front in time. The transition and explosive growth regimes are denoted on the figure.

this calculation we assume that the heat deposited from the pump laser begins its diffusion starting from the limits of the laser beam. The heat diffusion length as a function of time is plotted in Figure 40 (filled black circles) where we took $D = 0.1 \text{ cm}^2/\text{s}$ [1] i.e. independent of the temperature for this simple estimation. The same figure shows also the measured mean length of Zone II in radial direction in the time resolved images (unfilled black triangle) and the observed velocities (filled blue squares) for ease in the comparison and the analysis. In the initial stages of growth, the mean length of Zone II is much shorter than the heat diffusion lengths. Thus, the interface of the crystalline-amorphous material is advancing in hot surrounding material resulting in lower undercooling. As a consequence, low velocities of growth are seen. This situation can be represented with point 1 in Figure

39. This hypothesis is confirmed by our observations. Up to ~ 250 ns the LREC lengths are significantly shorter than the heat diffusion lengths, resulting in lower growth velocities (Figure 40 – black broken line points the 250 ns delay). However, with advancement of the growth front the mean length of Zone II approaches the heat diffusion length and the velocity of crystallization increases suggesting that the LREC are experiencing higher undercooling (see Figure 40 – 250 ns delay and higher). This case can be represented with point 2 in Figure 39. Later, the LREC's mean length becomes commensurate with the heat diffusion length and the maximal velocity of growth at ~ 500 ns is reached. Following this rapid growth the growth front in Zone II surpasses the heat diffusion length and the undercooling increases, resulting in the decrease of the velocities for delays above 500 ns (Figure 40). This situation can be represented with point 3 in Figure 39. Figure 40 suggests that the transition region is formed at low undercooling of the liquid. At that point, the roughness is moderate (Figure 29) and the velocity of advancement of the growth front is low. Also, explosive crystallization characterised with significant increase of the mean length in the radial direction of Zone II and the RMS of the roughness (Figure 40 and Figure 29) is taking place some definite time after initiation of the growth in Zone II. Our result suggest that this occurs at time above ~ 250 ns. During the explosive crystallization Mullins-Sekerka type instability play critical role in the growth of the dendritic structure.

To examine whether the outlined hypotheses are supported by the theoretical simulation of the temperature, we will show the results of the simulated time-dependent temperature in the radial direction by solving the heat diffusion and generation equations in the radial direction in thin films made by M. Stern (member of our McGill collaborator group) [17]. We will also comment on the dendritic growth model widely used for description in metallic systems dendritic growth presented in “Phase transformation in metal and alloys” by Porter, Easterling and Sharif.

4.3.2.a. Dendritic growth model (DG)

Dendritic growth in metal systems is well studied and documented. As introduced in Chapter III, for these systems a relationship between the observed growth velocity, the radius of the tip of the dendrite and the temperature at the interface was developed by

solving the heat diffusion equations in the radial direction from the tip of growing dendrite [13]. The mathematical expression for this relationship is given by equation (6) Chapter III.

In our experimental setup we can observe the growth of the crystals giving dendritic morphology in the time resolved images. However, once more the evaluation of the mean radius of the tips of these crystals with the time and post mortem proved to be challenging. One of the possible reasons is that these crystals complete their growth in wedge shape clearly seen in the post-mortem images (Figure 26) i.e. it is not straightforward to assign a radius of the dendrites' tips that will result in accurate evaluation of the temperature. We tried to extract an automatic value³ for the dendrites' mean tip radius by applying fast Fourier transformation (FFT) to the growth front curve, which had to give the mean distance of separation between the dendrites which might be used as estimation for the radii. However, the procedure did not yield a value for the main distance of separation between the crystals probably due to the high magnification of the images and the limited field of view of the whole growth front. For these reasons, we could not apply this model to evaluate the temperature during the growth in Zone II.

4.3.2.b. Model of heat diffusion and generation in thin films (HD>F)

In Chapter III we introduced the 2D model of the heat diffusion and generation in thin films developed by M. Stern in his MSc Thesis [17]. The calculation of the time dependent two dimensional temperature profile of the thin film was done by numerical solution of the heat equation using a finite element method. The model introduces a heat source which account for the amounts of heat released and absorbed at the growth front.

The results of the calculations using the HD>F model for estimation of the growth temperature of the dendrites are shown in Figure 41. The temperature in the beginning of the LREC growth is high ~ 1180 K and decreases with time to below ~ 1000 K at the end of the growth [18]. Since at the beginning of the growth in Zone II the velocity is low and increases afterwards, the estimation of the temperature obtained by solving of the HD>F model gives a realistic description of its evolution i.e. high temperature in the beginning of

³ We were interested to obtain an automatic value for the mean radius of the dendrites' tips with objective to avoid subjective evaluation of the values which is usually introduced if the analysis is made manually.

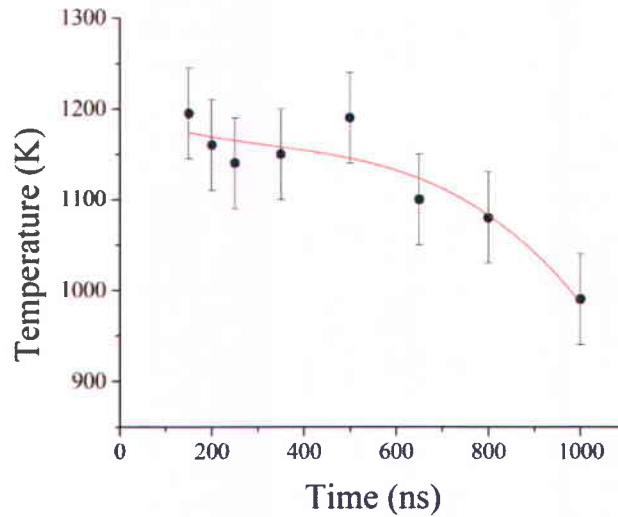


Figure 41. Evolution of the temperature in Zone II at the vicinity of the growth front according to the solution of the heat diffusion and generation equation in two dimensions (HD>F). The red curve represents the tendency in the evolution. The error bars are coming from the uncertainty related to the estimation of the position of the growth front and the calculation of the heat diffusion lengths.

the dendritic growth which is equivalent to low undercooling and lower temperature toward the end of the growth in Zone II which is equivalent to higher undercooling.

As showed earlier, the velocity of growth in glassy materials exhibits Gaussian type relationship on the temperature of the glass (Figure 39). Since a-Ge is obtained at very high cooling rate compared to the rates usually used for production of most of the glassy materials, its behaviour upon crystallization is slightly different from the crystallization behaviour of glasses heated above the glass transition temperature [11]. As a result, the crystallization is irreversible when heated at temperature above the temperature of melt of the amorphous material but below the temperature of melt of the crystalline material and it is impossible to obtain a-Ge by rapid quenching from the melt [19]. The melting temperature of amorphous germanium is $T_{ma} = 0.8 T_{mc} = 969$ K [20] which is higher than the temperature of glass transition in most glassy materials, which is found to be in the range $1/3 T_{mc}$ to $2/3 T_{mc}$ depending on the cooling rate used for fabrication of the glass [21]. Therefore, description of the crystallization process in a-Ge by the models developed for glassy materials does not warrant an adequate portrayal of the process. For these reasons, we looked at the evolution

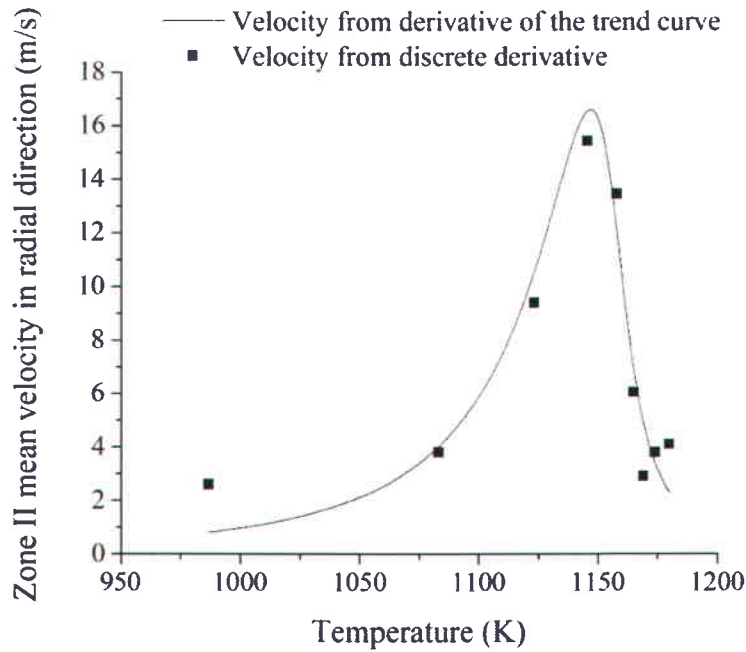


Figure 42. Evolution of the mean velocity of propagation of the growth front in radial direction in Zone II with increase of the temperature of the film at the vicinity of the growth front. The black filled squares represent the velocity obtained from the discrete derivative while the black curve is the velocity obtained by the differentiation of the trend curve in the evolution of the growth front in radial direction.

of crystallization velocity with temperature, obtained from the model, to estimate if the crystallization velocity in a-Ge exhibits a Gaussian-type relationship similar to glasses or whether it differs from this model. The results are presented in Figure 42. As the plot suggests, the maximal velocity of crystallization occurs at ~1150 K. Also, the dependence of the velocity of crystallization in a-Ge on the temperature does not exhibit a typical Gaussian-like type relationship because the curve is not symmetric. The observed dependence shows that after the maximal velocity is reached, the decrease of the velocity is more rapid with the increase of the temperature (because the curve is more steep) in comparison with the decrease of the velocity with decrease of the temperature (i.e. for $v < v_{max}$). This discrepancy may stem from the fact that, in contrast to glasses, the entire process in a-Ge crystallization develops above the temperature for melt of the amorphous material (969 K).

4.3.3. Zone III

The final microstructure in Zone III suggests an oscillating temperature gradient in the radial direction during growth. For this reason, Sharma and co-workers [1] suggested that very large liquefied regions exist which allow the growth of this structure. However, our observations do not support this theory because the time-resolved images show an azimuthal direction for the growth of the LTOC bands. The observed growth mode is similar to the 'zigzag' growth proposed by Chojnacka [11]. The direction of growth of the nanocrystalline bands remains an open question because with the current spatial resolution of the DTEM we cannot observe their growth. Closer inspection of the final layers of Zone III (Figure 43) reveals that the nanocrystalline bands may be forming due to explosive crystallization similar to that in Zone II. In Figure 43 three layers could be easily distinguished. The layers at the extremities clearly show that they complete with formation of a nanocrystalline structure surrounding the LTOC bands. The layer in the middle is mostly nanocrystalline. Its position suggests that it grew after the layer on the left side and before the layer on right. The texture of the nanocrystalline bands shows that the needle-like crystals are at $\sim 24\text{-}30^\circ$ to the direction of the LTOC bands which may serve as indication for the direction of the evacuation of the heat. Relation of the observed microstructure to the temperature evolution in this zone is not trivial since as outlined the oscillations in the structure are not understood yet. Moreover, we can evaluate only the velocity of crystallization in the radial direction while the actual growth as shown occurs in the azimuthal direction. Temperature decreases below 1000 K at the end of the growth in Zone II (see Figure 41), probably favouring higher nucleation rate than growth rate to allow the formation of the first nanocrystalline band.

If a comparison is made between the position of the growth front of Zone II in radial direction and the heat diffusion lengths, we find that at the initiation of Zone III growth, the heat diffusion length and the length of the crystallised material in radial direction (i.e. the width of the layered structure plus the Zone II mean length) are commensurable (Figure 44). However, the heat diffusion rapidly surpasses the length of the crystalline material in the radial direction with the radial advancement of the growth front. This may allow a small liquefied pocket to be formed (parallel to the net heat flow direction) and the crystallization to occur in similar fashion as the growth in Zone II. Unfortunately, with the present setup of the DTEM operation no further comment could be made on the crystallization in this zone.

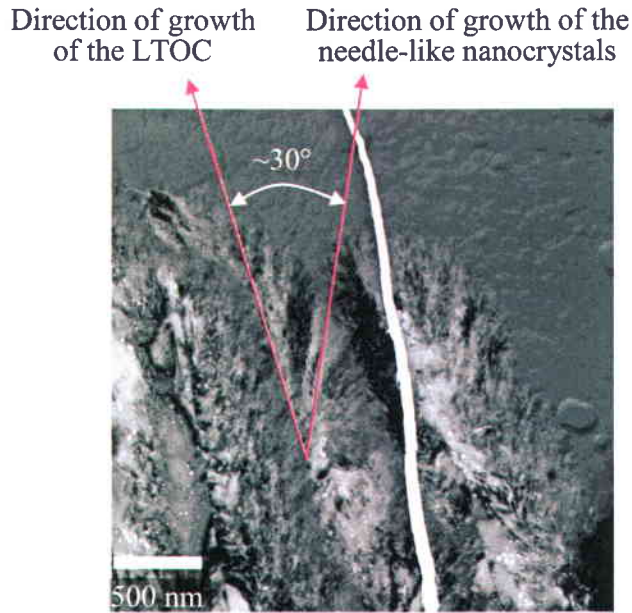


Figure 43. Post mortem image of the end of Zone III (image on left). Three layers are visible in the image. The orientation of the texture of the nanocrystalline bands suggests that their formation may occur due to explosive crystallization similar to that seen in Zone II. The wide white stripe seen in the image is a crack in the film.

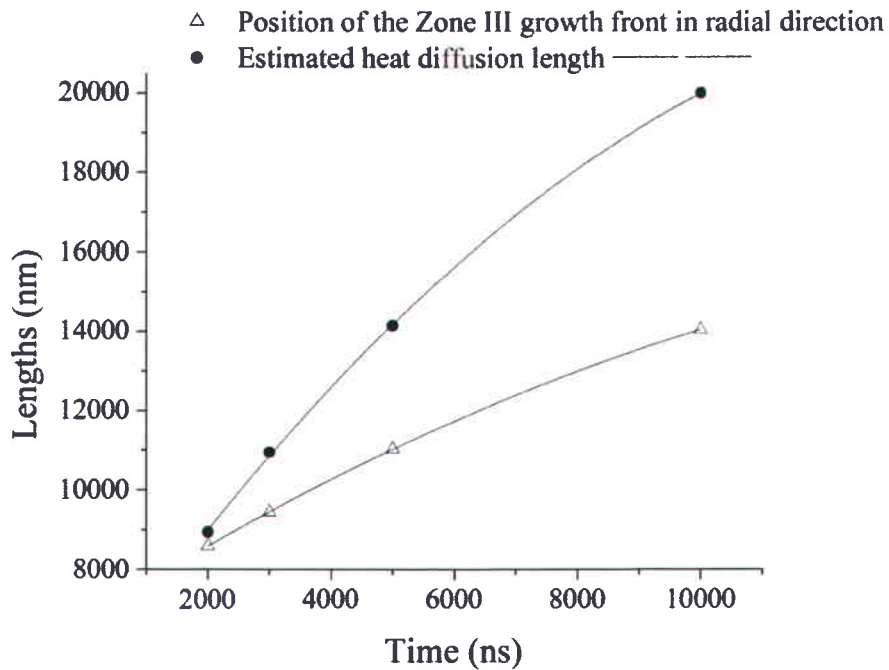


Figure 44. Comparison between the position of the growth front of Zone III in radial direction and the heat diffusion lengths for the time delays of formation of Zone III.

4.4. Conclusion

We observed the crystallization process in a-Ge in situ by DTEM and fulfilled our objectives of revealing the sequence in the change of morphology of the crystallising material, determination of the velocities of crystallization and estimation of the temperature of the film during the growth of the different microstructures.

We found that the crystallization in Zone I occurs at temperatures above the temperature of melt of the amorphous material but below the temperature of melt of the crystalline one and via random nucleation from the bulk. The growth in Zone II is a melt-mediated process resulting in “freely grown” dendrites in a supercooled liquid. Our data suggest that a transition region characterised by decrease of the roughness of the growth front and the velocity of crystallization is formed prior the explosive growth. Mullins-Sekerka type thermal instability plays critical role in the formation of the dendritic structure. However, this instability probably takes place some definite time after the initiation of the growth in Zone II. The velocity of growth of the LREC exhibits dependence from the temperature similar to that seen in glassy materials; yet, the entire process is taking place above the temperature for melt of the amorphous material. Zone III forms via growth in the azimuthal direction. Simulation of the temperature evolution in the film in the radial direction for the Zones I & II showed that the crystallization occurs at temperatures below the temperature for melt of the crystalline material and we did not find evidence that the initiation of Zone III takes place at $T > 1210$ K. The agreement in the heat diffusion length and the space position of the growth front in Zone III suggests that the crystallization in this zone proceeds via melt-mediated mechanism occurring at very narrow band parallel to the heat flow direction.

4.5. Concluding remarks on crystallization process observed in germanium

Here after, we will discuss the crystallization behaviour observed in amorphous germanium. For that, we summarized in Table I the quantitative findings obtained for the two sample configurations used in this work i.e. free standing and membrane supported a-Ge films.

Table I. Comparative table on the crystallization behaviour for extracted and calculated data in free standing 110 nm a-Ge films and membrane supported 110 nm a-Ge / 40 nm SiO for the respective pump laser fluences.

	Material	a-Ge	a-Ge/SiO	
	Fluence (mJ/cm ²)	110	110	128
Zone I	Time for complete crystallization τ (ns)	-	-	~55
	Activation energy (eV)	-	-	1.4 - 1.9
	Maximal nucleation rate N (nuclei/cm ³ ·s)	-	-	1.6×10^{22}
Zone II	Observed time of initiation (ns)	~100	~275	
	Observed time of completion (ns)	~1000	~1300	-
	Mean length of LREC (μm)	7 ± 2	8 ± 2	
	Average growth velocity (m/s)	8 ± 2	8 ± 2	-
Zone III	Minimal width of the zone (μm)	5	5	-
	Maximal width of the zone (μm)	7	17	-
	Average growth velocity in radial direction (m/s)	~1	~1	-
	Simultaneous growth of multiple layers	Yes	Yes	

Zone I

Crystallization in Zone I occurs within the bounds of the incident laser beam. According to the estimation of the temperature within the film, the process is initiated and proceeds at temperature above T_{ma} but below T_{mc} which creates the appropriate conditions for formation of a metastable liquid. The process could be described as random nucleation from the bulk at $T_{ma} < T < T_{mc}$. We were able to make estimation of the nucleation rate through our *in situ* observations and the time for complete crystallization in the film. However, more work by theoretical modeling of the nucleation process is needed to relate the findings obtained

from the time-resolved images and the data from the post mortem images.

Zone II

The time-resolved data strongly suggest that the process is melt mediated for the self-sustained a-Ge films as well as for the membrane supported films. In both cases the initiation of the LREC growth does not start immediately after arrival of the pump laser pulse but the system needs some time for either a threshold in the temperature to be reached or until the liquefied layer's dimensions increases so as to allow its propagation in front of the growing dendrites to allow crystallization at the observed high velocities and the roughness of the growth front. Although the growth in this zone is initiated at different time for the self-supported and membrane supported films (~100 ns and ~275 ns respectively), the crystallization process proceeds at similar mean velocity of growth which is an indication that the growth occurs under similar conditions. Simulation of the evolution of the temperature in radial direction showed that the temperature in the film decreases with increasing distance. Due to thermal instabilities at the growth front (Mullins-Sekerka instabilities), the crystals complete their formation in wedge shape. Capillary effects are apparently insufficient to maintain a smooth growth front [22] as suggested in earlier studies [6]. This finding is valid for the both sample types.

Zone III

Zone III exhibited very complex growth behaviour for the two types of samples. Notably the maximal width of the layered structure in the supported films is ~2.5 times larger than that obtained in self-sustained a-Ge films. The average growth velocity in radial direction is similar for the two types of samples at ~1 m/s. The match between the heat diffusion length and the time for initiation of the growth in Zone III suggests that the crystallization process in this zone is melt-mediated (through the creation of a very narrow liquid band parallel to the net heat flow and propagating in front of the growing LTOC). For the both sample configurations, simultaneous growth of multiple layers was observed.

4.6. Bibliography

- [1] R. K. Sharma, S. K. Bansal, R. Nath, R. M. Mehra, K. Bahadur, R. P. Mall, K. L. Chaudhary, and C. L. Garg, "Electron beam induced explosive crystallization of unsupported amorphous germanium thin films," *J. Appl. Phys.*, vol. **55**, p. 387–394 (1984).
- [2] O. Bostanjoglo and E. Endruschat, "Kinetics of laser-induced crystallization of amorphous germanium films," *Phys. Stat. Sol. (A)*, vol. **91**, p. 17–28 (1985).
- [3] C. A. Schneider, W. S. Rasband, & K. W. Eliceiri, "NIH Image to ImageJ: 25 years of image analysis," *Nature Methods*, vol. **9**, p. 671–675 (2012).
- [4] Image J website: rsb.info.nih.gov/ij/
- [5] L. Csepregi, R.P. Küllen, J.W. Mayer, T.W. Sigmon, "Regrowth kinetics of amorphous Ge layers created by ^{74}Ge and ^{28}Si implantation of Ge crystals," *Solid State Commun.*, vol. **21**, p. 1019–21 (1977).
- [6] O. Bostanjoglo, R. P. Tornow and W. Tornow, "Nanosecond-exposure electron microscopy of laser-induced phase transformations," *Ultramicroscopy*, vol. **21**, p. 367–372 (1987).
- [7] Initial results from orientation imaging microscopy (OIM) obtained at LLNL by T. LaGrange.
- [8] Estimation of the temperature was made by M. Stern.
- [9] E. P. Donovan, F. Spaepen, D. Turnbull, J. M. Poate, and D. C. Jacobson, "Calorimetric studies of crystallization and relaxation of amorphous Si and Ge prepared by ion implantation," *J. Appl. Phys.*, vol. **57**, p. 1795–1804 (1985).
- [10] W. W. Mullins, and B. F. Sekerka, "Morphological Stability of a Particle Growing by Diffusion or Heat Flow," *J. Appl. Phys.*, vol. 34, p. 323–329 (1963).
- [11] A. P. Chojnacka, Ph.D. Thesis: Explosive crystallization of germanium films: Kinetics and Morphologies, Cornell University (2002).
- [12] J. S. Langer, "Instabilities and pattern forestation in crystal growth," *Rev. Mod. Phys.*, vol. **52**, p. 1–30 (1980).
- [13] D. A. Porter, K. E. Easterling and M. Y. Sherif, Phase transformation in metal and alloys, 3rd ed., CRC Press – Taylor and Francis Group LLC (2009).

- [14] N. E. Cusack, The physics of structurally disordered matter: An Introduction, Adam Hilger, IOP Publishing (1987).
- [15] G. Devaud and D. Turnbull, “Undercooling of Liquid Germanium”, MRS Symp. Proc., vol. **57**, p. 89–97 (1987).
- [16] N. H. March, R. A. Street and M. Tosi, Amorphous Solids and the Liquid State, Plenum Press – New York (USA) (1985).
- [17] M. Stern, M.Sc. Thesis: Time resolved transmission electron microscopy: the structural dynamics of explosive crystallization in amorphous germanium, McGill University, Montréal, Québec, Canada (2012).
- [18] Estimation of the temperature was made by Mark Stern with the same model developed in his M.Sc. Thesis.
- [19] D. Adler, Amorphous semiconductors, CRC Press, The Chemical rubber Co. Cleveland, OH, USA (1971).
- [20] H. S. Chen and D. Turnbull, “Specific heat and heat of crystallization of amorphous germanium,” J. Appl. Phys., vol. **40**, p. 4214–4215 (1969).
- [21] P. M. Ossi, Disordered Materials: An Introduction, 2nd ed., Springer-Verlag Berlin Heidelberg, (2006).
- [22] L. Nikolova, T. Lagrange, M. J. Stern, J. M. MacLeod, B. W. Reed, H. Ibrahim, G. H. Campbell, F. Rosei, B. J. Siwick, “Complex crystallization dynamics in amorphous germanium followed with dynamic transmission electron microscopy,” Phys. Rev. B, vol. **87**, p. 064105-1–6 (2013).

Chapter V

Crystallization in amorphous silicon films deposited onto silicon dioxide windows

An in depth understanding of the crystallization of amorphous silicon (a-Si) is of considerable technological interest because polycrystalline silicon (poly-Si) finds ample application in thin film transistors and solar cells [1]. At present, poly-Si with grains of micrometric size is used in the thin film transistor industry because the mobility of the carriers in poly-Si is higher than in a-Si [6]. Thin poly-Si films are usually obtained through excimer laser crystallization of a-Si [1]. Insights on the role of the silicon grain size and defect concentration in the growth of poly-Si will lead to an improved control over the properties of this material [7].

In this chapter we present results pertaining to laser-induced crystallization in a-Si films deposited onto silicon dioxide (SiO_2) windows. The objectives of this study were to show the evolution of the microstructures in a-Si upon crystallization under different laser fluences and to investigate the times for crystallization. For that, we acquired time resolved images of the process with high temporal resolution in the DTEM using bright field imaging mode. At the end of this chapter, an estimation of the temperature will be given and we will discuss the possible growth modes.

We used 130 nm thick a-Si films deposited onto 50 nm silicon dioxide (SiO_2) windows. The thickness of the a-Si film was chosen for better absorption of the green light in the film [9]. For brevity and clarity of the text, the abbreviation “a-Si/ SiO_2 ” will be used for this sample configuration. Details on the procedure for film fabrication are given in Chapter II. We kept the same parameters for the pump laser as for the previous studies i.e. 532 nm with pulse duration of 15 ns. We used a laser beam spot with a diameter of 100 μm incident at 45° to the sample, thus, giving an elliptical shape of the crystallised area. The fluences were varied between 110 mJ/cm^2 and 180 mJ/cm^2 (the fluences were calculated in the same way as described in Chapter III). The time delays ranged between 20 ns and 300 ns.

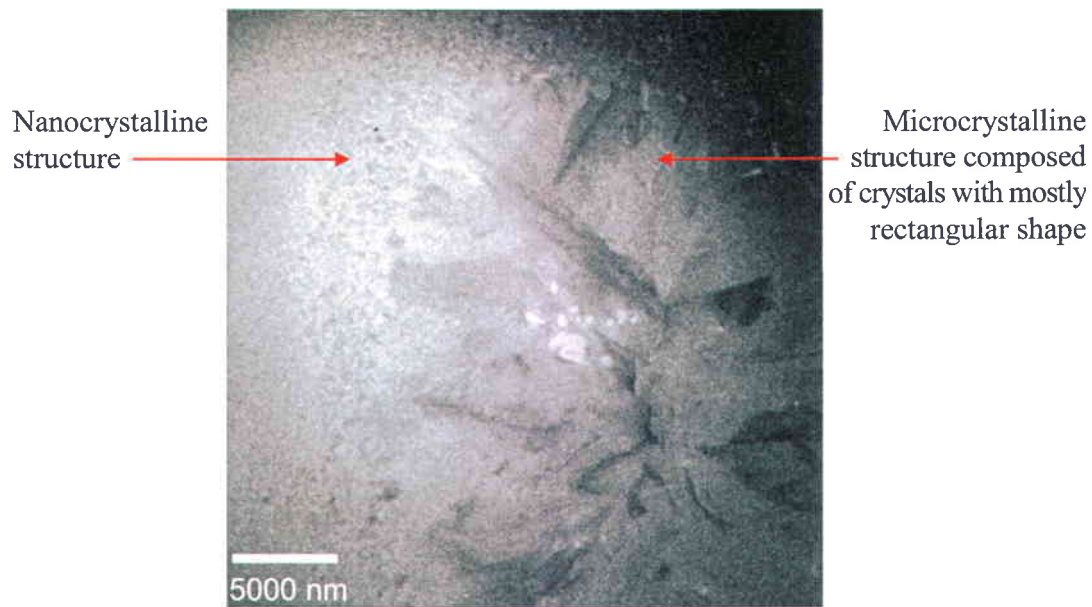


Figure 45. Typical morphology formed in single shot laser induced crystallization in 130 nm a-Si on 50 nm SiO₂. The regions of the micro- and nanocrystalline structures are indicated on the micrograph.

These fluences and time delays were chosen according to the findings in earlier studies made on a-Si crystallization by excimer laser annealing [10]. Time zero, i.e. $t = 0$ ns, for the probe pulse was defined as the moment at which the pump laser pulse initiating the crystallisation was released.

5.1 Microstructures formed

In contrast to the laser induced crystallization behaviour seen in a-Ge, nanosecond laser heating in a-Si for the range of fluences mentioned above leads to the formation of only two different morphologies: (i) a central microcrystalline structure with length of the crystals up to $\sim 12 \mu\text{m}$ and (ii) an annular nanocrystalline structure surrounding the micro-sized crystals with grain sizes up to ~ 200 nm. A typical image of these structures is shown in Figure 45. Post mortem examination revealed that the large crystals with micrometric size have large number of defects in their structure. Figure 46A shows a bright field image of these crystals where a lot of defects can be seen in their structure. Image B of the same figure

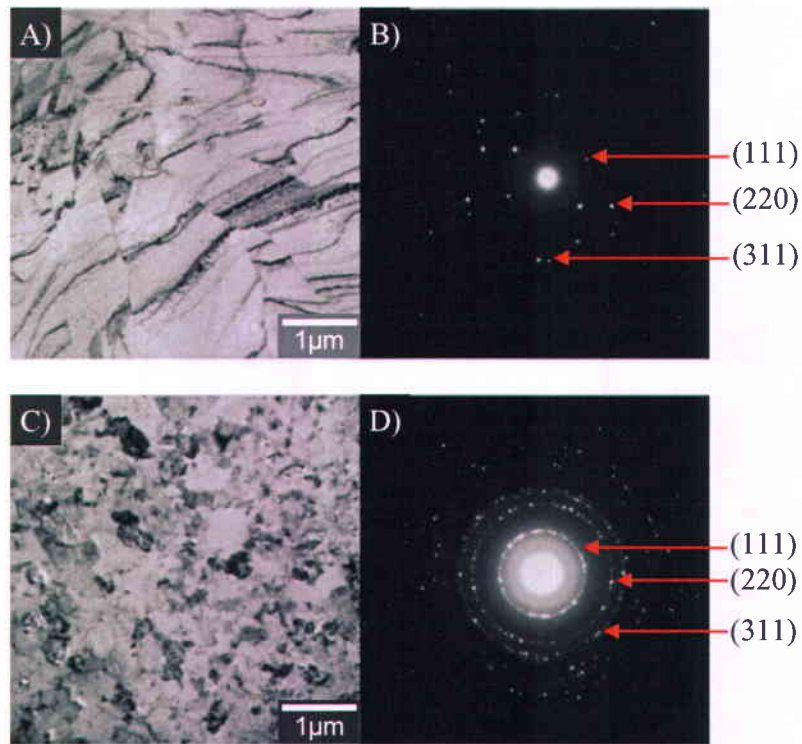


Figure 46. Post mortem high magnification images of a-Si/SiO₂ of the microcrystalline (A) and the nanocrystalline regions (C) with the respective diffraction patterns (B & D) (only the first three diffractions are annotated on the figure).

shows the corresponding diffraction pattern. Unfortunately, due to the fragility of the samples¹, additional studies on the crystallographic orientations present in these crystals could not be conducted. Examination of the nanocrystalline structure showed that the crystallites have random orientation (Figure 46 image C – bright field micrograph of the nanocrystals, image D – the corresponding diffraction pattern).

5.2 Effect of the pump laser fluence on the post mortem structure

We were interested in observing the influence of the pump laser fluence on the final morphology of the sample. To do so, we gradually increased the laser fluence and acquired

¹ The samples were severely damaged while in transit from LLNL to the TEM at McGill University where the post mortem imaging was carried out. Only a part from one window remained intact which allowed the acquisition of the images presented in Figure 46. For these reasons, further investigation was not possible.

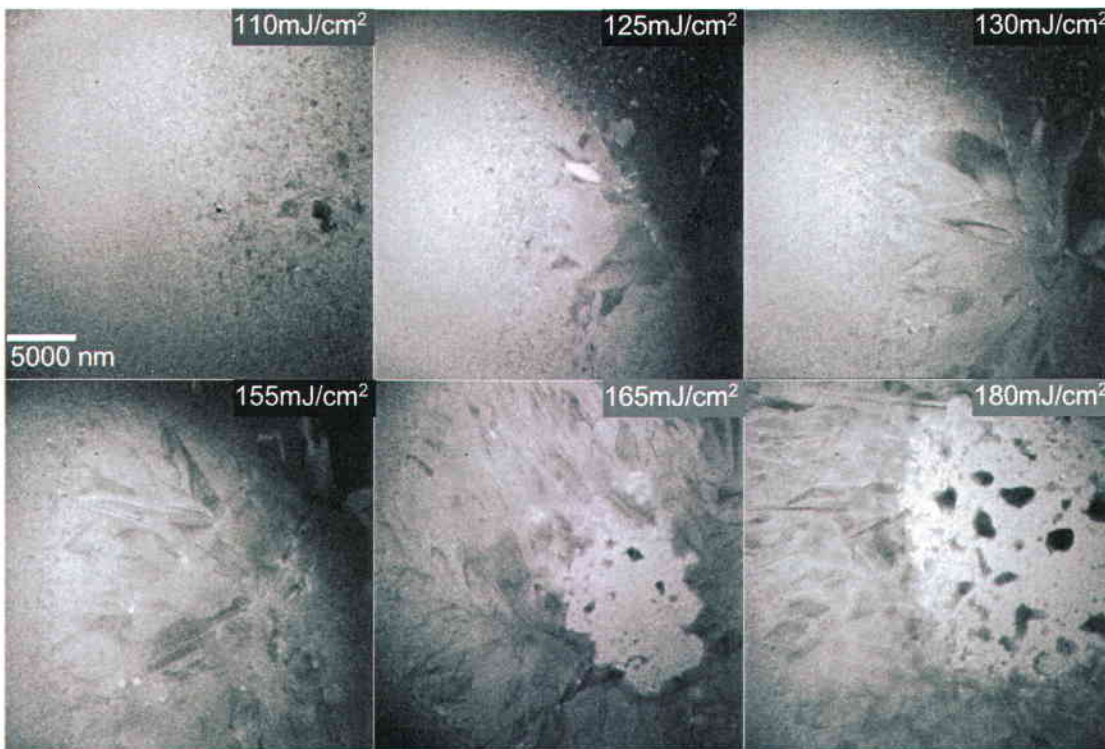


Figure 47. Full view of the microstructures formed for different fluences after single shot laser induced crystallization in a-Si/SiO₂. For fluences of 165 mJ/cm² and higher, the central region of with lighter contrast is formed probably due to melting of the a-Si film. The large dark features seen in these micrographs are silicon droplets that crystallised upon cooling of the specimen. The scale bar is the same for all the images and it is given in the first block image. The fluences are indicated in each block image in the right upper corner.

images of the sample after completion of the crystallization process. Figure 47 presents the observed post mortem structure for fluences increasing from 110 mJ/cm² to 180 mJ/cm². As the figure shows, the nanocrystals forming at the periphery of the crystallised region are always present regardless of the pump laser fluence, and the large microcrystals visibly increase in size with increasing pump laser fluence up to ~155 mJ/cm². Such a change in the morphology with increase of the laser fluence could be a result from solidification starting at the periphery of the heated region and growth of the microsized crystals in the inward direction i.e. parallel to the direction of solidification. This morphology is similar to that observed by Moon and co-workers [11] where directional solidification resulted from interfacial (liquid-

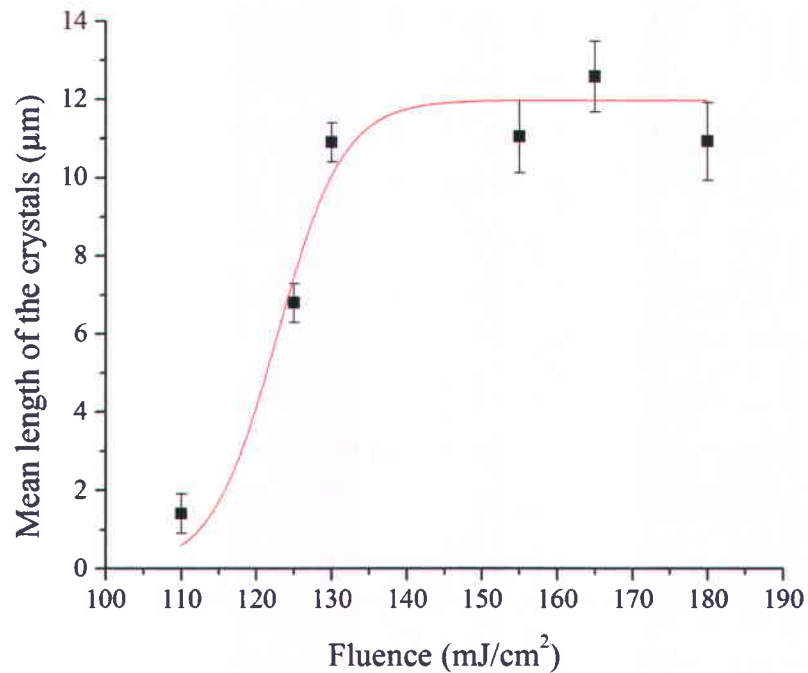


Figure 48. Mean length of the large crystals seen in the post mortem images of a-Si/SiO₂ crystallised at different fluences. The red curve shows the tendency in the evolution of the mean length of the crystals with increase of the incident fluence.

solid) undercooling. For fluences above 155 mJ/cm² (Figure 47), a lighter region almost uniform in contrast with dark randomly dispersed features is produced, suggesting complete melting of the a-Si film leading to exposure of the bare supporting SiO₂ window.

Measurement of the mean length of the large crystals seen in the post mortem images showed that the average length of the crystals increases with increase of the fluence used up to ~140 mJ/cm² giving maximal length of ~12 μm (Figure 48). For higher fluences the mean length of the crystals does not change significantly, indicating saturation of the growth. This also indicates that the maximal length of the large crystals is achieved prior to the complete melting in the central part of the a-Si film and that the melting in the center actually does not allow larger growth of these crystals probably due to inefficient heat transfer for growth of larger crystals. It is evident that the film dewets and forms large droplets on the bare SiO₂ window. However, due to the high energy, it is also possible that part of the material is ablated. If ablation occurs, then the heat transfer from the laser pulse to the remaining a-Si will not be efficient because the deposited energy will be mostly

confined in the region of the ablation and will be used as kinetic energy for the removed material. In addition, the SiO₂ supporting layer has very low absorption at 532 nm i.e. will not transfer significant heat to the remaining part of the a-Si layer. Similar results were obtained by Im et al. [12] where gradual increase in grain size with increase of the pump laser fluence was observed for low energies (before complete melting of the film).

The results on the micro-sized grains support the hypothesis that the a-Si film has fully melted in the central region exhibiting lighter contrast for fluences of 165mJ/cm² and higher and the region lighter in contrast seen in the images was the remaining SiO₂ window. For the very dark features seen in the center of these micrographs, we concluded that they are polycrystalline silicon which formed quasi-spherical droplets after melting of the a-Si layer (confirmed by SAED). The rectangular shape of the large crystals suggests that super lateral growth took place (Figure 45 and Figure 47). This growth mode occurs when the material is partially melted (at least on the surface) and solidifies by rapid, anisotropic growth at the liquid-solid interface [12], [14]. In this growth mode the crystallization begins from the periphery with direction of the solidification toward the center where the temperature was the highest. The initiation of the super lateral growth is believed to occur either via solid state crystallization at the periphery or due to pre-existence of nanocrystals acting as nucleation sites for the rapid lateral growth that produces these large grains [15]. We will return to these hypotheses in the discussion section of this chapter where an estimation of the temperature of the film will be given.

5.3 Time resolved study of the amorphous to crystalline phase transition in a-Si/SiO₂

Here, time-resolved images of the crystallization in a-Si upon single shot laser heating will be presented. We used 130 mJ/cm² and higher fluences for the time-resolved investigation of a-Si crystallization because the crystalline structures produced had micrometric sizes, and were therefore easier to discern. Due to the thicker samples², lower electron scattering power of silicon and the lower number of electrons in the pulse at the times of these studies, the spatial resolution and contrast of the images are poorer in comparison with the images

² The total thickness of a-Si/SiO₂ is 180 nm = 130 nm a-Si + 50 nm SiO₂ window in comparison to 150 nm in a-Ge/SiO and 110 nm in self-supported a-Ge films.

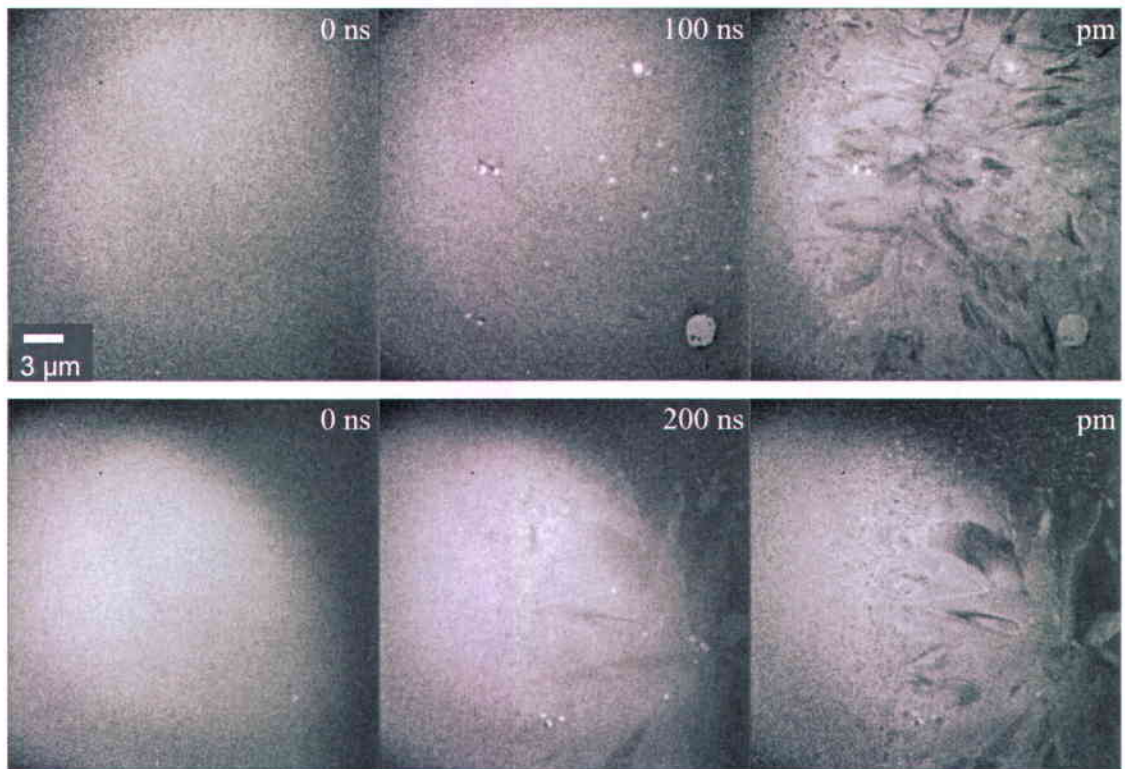


Figure 49. Time resolved images of the crystallization in a-Si/SiO₂ at fluence of 130 mJ/cm². The time delays are shown in the upper right corner of each image. The 'pm' abbreviation stands for post mortem.

obtained for germanium. For these reasons, the nanocrystallization at the periphery of the crystalline region could not be detected and we focused on observation of the evolution of the microcrystalline structure. The pump laser beam was aligned so as to observe the crystallization in part at the central region together with part of the periphery visible in the images. Since the windows had size of $100 \times 100 \mu\text{m}^2$, the laser beam (100 μm in diameter) was aligned to affect part of the window i.e. part of the energy in the beam was dissipated in the Si wafer substrate used as frame for the windows (for more details on the sample configuration, refer to Chapter II).

5.3.1. Fluence $130 \text{ mJ/cm}^2 \pm 5\%$.

Figure 49 shows time-resolved images of the crystallization in a-Si/SiO₂ subjected to a laser fluence of 130 mJ/cm^2 . At 100 ns neither the microcrystalline structure nor the

nanocrystals were visible. However, light spots appeared in the image and they do not change their position in the post mortem image. These spots are probably pores occurring due to densification of the a-Si upon crystallization or melting of very small volumes of the film revealing the SiO₂ window beneath the a-Si layer. This hypothesis is based on the fact that there is a difference in the density of a-Si (2.26 g/cm³) and the density of crystalline Si (2.31 g/cm³) [8], [16] which allows up to ~2% of the volume to be transformed into pores. From the visible pores, we estimated their volume to be ~1% which is consistent with the theoretical estimation. Similar behaviour was seen in the crystallization of a-Ge.

The 200 ns delay image shows difference in contrast in comparison with the post mortem image in the central part of the reacting region but the evolution of most of the features is evident. Also, the nanocrystals at the periphery are visible. Therefore, we inferred that the crystallization process approaches its completion at 200 ns for fluence of 130 mJ/cm². The difference in contrast between the 200 ns time-resolved image and the post mortem one is probably due to the thermal scattering that occurs when an image is taken from a specimen at elevated temperature in comparison with the image of the specimen at room temperature.

5.3.2. Fluence 140 mJ/cm² ± 5%.

At 140 mJ/cm² the evolution of the microstructure is similar to the previous fluence of 130 mJ/cm² (Figure 50). At 100 ns only a few light in contrast spots are visible which may be formed due to densification or melting of very small volumes of the film. At 300 ns the crystallization appears to be toward completion since there is minimal difference between the time-resolved and the post mortem image including the presence of the nanocrystals at the periphery of the crystalline region. Although the number of the nanocrystals at the periphery appears to be higher in the post-mortem image in comparison with the time resolved image, this could be a result of ripening of the crystals but also due to cooling of the sample. In general the nanocrystals are less visible in these images due to the thermal scattering, the thicker specimen and the lower density of charges in the electron beam pulse used in this study. Therefore, the higher visibility of the nanocrystals may not be related solely to the crystallization process. Note that for this experiment the electron beam taking the image and the pump laser beam were not well aligned, for this reason the

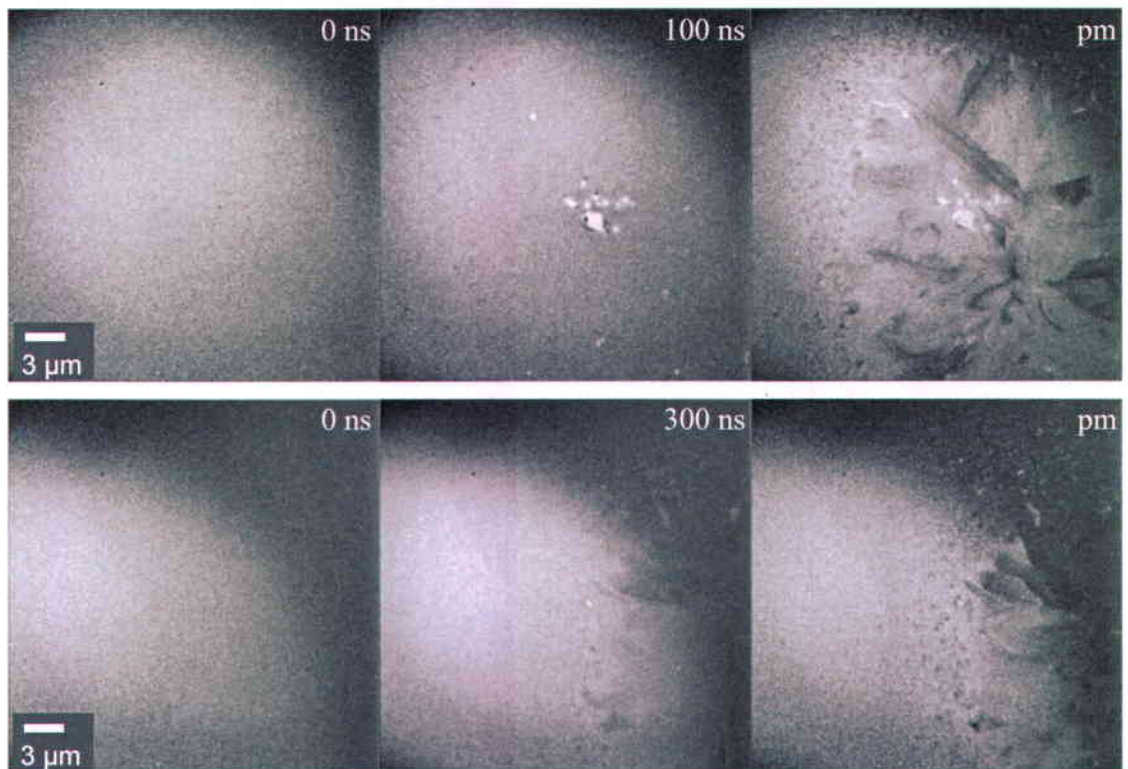


Figure 50. Time resolved images of the crystallization in a-Si/SiO₂ at fluence of 140 mJ/cm². The time delays are shown in the up-right corner of each image. The ‘pm’ abbreviation stands for post mortem.

image shows mostly the periphery of the crystalline region.

5.3.3. Fluence 155 mJ/cm² ± 5%.

This fluence provokes formation of a larger region with microcrystalline structure (Figure 51). At 200 ns white spots are present, as in the previous cases; however, at 300 ns the images does not indicate that the crystallization is complete as for the previous energies. This is probably due to the higher energy input coming from the laser pulse allowing the film to attain a higher temperature. For this reason, it will take longer for the temperature to decrease and allow the growth of the microcrystalline structure. In the 300 ns delay image there is a distinct boundary that delimits the region of the microcrystalline structure and separates it from the nanocrystalline region (indicated by white arrows on the micrograph). On the left side of the boundary some nanocrystals can be seen (red arrow) which indicates

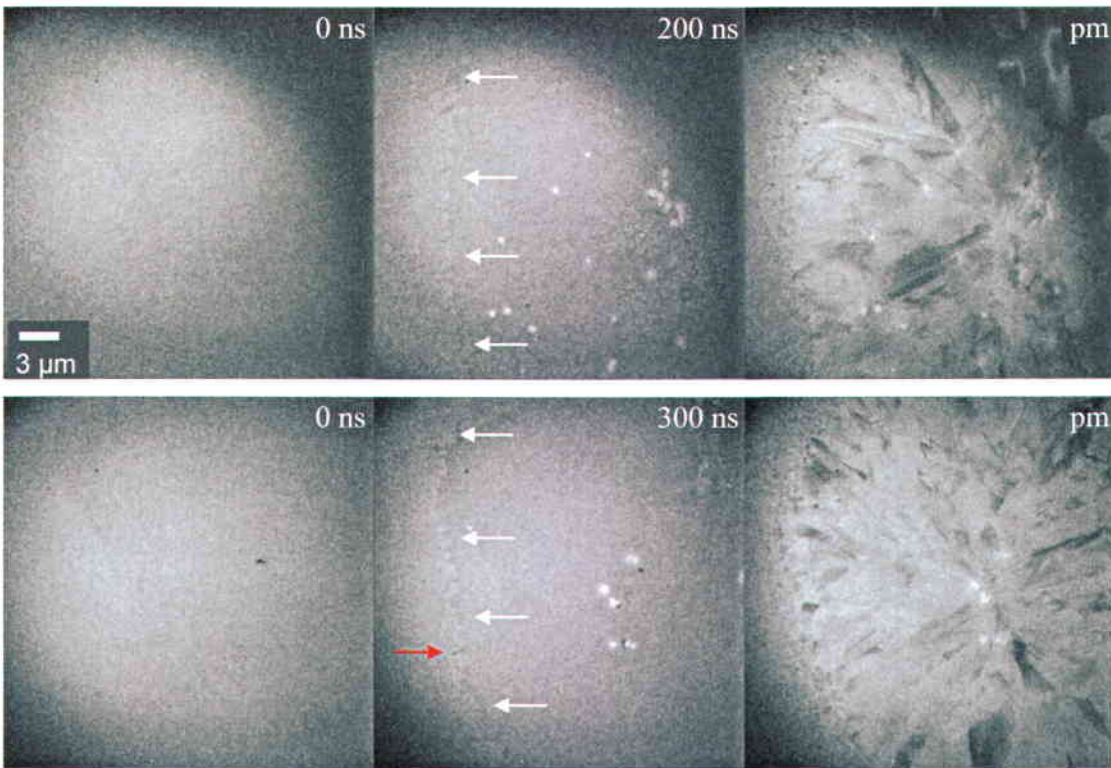


Figure 51. Time-resolved images of the crystallization in a-Si/SiO₂ produced by a laser fluence of 155 mJ/cm². The time delays are shown in the upper right corner of each image. The ‘pm’ abbreviation stands for post mortem. The white arrows in the 200 ns time resolved image point the boundary from where the microcrystalline structure will grow. A similar boundary is clearly visible in the 300 ns delay image.

that the nanocrystalline growth occurs probably at lower temperature because the Gaussian distribution of the pump laser beam dictates that less energy was deposited at the periphery than in the center. We hypothesize that on the right side of the boundary, melting of the material has occurred (at least on the surface), while on the left side of the boundary the temperature was not high enough for melting to occur. The same boundary of the solidification front is also slightly visible on the 200 ns delay image (denoted with the white arrows on the micrograph).

5.3.4. Fluence 180 mJ/cm² ± 5%.

The fluence used here was sufficient to completely melt the center of the a-Si layer

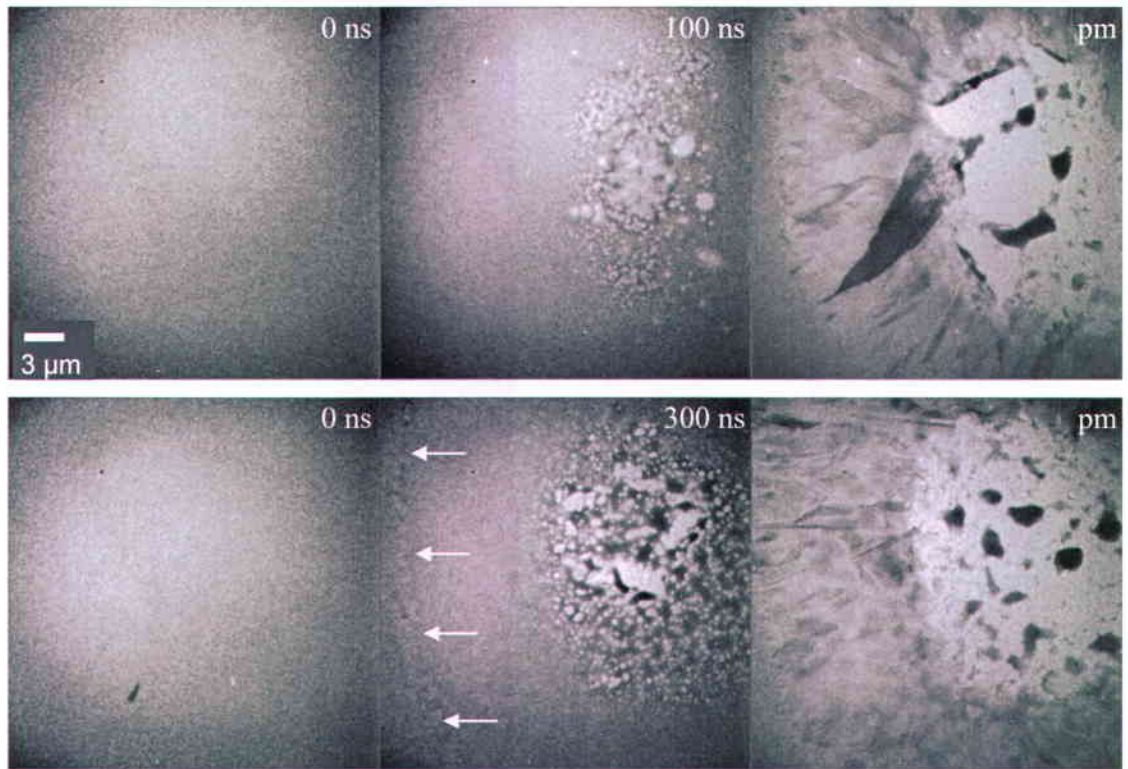


Figure 52. Time-resolved images of the crystallization in a-Si/SiO₂ at fluence of 180 mJ/cm². The time delays are shown in the upper right corner of each image. The ‘pm’ abbreviation stands for post mortem. The interface a-Si – partially melted Si is pointed with the white arrow on the two time resolved images.

(Figure 52). The time-resolved images clearly show that the material was molten in the center (Figure 52 image 100 ns and 200 ns delays – the a-Si looks like is “boiling”). The voids seen in these images probably result from dewetting of the silicon layer or outgassing of trapped residual gases in the SiO₂ substrate because they are much larger in size (mostly above 1 μm compared to ~200 nm for the pores). The high temperature will allow dewetting of the films and formation of bubbles from gases in the molten silicon to facilitate the formation and coalescence of the silicon droplets on the SiO₂ window by displacing the molten material. A post mortem examination of the sample showed that these droplets transform into fully crystalline particles with sizes between ~5 μm down to ~10 nm. Again, the interface between solid and liquid silicon is visible at 300 ns.

5.4 Discussion

Estimation of the temperature is crucial for the understanding of the growth mode that occurs in a-Si. Therefore, a model for estimation of the evolution of the temperature in the depth of the a-Si film was developed. The detailed calculations and boundary conditions can be found in S. McGowan's MSc thesis from McGill University [18] and Annex B.

An average fluence of 180 mJ/cm^2 was assumed in the estimation of the temperature profile because the experimental results clearly showed the presence of a completely melted region in the center of the sample (see Figure 52 – 100 ns, 200 ns and the post mortem images). Similar to the case of a-Ge crystallization, a simple analytical estimation of the temperature within the film, assuming that all the deposited pump laser energy is absorbed in the film and the properties of the film do not change with time and with increase of the film depth, gives that the associated temperature increase in the film is a few hundred degrees above the melting temperature of crystalline silicon ($T_{mc} = 1400 \text{ K}$) over the entire area covered by the laser beam spot. Figure 53 presents the results of the estimation of the temperature in the depth of the film for different time delays where no change in the properties of the film is assumed. Note that $t = 0$ corresponds to the temperature distribution immediately after arrival of the laser pulse. As the figure shows the temperature of the film increases very rapidly (on the order of the pump pulse duration) and should be above 2500 K throughout the entire thickness of the film at 25 ns i.e. the entire film should be melted after the arrival of the laser pulse and its absorption. However, the melted area that we observed is much smaller than the pump laser beam spot, which was $100 \mu\text{m}$ in diameter (see in Figure 54). The red curve traced on the image outlines the boundary of the region completely melted and the yellow curve delimits the region of partial melting. Since the analytical estimation of the temperature predicts a much larger melted region than our observations show, we included the phase change in the model, along with the associated changes in thermal and optical properties of the silicon that occur as a result, to give a realistic description of the process.

If change in the properties of the material is assumed and considering that this change occurs in shorter time than the duration of the pump laser pulse, the calculated temperature within the film can change dramatically. To estimate this change, the sample was divided into 'n' slices in depth with the first slice at the surface and the last one at the interface a-Si/SiO₂.

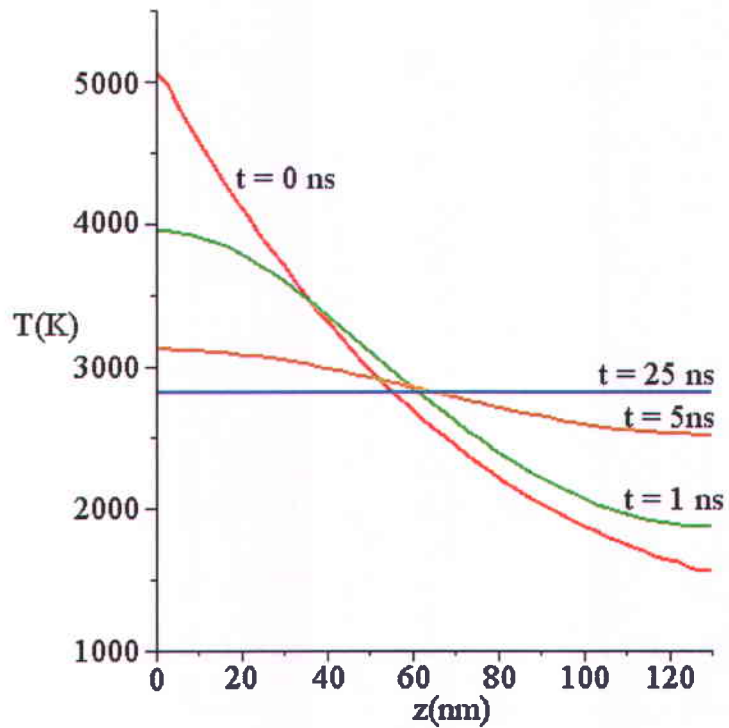


Figure 53. Analytical estimation of the evolution of the temperature in the depth of a-Si film at fluence 180 mJ/cm^2 assuming that the properties of the film do not change with time and with increase of the depth of the film. $t = 0$ corresponds to the temperature distribution immediately after the arrival of the laser pulse. Figure taken from [18].

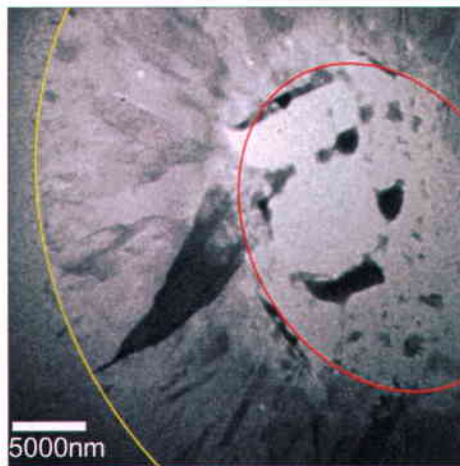


Figure 54. Partial view image of the sample after irradiation with fluence of 180 mJ/cm^2 . The red ellipse delimits the outer boundary of the region of complete melting of the film where the temperature was above the temperature for melt of silicon. The yellow ellipse delimits the outer boundary of the region of partial melting of the film. Beyond this limit, no melting of the material occurred.

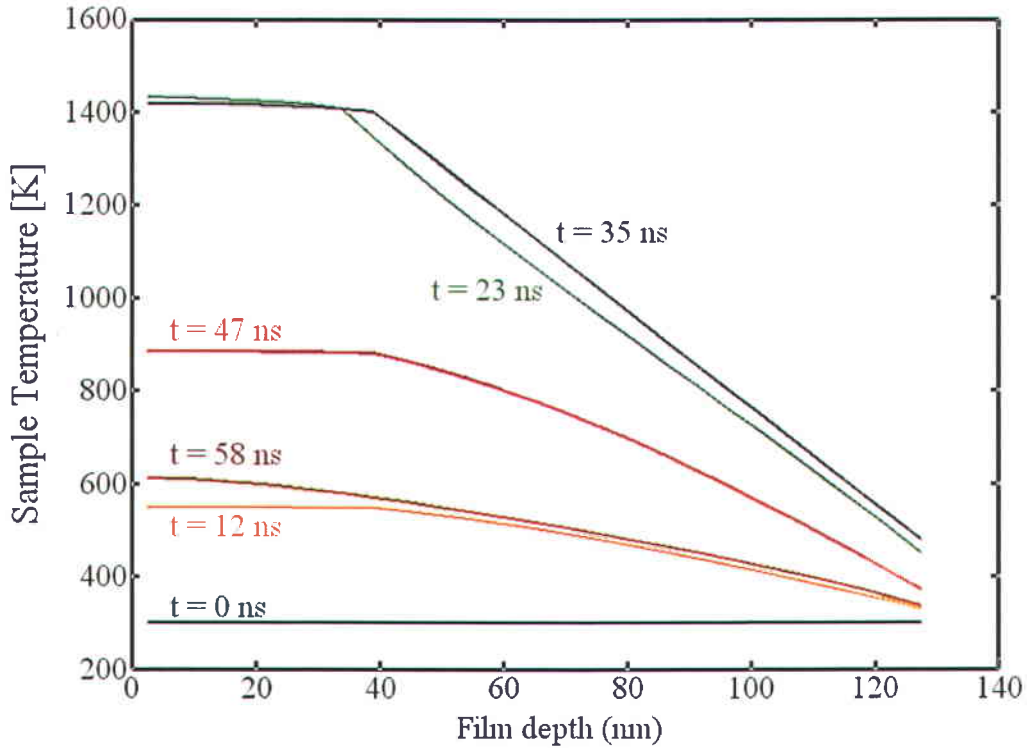


Figure 55. Temperature distribution within the 130 nm a-Si film in depth at different time delays where change in the optical and thermodynamic parameters of silicon with phase changes is assumed. Time zero is the beginning of the pump pulse, which has a duration of 15 ns at FWHM. Figure taken from [18].

Then, the temperature in the film was calculated for each slice in a cascade sequence as follows. When the laser pulse arrives, the first layer reaches the melting temperature and its thermodynamic parameters such as absorption, heat diffusion and reflectivity change from the properties of the amorphous material to the properties of the liquid material. Subsequently, the following slice undergoes the same transition. Thus, during the time interval of the heating on the top of the a-Si film a liquid layer is formed while on the bottom (i.e. at the interface a-Si to SiO₂) the film is still solid. This approach for cascade heating and phase transformation allows to achieve a temperature profile consistent with the crystallization observed in the a-Si film. The results of these calculations are presented in Figure 55 for the same fluence as the results in Figure 53. The plot suggests that the maximal temperature of the film, which is above ~1400 K, is reached within the first 20 ns

after arrival of the pump laser pulse, which corresponds to the peak of the illumination. This temperature is much lower than was calculated analytically, as the computational model shows only the first few nanometers of the film reach the melting temperature.

Since our experimental results show that complete melting of the film occurs in a much smaller area than predicted by the analytical solution for the heat within the film, where the entire film had to be melted (Figure 53 and Figure 54), we looked at the fluence distribution within the bounds of the laser beam. The average fluence of 180 mJ/cm^2 has a Gaussian distribution in the plane of the sample which implies that the fluence is not homogeneously deposited and absorbed in the film. Based on these measured boundaries, the fluence required to melt a surface layer of the silicon film is $240 \pm 20 \text{ mJ/cm}^2$. The threshold for complete melting of the 130 nm film is approximately $330 \pm 20 \text{ mJ/cm}^2$. We used the model with change of the properties of the material to estimate the evolution of the temperature at these fluences.

Figure 56A shows the evolution of the estimated temperatures at 330 mJ/cm^2 at different depths in the film for different times after arrival of the laser pulse. Within the model this fluence melts $\sim 100 \text{ nm}$ of the thickness of the film (i.e. almost the entire film thickness) for time duration up to $\sim 60 \text{ ns}$, and then falls rapidly. However, the silicon/substrate interface remains unmelted. About 30 ns after the start of the pump pulse, the film begins to cool. After an additional 15 ns , the silicon has cooled sufficiently to resolidify. To completely melt the film within the model, the fluence required is $\sim 355 \text{ mJ/cm}^2$. This value is only 8% higher than the experimental fluence.

By using 240 mJ/cm^2 fluence (partial melting), the model predicts that the temperature reaches $\sim 1400 \text{ K}$ for depths up to $\sim 65 \text{ nm}$ and lasts to about 50 ns (Figure 56B). However, the temperature never increases above $\sim 700 \text{ K}$ at a depth of 130 nm i.e. at the interface a-Si/SiO₂ the melting never occurs. According to the results of the heat conduction model, the minimum fluence for surface melting is estimated to be 195 mJ/cm^2 . This is 19% smaller than the fluence of the image. It is possible that it is necessary to melt not just the surface layer, but some minimum film thickness to achieve the large grained crystal structures observed. However, this could be also a result of the uncertainties related to calculations with this model. Our observations and estimation of the temperature support our hypothesis that the large crystals form by super lateral growth because the crystals grow inward and the fluence should be sufficient to partially melt the film at least on the surface.

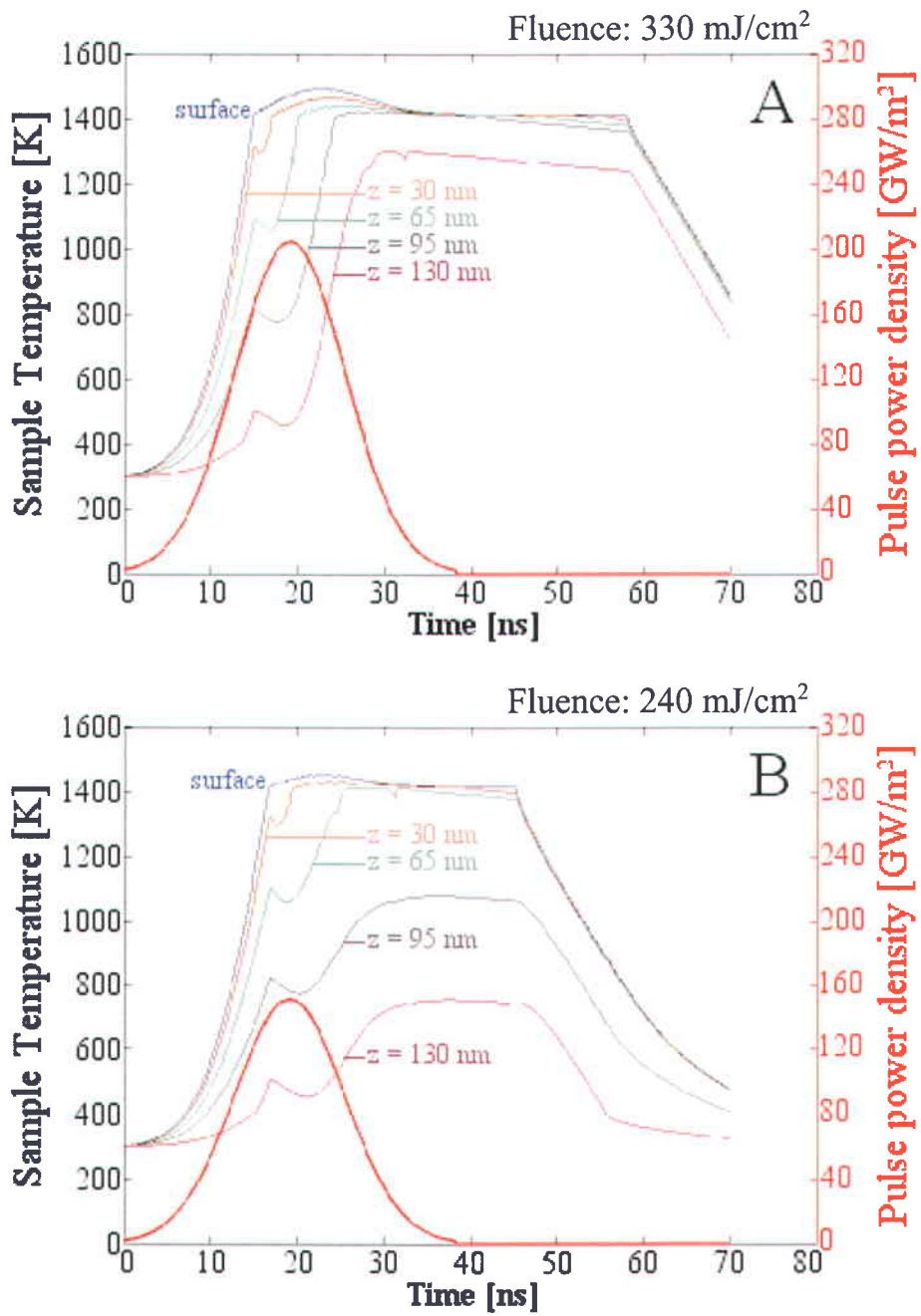


Figure 56. Evolution of the temperature with the time in a-Si irradiated for different depths of the film at the melt boundary (A – fluence 330 mJ/cm²) and at the partially melted boundary (B – fluence 240 mJ/cm²). The equivalent pump laser intensity is also given in the graphs. Figure taken from [18].

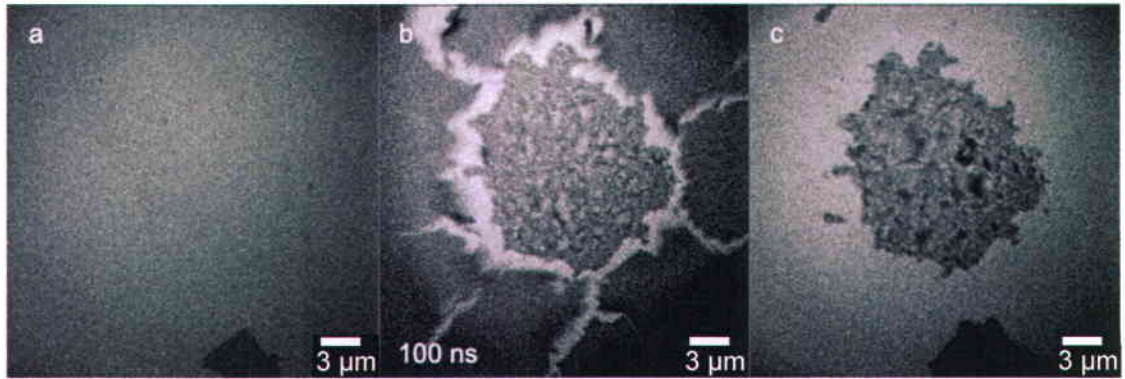


Figure 57. Delamination of the a-Si film at fluence 135 mJ/cm^2 . The images are denoted as follows: a) the sample prior the crystallization, b) time resolved image at 100 ns delay showing the delamination of the a-Si film from the SiO_2 window, and c) the post mortem image where only small crystalline part of the film remained on the supporting window.

In addition, since these crystals form above a minimal threshold of the pump laser fluence, then a threshold in the thickness of the liquefied region has to be reached to allow such a growth mode (see section 5.2 and Figure 47).

Inconsistencies in the crystallization process in a-Si/ SiO_2

Significant inconsistencies were observed in the crystallization behaviour in a-Si/ SiO_2 . Although samples were taken from the same lot i.e. samples were obtained from one fabrication process on the same wafer, and deposition of the a-Si was done at the same time for all samples, strong delamination of the a-Si film from the SiO_2 window was observed for some windows. An example of this type of delamination is shown in Figure 57. The same phenomena occurred on different samples as well as in different windows on the same sample, even at a constant fluence of the pump laser.

The explanation of this behaviour given by S. McGowan relates to possible variations in the thickness of the silicon film, variation of the thickness of the SiO_2 windows, or changes of the pump laser from one day to another (i.e. a larger or smaller spot size at the sample). Since the thickness of the a-Si films was estimated by ellipsometry (at École Polytechnique de Montréal where the e-beam deposition was done) and by profilometer (at INRS) to be $130 \text{ nm} \pm 5\%$ and the lenses' settings used in the DTEM to focus the pump

laser beam on the sample were not changed, then variation of the thickness of the SiO₂ windows or contamination of the a-Si films could be the source for these inconsistencies. The thickness of the SiO₂ was not explicitly verified by our collaborators. In addition, contamination of the films was possible since the etching process used in the fabrication of the SiO₂ windows used by S. McGowan appears to have left behind particulate, as indicated by TEM investigation of the bare SiO₂ windows which revealed small particles of crystalline silicon. During the etching process the removal of material does not occur layer by layer but may happen by the removal of small particles [19]. As a consequence, if proper rinsing is not performed on the etched wafers, there is a possibility that these particles will deposit on the SiO₂. Another important aspect of the rinsing is the proper removal of the organic solvent used in the etching process as this could also lead to contamination of the a-Si film. Therefore, without careful control of the fabrication process of the SiO₂ windows, contamination can occur and could lead to the consecutive unpredictable behaviour of the a-Si material crystallised by laser heating.

5.5 Conclusion

Laser-induced crystallization in a-Si on SiO₂ was successfully observed with high temporal resolution *in situ* in the DTEM. For all the fluences used in this study, two types of structures formed after single shot laser heating of the amorphous film: (i) a microcrystalline structure mostly in the central region of the irradiated area by the laser beam spot and (ii) nanocrystalline structure at the periphery. Due to the large thickness of the samples, the nanocrystallization process occurring at the periphery of the crystallised region could not be observed.

For lower fluences, up to $\sim 155 \text{ mJ/cm}^2$, the central part of the film partially melts, allowing super lateral growth to take place, while for high fluences complete melting of the film in the center of the heated region occurs and the molten material coalesces in droplets with different sizes on the SiO₂ window.

The times for complete crystallization were shown to be fluence dependant. At higher fluences, longer times for crystallization were needed probably due to the higher energy deposited from the laser pulse.

Modeling of the film temperature as a function of depth and of time showed that complete melting can occur in the central part of the irradiated area for fluences of 165 mJ/cm² and higher and partial melting for lower fluences. Our observations suggest that the growth of the nanocrystals at the periphery occurs via solid-state crystallization and a minimal thickness of melted film is necessary for the growth of the microcrystalline structure.

Future studies on this material should focus on the fabrication of uncontaminated, uniform in thickness a-Si films and thinner SiO₂ windows to avoid inconsistencies in the crystallization behaviour observed in this work. This will allow *in situ* observation of the nanocrystallization and should reveal the crystallization front evolution. Additional modeling of the temperature in the radial direction will permit further investigation of the solid-state crystallization at the periphery.

5.6 Concluding remarks on the crystallization processes observed in germanium and silicon

As was mentioned in the beginning of this chapter, the laser induced crystallisation in a-Si completes with the formation of a central microcrystalline region surrounded by a nanocrystalline structure that is significantly different than the three-fold microstructure formed in a-Ge, which was observed for membrane supported layers as well as for self-sustained films. Our experimental results suggest that the mechanisms governing the phase transitions in the two group IV semiconducting materials are different. To address this discrepancy, we comment here on the properties of the two materials as well as on our experimental set up in an attempt to shed more light on the crystallisation process in the two materials.

As shown by Im and co-workers [12], [14], [20] various melt-mediated transformation mechanisms can be observed in single-pulse-induced crystallization of a-Si films on SiO₂ depending on the energy density of the laser pulse used to initiate the process. Two major regimes were observed to lead to different morphologies: the low energy density regime and the high energy density regime. Low energy density (i.e. low fluence) induced crystallisation results in partial melting of the film. In this regime, a continuous layer of unmelted film

remains near the SiO₂ interface, i.e. the melt depth is smaller than the thickness of the film, and explosive crystallisation occurs. On other hand, high energy density induced crystallisation (i.e. high fluence) leads to complete melting of the film. In this regime the laser excitation leaves the material in a fine-grained polycrystalline state. An important sub-regime that produces the largest grain size of polycrystalline silicon was discovered to take place within a narrow experimental window at the transition between the two major regimes. This phenomenon is referred to as super-lateral growth (SLG) because it results in grains a few micrometers in length. This regime was explained in terms of liquid-phase regrowth from the surviving solid seeds at the bottom of the oxide interface when near-complete melting of the film occurs.

The laser used to induce the crystallisation process in the two materials had a wavelength of 532 nm. The absorption depth at this wavelength in a-Si is ~100 nm, compared to ~50 nm in a-Ge [21]. This indicates that for the similar fluences of ~130 mJ/cm² the energy from the pump pulse is absorbed in almost the entire thickness of the a-Si while in just half of the thickness of the a-Ge film. Our studies showed that while a-Si crystallises via SLG, a-Ge at a similar fluence develops a threefold nano- to microcrystalline structure due to explosive crystallisation. In both cases the crystallisation is melt-mediated, as it takes place at the solid-liquid interface. However, the solidification front moves in opposite directions. In the case of crystallisation in a-Si, the solidification proceeds towards the center of the excited region, whereas in a-Ge the growth proceeds in the radial direction reaching beyond the boundaries of the irradiated area. Although our experimental setup and results cannot provide information on the time periods for the transition from solid amorphous state to the liquid state, i.e. on the time interval for the change of the thermodynamic parameters assigned to the solid state to those observed for the liquid state, our observations suggest that the absorption depth could play a critical role in the crystallisation mechanism. This could stem from the commensurability of the thickness of the thin films and the absorption depths. As mentioned above, the a-Si film is 130 nm thick meaning that the energy from the laser beam is absorbed in slightly less than the entire thickness of the film (absorption in the SiO₂ is negligible and thus can be ignored). As a result, about half of the film thickness is melted (reaching the temperature of melt of the crystalline silicon 1400 K), while the material at the a-Si/SiO₂ interface never reaches temperatures above ~800 K. On

other hand, in a-Ge the absorption depth is about half of the film thickness and the temperature of the film never reaches the temperature of melt of the crystalline material (1200 K). This indicates that a similar fluence leads to two different thermodynamic conditions for a-Si and a-Ge. In the case of a-Si a large amount of liquefied material at a temperature near the crystalline melting temperature is formed, which leads to super-lateral growth. On the other hand, a similar fluence used for the crystallisation of a-Ge leads to a temperature below the T_{mc} and results in melt-mediated explosive crystallisation. This hypothesis must be further investigated by additional DTEM studies on explosive crystallisation in a-Si and ultrafast electron diffraction for the estimation of the time intervals for the phase transition from amorphous solid to liquid material.

5.7 Bibliography

- [1] S. Uchikoga and N. Ibaraki, "Low temperature poly-Si TFT-LCD by excimer laser anneal," *Thin Solid Films*, vol. **383**, p. 19–24 (2001).
- [2] J. B. Boyce, P. Mei, R. T. Fulks, and J. Ho, "Laser Processing of Polysilicon Thin-Film Transistors: Grain Growth and Device Fabrication," *Phys. Stat. Sol. A*, vol. **166**, p. 729–741 (1998).
- [3] G. Andrä, J. Bergmann, F. Falk, E. Ose, and Stafast H., "Laser induced crystallization of amorphous silicon films on glass for thin film solar cells," *Phys. Stat. Sol. A*, vol. **166**, p. 629–634 (1998).
- [4] T. Suzuki, "Flat panel displays for ubiquitous product applications and related impurity doping technologies," *J. Appl. Phys.*, vol. **99**, p. 111101-1–15 (2006)
- [5] M. A. Green, et al., "Crystalline silicon on glass (CSG) thin-film solar cell modules," *Sol. En.*, vol. **77**, p. 857–863 (2004).
- [6] S D Brotherton, "Polycrystalline silicon thin film transistors," *Semicond. Sci. Technol.*, vol. **10**, p. 721–738 (1995)
- [7] N. H. Nickel, N. M. Johnson, W.B. Jackson, "Hydrogen passivation of grain boundary defects in polycrystalline silicon thin films," *Appl. Phys. Lett.*, vol. **62**, p. 3285–3287 (1993)
- [8] I.-W. Wu, A. Chiang, M. Fuse, L. Öveçoglu, and T. Y. Huang, "Retardation of nucleation rate for grain size enhancement by deep silicon ion implantation of low-pressure chemical vapor deposited amorphous silicon films," *J. Appl. Phys.*, vol. **65**, 4036–4039 (1989).
- [9] J. Poate and J. W. Mayer, editors, "Laser Annealing of Semiconductors," Academic Press (1982).
- [10] C.-C. Kuo, W.-C. Yeh, J.-B. Chen, J.-Y. Jeng, "In-Situ and Ex-Situ Measurements on Silicon Thin Films Fabricated by Excimer Laser Annealing," *J. Phys.: Conf. Series*, vol. **48**, p. 937–944 (2006).
- [11] S.-J. Moon, M. Lee, and C. P. Grigoropoulos, "Heat Transfer and Phase Transformations in Laser Annealing of Thin Si Films," *ASME J. Heat Transfer*, vol. **124**, p. 253–264 (2002).

- [12] J. S. Im, H. J. Kim, and M. O. Thompson, "Phase transformation mechanisms involved in excimer laser crystallization of amorphous silicon films," *Appl. Phys. Lett.*, vol. **63**, p. 1969–1971 (1993).
- [13] M. Hatano, S. Moon, M. Lee, K. Suzuki, and C. P. Grigoropoulos, "Excimer laser-induced temperature field in melting and resolidification of Si thin films," *J. Appl. Phys.*, vol. **87**, p. 36–43 (2000).
- [14] J. S. Im and H. J. Kim, "On the super lateral growth phenomenon observed in excimer laser induced crystallization of thin Si films," *Appl. Phys. Lett.*, vol. **64**, p. 2303–2305 (1994)
- [15] M. L. Taheri, S. McGowan, L. Nikolova, J. E. Evans, N. Teslich, J. P. Lu, T. LaGrange, F. Rosei, B. J. Siwick, and N. D. Browning, "In situ laser crystallization of amorphous silicon: Controlled nanosecond studies in the dynamic transmission electron microscope," *Appl. Phys. Lett.*, vol. **97**, p. 032102-1–3 (2010).
- [16] *Properties of Amorphous Silicon (EMIS Data Review I)*, London: IEE Inspec (1985)
- [17] *Properties of Silicon (EMIS Data Review 4)*, London: IEE Inspec (1988)
- [18] S. McGowan, MSc Thesis: "In situ study of amorphous semiconductor crystallization by Dynamic Transmission Electron Microscopy," McGill University, Montréal, Québec, Canada (2009).
- [19] Course "Nanoscience and Nanotechnology" given by professor P. Grutter at McGill University, course taken in the autumn term of 2009.
- [20] J. S. Im, M. A. Crowder, R. S. Sposili, J. P. Leonard, H. J. Kim, J. H. Yoon, V. V. Gupta, H. Jin Song and H. S. Cho, "Controlled Super-Lateral Growth of Si Films for Microstructural Manipulation and Optimization," *Phys. Stat. Solidi A*, vol. **166**, p. 603–617 (1998).
- [21] M. Von Allmen, Laser-Beam Interactions with Materials. Physical Principles and applications, Springer-Verlag Berlin Heidelberg (Germany) (1987).

General conclusion and outline

6.1. Objectives

Group IV semiconductors are widely used in modern electronics. With the expanding market demands for smaller, faster and cheaper devices, more attention is being paid to the laser-induced crystallization of amorphous films of these materials. Preference is given to crystalline germanium because this material possesses the highest hole-mobility of all known semiconductors [1]. Laser heating offers a localised increase of temperature, and thus facilitates the creation of more complex designs of devices. The heating rate is significantly higher than in conventional furnace annealing, and the process evolves very rapidly (in a few nanoseconds to a few microseconds range). Therefore, it is critical to have in depth understanding on the kinetics and thermodynamics of the amorphous to crystalline phase transition. This will allow control of the microstructure, which reflects directly into the properties of the material and the functionality of the device.

When exposed to laser annealing, a-Ge and a-Si complete the amorphous to crystalline phase transformation with a complex final structure. For a-Ge, three distinct microstructures with feature sizes from a few nanometers to a few micrometers form upon laser-induced crystallization while for a-Si only two are present. In both cases the process evolves in a time interval from a few nanoseconds to a few microseconds after the heating pulse. Therefore, to study the transient structures during this process, temporal resolution of nanoseconds combined with spatial resolution of nanometers is necessary.

The principal objectives of this thesis were to reveal the sequence of change in the morphology during the growth of the different structures, to unveil the shape of the growth front during its propagation, to estimate the velocities of crystallization and to give an overview of the possible growth modes taking into account the estimations of the temperature within the films. For this we used free-standing and membrane-supported films with the goal of elucidating the influence of the supporting layer on the kinetics and thermodynamics of the phase transformation.

6.2. Main results

In this work we used dynamic transmission electron microscopy for *in situ* investigation of the evolution of the laser-induced crystallization process. We showed that DTEM is uniquely suited for studies of such processes due to the high temporal and spatial resolutions offered by the instrument. To complement these results, we used conventional TEM for visualisation of the fine structural details in the post-mortem structure.

Crystallization in amorphous germanium

We studied the crystallization dynamics in self-sustained and membrane-supported a-Ge films. We found that the crystallization begins less than 20 ns after arrival of the pumping laser pulse and completes about 10 μ s later. The process proceeds in cascade sequence. At first, nucleation and nanocrystallization take place forming a central coarse nanocrystalline region. After that, the growth of the second structure (dendritic) is initiated and it occurs in the radial direction i.e. parallel to the heat flow. The growth of the final layered structure is initiated upon completion of the dendritic growth and advances in the azimuthal direction i.e. perpendicular to the net heat flow. We did not observe a pause in the evolution of these structures.

The crystallization in the central nanocrystalline zone is provoked by the energy deposited from the pump laser beam and is nucleation-dominated until the time for complete crystallization, followed by a growth-dominated regime for higher time delays. The maximum temperature in this zone was estimated to be between ~ 1000 K and ~ 1100 K. The growth of the second structure (dendritic zone) is fueled by the heat release from the amorphous to crystalline phase transition which allows propagation of the growth front to ~ 10 μ m away from the boundary of the central Zone I. The speed of crystallization is relatively low in the beginning of the growth (< 6 m/s) and a transition region is formed. Later, the crystallization velocity increases rapidly to ~ 16 m/s during the explosive regime. Estimation of the evolution of the temperature permitted us to conclude that the increase of the velocity of crystallization is an effect of increased undercooling. After the maximal velocity of crystallization is reached, the velocity decreases again, which we attribute to the continued increase of the undercooling. The dependence of the velocity of crystallization in Zone II on the temperature is similar to that for glassy materials. Estimation of the temperature with the dendritic growth (DG) proved to be challenging because the dendrites

complete their growth in wedge shape, making the estimate the radius of the growing dendrite ambiguous, and the estimation of the temperature of the film less accurate. For this reason, we instead used a model to give a qualitative estimation of the temperature in the film from the post mortem images. The heat diffusion and generation in thin films (HD>F) model describes the growth well for the two types of samples used in this study. It showed that the temperature is decreasing throughout Zone II. Upon completion of the dendritic growth, the temperature favors nucleation to allow the formation of the first nanocrystalline band in the final layered structure. Although the radial velocity of advancement of the growth front in the layered structure was measured to be ~ 1 m/s, we cannot directly measure the growth velocity in the azimuthal direction.

We found that in the central region, nucleation from the bulk occurs at temperatures below the melting temperature of the crystalline material. The dendritic growth occurs by co-propagation of two interfaces, crystalline-liquid and liquid-amorphous some distance ahead, thus forming a thin metastable liquid layer, to allow such high velocities to occur. Since the microstructure of the dendrites did not show any particularity in the crystallographic orientations of the dendrites as observed for crystallization of a-Ge under similar conditions, we classify the dendrites seen in our films as “free grown” dendrites in a supercooled liquid [2]. Capillary effects are insufficient to keep the growth front smooth and a Mullins-Sekerka type instability plays critical role in the formation of the final shape of the dendrites. Our data suggest that the layered structure growth occurs in the azimuthal direction through melt-mediated mechanism where liquefied pockets are propagating in front on the growth front. The growth of the nanocrystalline bands may be occurring due to heat dissipation during the propagation of the liquefied pockets.

Crystallization in amorphous silicon

Crystallization dynamics in amorphous silicon were shown to be dependent on the pump fluence: we observed a delay in the initiation of the growth with an increase of the energy in the laser pulse. At the fluences used in this study the process is melt-mediated favoring super-lateral growth. Nanocrystallization occurs at the periphery of the melted zone but with very limited extent. The crystallization proceeds inward i.e. toward the center of the heated region resulting in the observed long-grained microstructure.

6.3. Original contributions of the thesis

This thesis contributes to the advancement of knowledge of laser induced crystallization in Group IV semiconductors with the following original approaches and findings:

- *We showed that DTEM is uniquely suited for the in situ investigation of the irreversible crystallization in amorphous semiconductors* [3]. We demonstrated that the instrument is a new tool for characterisation of nanoscale systems and has very high potential to provide crucial new insights on the transformation mechanisms at the nanoscale level. Its major advantage is the single shot operation that allows studies of irreversible processes unachievable by multi-shot operating instruments.

- *We were able to visualise in situ the nanocrystallization in a-Ge and to estimate the nucleation rate during the crystallization.* [5]. Our study permitted real-time and real-space visualisation and quantification of the mean size and the number of the nanocrystals. The approach is unique because earlier studies estimated these parameters based only on the post-mortem structure of the a-Ge. This work is the first to offer *in situ* direct evaluation of the maximal nucleation rate in a-Ge.

- *We unveiled the complex crystallization dynamics in a-Ge* [6]. We gave unambiguous proof for the growth directions in the dendritic and layered structures. The high spatial and temporal resolutions of the DTEM allowed visualisation of the growth front during the formation of the two structures, as well as the determination of the growth velocities. That permitted us to estimate the evolution of the temperature both in time and in the radial direction in the film and to elucidate the mechanisms governing the phase transition for the two microstructures.

- *We showed that presence of a supporting layer has little influence on the kinetics of the dendritic growth in a-Ge but plays a more important role in the layered structure growth* [7]. We showed that the heat transfer and generation in two dimensions model describes the crystallization behaviour well for both types of

samples i.e. free standing and membrane-supported a-Ge films, and allows for a determination of the dependence of the growth velocity on temperature within the film.

- *We were able to elucidate the kinetics in a-Si crystallization* [8]. The DTEM investigation of a-Si crystallization allowed us to confirm that the growth is melt-mediated with a liquefied layer existing at least on the surface of the film. Therefore, we affirmed that the formation of the large crystals in the central part of the excited region and surrounded by nanocrystals at the periphery is due to super lateral growth. Also, we showed that the times for complete crystallization is fluence dependant i.e. higher fluences required longer times for crystallization.

6.4. Perspectives

In terms of future work on laser-induced a-Ge crystallization, it would be interesting to observe the process by ultrafast electron diffraction (UED) in the center of Zone I because this technique will allow the determination of the time for initiation of the crystallization in Zone I, as well as allowing for the detection of a liquefied material through the measurement of the coordination number of the material [9]. Amorphous Ge possesses four-fold coordination and its thermodynamically stable liquid has 11-12 fold coordination [11]. However, little is known about the coordination number of the metastable liquid that exists at temperatures below the melting temperature of the crystalline material due to the very short lifetime of the liquid. Turnbull hypothesized that there might not be a change in the coordination number between the amorphous solid and the supercooled liquid [12]. On the other hand, recent work by Koga and Yamaguchi suggests that the change in the coordination number might be very small, with the phase possessing between 4- and 6-fold coordination [13]. It will be possible by UED to answer this question. UED will not allow selection of the area for acquisition of the diffraction pattern; therefore, this technique cannot be used to observe the melt-mediated process in Zone II or to give more information on the crystallization in Zone III.

Movie-mode operation of the DTEM, where it will be possible to acquire up to nine frames in sequence in one experiment, should reveal the growth velocities in Zone III [14].

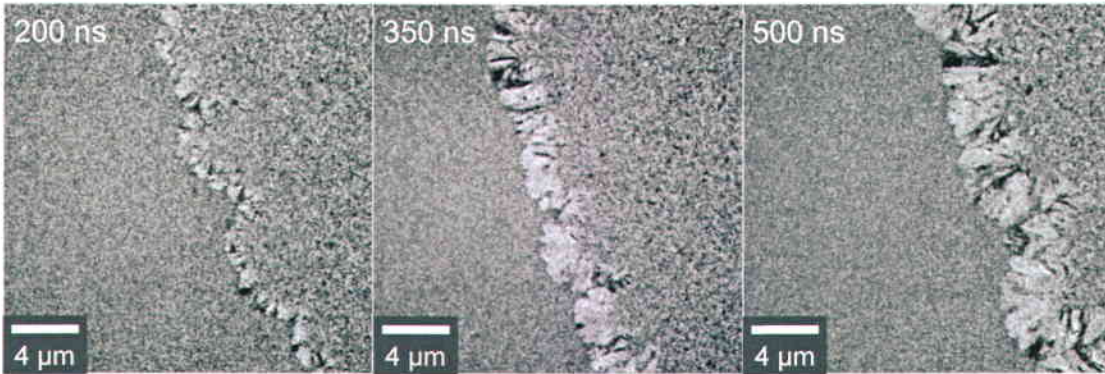


Figure 58. Dendritic growth in 110 nm a-Si film deposited onto 40 nm SiO at fluence of 150 mJ/cm^2 showing very large oscillations of the growth front. The delay is given in the left-upper corner of each micrograph.

This information, combined with OIM, will help to further elucidate the growth mode in this region and to allow the direct measurement of the growth velocity in the direction parallel to the propagation of the growth front.

Future work on a-Si should focus on explosive crystallization dynamics in this material. Initial results showed that silicon deposited onto SiO membranes crystallises explosively with well-defined oscillations of the growth front during the dendritic growth (Figure 58). So, it should be straightforward to extract the mean distance between the protrusions of the growth front and to evaluate if the dendritic growth model which is used for description in metallic systems can be applied in the case of amorphous semiconductors crystallization. Also, a-Si/SiO showed the formation of only one to two layers in the layered structure (Figure 59). Unfortunately, due to the fragility of the samples we could not confirm that the large tangentially oriented crystals are separated by nanocrystalline bands as in the case of a-Ge. Therefore, an extensive DTEM study of the kinetics of crystallization in a-Si and post-mortem examinations with conventional TEM will provide new information on the crystallization of this material.

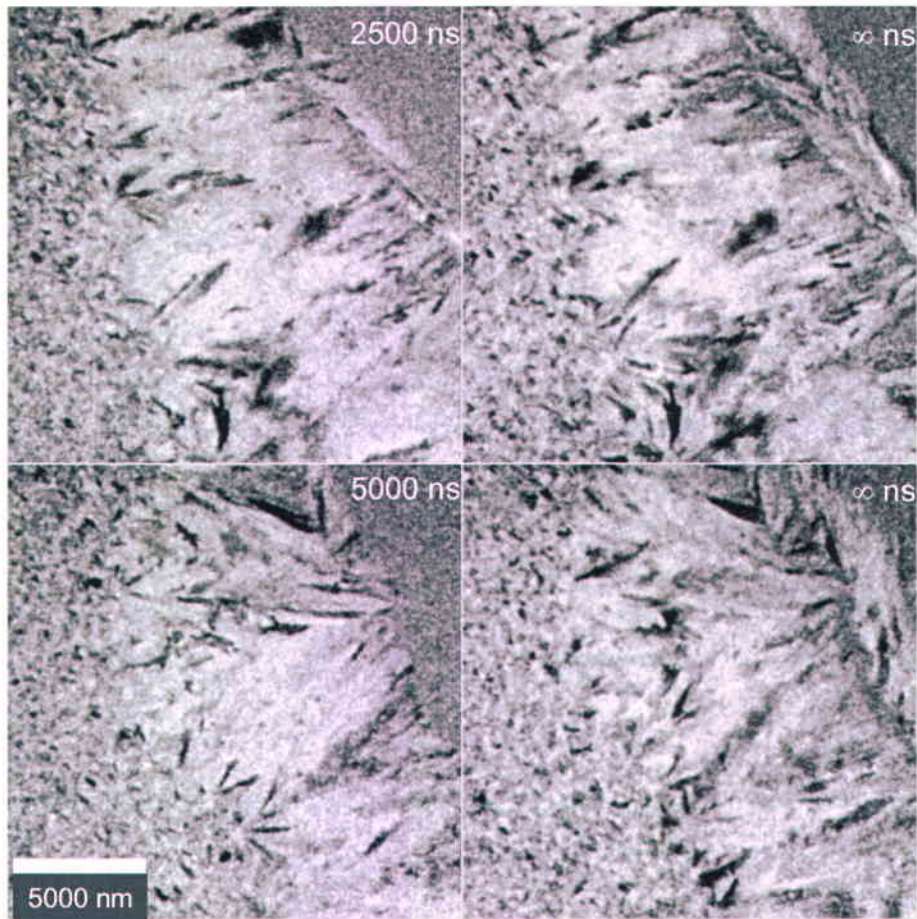


Figure 59. Formation of the layered structure in 110 nm a-Si film deposited onto 40 nm SiO at fluence 150 mJ/cm^2 . The time delays are shown on left side images. The right side micrographs are the corresponding post-mortem images. The scale bar is $5 \mu\text{m}$.

6.5. Bibliography

- [1] R. Pillarisetty, “Academic and industry research progress in germanium nanodevices,” *Nature*, vol. **479**, p. 324–328 (2011).
- [2] J. S. Langer, “Instabilities and pattern forestation in crystal growth,” *Rev. Mod. Phys.*, vol. **52**, p. 1–30 (1980).
- [3] T. LaGrange, B. W. Reed, M. K. Santala, J. T. McKeown, A. Kulovits, J. M. K. Wiezorek, L. Nikolova, F. Rosei, B. J. Siwick, G. H. Campbell, “Approaches for ultrafast imaging of transient materials processes in the transmission electron microscope,” *Micron*, vol. **43**, p. 1108–1120 (2012).
- [4] L. Nikolova, D. Riabinina, B. Kadari, J. M. MacLeod, M. Chaker, F. Rosei, “Synthesis and Characterization of Group IV Nanocrystals,” *ECS Transactions*, vol. **28**, p. 15–31 (2010).
- [5] L. Nikolova, T. LaGrange, B. W. Reed, M. J. Stern, N. D. Browning, G. H. Campbell, J.-C. Kieffer, B. J. Siwick, and F. Rosei, “Nanocrystallization of amorphous germanium films observed with nanosecond temporal resolution,” *Appl. Phys. Lett.*, vol. **97**, p. 203102-1–3 (2010).
- [6] L. Nikolova, T. Lagrange, M. J. Stern, J. M. MacLeod, B. W. Reed, H. Ibrahim, G. H. Campbell, F. Rosei, B. J. Siwick, “Complex crystallization dynamics in amorphous germanium followed with dynamic transmission electron microscopy,” *Phys. Rev. B*, vol. **87**, p. 064105-1-6 (2013).
- [7] L. Nikolova, M. Stern, J. M. MacLeod, B. W. Reed, H. Ibrahim, G. H. Campbell, F. Rosei, T. LaGrange, and B. Siwick, “*In situ* investigation of explosive crystallization in a-Ge: Experimental determination of the interface response function using dynamic transmission electron microscopy,” *Manuscript submitted to J. App. Phys.* (2014).
- [8] M. L. Taheri, S. McGowan, L. Nikolova, J. E. Evans, N. Teslich, J. P. Lu, T. LaGrange, F. Rosei, B. J. Siwick, and N. D. Browning, “In situ laser crystallization of amorphous silicon: Controlled nanosecond studies in the dynamic transmission electron microscope,” *App. Phys. Lett.*, vol. **97**, p. 032102-1–3 (2010).

- [9] B. J. Siwick, J. R. Dwyer, R. E. Jordan, and R. J. D. Miller, "An Atomic-Level View of Melting Using Femtosecond Electron Diffraction," *Science*, vol. **302**, p. 1382–1386 (2003).
- [10] B. J. Siwick, J. R. Dwyer, R. E. Jordan, R. J. D. Miller, "Femtosecond electron diffraction studies of strongly driven structural phase transitions," *Chem. Phys.*, vol. **299**, p. 285–305 (2004).
- [11] E. P. Donovan, F. Spaepen, D. Turnbull, J. M. Poate, and D. C. Jacobson, "Calorimetric studies of crystallization and relaxation of amorphous Si and Ge prepared by ion implantation," *J. Appl. Phys.*, vol. **57**, p. 1795–1804 (1985).
- [12] D. Turnbull, "On the melting of amorphous Ge and Si", *MRS Symposia Proc.: Metastable materials formation by ion implantation*, Elsevier Science Publishing Company, Inc., p. 103-108 (1982).
- [13] J. Koga and T. Yamaguchi, "Structural transitions in disordered phases of germanium under rapid quenching and pressuring," *Phys. Chem. Glasses.*, vol. **46**, p. 425–432 (2004).
- [14] B. W. Reed, M. R. Armstrong, N. D. Browning, G. H. Campbell, J. E. Evans, T. LaGrange, and D. J. Masiel, "The evolution of ultrafast electron microscope instrumentation," *Microsc. Microanal.*, vol. **15**, p. 272–281 (2009).

List of publications

- [1] **L. Nikolova**, T. Lagrange, M. J. Stern, J. M. MacLeod, B. W. Reed, H. Ibrahim, G. H. Campbell, F. Rosei, B. J. Siwick, “Complex crystallization dynamics in amorphous germanium followed with dynamic transmission electron microscopy,” *Phys. Rev. B*, vol. **87**, p. 064105-1-6 (2013).
- [2] **L. Nikolova**, M. J. Stern, J. M. MacLeod, B. W. Reed, H. Ibrahim, G. H. Campbell, F. Rosei, T. LaGrange, B. J. Siwick, “In situ investigation of explosive crystallization in a-Ge: Experimental determination of the interface response function using dynamic transmission electron microscopy,” Manuscript submitted at *J. App. Phys.* (2014).
- [3] T. LaGrange, B. W. Reed, M. K. Santala, J. T. McKeown, A. Kulovits, J. M. K. Wiezorek, **L. Nikolova**, F. Rosei, B. J. Siwick, G. H. Campbell, “Approaches for ultrafast imaging of transient materials processes in the transmission electron microscope,” *Micron*, vol. **43**, p. 1108–1120 (2012).
- [4] **L. Nikolova**, T. LaGrange, B. W. Reed, M. J. Stern, N. D. Browning, G. H. Campbell, J.-C. Kieffer, B. J. Siwick, and F. Rosei, “Nanocrystallization of amorphous germanium films observed with nanosecond temporal resolution,” *Appl. Phys. Lett.*, vol. **97**, p. 203102-1–3 (2010).
- [5] M. L. Taheri, S. McGowan, **L. Nikolova**, J. E. Evans, N. Teslich, J. P. Lu, T. LaGrange, F. Rosei, B. J. Siwick, and N. D. Browning, “In situ laser crystallization of amorphous silicon: Controlled nanosecond studies in the dynamic transmission electron microscope,” *App. Phys. Lett.*, vol. **97**, p. 032102-1–3 (2010).
- [6] **L. Nikolova**, D. Riabinina, B. Kadari, J. M. MacLeod, M. Chaker, F. Rosei, “Synthesis and Characterization of Group IV Nanocrystals,” *ECS Transactions*, vol. **28**, p. 15–31 (2010).

Statement of Originality

All e-beam evaporations of a-Ge and a-Si were done by the author with the equipment at École Polytechnique de Montréal.

All estimations of the thickness of the a-Ge and a-Si layers were done by the author with the equipment at École Polytechnique de Montréal and INRS Centre EMT.

The silicon dioxide windows for the a-Si crystallisation study were fabricated by S. McGowan at McGill University.

All post mortem real and reciprocal space TEM images were acquired by the author with the TEM instruments at McGill University and École Polytechnique de Montréal. Time resolved images of a-Ge (zones II & III) and a-Ge/SiO for (zone III) were taken by the author with the DTEM at LLNL, USA (the author obtained a temporal permission from LLNL to operate the instrument).

The following time resolved images were taken by Dr. Thomas Lagrange at LLNL upon request from the author because at the time of acquisition of the images the author was not authorised to operate the DTEM due to the very strict policy of the LLNL regarding foreign nationals working on the territory and with equipment of the lab:

Chapter III crystallisation in a-Ge/SiO – Zone I and Zone II

Chapter IV crystallisation in a-Ge – Zone I

Time resolved images of a-Si/SiO₂ crystallisation were taken by Dr. James Evans at LLNL upon request from the author for the same reasons as cited above.

All the measurements on mean sizes of the grains, calculation of the nucleation rate, velocities of crystallisation, RMS of the roughness and estimation of the time for complete

crystallisation and activation energy were done by the author.

Results on thermal modelling on a-Ge/SiO and self-sustained a-Ge films done by M. Stern were taken from his MSc thesis “Time resolved transmission electron microscopy: the structural dynamics of explosive crystallization in amorphous germanium,” McGill University, Montréal, Québec, Canada (2012).

Results on thermal modelling on a-Si/SiO₂ done by S. McGowan were taken from her MSc thesis “In situ study of amorphous semiconductor crystallization by Dynamic Transmission Electron Microscopy,” McGill University, Montréal, Québec, Canada (2009).

Calculations on the temperature evolution in Zone II for a-Ge and a-Ge/SiO by the Dendritic Growth Model were made by the author (source for the model: D. A. Porter, K. E. Easterling and M. Y. Sherif, “Phase transformation in metal and alloys,” 3rd ed., CRC Press – Taylor and Francis Group LLC (2009).

All false color images preparation was done by the author except of Figure 2 and image A in Figure 16 which were done by Dr. J. MacLeod.

Since the project is a collaborative work between INRS, LLNL and McGill the following figures were taken from the joint publications:

Figure #	Sources:
2, 16A, 25, 34, 40, 48	L. Nikolova, T. Lagrange, M. J. Stern, J. M. MacLeod, B. W. Reed, H. Ibrahim, G. H. Campbell, F. Rosei, B. J. Siwick, “Complex Crystallization Dynamics in Amorphous Germanium Followed with Dynamic Transmission Electron Microscopy,” Phys. Rev. B, vol. 87 , p. 064105-1-6 (2013)

Figure #	Sources:
10	L. Nikolova, T. LaGrange, B. W. Reed, M. J. Stern, N. D. Browning, G. H. Campbell, J.-C. Kieffer, B. J. Siwick, and F. Rosei, "Nanocrystallization of amorphous germanium films observed with nanosecond temporal resolution," <i>Appl. Phys. Lett.</i> , vol. 97, p. 203102 (2010)
55	Part of the images are in M. L. Taheri, S. McGowan, L. Nikolova, J. E. Evans, N. Teslich, J. P. Lu, T. LaGrange, F. Rosei, B. J. Siwick, and N. D. Browning, "In situ laser crystallization of amorphous silicon: Controlled nanosecond studies in the dynamic transmission electron microscope," <i>Appl. Phys. Lett.</i> , vol. 97, p. 032102 (2010)
59	M. L. Taheri, S. McGowan, L. Nikolova, J. E. Evans, N. Teslich, J. P. Lu, T. LaGrange, F. Rosei, B. J. Siwick, and N. D. Browning, "In situ laser crystallization of amorphous silicon: Controlled nanosecond studies in the dynamic transmission electron microscope," <i>Appl. Phys. Lett.</i> , vol. 97, p. 032102 (2010)

The following figures were adapted from the literature:

Figure #	Sources:
1	E. P. Donovan, F. Spaepen, D. Turnbull, J. M. Poate, and D. C. Jacobson, "Calorimetric studies of crystallization and relaxation of amorphous Si and Ge prepared by ion implantation," <i>J. Appl. Phys.</i> , vol. 57, p. 1795–1804 (1985)
3	A. Chojnacka and M. O. Thompson, "Morphological Instabilities during Explosive Crystallization of Germanium Films," <i>MRS Symp. Proc.</i> , vol. 648, p. P11.12.1 (2001) and R. K. Sharma, <i>et al.</i> , "Electron beam induced explosive crystallization of unsupported amorphous germanium thin films," <i>J. Appl. Phys.</i> , vol. 55, p. 387–394 (1984)

Figure

Sources:

- 4 D. B. Williams and C. B. Carter, Transmission Electron Microscopy – A Textbook for Materials Science (2nd edition), Springer, New York, NY, USA (2009)
- 5 M. R. Armstrong, , K. Boyden, N. D. Browning, G. H. Campbell, J. D. Colvin, W. J. DeHope, A. M. Frank, D. J. Gibson, F. Hartemann, J. S. Kim, W. E. King, T. B. LaGrange, B. J. Pyke, B. W. Reed, R. M. Shuttlesworth, B. C. Stuart, B. R. Torralva, “Practical considerations for high spatial and temporal resolution dynamic transmission electron microscopy,” *Ultramicroscopy*, vol. 107, p. 356-367 (2007)
- 6 Website of Kimball Physics Inc. <http://www.kimballphysics.com/>
- 23 D. A. Porter, K. E. Easterling and M. Y. Sherif in “Phase transformation in metal and alloys” (A-C) and J. S. Langer in “Instabilities and pattern forestation in crystal growth” (D)
- 25 M. Stern, MSc thesis “Time resolved transmission electron microscopy: the structural dynamics of explosive crystallization in amorphous germanium,” McGill University, Montréal, Québec, Canada (2012)
- 39 N.H. March, R.A. Street and M. Tosi, “Amorphous Solids and the Liquid State”, Plenum Press – New York (USA) (1985)
- 53, 55, 56 S. McGowan, MSc Thesis: “In situ study of amorphous semiconductor crystallization by Dynamic Transmission Electron Microscopy,” McGill University, Montréal, Québec, Canada (2009)

Résumé en français

Observation *in situ* de la cristallisation induite par faisceau laser dans les semi-conducteurs du groupe IV

Mise en contexte

Les semi-conducteurs du groupe IV sont largement utilisés dans la fabrication de dispositifs de l'électronique moderne. Avec l'augmentation de la demande du marché pour les appareils de petite taille qui fonctionnent plus rapidement et qui sont moins coûteux, de plus en plus d'attention est accordée à la cristallisation induite par faisceau laser des couches amorphes de silicium et de germanium. En particulier, des études ont été entreprises pour l'utilisation de germanium cristallin dans de nouveaux dispositifs, car ce matériau possède la plus grande mobilité de charges positives parmi tous les semi-conducteurs connus qui existent en forme massive [1]. Le recuit par faisceau laser offre la possibilité d'augmenter la température au niveau local et, donc, de faciliter la fabrication de dispositifs complexes. Le taux d'augmentation de la température par laser est plus élevé que dans un four classique de cristallisation. De plus, le processus de cristallisation par laser évolue extrêmement vite. En conséquence, il est essentiel d'avoir une compréhension profonde de la cinétique et de la thermodynamique liées à la transformation de l'état amorphe à l'état cristallin. Cela permettra le contrôle de la microstructure finale qui se reflète directement sur les propriétés du matériau et la fonctionnalité du dispositif final.

La cristallisation de germanium amorphe (Ge-a) ou de silicium amorphe (Si-a) induite par faisceau laser produit une structure cristalline finale qui est très complexe. Dans le cas de la cristallisation induite par laser du Ge-a, trois microstructures distinctes sont formées avec des tailles de cristaux qui varient de quelques nanomètres à quelques micromètres. La figure 1 montre une image obtenue en microscopie électronique en transmission (MET) en champ clair de la structure cristalline du film de germanium induite par une impulsion laser.

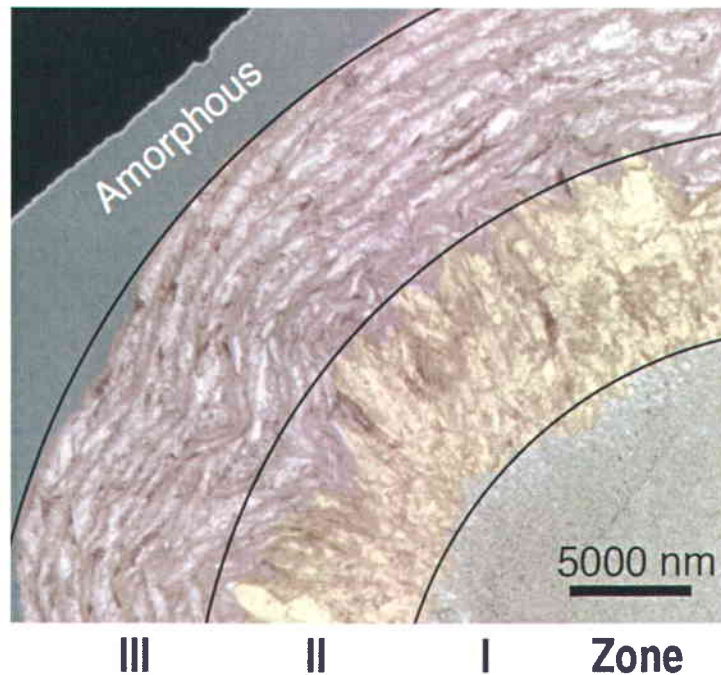


Figure. 1. Image MET conventionnelle en champ clair montrant les trois régions avec des morphologies qualitativement distinctes produites par une impulsion laser dans du Ge-a. Une symétrie radiale est observée car la pointe du faisceau laser utilisé pour initier la cristallisation était de forme circulaire. Les trois morphologies sont indiquées sur la figure comme suit : Zone I – région nanocristalline centrale où le faisceau laser a déposé son énergie; Zone II – région des grands cristaux ayant une orientation radiale et une structure dendritique; Zone III – structure multicouche composée de couches nanocristallines en alternance avec des couches de grands cristaux orientés tangentiellement. Des fausses couleurs sont utilisées pour accentuer les différentes morphologies. Figure réimprimée de [2].

On peut y distinguer trois zones morphologiques que nous nommerons comme suit: Zone I – région nanocristalline centrale où le faisceau laser a déposé son énergie; Zone II – région des grands cristaux avec une orientation radiale qui forment une structure dendritique; Zone III – structure multicouche composée de couches nanocristallines en alternance avec des couches de grands cristaux orientés tangentiellement. Dans le cas de la cristallisation du Si-a, seulement deux morphologies sont présentes (Figure 2): structure microcristalline centrale composée de cristaux de forme rectangulaire et structure nanocristalline qui entoure la structure microcristalline. Pour les deux matériaux, le processus évolue dans un intervalle de

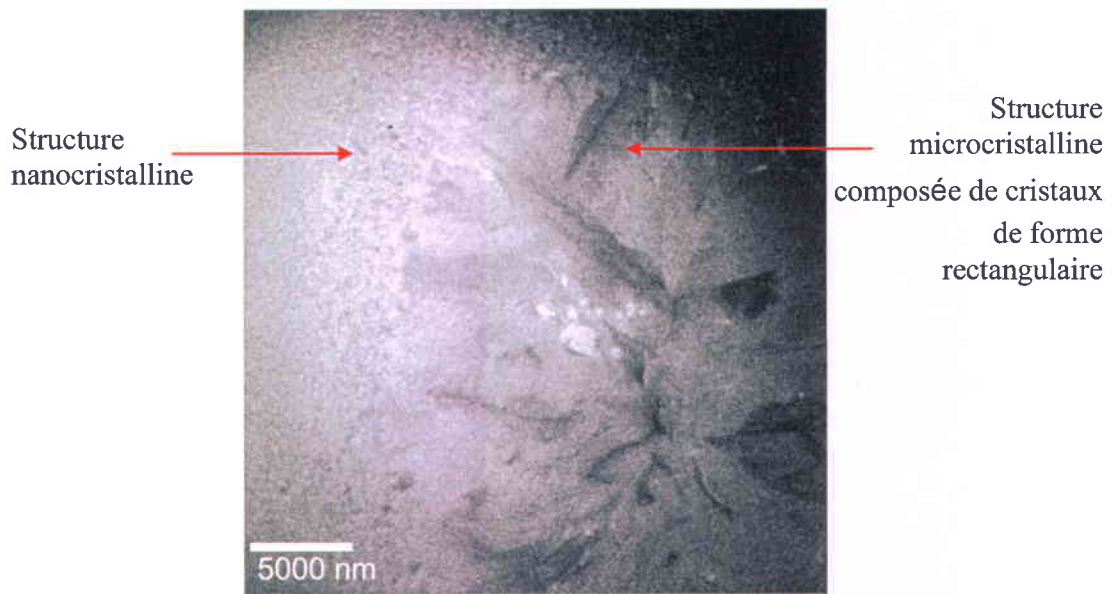


Figure. 2. Image MET conventionnelle en champ clair montrant la morphologie typique formée après une cristallisation induite par une impulsion laser dans du Si-a.

temps allant de quelques nanosecondes à quelques microsecondes après que l'impulsion laser ait déposé son énergie. Par conséquent, pour étudier les structures transitoires formées au cours de ces processus, une résolution temporelle de quelques nanosecondes et une résolution spatiale de quelques nanomètres sont nécessaires.

Techniques expérimentales

La microscopie électronique en transmission dynamique (METD) est la technique principale qui a été employée dans cette étude. L'instrument utilisé pour les investigations *in situ* et pour l'acquisition des images résolues en temps est un MET conventionnel qui a été modifié pour permettre la visualisation avec hautes résolutions temporelle et spatiale des changements structuraux survenant au cours d'une transformation (Figure 3). La technique consiste à employer un paquet d'électrons de courte durée comme une sonde d'imagerie, de manière à acquérir une image instantanée de la structure de l'échantillon au cours de la transition de phase ou lors d'une réaction à un champ externe. Pour cela, deux modifications majeures ont été faites sur l'instrument. Dans un premier temps, le canon d'électrons conventionnel

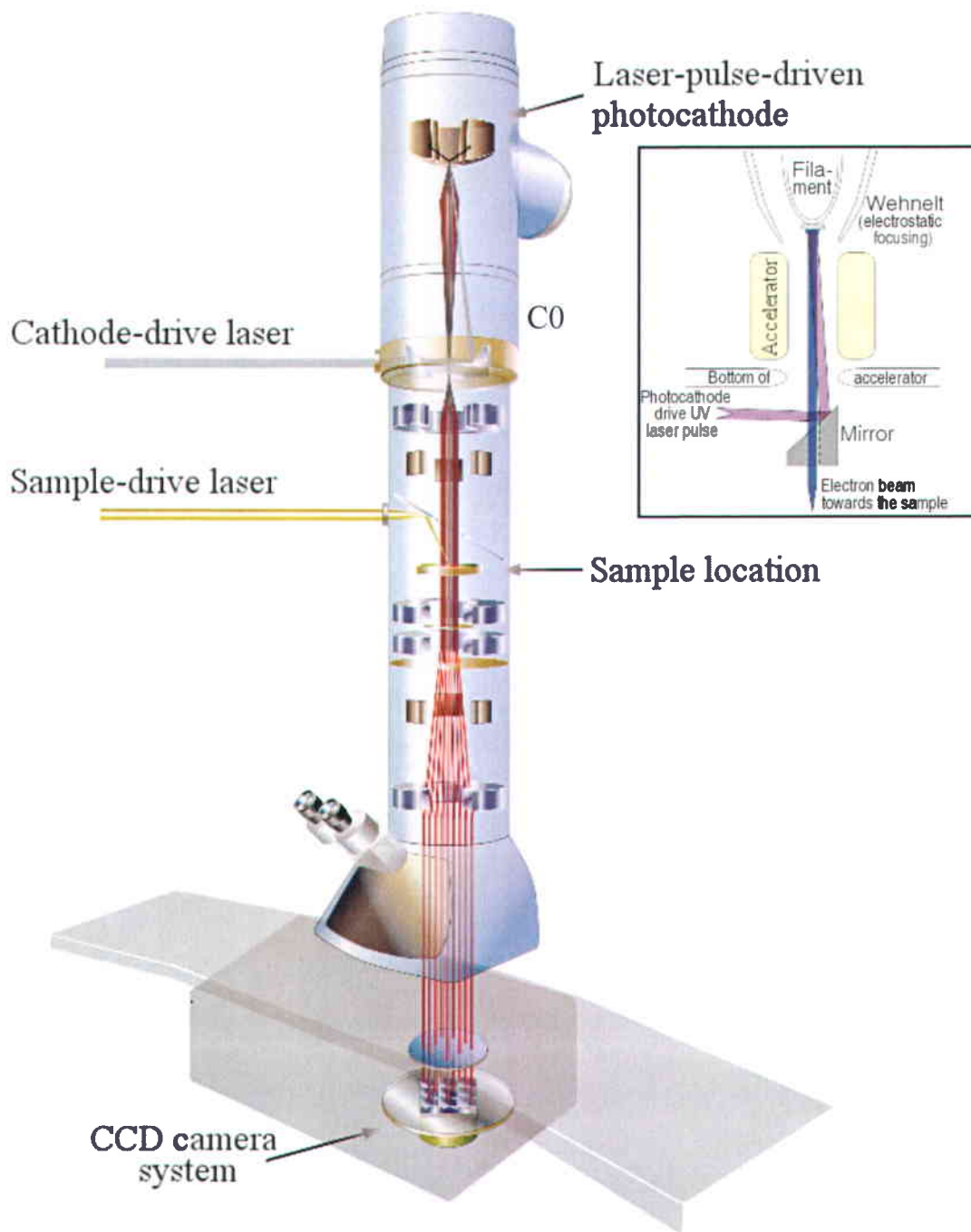


Figure. 3. Représentation schématique du METD développé au LLNL (figure adaptée de [3]). La position du miroir de molybdène est donnée sur la droite plutôt que dans le trajet du faisceau d'électrons pour plus de clarté sur les voies des faisceaux laser et électronique. L'encart donne une représentation réaliste du chemin du faisceau laser qui excite la cathode et la position spatiale du miroir.

a été remplacé par une photocathode. Par la suite, deux lasers ont été attachés à la colonne. Les paquets d'électrons sont générés par effet de photoémission lors de l'irradiation de la photocathode par une impulsion laser UV d'une durée de quelques nanosecondes. Pour cette raison, le laser qui excite la source d'électrons est appelé 'cathode-drive laser'. Le faisceau de ce laser est introduit dans la colonne et dirigé vers la photocathode par un miroir (Figure 3 encart). Une transformation est induite dans l'échantillon par le deuxième laser qui est nommé 'sample-drive laser'. La longueur d'onde et la durée d'impulsion de ce laser sont choisies selon le procédé à étudier. Dans notre cas, nous avons utilisé un laser de 211 nm et une durée d'impulsion de 15 ns pour exciter la source d'électrons. Pour induire la transformation de phase dans l'échantillon, nous avons utilisé un laser de 532 nm avec une durée d'impulsion de 15 ns pour avoir une bonne absorption de la longueur d'onde dans l'épaisseur de la couche [4]. Les images de la structure de l'échantillon sont prises à différents intervalles de temps après le début de la transformation. Puisque la densité des charges dans l'impulsion électronique est très élevée ($\sim 10^9$ électrons par impulsion) [5], [6], le MTED permet l'acquisition d'images instantanées et complètes de la microstructure de l'échantillon avec une seule expérience. C'est pour cette raison qu'il est possible de reconstruire la séquence des changements à l'échelle nanométrique au cours du processus. Le principal avantage de cet appareil est qu'il permet l'investigation *in situ* des processus *irréversibles* en raison de la possibilité d'acquérir une image complète avec une seule expérience. Le MTED utilisé pour exécuter les expériences dans ce travail a été élaboré et construit au Lawrence Livermore National Laboratory (LLNL) [7].

Pour étudier la structure des échantillons après la cristallisation, nous avons utilisé la MET conventionnelle en champ clair et en champ sombre, ainsi que l'acquisition de clichés de diffraction sur les différentes régions cristallines de l'échantillon.

Objectifs de la thèse

Les objectifs principaux de cette thèse étaient de révéler la séquence de changement de la morphologie lors de la croissance des différentes structures, de dévoiler la forme du front de cristallisation au cours de sa propagation, d'estimer les vitesses de cristallisation et de donner un aperçu sur les modes de croissance possibles en tenant compte des

estimations de la température dans la couche. Pour cela, nous avons utilisé des couches de Ge-a sans substrat qui sont soutenues par une grille de cuivre standard ainsi que des couches de Ge-a déposées sur une membrane de monoxyde de silicium. Les échantillons ont été conçus avec cette configuration dans le but d'élucider l'influence du substrat sur la cinétique et la thermodynamique de la transformation de phase. Dans le cas de la cristallisation du Si-a nous avons utilisé des couches déposées sur des fenêtres d'oxyde de silicium formées sur un substrat de silicium monocristallin (Figure 5).

Résultats principaux

Cristallisation du germanium amorphe

Nous avons étudié la dynamique de cristallisation des couches de Ge-a soutenues par une grille de cuivre standard et de couches de Ge-a déposées sur une membrane isolante. Nous avons constaté que la cristallisation commence moins de 20 ns après l'arrivée de l'impulsion laser pompe et s'achève environ 10 μ s plus tard. Le processus se déroule en séquences. Dans un premier temps, la nucléation et la nanocristallisation se produisent et forment une région nanocristalline centrale (Figure 1 – Zone I) avec une taille des grains qui peut atteindre quelques centaines de nanomètres. Par la suite, la croissance de la seconde structure (dendritique) est initiée et elle se produit dans la direction radiale, soit parallèle à la diffusion de la chaleur (Figure 1 – Zone II et Figure 4). La croissance de la structure multicouche finale est lancée à la fin de la croissance dendritique et progresse dans la direction azimutale, c'est-à-dire en direction perpendiculaire au flux net de la chaleur (Figure 1 – Zone III et Figure 6). Contrairement aux prédictions théoriques, nous n'avons pas observé de pause dans l'évolution de ces structures.

La cristallisation de la zone centrale nanocristalline est provoquée par l'énergie déposée par le faisceau laser qui initie la transformation. Nous avons trouvé que le processus est dominé par la nucléation jusqu'à ce que le temps de cristallisation complète soit atteint. Par la suite, la nanocristallisation se poursuit par la croissance des grains. Ce processus est contrôlé par la diffusion et la coalescence des cristaux voisins ayant à peu près la même orientation de leurs plans cristallographiques. Nous avons estimé que la température maximale dans la Zone I se situe entre ~ 1000 K et ~ 1100 K. La croissance de la deuxième structure

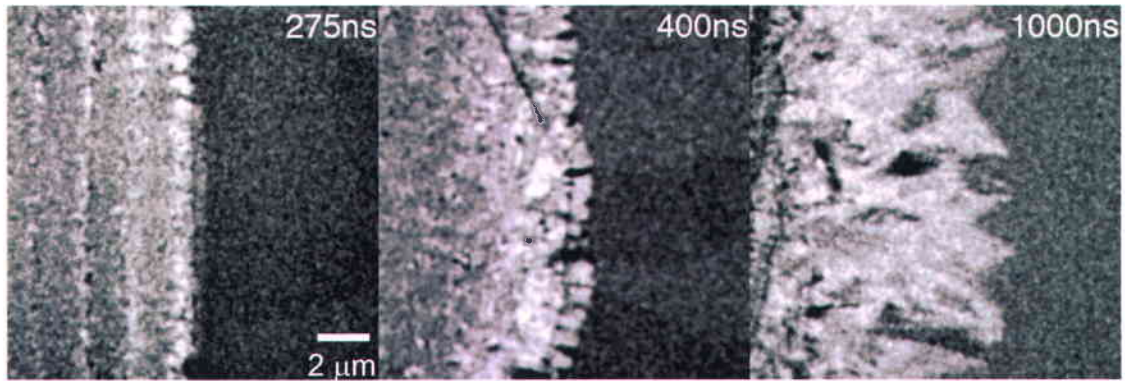


Figure. 4. Images de la croissance dendritique résolues en temps montrant la forme du front de cristallisation au cours de sa propagation et l'augmentation de sa rugosité. Les délais sont indiqués dans le coin supérieur droit de chaque image. La barre d'échelle est la même pour toutes les images.

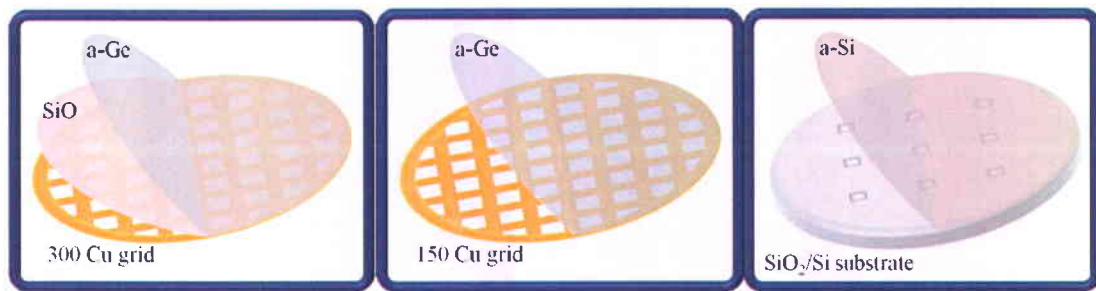


Figure. 5. Configuration des échantillons. De gauche à droite : 110 nm Ge-a / 40 nm SiO / grille de cuivre de 300 mailles; 110 nm Ge-a / grille de cuivre de 150 mailles; 130 nm Si-a / 50 nm SiO₂ / substrat de silicium.

(zone dendritique) est soutenue par le dégagement de chaleur lors de la transformation de phase de l'état amorphe à l'état cristallin. Cela permet la propagation du front de cristallisation à presque 10 μm à l'extérieur de la limite de la zone centrale. La vitesse de cristallisation est relativement faible au début de la croissance ($< 6 \text{ m/s}$) et une zone de transition se forme entre la structure nanocristalline de la Zone I et la structure dendritique de la Zone II. Par la suite, la cristallisation dans la Zone II suit un régime explosif et la vitesse de cristallisation augmente rapidement jusqu'à environ 16 m/s. Après que la vitesse maximale de cristallisation soit atteinte, celle-ci diminue de nouveau. Une estimation de la température au moyen d'un modèle pour la croissance dendritique, qui a été développé pour des systèmes métalliques,

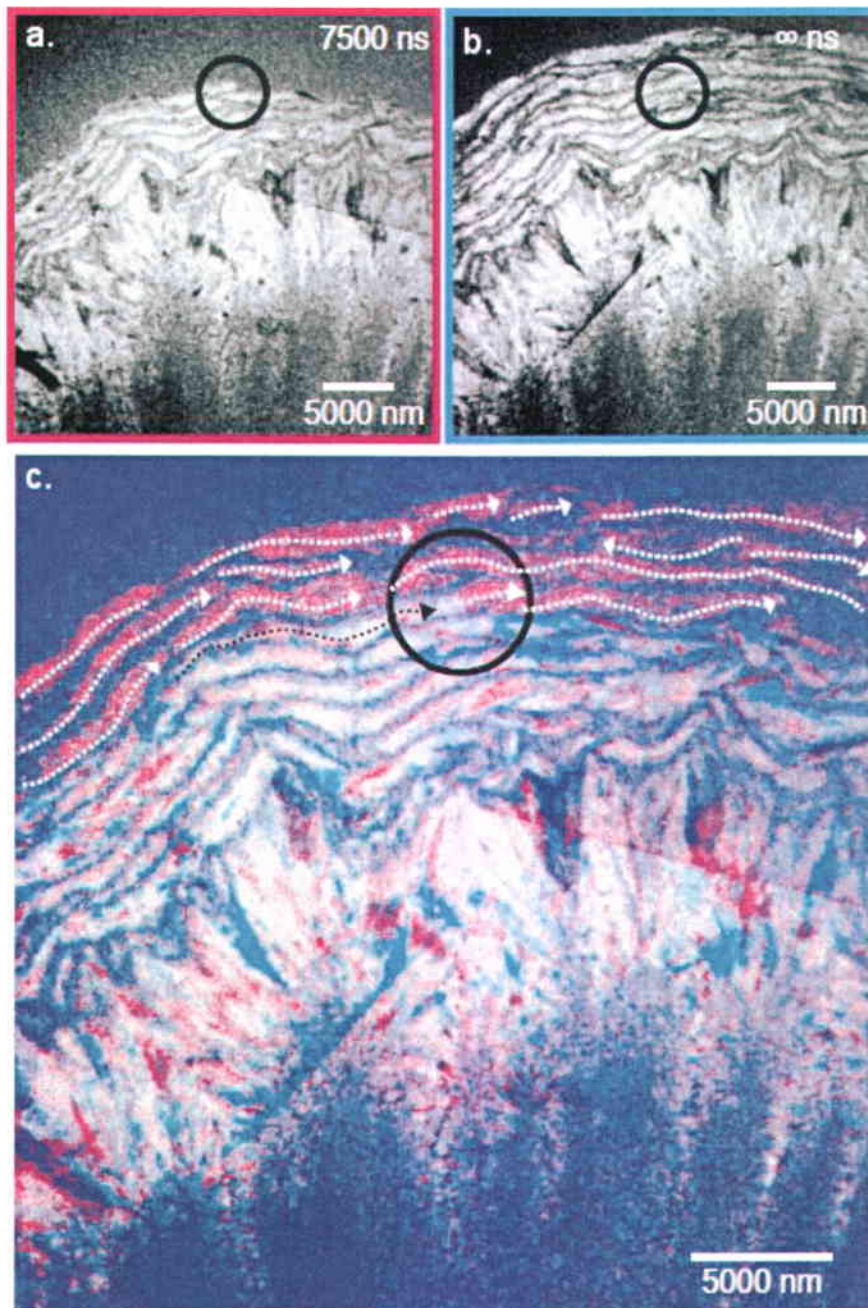


Figure. 6. Front de cristallisation dans la Zone III. (a) une image METD instantanée de la microstructure 7500 ns après l'exposition au laser. Une couche externe partiellement formée est indiquée par un cercle. (b) La microstructure finale à la fin de la cristallisation. (c) des images colorées et empilées montrant la relation entre les microstructures instantanée (blanc) et finale (rose). L'avancement radial du front de cristallisation se produit par l'accumulation de couches supplémentaires comme indiqué schématiquement avec des flèches en pointillés. Figure réimprimée de [2].

s'est avérée très complexe parce que les dendrites complètent leur croissance en formant des pointes. Ainsi, il est difficile d'estimer sans ambiguïté le rayon de la dendrite lors de la croissance. C'est pourquoi nous avons conclu que ce modèle peut donner une estimation qualitative de la température dans la couche à partir des images post-mortem, mais que l'estimation quantitative de la température obtenue par cette méthode est peu fiable. Cependant il s'avère que qu'un modèle développé pour décrire la diffusion et la génération de la chaleur dans une couche mince décrit bien la croissance cristalline et cela pour les deux types d'échantillons utilisés dans cette étude. Ce modèle¹ a montré que la température est en baisse tout au long de la Zone II (Figure 7). À la fin de la croissance dendritique, il est probable que la température favorise la nucléation pour permettre la formation de la première bande nanocristalline dans la structure multicouche (Zone III). Bien que la vitesse radiale de l'avancement du front de cristallisation pour la structure multicouches ait été mesurée à ~ 1 m/s, la vitesse de croissance dans la direction azimutale reste à déterminer.

Nous avons estimé que dans la région centrale, la nucléation se produit à une température inférieure à la température de fusion du matériau cristallin. La croissance dendritique se produit par co-propagation de deux interfaces : cristallin-liquide (où la chaleur est libérée) et liquide-amorphe (où la chaleur est absorbée). L'interface liquide-amorphe se propage en direction radiale avant l'interface cristallin-liquide (Figure 8). Par conséquent, une couche de liquide métastable mince est formée, ce qui permet la croissance des cristaux aux vitesses élevées observées. L'estimation de l'évolution de la température nous a permis de conclure que l'augmentation de la vitesse de cristallisation est un effet de l'augmentation du sous-refroidissement du liquide métastable. L'augmentation continue du sous-refroidissement entraîne ensuite la diminution de la vitesse de cristallisation pour les plus longs délais. Puisque la microstructure des dendrites n'a montré aucune particularité dans les orientations cristallographiques de ces cristaux, et que les microstructures observées lors de la cristallisation du Ge-a présentent toujours des caractéristiques similaires, nous qualifions les dendrites vues dans nos échantillons comme des dendrites en "libre croissance" dans un liquide sous-refroidi [11]. Les effets capillaires sont insuffisants pour maintenir le front de croissance lisse parce que nos observations montrent que la rugosité du front de cristallisation augmente avec le temps (Figure 4). C'est pour cette raison que nous avons conclu que l'instabilité

¹ Plus de détails sur le modèle peuvent être trouvés à [10] et en Annexe A.

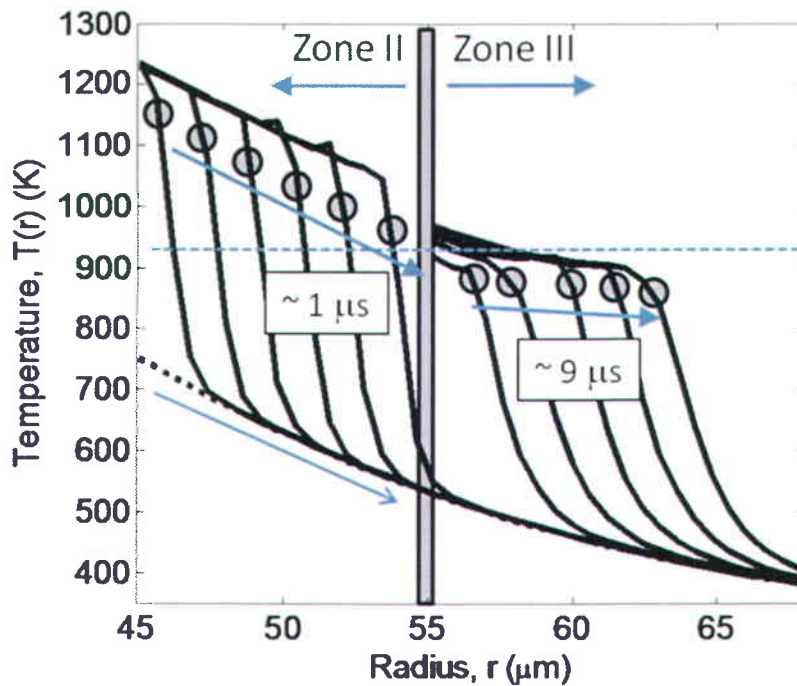


Figure. 7. Evolution de la température $T(r)$ dans la direction radiale (symétrie circulaire) dans le film de Ge-a déposé sur une membrane de monoxyde de silicium, dans les zones II et III dans le voisinage du front de cristallisation, à chaque 150 ns à travers la zone II et à chaque 1,8 μs à travers la zone III. La position radiale du front de cristallisation à chaque délai est indiquée par un cercle gris. La diminution de la température à travers la zone II suit approximativement la diminution de $T(r)$ en raison de la distribution gaussienne de l'énergie déposée par le laser (ligne de base en pointillés). Une distribution similaire de la température en direction radiale a été observée pour la cristallisation du Ge-a auto-soutenu. Figure réimprimée avec la permission de [2].

de type Mullins-Sekerka [12] joue un rôle crucial dans le développement de la forme finale des dendrites. Nous avons trouvé que la dépendance de la vitesse de cristallisation dans la Zone II par rapport à la température est similaire à celle des matériaux vitreux; cependant, la cristallisation dans le Ge-a se produit au-dessus de la température de fusion du matériau amorphe. Nos données suggèrent que la croissance de la structure multicouche se fait dans la direction azimutale par un mécanisme similaire à la croissance de la structure dendritique, i.e. par l'intermédiaire d'une couche liquide métastable. Cette dernière forme des poches qui se propagent devant le front de cristallisation. Le temps de formation de la Zone III et

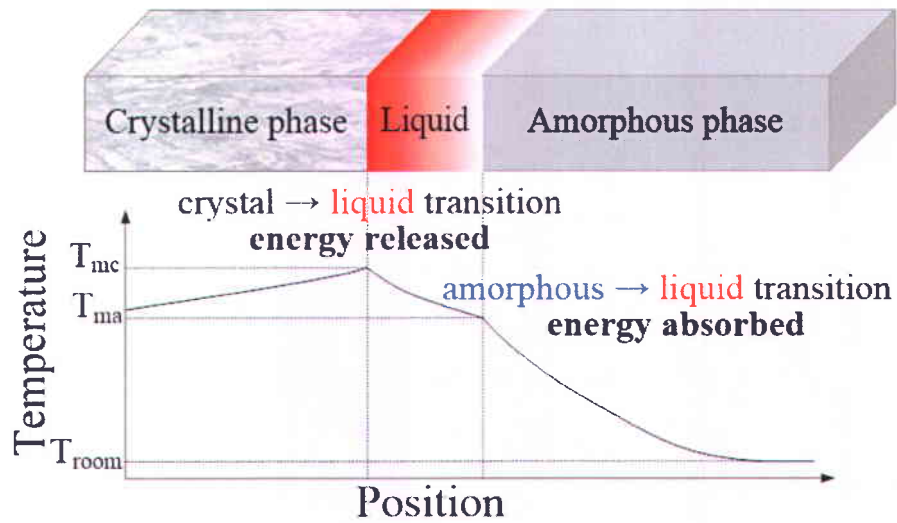


Figure. 8. Représentation schématique de la co-propagation des interfaces amorphe-liquide et cristal-liquide avec un profil possible de la température. Figure adaptée de [8] et [9].

les estimations de la diffusion de la chaleur provenant de l'énergie du laser et de la chaleur générée par la transformation de la phase indiquent que la formation de la structure multicouche est influencée par deux effets opérant dans des directions perpendiculaires. La diffusion de la chaleur en direction radiale entraîne la création d'une bande fine parallèle au front de la diffusion de la chaleur qui résultera en une distribution quasi-homogène de la température dans la direction radiale et la propagation du front de cristallisation en direction azimutale. Cependant, il n'est pas clair quelle est la vitesse de cristallisation dans cette direction. Avec la configuration et le mode d'opération du METD d'aujourd'hui, il n'est pas possible d'évaluer cette vitesse. De plus, puisque les cristaux ayant une orientation azimutale possèdent beaucoup de défauts, il n'est pas possible de déterminer précisément où un cristal commence et où il finit. C'est pourquoi l'estimation de la vitesse de croissance à partir des images post-mortem est plutôt spéculative. La morphologie des bandes nanocristallines indique que la croissance peut se produire en raison de la dissipation de la chaleur au cours de la propagation des poches liquéfiées. Malheureusement, la formation de nanocristaux dans la structure multicouche ne peut pas être observée en raison de la petite taille de ces cristaux. Néanmoins, ces études nous ont permis de confirmer une des théories sur la croissance de la structure multicouche [9] et d'affirmer que la croissance se

produit par l'intermédiaire d'un liquide métastable [13].

La cristallisation du silicium amorphe

La dynamique de cristallisation du Si-a s'est avérée dépendante de la fluence du laser utilisée pour initier la cristallisation car nous avons observé un retard dans l'initiation de la croissance qui augmente avec l'augmentation de l'énergie de l'impulsion laser. Nous avons constaté que pour les fluences laser utilisées dans cette étude, le processus est accompagné par la fusion d'une partie de la couche de Si-a favorisant une « croissance super-latérale » ('super lateral growth') [14], [15] des cristaux². La nanocristallisation se produit à la périphérie de la région fondue, mais à une distance très limitée. La cristallisation se produit vers l'intérieur, c'est-à-dire vers le centre de la région chauffée, ce qui provoque la formation de la microstructure à grains longs observée dans les images. Nos observations soutiennent la théorie que la croissance de grands cristaux se fait par le mécanisme de « croissance super-latérale ».

Nous avons trouvé qu'une fluence similaire mène vers deux mécanismes différents pour la cristallisation du Si-a et du Ge-a. Nous avons émis l'hypothèse que ceci résulte de la profondeur d'absorption de l'énergie du laser. Pour la couche de Si-a, le laser de 532 nm est absorbé à une profondeur de ~100 nm (i.e. presque sur l'épaisseur totale de la couche) tandis que dans le Ge-a, la profondeur est de ~50 nm [4] (i.e. sur la moitié de l'épaisseur totale de la couche). Ceci mène à la formation d'une grande quantité de silicium liquide à la température de fusion du matériau cristallin, ce qui favoriserait la croissance super-latérale. Dans le cas du Ge-a, la même fluence est absorbée sur la moitié de l'épaisseur de la couche ce qui empêcherait le film entier d'atteindre la température de fusion du matériau cristallin. En conséquence, le Ge-a cristallise plutôt par cristallisation explosive par l'intermédiaire d'un liquide métastable. Cependant, il est important de noter que cette hypothèse doit être confirmée par des études METD sur la cristallisation explosive dans le Si-a et la diffraction électronique ultrarapide pour l'évaluation des intervalles de temps nécessaire pour la transition de phase du solide amorphe vers la phase liquide.

² Plus de détails sur le modèle peuvent être trouvés à [16] et en Annexe B.

Contributions originales de la thèse

Cette thèse contribue à l'avancement des connaissances sur la cristallisation induite par laser pour les semi-conducteurs du groupe IV par les approches et les contributions scientifiques originales suivantes:

- *Nous avons démontré que la METD est une technique indispensable pour les études in situ des processus ultrarapides irréversibles qui conduisent à la formation de microstructures complexes* [17], [18]. Nous avons démontré que l'instrument utilisé est un nouvel outil pour la caractérisation des systèmes nanométriques et possède un très grand potentiel pour fournir de nouvelles connaissances cruciales sur les mécanismes de transformation à l'échelle nanométrique. Son principal avantage est l'opération en mode d'acquisition d'une image instantanée dans une seule expérience, ce qui permet l'étude des processus irréversibles. Cela est irréalisable au moyen d'instruments qui forment l'image par des pompages laser multiples de l'échantillon et de la source d'électrons.

- *Nous avons été en mesure de visualiser in situ la nanocristallisation du Ge-a et d'estimer le taux de nucléation pendant la cristallisation.* [19]. Notre étude a permis la visualisation et la quantification en temps réel et en espace de la taille moyenne et du nombre des nanocristaux. L'approche est unique parce que l'estimation de ces paramètres effectuée dans les études antérieures était basée uniquement sur la structure post-mortem du matériau. Ce travail est le premier à offrir l'évaluation directe *in situ* du taux de nucléation maximale dans le Ge-a.

- *Nous avons dévoilé la dynamique complexe de la cristallisation dans le Ge-a* [2]. Nous avons déterminé sans équivoque les directions de la croissance des structures dendritique et multicouche. Les résolutions spatiale et temporelle élevées du METD ont permis la visualisation du front de croissance des deux structures, ainsi que la détermination des vitesses de croissance. Cette étude a aussi permis d'estimer l'évolution de la température dans le temps et dans la direction radiale et d'élucider les mécanismes qui gouvernent la transition de phase pour les deux structures.

- *Nous avons montré que la présence d'une couche de support a peu d'influence sur la cinétique de la croissance dendritique du Ge-a, mais joue un rôle plus important dans la croissance de la structure multicouche* [20]. Nous avons montré que le modèle de la génération et le transfert de la chaleur dans une couche mince décrit bien le processus de cristallisation pour les deux types d'échantillons (auto-soutenu et couche de Ge-a déposée sur une membrane) et permet ainsi une détermination de la dépendance de la vitesse de croissance par rapport à la température à l'intérieur de la couche.

- *Nous avons réussi à élucider la cinétique de la cristallisation dans le Si-a* [21]. L'étude de la cristallisation du Si-a par METD a permis de confirmer que la croissance s'effectue par l'intermédiaire d'une couche liquéfiée qui existe à la surface du film amorphe. Par conséquent, nous pouvons affirmer que la formation de cristaux de taille micrométrique dans la partie centrale de la région excitée, et entourée de nanocristaux à la périphérie, est due au mécanisme de « croissance super-latérale ». En outre, nous avons montré que les temps de cristallisation complète dépendent de la fluence laser, de telle façon que les fluences plus élevées requièrent plus de temps pour que la cristallisation soit complète.

Liste de références :

1. R. Pillarisetty, "Academic and industry research progress in germanium nanodevices," *Nature*, vol. 479, p. 324–328 (2011).
2. L. Nikolova, T. LaGrange, M. J. Stern, J. M. MacLeod, B. W. Reed, H. Ibrahim, G. H. Campbell, F. Rosei, and B. J. Siwick, "Complex crystallization dynamics in amorphous germanium observed with dynamic transmission electron microscopy," *Phys. Rev. B*, vol. 87, 064105–1-6 (2013).
3. M. R. Armstrong, K. Boyden, N. D. Browning, G. H. Campbell, J. D. Colvin, W. J. DeHope, A. M. Frank, D. J. Gibson, F. Hartemann, J. S. Kim, W. E. King, T. B. LaGrange, B. J. Pyke, B. W. Reed, R. M. Shuttlesworth, B. C. Stuart, B. R. Torralva, "Practical considerations for high spatial and temporal resolution dynamic transmission electron microscopy," *Ultramicroscopy*, vol. 107, p. 356–367 (2007).
4. M. Von Allmen, Laser-Beam Interactions with Materials. Physical Principles and applications, Springer-Verlag Berlin Heidelberg (Germany) (1987).
5. W. E. King, G. H. Campbell, A. Frank, B. W. Reed, J. F. Schmerge, B. J. Siwick, B. C. Stuart, and P. M. Weber, "Ultrafast electron microscopy in materials science, biology, and chemistry," *J. Appl. Phys.*, vol. 97, p. 111101-1–27 (2005).
6. T. LaGrange, M. R. Armstrong, K. Boyden, C. G. Brown, G. H. Campbell, J. D. Colvin, W. J. DeHope, A. M. Frank, D. J. Gibson, F. V. Hartemann, J. S. Kim, W. E. King, B. J. Pyke, B. W. Reed, M. D. Shirk, R. M. Shuttlesworth, B. C. Stuart, B. R. Torralva, and N. D. Browning, "Single-shot dynamic transmission electron microscopy," *Appl. Phys. Lett.*, vol. 89, p. 044105–044107 (2006).
7. B. W. Reed, M. R. Armstrong, N. D. Browning, G. H. Campbell, J. E. Evans, T. LaGrange and D. J. Masiel, "The Evolution of Ultrafast Electron Microscope Instrumentation," *Microsc. Microanal.*, vol. 15, p. 272–281 (2009).
8. A. Chojnacka and M. O. Thompson, "Morphological Instabilities during Explosive Crystallization of Germanium Films," *MRS Symp. Proc.*, vol. 648, p. P11.12.1-1–8 (2001).
9. R. K. Sharma, S. K. Bansal, R. Nath, R. M. Mehra, K. Bahadur, R. P. Mall, K. L. Chaudhary, and C. L. Garg, "Electron beam induced explosive crystallization of

- unsupported amorphous germanium thin films,” *J. Appl. Phys.*, vol. 55, p. 387–394 (1984).
10. M. Stern, MSc Thesis: Time resolved transmission electron microscopy: the structural dynamics of explosive crystallization in amorphous germanium, McGill University, Montréal, Québec, Canada (2012).
 11. J. S. Langer, “Instabilities and pattern forestation in crystal growth,” *Rev. Mod. Phys.*, vol. 52, p. 1–30 (1980).
 12. W. W. Mullins, and B. F. Sekerka, “Morphological Stability of a Particle Growing by Diffusion or Heat Flow,” *J. Appl. Phys.*, vol. 34, p. 323–329 (1963).
 13. A. P. Chojnacka, PhD Thesis: Explosive crystallization of germanium films: Kinetics and morphologies, Cornell University (2002).
 14. J. S. Im, H. J. Kim, and M. O. Thompson, “Phase transformation mechanisms involved in excimer laser crystallization of amorphous silicon films,” *Appl. Phys. Lett.*, vol. 63, p. 1969–1971 (1993).
 15. J. S. Im and H. J. Kim, “On the super lateral growth phenomenon observed in excimer laser induced crystallization of thin Si films,” *Appl. Phys. Lett.*, vol. 64, p. 2303–2305 (1994).
 16. S. McGowan, MSc Thesis: “In situ study of amorphous semiconductor crystallization by Dynamic Transmission Electron Microscopy,” McGill University, Montréal, Québec, Canada (2009).
 17. T. LaGrange, B. W. Reed, M. K. Santala, J. T. McKeown, A. Kulovits, J. M. K. Wiezorek, L. Nikolova, F. Rosei, B. J. Siwick, G. H. Campbell, “Approaches for ultrafast imaging of transient materials processes in the transmission electron microscope,” *Micron*, vol. 43, p. 1108–1120 (2012)
 18. L. Nikolova, D. Riabinina, B. Kadari, J. M. MacLeod, M. Chaker, F. Rosei, “Synthesis and Characterization of Group IV Nanocrystals,” *ECS Transactions*, vol. 28, p. 15–31 (2010).
 19. L. Nikolova, T. LaGrange, B. W. Reed, M. J. Stern, N. D. Browning, G. H. Campbell, J.-C. Kieffer, B. J. Siwick, and F. Rosei, “Nanocrystallization of amorphous germanium films observed with nanosecond temporal resolution,” *Appl. Phys. Lett.*, vol. 97, p. 203102-1–3 (2010).

20. L. Nikolova, M. Stern, J. M. MacLeod, B. W. Reed, H. Ibrahim, G. H. Campbell, F. Rosei, T. LaGrange, and B. Siwick, “*In situ* investigation of explosive crystallization in a-Ge: Experimental determination of the interface response function using dynamic transmission electron microscopy,” Manuscript soumis à J. App. Phys. (2014).
21. M. L. Taheri, S. McGowan, L. Nikolova, J. E. Evans, N. Teslich, J. P. Lu, T. LaGrange, F. Rosei, B. J. Siwick, and N. D. Browning, “In situ laser crystallization of amorphous silicon: Controlled nanosecond studies in the dynamic transmission electron microscope,” App. Phys. Lett., vol. 97, p. 032102-1–3 (2010).

Annex A

Thermal modeling developed by M. Stern at McGill University under the supervision of prof. B. Siwick based on the DTEM images acquired by the author of the present work

DTEM can reveal in significant detail the microstructural evolution during the complex and extremely rapid nanosecond laser-induced crystallization of an amorphous semiconductor film, as shown in the previous chapter. Interpreting these images with the goal of explaining the growth mechanisms is further aided by an understanding of the time dependent temperature distribution in the sample. Since the DTEM provides accurate data for the distribution of the distinct crystallized zones and the speed and direction of crystal growth, these results also facilitate a temperature calculation based on thermal diffusion of the laser deposited energy and the exothermic crystallization front using a phenomenological approach. In this chapter the finite element algorithm developed to model the temperature profile in the film is described and results on the temperature evolution at the crystallization front through zone II are presented. This approach has the advantage of being a fully 2D calculation, allowing for angular asymmetry in the source terms and boundary conditions as necessary.

A.1. Thermal modelling

A simple model is constructed to estimate the time dependent temperature profile of the film. The simplest model for 2D heat flow in a thin film is given by [1]

$$\frac{\partial u(x, y, t)}{\partial t} = D\Delta u(x, y, t) + f(x, y, t) \quad (A1)$$

where $u(x, y, t)$ is the temperature of the film at 2D position, (x, y) , and time, t . The source term, $f(x, y, t)$ is the rate at which the temperature changes at a point in time in units of

[TemperatureDifference]/[Time]. The thermal diffusivity of the material is given by

$$D = \frac{k}{\rho C_p} \quad (\text{A2})$$

where k is the thermal conductivity, ρ is the mass density and C_p is the specific heat at constant pressure. D is given in units of [Distance]²/[Time]. This quantity can be used to calculate the diffusion length, L_d , which characterizes how far heat will propagate in the substance after a given time

$$L_d = 2\sqrt{Dt}, \quad (\text{A3})$$

or

$$L_d = \frac{2D}{v_n}, \quad (\text{A4})$$

where v_n is the directional derivative of the temperature by time in the n direction. This quantity can be used for comparing crystal nucleation and growth rates with the speed of the temperature front. An algorithm for finding solutions to Eq. A1 is discussed here.

A.1.1. 2D heat diffusion

Consider the 2D heat equation on the domain, $\Omega \in \mathbb{R}^2$, and its polygonal boundary Γ . Let $\Gamma_N := \Gamma/\Gamma_D$, where Γ_D is the region where a solution must be set at specific values (Dirichlet) and Γ_N is the region where this holds for the first derivative (Neumann).

$$\frac{\partial u}{\partial t} = \Delta u + f \quad \text{in } \Omega \times [0, \tau] \quad (\text{A5})$$

$$u = u_d \quad \text{on } \Gamma_D$$

$$\frac{\partial u}{\partial n} = g \quad \text{on } \Gamma_N$$

A.1.2. Weak formulation

Where, $u(x, y, t)$ is the variable to be solved and $f(x, y, t)$ is the inhomogeneous

term or applied heat. $u_D(t)$ is the fixed value of u on the boundary defined by the Dirichlet condition. g is the value of the directional derivative of u pointed in the normal direction, n , defined by the Neumann condition.

For simplicity, let us assume Dirichlet conditions, that is to say $g \equiv 0$. We will now discretize the time dependence of the problem. We first partition the time interval into n subintervals, $[t_0 = 0, t_1], [t_1 = t_2] \dots [t_{n-1}, t_n = \tau]$. Define, $u_i = u(x, y, t_i)$, and apply the following scheme to Eq. A5

$$(1 - dt\Delta)u_n = dtf_n + u_{n-1} \quad (\text{A6})$$

This is known as an implicit Euler scheme. Now, after integrating both sides over the domain, Ω , a test function, $v(x, y)$, is applied to both sides.

$$\int_{\Omega} u_n v dx - dt \int_{\Omega} \Delta u_n v dx = dt \int_{\Omega} f_n v dx + \int_{\Omega} u_{n-1} v dx \quad (\text{A7})$$

This is called the weak formulation of the boundary problem. The solution to this equation (called the weak solution) may not be an analytic function but will satisfy the above equation. The weak solution can be proved to exist using the Lax-Milgram lemma [2]. Finally, both sides are integrated by parts to explicitly apply the boundary conditions.

$$\int_{\Omega} u_n v dx + dt \int_{\Omega} \nabla u_n \cdot \nabla v dx = dt \left(\int_{\Omega} f_n v dx + \int_{\Gamma_D} g_n v ds \right) + \int_{\Omega} u_{n-1} v dx \quad (\text{A8})$$

A.1.3. Discretization

The problem will be reduced to a linear matrix equation. This will be implemented using a Galerkin method where u_n and v_n are replaced U_n and V_n which exist in a N -dimensional dimensional subspace, S , of the original function space.

$$\int_{\Omega} U_n V dx + dt \int_{\Omega} \nabla U_n \cdot \nabla V dx = dt \left(\int_{\Omega} f_n V dx + \int_{\Gamma_D} g_n V ds \right) + \int_{\Omega} U_{n-1} V dx \quad (\text{A9})$$

Now S will have a finite number of basic functions η_k and

$$U_n = \sum_{k \in I} u_{nk} \eta_k \quad (\text{A10})$$

$$V_n = \sum_{k \in I} v_{nk} \eta_k \quad (\text{A11})$$

where $I = [1, N]$. Applying Eq. A10 and A11 to A8

$$\int_{\Omega} U_n \eta_j dx + dt \int_{\Omega} \nabla U_n \cdot \nabla \eta_j dx = dt \left(\int_{\Omega} f_n \eta_j dx + \int_{\Gamma_D} g_n \eta_j ds \right) + \int_{\Omega} U_{n-1} \eta_j dx \quad (\text{A12})$$

Finally, the problem may be written in the form:

$$(dtA + B)U_n = dtf_n + BU_n \quad (\text{A13})$$

where

$$A_{jk} = \int_{\Omega} \nabla \eta_j \cdot \nabla \eta_k dx \quad (\text{A14})$$

$$B_{jk} = \int_{\Omega} \eta_j \eta_k dx \quad (\text{A15})$$

These are known as the Stiffness and Mass matrices respectively due to the analogous system of a restoring force (i.e. Hooke's law).

A.1.4. Constructing the Stiffness and Mass Matrices

Supposing that the domain Ω has a polygonal boundary, it is trivial to prove that there exists a set of triangles and quadrilaterals, \mathcal{T} , that covers Ω and whose intersection is zero [3]. Let \mathcal{N} be the set of N nodes that comprise the vertices of the triangles in \mathcal{T} . The basic functions η_k may now be chosen to be delta functions corresponding to these nodes,

$$\eta_j(x_k, y_k) = \delta_{jk} \quad j, k = 1, \dots, N \quad (\text{A16})$$

Now, consider a single element, $\in \mathcal{T}$, which only has three vertices,

$$\eta_j(x_k, y_k) = \delta_{jk} \quad j, k = 1, 2, 3 \quad (\text{A17})$$

one can show that,

$$\eta_j(x, y) = \det \begin{pmatrix} 1 & x & y \\ 1 & x_{j+1} & y_{j+1} \\ 1 & x_{j+2} & y_{j+2} \end{pmatrix} / \det \begin{pmatrix} 1 & x_j & y_j \\ 1 & x_{j+1} & y_{j+1} \\ 1 & x_{j+2} & y_{j+2} \end{pmatrix} \quad (\text{A18})$$

and taking the gradient,

$$\nabla \eta_j(x, y) = \frac{1}{2|T|} \det \begin{pmatrix} y_{j+1} - y_{j+2} \\ x_{j+2} - x_{j+1} \end{pmatrix}, \quad (\text{A19})$$

where the area of a triangle, T is simply given by half the following determinant,

$$2|T| = \det \begin{pmatrix} x_2 - x_1 & x_3 - x_1 \\ y_2 - y_1 & y_3 - y_1 \end{pmatrix}. \quad (\text{A20})$$

Using this result, the stiffness matrix may now be assembled,

$$\int_T \nabla \eta_j \cdot \nabla \eta_k dx = \frac{1}{4|T|} \det \begin{pmatrix} y_{j+1} - y_{j+2} & x_{j+2} - x_{j+1} \\ y_{k+1} - y_{k+2} & x_{k+2} - x_{k+1} \end{pmatrix} \quad (\text{A21})$$

Similarly, using the same identity (Eq. A17), the mass matrix is calculated.

$$\int_T \eta_j \eta_k dx = \frac{1}{24} \det \begin{pmatrix} x_2 - x_1 & x_3 - x_1 \\ y_2 - y_1 & y_3 - y_1 \end{pmatrix} \begin{pmatrix} 2 & 1 & 1 \\ 1 & 2 & 1 \\ 1 & 1 & 2 \end{pmatrix}. \quad (\text{A22})$$

Lastly, consider the source term on the right hand side of the equation

$$\int_T f \eta_j dx \approx \frac{1}{6} \det \begin{pmatrix} x_2 - x_1 & x_3 - x_1 \\ y_2 - y_1 & y_3 - y_1 \end{pmatrix} f(x_s, y_s) \quad (\text{A23})$$

$$b_j = \sum_{T \in \mathcal{T}} \int_T f \eta_j dx. \quad (\text{A24})$$

A.2. The source terms and geometry

The parameters and dimensions of the DTEM geometry are $300\mu\text{m} \times 300\mu\text{m} \times 100\text{nm}$ a-Ge film supported by 40 nm of SiO. The thermal properties of the film are given in Table AI.

Table AI: Physical Properties of amorphous germanium

Property	Value	Source
Density	$5.0 \pm 0.3 \text{ g/cm}^3$	[4]
Thermal Conductivity	$130 \pm 20 \text{ mW/cm}^3 \text{ K}$	[5]
Specific Heat	$1.6 \text{ J/cm}^3 \text{ K}$	[6]
Heat of Crystallisation $a \rightarrow c$	800 J/cm^3	[6]
Reflectivity at 532 nm	0.51 ± 0.1	[7]
Absorption Length at 532 nm	$2 \times 10^5 \text{ cm}^{-1}$	[8]

The diffusion length for $10 \mu\text{s}$ (Eq. A3) is $l_d = 16 \mu\text{m}$. So the temperature will not diffuse far enough to approach the boundary, thus we can assume simple Dirichlet boundary conditions where the film edges are held at room temperature.

For Zone I, the thermal behaviour is extremely non-trivial. The initial pulse will certainly cause the a-Ge temperature to pass T_{ma} and melt the film. If one calculates the temperature increase and naively neglects the phase transition that will occur, the temperature in Zone I will reach nearly 2000 K. Of course, the actual temperatures will be much lower due to the different reflectivity and heat capacity of liquid germanium. Near the Zone I boundary, however, the pump pulse imparts nearly a 10^{th} of this energy. One must assume that somewhere in the illuminated region the temperature is enough to melt the film but not heat it past the crystalline melting temperature (1200 K). This will ensure an area composed of undercooled melted film. Due to the metastable nature of the undercooled liquid germanium, the liquid will crystallize very quickly releasing exothermic energy into the film. This is the largest source of heat evolution in the film on the microsecond time scale. Since the thermal diffusion is slow, we assume the temperature in Zone I is constant near the amorphous melting temperature, and phenomenologically model the source term based on the observed behaviour in Zone II. The underlying temperature profile outside of Zone I is initially set using the energy imparted from the excitation pulse. The Gaussian shape of the pulse causes the initial temperature profile outside of Zone I to be shaped as a Gaussian tail.

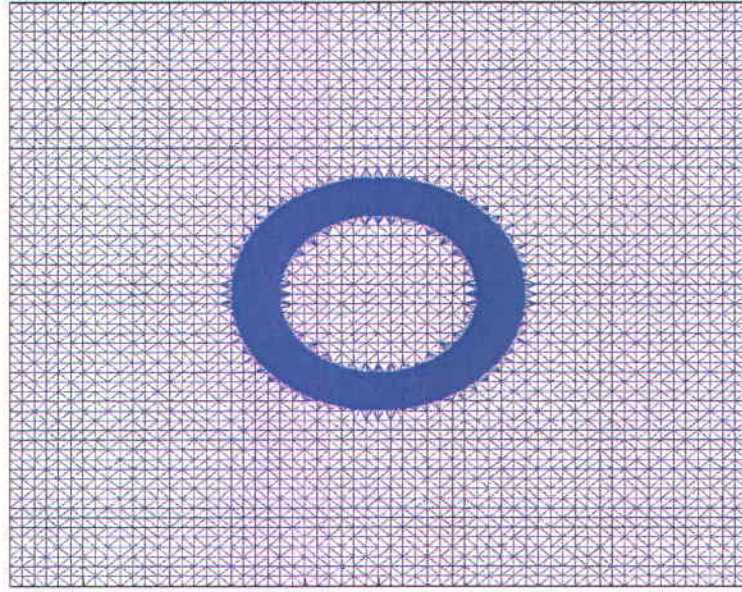


Figure. A1. Triangulation of the grid used with $r_{zI} = 45$ highlighting the area of interest. Grid spacing is ten times finer in this region

For Zone II and III, we have a travelling source term moving at $v_g = 8 \text{ m/s}$ and $v_g = 1 \text{ m/s}$ respectively starting at $t_{i_{zI}} = 0 \text{ ns}$ and ending at $t_{f_{zII}} = 10000 \text{ ns}$. The dendritic crystallization front is discretized into a $\Delta_r = 50 \text{ nm}$ band which moves at v_g starting from r_{zI} releasing the latent heat at a time $\Delta t = 5 \text{ ns}$.

$$f_{zII}(x, y, t) = \frac{L}{C_p \Delta t} h(t_{i_{zII}} - t) h(t - t_{f_{zII}}) h(r_{zI} + v_g(t - t_{i_{zII}}) - r) h(r - (r_{zI} + v_g(t - t_{i_{zII}}) + \Delta r)) \quad (\text{A25})$$

The small lengths required for this term require a very high spatial sampling which makes computation times impractical. Thus a grid with varying element sizes is used (Figure. A1).

A.3. Bibliography

- [1] M. Grimaldi, P. Baeri, and M. Malvezzi, "Melting temperature of unrelaxed amorphous silicon," *Physical Review B*, vol. **44**, p. 1546–1553 (1991).
- [2] J. Alberty, C. Carstensen, and S. A. Funken, "Remarks around 50 lines of MATLAB: short finite element implementation," *Numerical Algorithms*, vol. **20**, 117–137 (1999).
- [3] P. Ciarlet, *The Finite Element Method for Elliptic Problems*, North-Holland, Amsterdam (1978).
- [4] R. K. Sharma, S. K. Bansal, R. Nath, R. M. Mehra, K. Bahadur, R. P. Mall, K. L. Chaudhary, and C. L. Garg, "Electron beam induced explosive crystallization of unsupported amorphous germanium thin films," *J. Appl. Phys.*, vol. **55**, p. 387–394 (1984).
- [5] P. Nath and K. L. Chopra, "Thermal conductivity of amorphous and crystalline Ge and GeTe films," *Phys. Rev. B*, vol. **10**, p. 3412–3418 (1974)).
- [6] H. S. Chen and D. Turnbull, "Specific heat and heat of crystallization of amorphous germanium," *J. Appl. Phys.*, vol. **40**, p. 4214–4215 (1969).
- [7] J. Prins, *Physics of non-crystalline solids proceedings of the international conference, Delft, July, 1964*, North-Holland Pub. Co.; Interscience Publishers, Amsterdam; New York (1965).
- [8] J. Stuke, "Review of optical and electrical properties of amorphous semiconductors," *Journal of Non-Crystalline Solids*, vol. **4**, p. 1–26 (1970).

Annex B

Thermal modeling developed by S. McGowan at McGill University under the supervision of prof. B. Siwick based on the DTEM images acquired by the author of the present work

B.1. Thermodynamics of crystallization: A simple model

The threshold energy for melting a thin film of thickness z can be estimated from the solution to the heat diffusion equation [1].

$$\frac{\partial T}{\partial t} = \frac{1}{\rho C_p} \frac{\partial}{\partial z} \left(k \frac{\partial T}{\partial z} \right) + \frac{\alpha}{\rho C_p} I(z, t) \quad (\text{B1})$$

where ρ is the density, C_p is the specific heat, k is the thermal conductivity, α is the optical absorption coefficient and $I(z)$ is the optical power density

$$I(z) = I_0(1 - R)e^{-\alpha z} \quad (\text{B2})$$

where I_0 is the incident power density and R is the reflectivity. Assuming the material constants are not temperature dependent and that the thermal diffusion length, $L = \sqrt{Dt}$, is greater than the optical absorption depth, α^{-1} , the solution is:

$$T(z, t) = \frac{2I_0(1 - R)L}{k} \text{ierfc} \frac{z}{2L} \quad (\text{B3})$$

where

$$D = \frac{k}{\rho C_p} \quad (\text{B4})$$

Taking

$$I_0 = \frac{E_0}{\tau} \quad (\text{B5})$$

where E_0 is the incident uence on the sample and τ is the laser pulse duration, the surface

temperature at the end of the pulse is

$$T(0, \tau) = \frac{2E_0(1 - R)}{\sqrt{\pi}\rho C_p L} \quad (\text{B6})$$

Thus, the threshold energy, E_T to raise the film surface to the melt temperature, T_m , from an initial temperature, T_0 is

$$E_T = \frac{(T_m - T_0)\sqrt{\pi}\rho C_p \sqrt{D\tau}}{2(1 - R)} \quad (\text{B7})$$

For a phase change (i.e. liquid to solid, amorphous to crystalline) the latent heat of the transition, ΔH , also needs to be taken into account:

$$E \simeq E_T + \frac{\Delta H \Delta z}{\rho(1 - R)} \quad (\text{B8})$$

To consider the temperature dependence of the thermal properties, it is necessary to solve the heat diffusion equation numerically, as discussed below.

B.2. Heat diffusion and estimate of film temperature

The time-evolution of the temperature distribution in the silicon thin film was calculated to validate the interpretation of the results obtained by DTEM. The sample surface was illuminated by a pump laser with a 100 μm diameter spot size. This is a very large diameter compared to the film thickness (130 nm). Due to the large heat gradient in the direction of the film thickness, the heat conduction in the plane is much slower than the conduction through in the z -direction. Thus, only the conduction through the thickness of the film needs to be considered.

B.2.1. Analytical solution

As described above, the temperature distribution in a thin film can be calculated by solving the heat diffusion equation. The temperature distribution immediately after the pump pulse is given by Eq. B.3. Assuming the film is perfectly insulated such that there is no heat flow out of the film and assuming that the thermal properties of the film remain constant,

Table BI: Optical and thermal constant of amorphous, crystalline and liquid silicon (a-Si, c-Si & l-Si respectively), and the SiO₂ substrate [2], [3].

	R @ 532 nm	α @ 532 nm (cm⁻¹)	T_m (K)	ρC_p (Jcm⁻³K⁻¹)	k (Wcm⁻¹K⁻¹)	ΔH (Jcm⁻¹)
a-Si	0.48	1 × 10 ⁵	1418 ± 40	2.5	0.013	2900 ± 160
c-Si	0.36	2 × 10 ⁴	1681	2.3	0.23	4158
l-Si	0.72	1 × 10 ⁷	—	3.1	0.5	—
SiO ₂	0.04	1	1893	2.6	0.007	—

the solution to the 1D heat equation in the z-direction is

$$u(z, t) = \frac{1}{2}c_0 + \sum_{n=1}^{\infty} c_n \cos\left(\frac{n\pi z}{L}\right) \exp\left(-D\left(\frac{n\pi}{L}\right)^2 t\right) \quad (\text{B9})$$

where $u(z, t)$ is the 1D temperature distribution in the film and c_n are constants is given by

$$c_n = \frac{2}{L} \int_0^L \cos\left(\frac{n\pi z}{L}\right) u(z, 0) dz \quad (\text{B10})$$

which are determined using the initial temperature distribution in the film, $u(z, 0)$, resulting from the assumed impulsive laser excitation.

Using the optical and thermal properties for amorphous silicon found in Table BI and a pulse energy of 180 mJ/cm², the temperature profile was determined for various times after excitation given in Figure 53 (Chapter V).

B.2.2. Heat diffusion model including melting

As the laser pulse heats the sample beyond the melting point, the optical and thermal properties are changed drastically. To correctly handle the transition from solid amorphous silicon to liquid silicon, the heat diffusion equation must be solved numerically including

the correct temperature dependence of the material properties.

To model the temperature evolution in the z -direction in the silicon film, the approach outlined in chapter 4 of Laser Annealing of Semiconductors [2]. In this method, the sample is divided into ' i ' slices of thickness Δz . Time zero is taken as the start of the laser pulse. For each time ' t ' and slice ' i ', the temperature, T_{b_i} , the structure (amorphous, liquid or crystalline) and, if the melting temperature is reached, the fraction of the layer which has melted is computed.

At the surface of the film, the incident laser power is

$$I_1 = I_0(t)(1 - R) \quad (\text{B11})$$

where $I_0(t)$ is gaussian in the time dimension. For the laser used in these experiments with a FWHM of 15 ns.

The power reaching the ' i^{th} ' layer is

$$I_i = I_{i-1} \exp(-\alpha_{i-1} \Delta z) \quad (\text{B12})$$

To calculate the new temperature, T_{a_i} at time $t + \Delta t$, first the energy absorbed from the laser pulse during this time interval is calculated: The energy absorbed in time Δt is

$$\Delta Q_{abs} = I_i (1 - e^{-\alpha_i \Delta z}) \Delta t \quad (\text{B13})$$

The energy per unit area transferred to the nearest-neighbour layers is

$$\Delta Q_{diff} = \left(k_- \frac{T_{b_{i-1}} - T_{b_i}}{\Delta z} + k_+ \frac{T_{b_{i+1}} - T_{b_i}}{\Delta z} \right) \Delta t \quad (\text{B14})$$

where

$$k_- = (k_{i-1} + k)/2 \quad \text{and} \quad k_+ = (k_{i+1} + k)/2 \quad (\text{B15})$$

The new temperature after heat absorption and diffusion is calculated from

$$T_{a_i} = T_{b_i} + \frac{\Delta Q_{abs} + \Delta Q_{diff}}{\rho C_p \Delta z} \quad (\text{B16})$$

If the film is melting or solidifying, the latent heat of the transition must be included

in the computation and Eq. B16 cannot be used. Instead, the energy available for melting (or released from the solidification), given by

$$\Delta Q' = \Delta Q_{abs} + \Delta Q_{diff} - (T_m - T_{b_i})\rho C_p \Delta z \quad (\text{B17})$$

is calculated. With this numerical approach, it is possible for more than one state to exist in a single layer, in which case, we must keep track of the fraction of each layer that has melted

$$\Delta FF = \frac{\Delta Q'}{\Delta H_m \rho \Delta z} \quad (\text{B18})$$

This increment is added to the existing melted fraction, $FF_i(t)$, and $FF_i(t + \Delta t)$ is used to calculate $\Delta Q''$, the heat available for raising (or lowering, if negative) the temperature following melting (or solidification).

The new temperature of the film is then calculated as follows:

$$T_{a_i} = T_m + \frac{\Delta Q''}{\rho C_p \Delta z} \quad (\text{B19})$$

To avoid instabilities in the modeling, it is crucial that certain stability criteria are met. The time increment is related to the slice thickness by the stability relation:

$$\frac{k \Delta t}{\rho C_p} (\Delta z)^2 < \frac{1}{2} \quad (\text{B20})$$

The initial temperature ($t = 0$) is set to $T = 300K$ throughout the film and substrate. The boundary condition at the top surface of the film assumes no loss of heat from the illuminated surface. This is a reasonable assumption since the sample was under vacuum, so there is minimal heat exchange with the surroundings. Heat loss through blackbody radiation could be included in the model, but it is likely negligible on the time scale investigated.

The boundary condition at the substrate is slightly more complicated. Although SiO_2 does not absorb the 532 nm pump pulse due to the low reflectivity and long absorption length at this wavelength, it can conduct heat from the sample. Thus it is not valid to assume that the substrate is thermally insulating. Since the substrate is very thin, it is also a poor assumption to model the oxide as a heat sink at a constant temperature. Thus, the substrate

is allowed to act as a heat bath; heat can be conducted to or from the substrate, but the substrate temperature is not allowed to vary independently of the film temperature.

The thermal conductivity of the substrate is approximately half that of a-Si, but the heat capacity is similar. An improved conduction model would treat the substrate as a series of slices in thickness with different optical and thermal properties than the silicon and model the temperature in both the sample and substrate using the same algorithm. Because this model is very computationally intensive, the simplified model which allowed conduction of heat to the substrate but did not calculate conduction within the substrate was chosen.

Since this model is in one dimension only, heat diffusion in the radial direction from the centre of the pump pulse is neglected. The lateral heat diffusion was modeled independently of the diffusion in the z-direction and, due to the gradual temperature gradient in this direction, was found to be very slow (on the order of milliseconds) and thus can be neglected on short time scales.

The estimations of the temperature with time obtained by this model are presented in Figure 55 (Chapter V).

B.3. Bibliography

- [1] M. Grimaldi, P. Baeri, and M. Malvezzi, "Melting temperature of unrelaxed amorphous silicon," *Physical Review B*, vol. **44**, p. 1546–1553 (1991).
- [2] J. Poate and J. W. Mayer, editors, Laser Annealing of Semiconductors, Academic Press, 1982.
- [3] S. Brotherton, "Polycrystalline silicon thin film transistors," *Semiconductor Science and Technology*, vol. **10**, p.721–738 (1995).

